



DISTORTIONAL-GLOBAL INTERACTION IN COLD-FORMED STEEL LIPPED
CHANNEL COLUMNS: BUCKLING ANALYSIS, STRUCTURAL BEHAVIOR
AND STRENGTH

João Alfredo De Lazzari

Dissertação de Mestrado apresentada ao Programa de Pós-graduação em Engenharia Civil, COPPE, da Universidade Federal do Rio de Janeiro, como parte dos requisitos necessários à obtenção do título de Mestre em Engenharia Civil.

Orientador: Eduardo de Miranda Batista

Rio de Janeiro
Março de 2020

DISTORTIONAL-GLOBAL INTERACTION IN COLD-FORMED STEEL LIPPED
CHANNEL COLUMNS: BUCKLING ANALYSIS, STRUCTURAL BEHAVIOR
AND STRENGTH

João Alfredo De Lazzari

DISSERTAÇÃO SUBMETIDA AO CORPO DOCENTE DO INSTITUTO ALBERTO
LUIZ COIMBRA DE PÓS-GRADUAÇÃO E PESQUISA DE ENGENHARIA DA
UNIVERSIDADE FEDERAL DO RIO DE JANEIRO COMO PARTE DOS
REQUISITOS NECESSÁRIOS PARA A OBTENÇÃO DO GRAU DE MESTRE EM
CIÊNCIAS EM ENGENHARIA CIVIL.

Orientador: Eduardo de Miranda Batista

Aprovada por: Prof. Eduardo de Miranda Batista
Prof. Juarez Moara Santos Franco
Prof. Maximiliano Malite

RIO DE JANEIRO, RJ - BRASIL
MARÇO DE 2020

Lazzari, João Alfredo De

Distortional-Global Interaction in Cold-Formed Steel Lipped Channel Columns: Buckling Analysis, Structural Behavior and Strength / João Alfredo De Lazzari. – Rio de Janeiro: UFRJ/COPPE, 2020.

xvii, 157 p.: il.; 29,7 cm.

Orientador: Eduardo de Miranda Batista

Dissertação (mestrado) – UFRJ/ COPPE/ Programa de Engenharia Civil, 2020.

Referências Bibliográficas: p. 126-139.

1. Distortional-global buckling interaction. 2. Cold-formed steel columns. 3. FSM elastic buckling analysis. 4. FEM numerical non-linear analysis. I. Batista, Eduardo de Miranda II. Universidade Federal do Rio de Janeiro, COPPE, Programa de Engenharia Civil. III. Título.

Acknowledgements

First and foremost, I would like to thank to the God for His blessings throughout my research work.

I would also like to express my sincere gratitude to my research supervisor, Dr. Eduardo de Miranda Batista, for giving me the opportunity to do research and providing invaluable guidance throughout this research.

I am extremely grateful to my parents, Dirceu and Otavia, for their love, prayers, caring and sacrifices for educating and preparing me for my future. Also, I express my thanks to my brother, Lorenzo, for his support and friendship. Additionally, I am thankful for my grandfather, grandmother, aunts, uncles and cousins for their continuing support and valuable prayers.

My Special thanks goes to all my new friends and research colleagues made during the master's program, and also to all my old friends for their constant encouragement and support.

I thank all the staff from LabEST, COPPE, Fundação COPPETEC and UFRJ, for the assistance in my research, specially to Santiago and Anísio, for helping with the experiments.

I am extending my thanks to the peers from MARKO Estruturas Metalicas, Carla, André and Murilo, for receive me at their factory and give me the columns for the tests. Moreover, I would like to thank Roberto and Cheila, from Usifer, for the great work on welding the columns in the base plates.

Finally, my thanks go to all the people who have supported me to complete the research work directly or indirectly.

This work was partially supported by Conselho Nacional de Desenvolvimento Científico e Tecnológico – CNPq (Proc. 131199/2018-8), also partially supported by grant E-26/200.825/2019 (242580), Fundação Carlos Chagas Filho de Amparo a Pesquisa do Estado do Rio de Janeiro (FAPERJ).

Resumo da Dissertação apresentada à COPPE/UFRJ como parte dos requisitos necessários para a obtenção do grau de Mestre em Ciências (M.Sc.)

INTERAÇÃO DISTORCIONAL-GLOBAL EM COLUNAS DE PERFIS
FORMADOS A FRIO COM SEÇÃO U ENRIJECIDO: ANÁLISE DA
FLAMBAGEM, COMPORTAMENTO ESTRUTURAL E RESISTÊNCIA

João Alfredo De Lazzari

Março/2020

Orientador: Eduardo de Miranda Batista

Programa: Engenharia Civil

O objetivo do presente trabalho é estudar a interação distorcional-global (D-G) em colunas de perfis de aço formados a frio (PFF) com seção U enrijecido (Ue), com relação ao comportamento estrutural e resistência. Alguns estudos sobre o tópico têm sido desenvolvidos na literatura, entretanto a interação D-G não é bem conhecida e precisa de atenção. Para a análise elástica de flambagem, um software denominado FStr *Computer Application Program* é criado. O aplicativo é desenvolvido com base no método das faixas finitas, com foco em uma interface fácil e amigável. O programa FStr gera os modos de flambagem e insere como imperfeição inicial no software de elementos finitos ANSYS, objetivando efetuar análise não-linear física e geométrica. Tanto o programa FStr, quanto o modelo em elementos finitos, são validados com exemplos numéricos e experimentos em escala real. Além disso, para o comportamento estrutural e determinação da carga última, são gerados caminhos de estabilidade, provenientes da análise não-linear, com diferentes combinações dos modos global e distorcional como imperfeição inicial. A combinação dos modos de flambagem como alternativa para a imperfeição inicial ajuda a compreensão do comportamento da interação D-G, o qual é difícil prever com uma análise de flambagem elástica. Os resultados para o estudo da combinação dos modos mostraram que, para aço com alta tensão de escoamento, a imperfeição inicial com o modo global apresentou a menor carga última. Adicionalmente, o estudo paramétrico variando o comprimento da coluna demonstrou que a equação da resistência à compressão axial nominal da flambagem global, já presente nas normas, é suficiente para considerar o efeito do fenômeno D-G.

Abstract of Dissertation presented to COPPE/UFRJ as a partial fulfillment of the requirements for the degree of Master of Science (M.Sc.)

DISTORTIONAL-GLOBAL INTERACTION IN COLD-FORMED STEEL LIPPED CHANNEL COLUMNS: BUCKLING ANALYSIS, STRUCTURAL BEHAVIOR AND STRENGTH

João Alfredo De Lazzari

March/2020

Advisor: Eduardo de Miranda Batista

Department: Civil Engineering

The goal of the present research is the distortional-global (D-G) buckling interaction of cold-formed steel (CFS) lipped channel (LC) columns, in its buckling, structural behavior and strength nature. Some studies on this topic have been conducted in the literature, however, the D-G interaction is not well known and needs more attention. For an elastic buckling analysis, a software entitled FStr Computer Application Program is developed. The application is based on the Finite Strip Method, mainly focused in a simple and accessible interface. The FStr program generates the modal shapes and insert as initial geometric imperfections in the finite element software ANSYS, in order to perform a geometric and material nonlinear analysis. Both, the FStr program and the finite element model are validated with available numerical examples and laboratory tests from the literature. Moreover, for the structural behavior and column strength, it is carried out stability paths from previous nonlinear analysis, for different combination of initial geometric imperfection of global and distortional modes. The buckling mode combination as initial geometric imperfection helps to understand the D-G buckling interaction, which is difficult to predict with a simple elastic buckling analysis. The results of the initial imperfection combination have shown that, for high yielding steel, the global initial geometric imperfection provides the most detrimental ultimate load. Additionally, a parametric study varying the column's length have shown that the nominal axial strength for global buckling equation, already in the standards, is enough to cover the D-G coupled phenomenon.

Index

INDEX	VII
SYMBOLS.....	X
1 INTRODUCTION	1
1.1 BACKGROUND	1
1.2 MOTIVATION	3
1.3 OBJECTIVES	3
1.4 OUTLINE.....	4
2 LITERATURE REVIEW	6
2.1 FUNDAMENTALS OF STRUCTURAL STABILITY	6
2.2 THE FINITE STRIP METHOD	11
2.2.1 <i>Matrix Formulation</i>	12
2.3 CRITICAL BUCKLING MODES.....	27
2.4 COMPUTER PROGRAM APPLICATIONS AND METHODS FOR THE BUCKLING ANALYSIS	31
2.5 COUPLED INSTABILITY PHENOMENA	33
2.5.1 <i>Distortional-Global Interaction concepts</i>	35
2.6 ANALYTICAL ELASTIC BUCKLING ANALYSIS	38
2.6.1 <i>Local Buckling</i>	38
2.6.2 <i>Distortional Buckling</i>	39
2.6.3 <i>Global Buckling</i>	42
2.7 DESIGN PROCEDURES FOR COLD-FORMED STEEL COLUMNS.....	43
2.7.1 <i>Effective Width Method (EWM)</i>	44
2.7.2 <i>Effective Section Method (ESM)</i>	45
2.7.3 <i>Direct Strength Method and Additional Procedures (DSM)</i>	46
2.8 STATE-OF-THE-ART	51
3 FSTR - COMPUTER APPLICATION PROGRAM	55

3.1	PROGRAM DESCRIPTION	55
3.2	ELASTIC BUCKLING ANALYSIS VALIDATION.....	60
3.2.1	<i>End Boundary Condition Validation</i>	60
3.2.2	<i>Local Buckling Validation</i>	67
3.2.3	<i>Analytical Validation</i>	70
3.2.4	<i>Finite Element Method Validation</i>	72
3.2.5	<i>Unrestricted Bending Validation</i>	75
4	NUMERICAL MODELING	79
4.1	MODEL DESCRIPTION.....	79
4.1.1	<i>Discretization</i>	80
4.1.2	<i>End boundary conditions</i>	82
4.1.3	<i>Loading</i>	83
4.1.4	<i>Material Model</i>	84
4.1.5	<i>Initial geometric imperfections</i>	85
4.1.6	<i>Analysis Methods</i>	86
4.2	NUMERICAL MODEL VALIDATION	87
4.2.1	<i>Global Buckling Mode Validation</i>	87
4.2.2	<i>Distortional Buckling Mode Validation</i>	92
5	PARAMETRIC ANALYSIS ON DISTORTIONAL-GLOBAL BUCKLING INTERACTION.....	95
5.1	STUDY OF INITIAL GEOMETRIC IMPERFECTION COMBINATION.....	95
5.1.1	<i>Imperfection Combination with different yield stress</i>	105
5.2	STUDY OF D-G BUCKLING INTERACTION NATURE.....	110
6	CONCLUDING REMARKS.....	120
6.1	FINITE STRIP METHOD COMPUTATIONAL TOOL.....	120
6.2	FINITE ELEMENT METHOD NONLINEAR ANALYSIS	121
6.3	THE GLOBAL-DISTORTIONAL BUCKLING MODE OF CFS LIPPED CHANNEL COLUMNS	121
6.4	THE ROLE OF THE NATURE OF THE D-G BUCKLING INTERACTION IN THE BEHAVIOR OF THE COLUMNS.....	123
6.5	SUGGESTIONS FOR FUTURE WORKS.....	124
7	BIBLIOGRAPHY.....	126

APPENDIX A.....	140
APPENDIX B.....	146
APPENDIX C.....	152

Symbols

Capital roman letters

A	Area of the full cross-section
\mathbf{A}	Winter's-type equation coefficient
A_1	Maximum amplitude for initial geometric imperfection of first mode
A_2	Maximum amplitude for initial geometric imperfection of second mode
A_{eff}	Effective cross-section area
A_{hs}	Area of half-section on centerline dimensions
\mathbf{B}	Winter's-type equation coefficient
$[B]$	Matrix with the appropriate partial differentiations of the strain-displacement relationship known as the strain matrix
$[B_{uv}]$	Strain matrix of the membrane assumption
$[B_w]$	Strain matrix of the bending and twisting assumption
C_w	Warping constant
D	Plate stiffness
$[D]$	Elasticity/property matrix
$[D_{uv}]$	Property matrix of an orthotropic material with plane stress assumptions
$[D_w]$	Property matrix of an orthotropic material with bending and twisting assumptions
E	Elastic modulus for isotropic material
E_t	Tangent slope modulus for plastic region
E_x	Elastic modulus for x directions
E_y	Elastic modulus for y directions
$\{F\}$	Vector with the superficial forces applied into the plane xy of the strip
G	Shear modulus of elasticity
G_{xy}	Axial shear moduli in xy plane
$[G]$	Matrix with the partial derivatives of the shape functions
$[G_{uv}]$	Matrix with partial derivatives of the shape functions for the plane stress

$[G_w]$	Matrix with partial derivatives of the shape functions for the bending and twisting.
I_0^*	Apparent polar moment of inertia with respect to web-flange junction point
I_1	Integral of $Y_p Y_q$ along the length of strip (a)
I_2	Integral of $Y_p' Y_q'$ along the length of strip (a)
I_3	Integral of $Y_p Y_q''$ along the length of strip (a)
I_4	Integral of $Y_p'' Y_q''$ along the length of strip (a)
I_5	Integral of $Y_p'' Y_q$ along the length of strip (a)
I_w	Stiffened-flange warping constant with respect to the rotation center
I_z	Moment of inertia of half-section about minor axis
I_{zw}	Cross-section geometric parameter
J	Torsion constant of cross-section
J_s	Lip constant of torsion
$[K]$	Assembled elastic stiffness matrix for global coordinates
$[KG]$	Assembled geometric stiffness matrix or the initial stress matrix for global coordinates
L	Column's length
L_x	Effective length of the member for buckling with bending about the x-x axis
L_y	Effective length of the member for buckling with bending about y-y axis
L_z	Effective length of the member for buckling with twisting
N_{cRd}	Compressive design strength of a member
N_e	Global buckling axial compressive load
N_ℓ	Local buckling axial compressive load
$[N]$	Shape function matrix
$[N_{uv}]$	Shape function matrix for the membrane, assuming only normal and shear stresses
$[N_w]$	Shape function matrix for bending and twisting actions
P_{cr}	Elastic critical load
P_n	Nominal axial strength
P_u	Ultimate load or column strength
P_{crD}	Elastic critical distortional buckling load
P_{nD}	Nominal axial strength for distortional buckling
P_{nDG}	Nominal axial strength for the distortional-global interactive buckling

P_{nDSM}	Nominal axial strength from DSM
P_{crG}	Elastic critical global buckling load
P_{nG}	Nominal axial strength for global buckling
P_{nGD}	Nominal axial strength for the global-distortional interactive buckling
P_{crL}	Elastic critical local buckling load
P_{nL}	Nominal axial strength for global buckling
P_{nLG}	Nominal axial strength for the local-global interactive buckling
P_{nLD}	Nominal axial strength for the local-distortional interactive buckling
P_{nLDG}	Nominal axial strength for the local-distortional-global interactive buckling
P_y	Squash load
$[R]_{8x8}$	Eight by eight rotation matrix (applied to nodal displacement)
$[R]_{3x3}$	Three by three rotation matrix (applied to displacement field)
R_{GD}	Ratio between the critical loads from global and distortional modes
$R_{\lambda DL}$	Ratio between the distortional and local slenderness factor
$R_{\lambda GD}$	Ratio between the global and distortional slenderness factor
T_1	Traction in the i^{th} left edge of a strip
T_2	Traction in the k^{th} right edge of a strip
U	Elastic strain energy of a conservative system
\mathbf{U}	Global orthogonal displacement relative to \mathbf{X} direction
\mathbf{V}	Global orthogonal displacement relative to \mathbf{Y} direction
W	Potential of the external forces
\mathbf{W}	Global orthogonal displacement relative to \mathbf{Z} direction
\mathbf{X}	Global orthogonal axis in \mathbf{U} direction
\mathbf{Y}	Global orthogonal axis in \mathbf{V} direction
	Y_p Trigonometric longitudinal functions (basic functions)
\mathbf{Z}	Global orthogonal axis in \mathbf{W} direction

Lowercase roman letters

a	Longitudinal length of strip
b	Width of strip
b_{eff}	Effective width
b_f	Flange width, out-to-out dimension
b_s	Lip width, out-to-out dimension

b_w	Web width, out-to-out dimension
\bar{b}_f	Flange width, centerline measurement
\bar{b}_s	Lip width, centerline measurement
\bar{b}_w	Web width, centerline measurement
dA	Differential of area
dV	Differential of volume
$\{d\}$	Nodal displacement vector, composed of $u_1, u_2, v_1, v_2, w_1, w_2, \theta_1$ and θ_2
$\{d_{uv}\}$	Nodal displacement vector for the membrane case, composed of u_1, u_2, v_1, v_2 .
$\{d_w\}$	Nodal displacement vector for the bending case, composed of w_1, w_2, θ_1 and θ_2 .
f_y	Yield stress
i	i^{th} left node of strip
j	j^{th} right node of strip
k	k^{th} middle node of strip or buckling coefficient
k_ℓ	Local buckling coefficient for full section under uniform compression
k_x	Buckling coefficient for bending about major axis x-x
k_y	Buckling coefficient for bending about minor axis y-y
k_z	Buckling coefficient for twisting about axis z-z
$[k]$	Elastic stiffness matrix
$[k^{ij}]_{pq}$	Elastic stiffness matrix for local coordinates corresponding to the p^{th} and q^{th} half-wave, from i^{th} node to j^{th} node (k^{th} strip)
$[k_B^{ij}]_{pq}$	Elastic stiffness matrix for bending and twisting case, corresponding to the p^{th} and q^{th} half-wave, from i^{th} node to j^{th} node (k^{th} strip)
$[k_M^{ij}]_{pq}$	Elastic stiffness matrix for the membrane case corresponding to the p^{th} and q^{th} half-wave, from i^{th} node to j^{th} node (k^{th} strip)
$[kg]$	Geometric stiffness matrix or the initial stress matrix
$[kg^{ij}]_{pq}$	Geometric stiffness matrix for local coordinates corresponding to the p^{th} and q^{th} half-wave, from i^{th} node to j^{th} node (k^{th} strip)
$[kg_B^{ij}]_{pq}$	Geometric stiffness matrix for bending and twisting case, corresponding to the p^{th} and q^{th} half-wave, from i^{th} node to j^{th} node (k^{th} strip)
$[kg_M^{ij}]_{pq}$	Geometric stiffness matrix for the membrane case corresponding to the p^{th} and q^{th} half-wave, from i^{th} node to j^{th} node (k^{th} strip)

m	Maximum number of longitudinal terms of series
p	Term of half-wave series
q	Term of half-wave series
r_x	Radius of gyration about major axis x-x
r_y	Radius of gyration about minor axis y-y
r_0	Polar radius of gyration
t	Strip/Section/Plate thickness
u	Local orthogonal displacement relative to x direction
u_1	Nodal displacement for node i , relative to x direction
u_2	Nodal displacement for node j , relative to x direction
v	Local orthogonal displacement relative to y direction
v_1	Nodal displacement for i node i , relative to y direction
v_2	Nodal displacement for node j , relative to y direction
w	Local orthogonal displacement relative to z direction
w_1	Nodal displacement for node i , relative to z direction
w_2	Nodal displacement for node j , relative to z direction
x	Local orthogonal axis in u direction
\bar{x}	Ratio between the x direction with the width of strip
x_0	Distance from central axis to shear center in x direction
y_0	Distance from central axis to shear center in y direction
y	Local orthogonal axis in v direction
z	Local orthogonal axis in w direction

Capital Greek letters

ΔY_s	Distance between the web-flange junction and the center of rotation
$[A]$	Eigenvalue matrix (diagonal matrix with the critical stress)
Π	Total potential energy of an elastic system
$[\Phi]$	Eigenvector matrix (matrix with the buckling modes)

Lowercase Capital Greek letters

β	Angle of rotation from local to global coordinates of strip
β	Correlation parameter corresponding to the cross-section “translation” per unit of flange-stiffener rotation needed to balance moments produced by the warping stress distribution
β_1	Initial geometric imperfection amplification coefficient of first mode

β_2	Initial geometric imperfection amplification coefficient of second mode
γ	Partial resistance factor
ε_x	Strain in x direction
ε_y	Strain in y direction
γ_{xy}	Shear strain in xy plane
$\{\varepsilon\}$	Strain vector
$\{\varepsilon_B\}$	Bending and twisting curvature strain vector
$\{\varepsilon_M\}$	Normal and shear strain vector
θ	Initial geometric imperfection combination parameter
θ_1	Nodal rotation for node i , correspondent to y rotation
θ_2	Nodal rotation for node k , correspondent to y rotation
κ_1	Correlation coefficient between overall lipped flange and web rotation
κ_2	Correlation coefficient between overall lipped flange and stiffener rotation
λ_c	Column slenderness factor
λ_{cr}	Critical slenderness
λ_D	Distortional slenderness
λ_{DG}	Distortional slenderness factor based on the global strength
λ_G	Global slenderness
λ_{GD}	Global slenderness factor based on the distortional strength
λ_L	Local slenderness
λ_{LG}	Local slenderness factor based on the global strength
λ_{LDG}	Maximum slenderness, between the distortional and the local slenderness factors based on the global strength
λ_{maxLD}	Maximum slenderness, between the distortional and the local slenderness
λ_p	Plate slenderness factor
λ_p	Coefficient with terms of series for basic functions ($p\pi/a$)
λ_q	Coefficient with terms of series for basic functions ($q\pi/a$)
ν_x	Poisson's ratio for x direction
ν_y	Poisson's ratio for y direction
$\{\sigma\}$	Stress vector related to the strains
$\{\sigma_B\}$	Stress vector assuming bending and twisting moments, and shearing forces
$\{\sigma_M\}$	Stress vector related to the normal and shear strain
σ_0	First stress point for bilinear material model

σ_1	Stress in the i^{th} left edge of a strip
σ_2	Stress in the k^{th} right edge of a strip
$\sigma_{crd,2}$	Critical distortional buckling stress (second model)
$\sigma_{cr\ell}$	Critical local buckling stress
σ_e	Elastic critical Euler stress
σ_{e1}	Least positive real elastic critical Euler stress
σ_{ex}	Elastic flexural buckling stress about major axis x-x
σ_{ey}	Elastic flexural buckling stress about minor axis y-y
σ_{ez}	Elastic torsional buckling stress about longitudinal axis z-z
χ	Member global buckling coefficient
χ_x	Curvature in x direction
χ_y	Curvature in y direction
χ_{xy}	Twisting in xy plane

Abbreviations

ABNT	Associação Brasileira de Normas Técnicas
AISI	American Iron and Steel Institute
ANSYS	Analysis System (finite element software)
APDL	ANSYS Parametric Design Language
AS/NZS	Australian/New Zealand code
CBCA	Centro Brasileiro de Construção do Aço
COPPE	Instituto Alberto Luiz Coimbra de Pós-Graduação e Pesquisa de Engenharia
C-C	Clamped-Clamped end boundary condition
C-F	Clamped-Free end boundary condition
C-G	Clamped-Guided end boundary condition
CFS	Cold-formed steel
C-S	Clamped-Simply end boundary condition
CUFSM	Constrained and Unconstrained Finite Strip Method
D	Distortional mode
D-G	Distortional-global mode
D-F	Distortional/minor-axis flexural mode
D-FT	Distortional/major-axis flexural-torsional mode
DSM	Direct strength method
EAM	Effective Area Method

ESM	Effective section method
EWM	Effective width method
FEM	Finite element method
FSM	Finite strip method
FStr	Finite Strip Method Computer Application Program
G	Global mode
GUI	Graphical user interface
GBTul	Generalized Beam Theory at the University of Lisbon
L	Local mode
LabEST	Laboratory of Structures and Materials Professor Lobo Carneiro
LC	Lipped channel cross section
L-D	Local-distortional mode
L-G	Local-global mode
L-D-G	Local-distortional-global mode
MATLAB	Matrix Laboratory
S-S	Simply-Simply end boundary condition
SDI	Secondary-distortional bifurcation D-G interaction
SGI	Secondary-global bifurcation D-G interaction
TI	True distortional-global interaction
UFRJ	Universidade Federal do Rio de Janeiro

1 Introduction

In the past few decades, steel cold-formed steel members have taken their place in the construction industry due to their high structural efficiency. In this chapter, some background, applications and current design codes about cold-formed steel structures are presented. Additionally, the motivation of this research, aligned with the objectives is introduced. The chapter ends with an outline of what the reader should expect in the next chapters.

1.1 Background

The major task of structural engineers is to design low-cost and safe solutions. Thus, saving weight on the structure will lead to solution with less material consumption and, consequently, a better economical option. Under these circumstances, light steel construction enables cost savings within the superstructure as well as in the substructure and foundation. Choosing thin-walled steel members may be a frequent option due to less material consumption, engineering design and architectural concepts. However, light gauge steel members are slender structures, which present additional stability problems, Batista [1].

The use of steel structural members is directly associated with a vast range of advantages, according to CBCA [2]. First of all, in terms of architectural design, the design projects in steel are more flexible during restoration, give a higher usable area and allow more freedom to develop modern architectural concepts. With respect to project management, it means a shorter execution time and a cleaner construction site, as a result of an industrialized system. The fact of being a manufactured product enables more compatibility with other materials and constructions technologies. Additionally, in terms of accuracy of the structure, it has a higher quality standard, which provides more reliable structural systems. Last but not least, it is a sustainable alternative, with 100% of recyclable material.

More specifically, thin-walled cold-formed steel members are structural options with a high efficiency, which means they have a large strength-to-weight ratio. As reported by Hancock [3], this structural alternative consists of bending flat sheets at ambient temperature into shapes that will sustain more than the flat sheets themselves. They have been produced for over a century since the primary flat steel sheets were manufactured by the steelworks. However, in recent years, higher strength materials and a broader range of structural applications have triggered a significant growth in cold-formed steel relative to the normal heavier hot-rolled steel structures.

The use of cold-formed steel structures has been growing fast, mainly in the industry. Figure 1.1 illustrates a representative example of application of cold-formed steel members in the construction of a wholesaler. According to the owner of the patented roofing system, MARKO [4], the *Poupaki Atacadista* establishment has an area of 7,843 m², located in the city of Guarulhos, state of São Paulo, Brazil, and it was launched in April 2019. Their roofing system, called Roll-on, is a patented product for large-scale constructions, that involves a set of cold-formed steel sections, in order to give a larger range of usable area without a column. The Roll-on system is manufactured as an industrial product, where the factory unit produces all the cross-section elements with all the roles pre-defined. Then, all the members are transported to the construction site, where all pieces are assembled.



Figure 1.1. Roll-on roofing system from MARKO Sistemas Metalicos, consisted of cold-formed steel members, illustrated in the construction of Poupaki wholesaler, located in the city of Guarulhos, São Paulo, Brazil [4].

Cold-formed steel (CFS) members are composed of thin-walled sections, forming very slender structural systems easily susceptible to buckling, obliging designers to deal with the complexity of the phenomenon and requiring research development to allow structural solution with simple equations. In terms of design procedures, these structural design equations are still under constant adjustments. The current codes, Brazilian standard ABNT NBR 14762:2010 [5], Australian/New Zealand code AS/NZS 4600 [6] and North-American standard AISI S100-16 [7], have been changing their designing approaches over the past decades. The need of constant modifications on the design procedures, due to the semi-empirical procedures, obliges laboratory experimental campaigns combined with accurate numerical solutions in order to calibrate the equations and procedures.

1.2 Motivation

The most widely applied design method for cold-formed steel structures is the Direct Strength Method, DSM. This method became so widespread attributable to its simplicity and accuracy in identifying the ultimate load of CFS members. However, the available equations of the method have some breaches. Heretofore, the current standards (*e.g.* ABNT NBR 14762:2010 [5], AS/NZS 4600 [6] and AISI S100-16 [7]), adopt the direct strength method considering only local, distortional, global and local-global buckling interaction design procedure. Nevertheless, further coupled buckling phenomena are not addressed, *i.e.* local-distortional, distortional-global, local-distortional-global and global-global buckling interaction. The motivation of this research is to comprehend the distortional-global interaction in order to propose a new direct strength method solution that contemplate the coupled phenomenon.

In the future, it is expected that the contribution of this research becomes useful for the development of general solution taking into account all the possible buckling modes interaction. In this case, the design approach should be efficient with respect to take into account all the possible failure events.

1.3 Objectives

The purpose of this work is to investigate the distortional-global coupled phenomenon in cold-formed steel lipped channel columns. More specifically, it is focused

on the phenomenon behavior and the column strength under different types of initial imperfections and the column slenderness, which can be achieved with appropriate variations of the columns' length and steel yield stress. Additionally, the obtained results of the strength of the columns under DG buckling interaction are compared with design procedures found in the literature.

In order to accomplish the main objective, this research offers: (i) elastic buckling analysis of CFS columns, using a suitable finite strip method computer application program developed by the author; (ii) non-linear analysis using a finite element model to acquire numerical data of the post-buckling behavior and the ultimate load of the columns; (iii) parametric study of columns under different types of initial geometric imperfection combination and different types of distortional-global buckling interaction.

1.4 Outline

2 Literature Review: The current chapter provides the reader with all the necessary literature background for the next chapters. First, the reader will understand some fundamentals of structural stability associated with thin-walled structures. Additionally, a formulation is shown for the finite strip method for the elastic buckling analysis. Sequentially, the coupled instability phenomenon is presented, with focus on the distortional-global interaction concepts. Finally, the chapter ends with analytical procedures, design approaches and the state-of-the-art associated with the couple phenomenon, mainly about the distortional-global interaction;

3 FStr - Computer Application Program: Here is present a finite strip method program, entitled FStr. The program is implemented in MATLAB and performs an elastic buckling analysis of thin walled structures. A graphical user interface is designed, with the purpose of provide a useful and easy tool to perform an elastic buckling analysis. Additionally, the section presents different types of validations, comparing with other programs, a finite element method and analytical procedures;

4 Numerical Modeling: This chapter presents a finite element model description. The finite element model is used with assistance of ANSYS Mechanical APDL, and the analysis is addressed to detect the post-buckling behavior and strength of a structural element, using shell finite element analysis. The model is validated with laboratory tests, of columns experiencing global and distortional buckling mode;

5 Parametric Analysis on Distortional-Global Buckling Interaction: In this chapter, a parametric study is accomplished, with assistance of the FStr Computer Application Program and the finite element software ANSYS. The non-linear analysis is performed with initial imperfection given by the developed program. Through the non-linear analysis, it is determined the ultimate strength and stability paths, in order to understand the distortional-global buckling interaction behavior. More specifically, it is conducted a study of lipped channel cold-formed steel columns with different combinations of initial imperfections, yield stress and lengths, under distortional-global coupled phenomenon;

6 Concluding Remarks: Summary of important remarks about the present study is exposed in this chapter;

7 Bibliography: All the references cited in this research is presented in this chapter;

APPENDIX A: This section presents the analytical solutions of some integrals considered in the finite strip method;

APPENDIX B: This appendix provides some post-buckling equilibrium paths of columns from the study of initial imperfection combination;

APPENDIX C: Here is presented only tables with modal participation, critical loads, slenderness factors, ultimate load and nominal axial strength from the columns studied on the distortional-global buckling interaction nature.

2 Literature Review

Some fundamentals of structural stability associated with thin-walled structures are presented, in order to support the concepts that are required for the next chapters. Additionally, in this chapter, a formulation for the finite strip method for the elastic buckling analysis is shown. With this formulation, it is possible to determine the elastic critical load associated with a critical buckling mode. Also, the coupled instability phenomenon is presented, with focus on the distortional-global interaction concepts. Finally, the chapter ends with design procedures and the state-of-the-art associated with the couple phenomenon, mainly concerning the distortional-global interaction.

2.1 Fundamentals of Structural Stability

In general, the perception of an unstable structure can be identified by anyone. It is not necessary to be a structural engineer to assume that. Basically, this perception is already deep-seated in our consciousness and it can be defined as a structural instability, in which a small variation of the load applied to the unstable structure will lead to a considerable change in the displacement configuration. Assuming that this change in displacement is considerable large in a critical element of the integrated structure, then, this member instability might induce local or global structural collapse. The study of the mechanics of unstable structures is a singular subspace of the engineering mechanics that requires relevant attention to design safe structures, Galambos and Surovek [8].

According to Galambos and Surovek [8], structural instability occurs in the presence of compressive stress in a plate element, *e.g.* in the part of a cross-section of a beam or column. In an isolated structural element, the following can occur: (i) a local instability, which is associate with an instability of a single fraction of the element (*e.g.* local web buckling of a steel beam); (ii) and/or the member instability, which is related to an instability of the entire isolated structural element (*e.g.* buckling of a diagonal brace). Between these two instability cases, the entire member instability has a high

probability to collapse the structural system and this system instabilities are generally catastrophic.

As reported by Alexander Chajes [9], slender columns are mostly subjected to a behavior commonly characterized as buckling. This behavior occurs when a certain load is reached, causing large deformations after a small increase of loading. The load characterizing this behavior is called critical load. Due to that critical phenomenon, this load is used as a reference for design criterion.

In order to better understand the fundamental concepts of stability an example of the behavior of a simple structural system is illustrated in Figure 2.1, by a perfect spring-bar system.

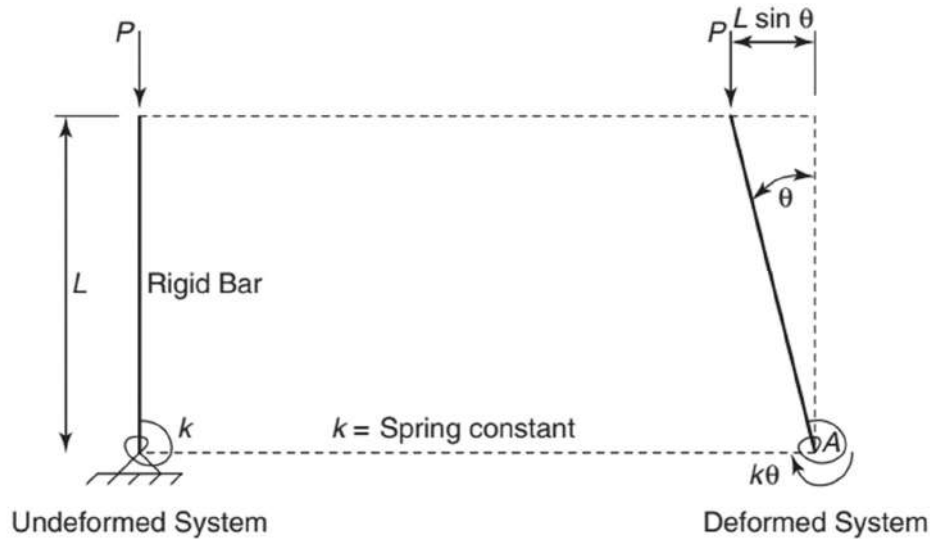


Figure 2.1. Structural model of a perfect spring-bar system [8].

The spring-bar system in Figure 2.1 is composed of a vertical rigid bar of length, L , with an elastic spring restraining at one of the bar extremities. At the other extremity a conservative compressive axial load P is applied. Since the bar is rigid, when the load P is increased, the bar tends to rotate, as it is shown in Figure 2.1.

To detect the critical load of the spring-bar system, it is necessary to find the load that when applied to the structure, causes it to cross from a stable to an unstable state. Graphically, this critical load can be determined at a bifurcation point. Figure 2.2 shows the path performed by the increasing load, until it reaches the critical load versus the angle of rotation θ of the rigid bar.

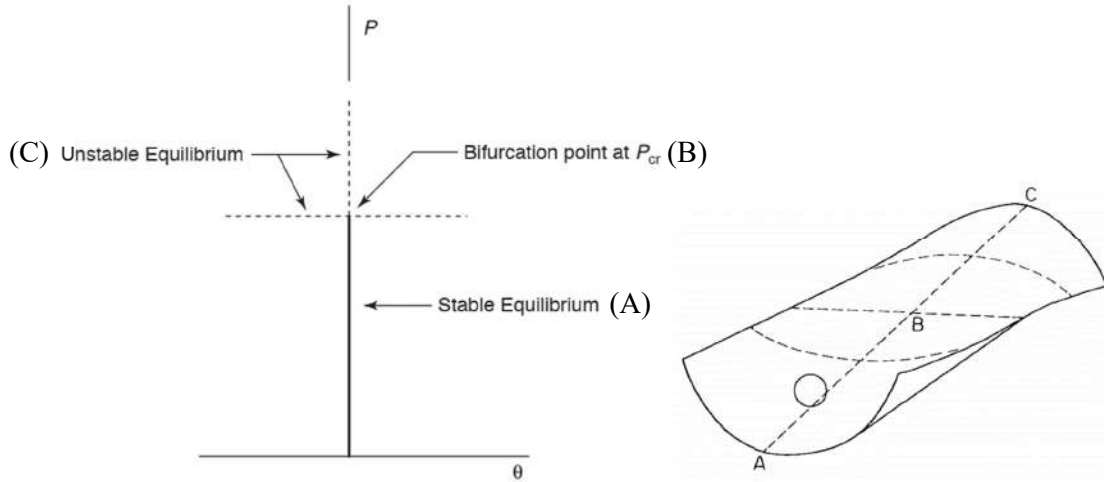


Figure 2.2. Force versus rotation of a perfect spring-bar system and the stability surface [8] and [9].

Note in Figure 2.2 that the critical load is defined at a bifurcation point, which is delimited by a stable and unstable equilibrium path. The unstable equilibrium for the spring-bar system can be divided into two possible paths. The upper path is reached when increasing the force P with no lateral displacement. This equilibrium path exists only on a perfect structure, with no perturbation, therefore it is only a theoretical path.

Generally, the stability evaluation of any system can be analyzed by different methods: (i) small deflection method, giving only the buckling load; (ii) large deflection method for a perfect structure, giving the post-buckling behavior information; (iii) large deflection method for an imperfect system, giving the complete stability analysis, as well as stiffness reduction in the proximity of the critical load.

There are two ways to solve analytically these methods, by a static equilibrium method or an energy method. It will be focused on the energy method, which is used later to describe the finite strip method. The energy method is based on the law of conservation of energy¹, for which a conservative system depends only on the initial and final position, regardless of the path performed by the work of internal and external forces. Therefore, according to Chajes [9], the presence of internal friction related to inelastic behavior or external friction would culminate in a nonconservative system.

Based on the law of conservative energy, the total potential energy of an elastic system (Π) is then defined as the sum of the elastic strain energy of a conservative system

¹ According to Chajes [9], the principle states: “A conservative system is in equilibrium if the strain energy stored is equal to the work performed by the external loads.”

(U) plus the potential of the external forces (W). Since the total potential energy is stationary, the equilibrium position of a system can be reached by detecting the minimum or maximum of the total potential Π . Figure 2.3 is illustrating a table with the three possible stability states (stable, unstable and neutral), using the concept of total potential energy.


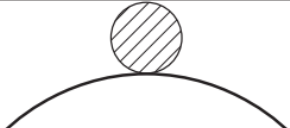
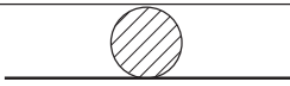
<ul style="list-style-type: none"> • Minimum of Π • Stable equilibrium • Energy must be added to change configuration. 	$\frac{d^2\Pi}{d\theta^2} > 0$		<i>Ball in cup can be disturbed, but it will return to the center.</i>
<ul style="list-style-type: none"> • Maximum of Π • Unstable equilibrium • Energy is released as configuration is changed. 	$\frac{d^2\Pi}{d\theta^2} < 0$		<i>Ball will roll down if disturbed.</i>
<ul style="list-style-type: none"> • Transition from minimum to maximum • Neutral equilibrium • There is no change in energy. 	$\frac{d^2\Pi}{d\theta^2} = 0$		<i>Ball is free to roll.</i>

Figure 2.3. Table illustrating the stability states the total potential energy, related to the example of the spring-bar system [8].

The state of stable equilibrium is obtained as the minimum total potential energy. Therefore, to change the stable state it is necessary to add energy to the system. On the other hand, the state of unstable equilibrium is accessed as the maximum total potential energy. In this case, for changing the state it is necessary a small perturbation to the system and energy would be released. At last, but not least, the neutral state of equilibrium is characterized as a situation of inflection, when it changes from stable to unstable equilibrium. For this state, there is no quantitative change on the total potential energy.

In addition, Figure 2.2 shows the stability surface, representing the changing of the stability states, from (A) stable to (C) unstable.

In general, structural stability analysis can be exhausting and time consuming, due to the system model complexity² and the monitoring the total potential energy during the loading. Due to that, it might be advisable to adopt a displacement control during the loading, in order to find the fundamental paths before and after the bifurcation point. In order to show the complexity of these analyses, Figure 2.4 presents different types of equilibrium paths (load vs. displacement).

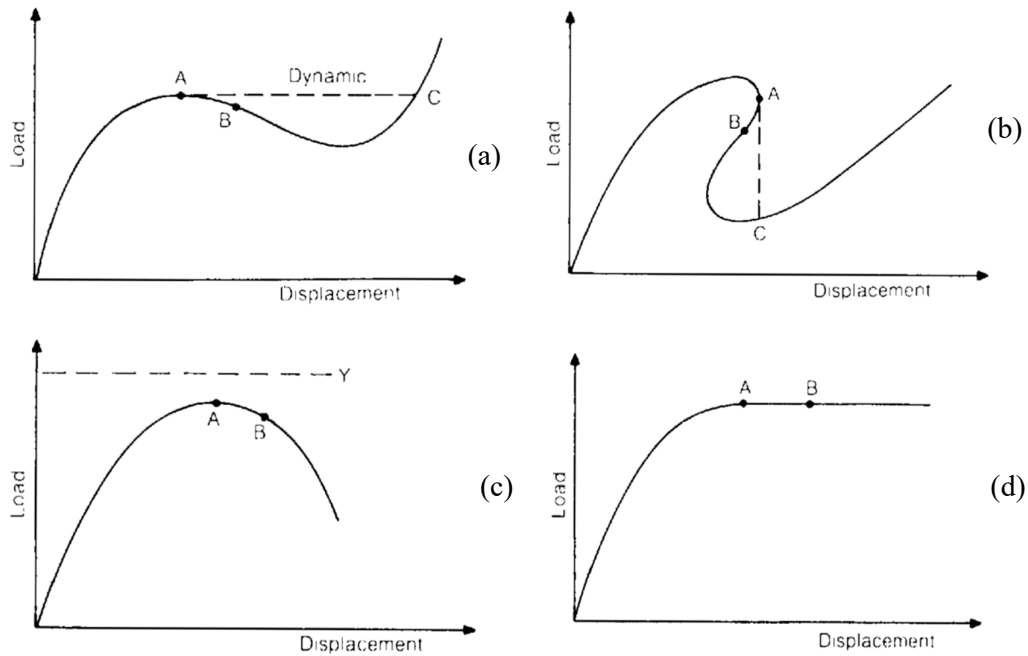


Figure 2.4. Different types of equilibrium paths: (a) snap-through; (b) snap-back; (c) ‘brittle’ collapse; (d) ‘ductile’ collapse [10].

Buckling of arches, cylindrical shells, and cracking of reinforced concrete are some examples of equilibrium paths as shown, respectively, in Figure 2.4 (a), (b) and (c). There are several algorithms to detect these paths, *e.g.* line searches, modified Newton-Raphson method, arc-length method, where the arc-length method is the most robust of the non-linear methods and it is discussed in more detail in the section 4 (Numerical Modeling).

² *i.e.* adopting geometric and material nonlinearity

2.2 The Finite Strip Method

The present work adopts the finite strip method (FSM) for the elastic buckling analysis. The FSM was originally formulated by Yau Kai Cheung, honorary professor of The University of Hong Kong (Cheung [11]). On the other hand, it was Gregory J. Hancock, emeritus professor of The University of Sydney, who began using the method in structural elements as hot-rolled sections and cold-formed steel sections (Hancock *et al.* [12], [13] & [14]). Hancock changed the stiffness matrix of Cheung and developed his own computational program, BFINST (Hancock *et al.* [15]), which gives the solution for the buckling analysis on thin-walled members with open cross sections.

The Finite Strip Method is a particular case of the Finite Element Method (FEM). Briefly, the FEM uses polynomial shape functions in all directions, while the FSM uses polynomials shape functions in transverse direction and trigonometric shape functions in longitudinal direction, which satisfies the boundary conditions for the case of small displacements of the structural system. The main advantage in using the FSM is to reduce the structure's degrees of freedom, in order to acquire performance and time consuming in the elastic buckling analysis.

The FSM is an extremely useful and a more powerful tool when applied to an appropriate situation for a buckling analysis, when compared to the FEM. Basically, the FEM is a more generic, versatile and powerful method, while the FSM is more used for thin-walled structural models with two extremities that have a well-defined boundary condition, *e.g.* bridges, beams, columns (see Figure 2.5). Also, while the FEM uses a large number of equations, the FSM uses fewer number of equations, for the same model as discretized in FEM. In addition, the amount of information about the model that should be discretized on the pre-processing is denser in the FEM, which increases the probability of user's error in the process of modeling. Likewise, the post-processing of the FSM is easier to interpret, compared to the FEM post-processing. Lastly, the FEM needs more computational effort and is harder to implement, while the FSM is quicker and straightforward to implement, Cheung [11].

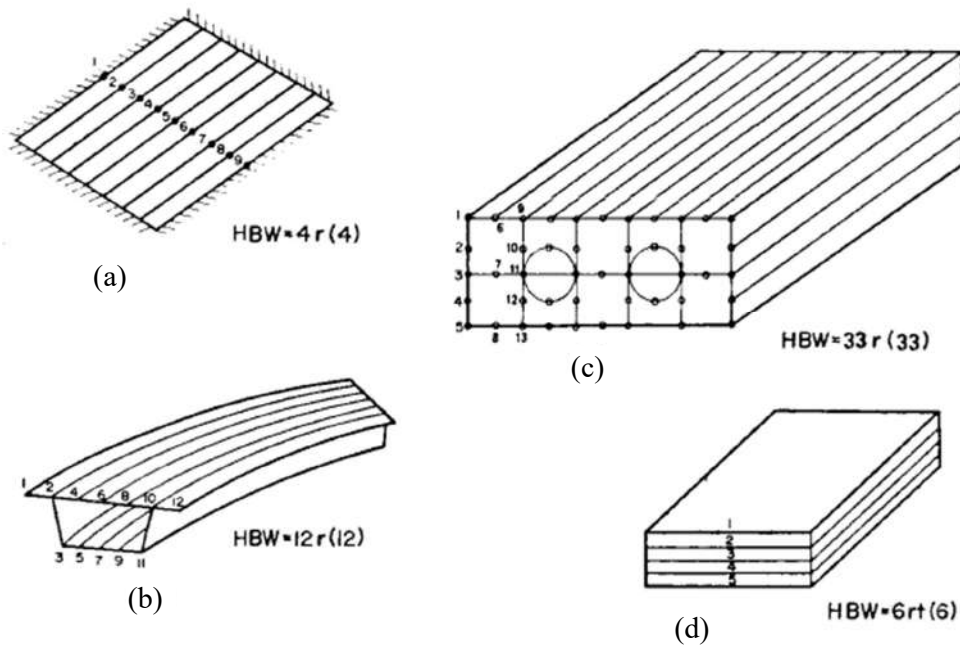


Figure 2.5. Strip discretization on typical structural models. (a) Encastred slab (plate strips). (b) Curved box girder bridge (shell strips). (c) Voided slab bridge (quadrilateral finite prims). (d) Multilayer plate (finite layers). [11]

2.2.1 Matrix Formulation

The finite strip method formulation is based on the classical plate theory assumptions, which is described in detail by Timoshenko and Woinowsky-Krieger [16]. For this work, the computational matrix formulation is presented with the main reference by Cheung [11], which includes different types of finite strip model formulations (see Figure 2.5). According to Cheung [11], the first paper that presented the finite strip method was from Cheung [17] for a simply supported plate-bending rectangular strip. Later, in Cheung [18] the formulation was generalized, including other end-conditions. Some other sources are also used in the present work – *i.e.* Bradford and Azhari [19], Li and Shafer [20], Schafer [21] and Li [22].

The strip element is a lower order rectangular strip with two nodal lines (LO2) as shown in Figure 2.6. For each strip, the membrane strain is examined, considering plane stress assumptions and the bending strain, in accordance with Kirchoff thin plate theory assumptions, Cheung [11]. Due to these assumptions, each strip has 8 degrees of freedom and 4 degrees per nodal line.

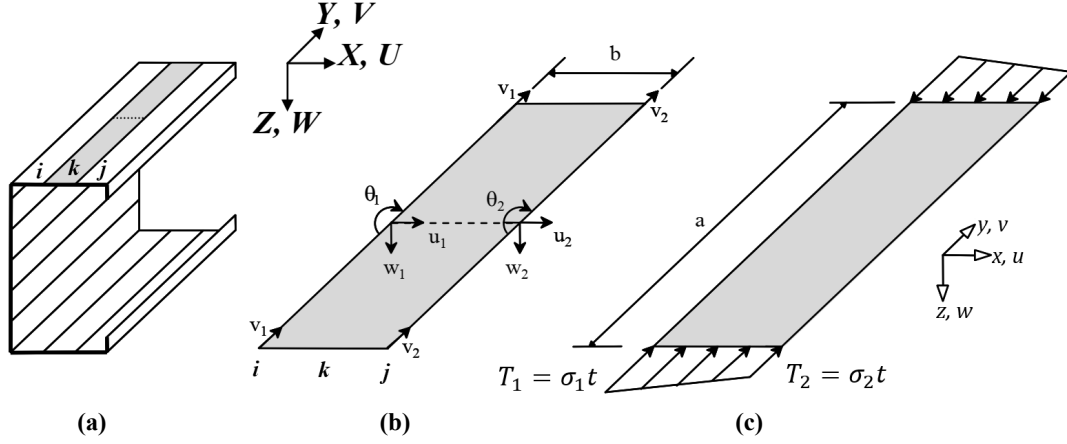


Figure 2.6. Lower order rectangular strip with two nodal lines (LO2). (a) Strip discretization in a Lipped channel section. (b) Degrees of freedom on nodal lines. (c) External end tractions applied to the strip. [20]

The matrix formulation is first computed with the displacement field. After the elastic stiffness matrices for the membrane and bending actions are defined, the geometric stiffness matrices for membrane and bending actions are computed. Finally, the matrices are assembled, in order to obtain the critical loads and buckling modes, as a solution of an eigenvalue problem.

The displacement field is computed in x , y and z local direction, corresponding to the displacements u , v and w , respectively. In order to determine the displacement in any region of the strip, the nodal displacements are interpolated with polynomials functions in the transversal direction of the strip and summations of trigonometric functions in the longitudinal direction of the strip.

First, in matrix form, the displacement field inside de strip can be approximated by Eq. (2.1), using the nodal displacements $\{d\}$, shown in Figure 2.6-b, and the shape function matrix $[N]$ (Eq. (2.2)). The displacements field for each strip, $\{u \ v \ w\}^T$, is determined as a summation of all longitudinal terms, from 1 to $m \in \mathbf{N}$.

$$\begin{Bmatrix} u \\ v \\ w \end{Bmatrix} = [N]\{d\} = \sum_{p=1}^m [N]_p \{d\}_p = \sum_{p=1}^m \begin{bmatrix} [N_{uv}]_p & [0]_{2 \times 4} \\ [0]_{1 \times 4} & [N_w]_p \end{bmatrix} \begin{Bmatrix} u_1 \\ v_1 \\ u_2 \\ v_2 \\ w_1 \\ w_2 \\ \theta_1 \\ w_2 \\ \theta_2 \end{Bmatrix}_p. \quad (2.1)$$

The shape function matrix is given in the Eq. (2.2). Note that this matrix is composed of polynomial functions times Y_p , which is a trigonometric function, given in Table 2.1, depending on the boundary condition.

$$[N_{uv}]_p = \begin{bmatrix} (1 - \bar{x})Y_p & 0 & \bar{x} Y_p & 0 \\ 0 & (1 - \bar{x}) \frac{Y'_p}{\lambda_p} & 0 & \bar{x} \frac{Y'_p}{\lambda_p} \end{bmatrix}$$

$$[N_w]_p = [(1 - 3\bar{x}^2 + 2\bar{x}^3)Y_p \quad x(1 - 2\bar{x} + \bar{x}^2)Y_p \quad (3\bar{x}^2 - 2\bar{x}^3)Y_p \quad x(\bar{x}^2 - \bar{x})Y_p].$$

$$[N]_p = \begin{bmatrix} [N_{uv}]_p & [0]_{2 \times 4} \\ [0]_{1 \times 4} & [N_w]_p \end{bmatrix}. \quad (2.2)$$

Where $\bar{x} = x/b$ and p is the half-wave series' term. Observe that the shape function matrix $[N]$ is assembled with the shape functions from the plane stress assumption (membrane action) and bending action, separately.

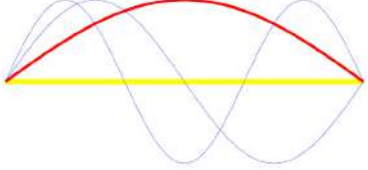
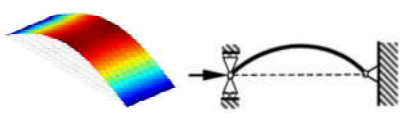
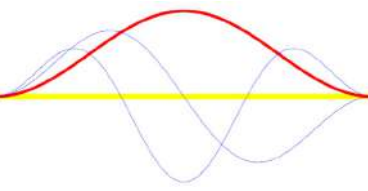
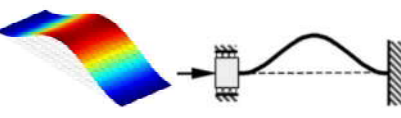
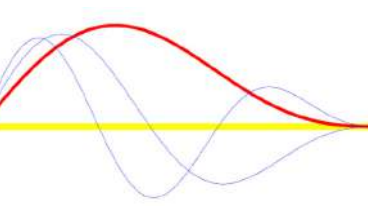
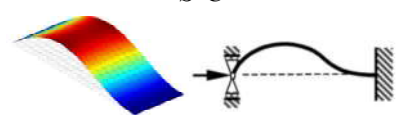
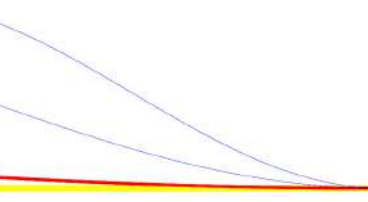
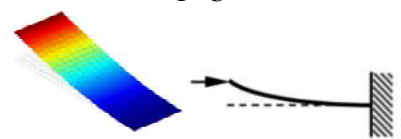
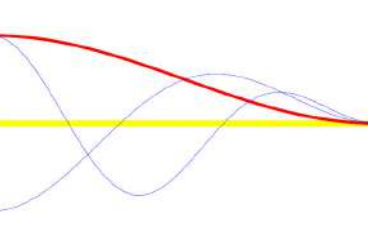
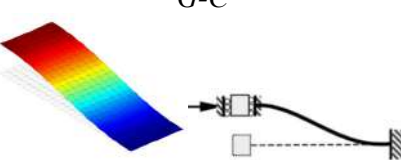
The formulation of the finite strip now can be defined using the principle of minimum total energy³, which is shown in mathematical form by Eq. (2.8).

$$\left\{ \frac{\partial \Pi}{\partial \{d\}} \right\} = \left\{ \begin{array}{c} \frac{\partial \Pi}{\partial \{d\}_1} \\ \frac{\partial \Pi}{\partial \{d\}_2} \\ \vdots \\ \frac{\partial \Pi}{\partial \{d\}_p} \\ \vdots \\ \frac{\partial \Pi}{\partial \{d\}_m} \end{array} \right\} = \{0\}, \quad \text{where } \Pi = U + W \quad (2.8)$$

in which Π is the total potential energy, U is the elastic strain energy stored in the body, W is the potential energy of external forces and $\{d\}$ is the nodal displacements for all degrees of freedom and all terms of the series.

³ According to Cheung [11], the principles states that “of all compatible displacements satisfying given boundary conditions, those which satisfy the equilibrium conditions make the total potential energy assume a stationary value”

Table 2.1. Trigonometric longitudinal functions (basic functions) for each boundary condition and each p^{th} term of the series.

<i>Longitudinal Displacement Shape</i>	<i>Basic Function</i>
	<p style="text-align: center;"><i>S-S</i></p>  <p style="text-align: right;">(2.3)</p> $Y_p = \sin(\lambda_p y).$
	<p style="text-align: center;"><i>C-C</i></p>  <p style="text-align: right;">(2.4)</p> $Y_p = \sin(\lambda_p y) \sin\left(\frac{\pi y}{a}\right).$
	<p style="text-align: center;"><i>S-C</i></p>  <p style="text-align: right;">(2.5)</p> $Y_p = \sin(\lambda_{p+1} y) + \left(\frac{p+1}{p}\right) \sin(\lambda_p y).$
	<p style="text-align: center;"><i>F-C</i></p>  <p style="text-align: right;">(2.6)</p> $Y_p = 1 - \cos(\lambda_{p-1/2} y).$
	<p style="text-align: center;"><i>G-C</i></p>  <p style="text-align: right;">(2.7)</p> $Y_p = \sin(\lambda_{p-1/2} y) \sin\left(\frac{\pi y}{2a}\right).$
<p>— Deformed shape $p = 1$</p> <p>— Undeformed shape</p> <p>— Additional deformed shapes ($p > 1$)</p>	<p>S: Simply Supported, C: Clamped, F: Free, G: Guided.</p> $\lambda_p = p\pi/a$ $\lambda_{p+1} = (p+1)\pi/a$ $\lambda_{p-1/2} = (p-1/2)\pi/a$

By definition, the strain energy of a three dimensional solid is defined by Eq. (2.9).

$$U = \frac{1}{2} \iiint_V \{\varepsilon\}^T \{\sigma\} dV = \frac{1}{2} \iiint_V \{d\}^T [B]^T [D] [B] \{d\} dV. \quad (2.9)$$

In Eq. (2.9) $\{\varepsilon\}$ is the strain, compound by the sum of the bending and twisting curvature strain ($\{\varepsilon_B\}$) with the normal and shear strain ($\{\varepsilon_M\}$). Also, $\{\sigma\}$ is the stress, related to the strains, dV is the differential of volume, $[B]$ is the matrix with the appropriate partial differentiations of the strain-displacement relationship known as the strain matrix and $[D]$ is the elasticity property matrix.

By definition, the potential energy of the external forces is defined by:

$$W = - \iint_A \begin{Bmatrix} u \\ v \\ w \end{Bmatrix}^T \{q\} dA = - \iint_A \{d\}^T [N]^T \{q\} dA \quad (2.10)$$

where $\{q\}$ is the vector with the external surface loading and dA is the differential of area.

Introducing Eq. (2.9) and Eq. (2.10) into Eq. (2.8) and differentiating with respect to $\{d\}$, leads to:

$$\left\{ \frac{\partial \Pi}{\partial \{d\}} \right\} = \iiint_V [B]^T [D] [B] \{d\} dV - \iint_A [N]^T \{q\} dA = \{0\}. \quad (2.11)$$

In matrix form, the Eq. (2.11) can be written as $[k]\{d\} - \{F\} = \{0\}$, where $[k]$ is the elastic stiffness matrix and $\{F\}$ the vector with the superficial forces applied into the plane xy of the strip.

Expanding the elastic stiffness matrix for all the terms of the series from 1 to m , we have

$$[k] = \iiint_V \begin{bmatrix} [B]_1^T [D] [B]_1 & [B]_1^T [D] [B]_2 & \cdots & [B]_1^T [D] [B]_q & \cdots & [B]_1^T [D] [B]_m \\ [B]_2^T [D] [B]_1 & [B]_2^T [D] [B]_2 & \cdots & [B]_2^T [D] [B]_q & \cdots & [B]_2^T [D] [B]_m \\ \vdots & \vdots & \ddots & \vdots & \vdots & \vdots \\ [B]_p^T [D] [B]_1 & [B]_p^T [D] [B]_2 & \cdots & [B]_p^T [D] [B]_q & \cdots & [B]_p^T [D] [B]_m \\ \vdots & \vdots & \vdots & \vdots & \ddots & \vdots \\ [B]_m^T [D] [B]_1 & [B]_m^T [D] [B]_2 & \cdots & [B]_m^T [D] [B]_q & \cdots & [B]_m^T [D] [B]_m \end{bmatrix} dV. \quad (2.12)$$

Note that the operation $[B]_p^T [D] [B]_q$ represents a submatrix, with size $s \times s$, where s is the total number of strips and it is always a null submatrix when $p \neq q$. Additionally,

for the k^{th} strip, there are the i^{th} and j^{th} nodal lines. Then, putting Eq. (2.12) in a summation form and applying its limits of integration defined by the strip volume, the general elastic stiffness matrix is given by:

$$[k] = \sum_{k=1}^s \sum_{p=1}^m \sum_{q=1}^m \int_0^t \int_0^a \int_0^b [B^i]_p^T [D] [B^j]_q dx dy dz. \quad (2.13)$$

The Eq. (2.13) shows in a compact form the elastic stiffness matrix for the finite strip method for a lower order strip with two nodal lines. The elastic stiffness matrix for the membrane and bending cases (Figure 2.7) based on Eq. (2.13) is introduced further ahead.

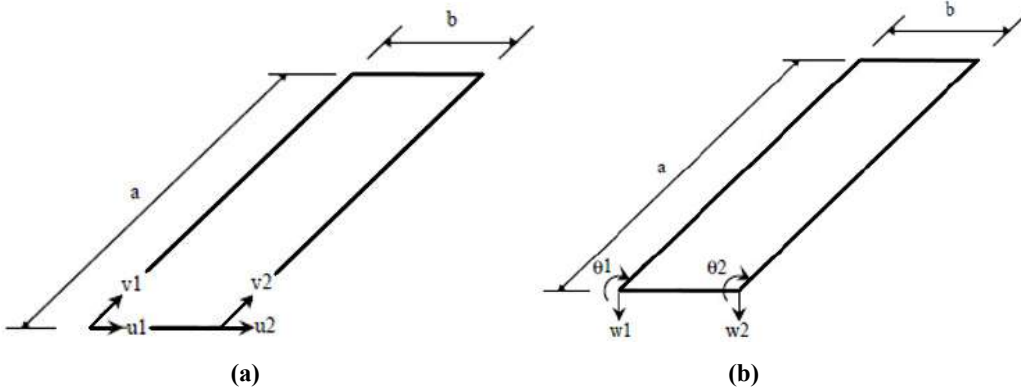


Figure 2.7. The degrees of freedom uncoupled of a rectangular low order strip with two nodal lines for the (a) membrane case (plane stress) and (b) bending case.

Assuming the case of plane stress, given in Figure 2.7-a, there are displacements only in the plane xy . From that, the strain matrix is obtained from the generalized strain relationship including only normal and shear strain, described in Eq. (2.14).

$$\{\varepsilon_M\} = \begin{Bmatrix} \varepsilon_x \\ \varepsilon_y \\ \gamma_{xy} \end{Bmatrix} = \begin{Bmatrix} \frac{\partial u}{\partial x} \\ \frac{\partial v}{\partial y} \\ \frac{\partial u}{\partial y} + \frac{\partial v}{\partial x} \end{Bmatrix} = \sum_{p=1}^m [B_{uv}]_p \begin{Bmatrix} u_1 \\ v_1 \\ u_2 \\ v_2 \end{Bmatrix}_p \quad (2.14)$$

where u and v are the displacements in the plane of the strip defined in Eq. (2.1) and $[B_{uv}]_p$ is the strain matrix of the membrane assumption for the p^{th} term of the series, given by the expression $\{\varepsilon_M\} = [B_{uv}]\{d_{uv}\}$ and shown in the Eq. (2.15).

$$[B_{uv}]_p = \begin{bmatrix} -\frac{Y_p}{b} & 0 & \frac{Y_p}{b} & 0 \\ 0 & (1-\bar{x})\frac{Y_p''}{\lambda_p} & 0 & \bar{x}\frac{Y_p''}{\lambda_p} \\ (1-\bar{x})Y_p' & -\frac{Y_p'}{\lambda_p b} & \bar{x}Y_p' & \frac{Y_p'}{\lambda_p b} \end{bmatrix}. \quad (2.15)$$

Thus, the property matrix of an orthotropic plane stress, $[D_{uv}]$, is given by the expression $\{\sigma_M\} = [D_{uv}]\{\varepsilon_M\}$, assuming only normal and shear stresses. In the matrix form $[D_{uv}]$ is expressed in Eq. (2.16) for the p^{th} term of the series.

$$E_1 = \frac{E_x}{1-\nu_x\nu_y} \quad E_2 = \frac{E_y}{1-\nu_x\nu_y} \quad G_{xy} = \frac{E_x E_y}{E_x(1+2\nu_y) + E_y}$$

$$[D_{uv}]_p = \begin{bmatrix} E_1 & \nu_x E_2 & 0 \\ \nu_x E_2 & E_2 & 0 \\ 0 & 0 & G_{xy} \end{bmatrix} \quad (2.16)$$

where E_x and E_y are the elastic moduli for x and y directions, ν_x and ν_y are the Poisson's ratio for x and y directions and G_{xy} is the axial shear modulus in xy plane. In the case of an isotropic material it can be assumed that $E_x = E_y = E$, $\nu_x = \nu_y = \nu$ and $G_{xy} = G = E/2(1+\nu)$.

Introducing Eq. (2.15) and Eq. (2.16) into Eq. (2.13), leads to the elastic stiffness matrix for the membrane, given by Eq. (2.17). The matrix corresponds to the p^{th} and q^{th} half-wave, from node i to node j (k^{th} strip).

$$[k_{M1}^{ij}]_{pq} = t \begin{bmatrix} \frac{E_1 I_1}{b} & -\frac{E_2 \nu_x I_3}{2\lambda_q} & -\frac{E_1 I_1}{b} & -\frac{E_2 \nu_x I_3}{2\lambda_q} \\ -\frac{E_2 \nu_x I_2}{2\lambda_p} & \frac{E_2 b I_4}{3\lambda_p \lambda_q} & \frac{E_2 \nu_x I_2}{2\lambda_p} & \frac{E_2 b I_4}{6\lambda_p \lambda_q} \\ -\frac{E_1 I_1}{b} & \frac{E_2 \nu_x I_3}{2\lambda_q} & \frac{E_1 I_1}{b} & \frac{E_2 \nu_x I_3}{2\lambda_q} \\ -\frac{E_2 \nu_x I_2}{2\lambda_p} & \frac{E_2 b I_4}{6\lambda_p \lambda_q} & \frac{E_2 \nu_x I_2}{2\lambda_p} & \frac{E_2 b I_4}{3\lambda_p \lambda_q} \end{bmatrix}$$

$$[k_{M2}^{ij}]_{pq} = G_{xy} I_5 t \begin{bmatrix} \frac{b}{3} & -\frac{1}{2\lambda_q} & \frac{b}{6} & \frac{1}{2\lambda_q} \\ -\frac{1}{2\lambda_p} & \frac{1}{b\lambda_p\lambda_q} & -\frac{1}{2\lambda_p} & -\frac{1}{b\lambda_p\lambda_q} \\ \frac{b}{6} & -\frac{1}{2\lambda_q} & \frac{b}{3} & \frac{1}{2\lambda_q} \\ \frac{1}{2\lambda_p} & -\frac{1}{b\lambda_p\lambda_q} & \frac{1}{2\lambda_p} & \frac{1}{b\lambda_p\lambda_q} \end{bmatrix}$$

$$[k_M^{ij}]_{pq} = [k_{M1}^{ij}]_{pq} + [k_{M2}^{ij}]_{pq} \quad (2.17)$$

where: $I_1 = \int_0^a Y_p Y_q dy$; $I_2 = \int_0^a Y_p' Y_q' dy$; $I_3 = \int_0^a Y_p Y_q'' dy$; $I_4 = \int_0^a Y_p'' Y_q'' dy$; $I_5 = \int_0^a Y_p'' Y_q dy$. These integrals are analytically solved for each boundary condition in the Appendix A, given originally by Bradford and Azhari [19] and also given by Li and Schafer [20].

With the elastic stiffness matrix for the membrane case established, the same procedure can be followed to detect the elastic stiffness matrix for the bending case (Figure 2.7-b). First, the generalized strain relationship including only bending and twisting curvatures is given by:

$$\{\varepsilon_B\} = \begin{Bmatrix} \chi_x \\ \chi_y \\ 2\chi_{xy} \end{Bmatrix} = \begin{Bmatrix} \frac{-\partial^2 w}{\partial x^2} \\ \frac{-\partial^2 w}{\partial y^2} \\ 2 \frac{\partial^2 w}{\partial x \partial y} \end{Bmatrix} = \sum_{p=1}^m [B_w]_p \begin{Bmatrix} w_1 \\ \theta_1 \\ w_2 \\ \theta_2 \end{Bmatrix}_p \quad (2.18)$$

where w is the displacement perpendicular to the plane of the strip defined in Eq. (2.1) and $[B_w]_p$ is again the strain matrix, but considering the bending assumption for the p^{th} term of the series, given by the expression $\{\varepsilon_B\} = [B_w]\{d_w\}$ and shown in the Eq. (2.19).

$$[B_w]_p = \begin{bmatrix} \frac{6}{b^2}(1-2\bar{x})Y_p & \frac{2}{b}(2-3\bar{x})Y_p & \frac{6}{b^2}(2\bar{x}-1)Y_p & \frac{2}{b}(1-3\bar{x})Y_p \\ (3\bar{x}^2-2\bar{x}^3-1)Y_p'' & x(2\bar{x}-\bar{x}^2-1)Y_p'' & (2\bar{x}^3-3\bar{x}^2)Y_p'' & x(\bar{x}-\bar{x}^2)Y_p'' \\ \frac{12}{b}(\bar{x}^2-\bar{x})Y_p' & (2-8\bar{x}+6\bar{x}^2)Y_p' & \frac{12}{b}(\bar{x}-\bar{x}^2)Y_p' & (6\bar{x}^2-4\bar{x})Y_p' \end{bmatrix} \quad (2.19)$$

Additionally, the elasticity matrix of an orthotropic plane stress, $[D_w]$, is given by the expression $\{\sigma_B\} = [D_w]\{\varepsilon_B\}$, assuming only bending and twisting moments and shearing forces. In matrix form $[D_w]$ is expressed in Eq. (2.20) for the p^{th} term of the series.

$$D_x = \frac{E_x t^3}{12(1 - \nu_x \nu_y)} \quad D_y = \frac{E_y t^3}{12(1 - \nu_x \nu_y)} \quad D_1 = \frac{\nu_x E_y t^3}{12(1 - \nu_x \nu_y)} = \frac{\nu_y E_x t^3}{12(1 - \nu_x \nu_y)}$$

$$D_{xy} = \frac{G_{xy} t^3}{12} \quad G_{xy} = \frac{E_x E_y}{E_x(1 + 2\nu_y) + E_y}$$

$$[D_w]_p = \begin{bmatrix} D_x & D_1 & 0 \\ D_1 & D_y & 0 \\ 0 & 0 & D_{xy} \end{bmatrix} \quad (2.20)$$

where E_x, E_y, ν_x, ν_y and G_{xy} are the elastic constants, D_x, D_y, D_1 and D_{xy} the orthotropic plate constants, t is the thickness of the strip. In case of an isotropic material it can be assumed that $E_x = E_y = E, \nu_x = \nu_y = \nu$ and $G_{xy} = G = E/2(1 + \nu)$.

Introducing Eq. (2.19) and Eq. (2.20) into Eq. (2.13), leads to the elastic stiffness matrix for the bending, given by Eq. (2.21). The matrix corresponds to the p^{th} and q^{th} half-wave, from node i to node j (k^{th} strip).

$$[k_{B1}^{ij}]_{pq} = \frac{2 D_x I_1}{b^3} \begin{bmatrix} 6 & 3b & -6 & 3b \\ 3b & 2b^2 & -3b & b^2 \\ -6 & -3b & 6 & -3b \\ 3b & b^2 & -3b & 2b^2 \end{bmatrix};$$

$$[k_{B2}^{ij}]_{pq} = \frac{D_1}{30 b} \begin{bmatrix} -36I_2 & -33bI_2 & 36I_2 & -3bI_2 \\ -33bI_3 & -4b^2I_2 & 3bI_2 & b^2I_2 \\ 36I_2 & 3bI_2 & -36I_2 & 33bI_2 \\ -3bI_2 & b^2I_2 & 33bI_3 & -4b^2I_2 \end{bmatrix};$$

$$[k_{B3}^{ij}]_{pq} = \frac{D_1}{30 b} \begin{bmatrix} -36I_3 & -3bI_3 & 36I_3 & -3bI_3 \\ -3bI_2 & -4b^2I_3 & 3bI_3 & b^2I_3 \\ 36I_3 & 3bI_3 & -36I_3 & 3bI_3 \\ -3bI_3 & b^2I_3 & 3bI_2 & -4b^2I_3 \end{bmatrix};$$

$$[k_{B4}^{ij}]_{pq} = \frac{D_y b I_4}{420} \begin{bmatrix} 156 & 22b & 54 & -13b \\ 22b & 4b^2 & 13b & -3b^2 \\ 54 & 13b & 156 & -22b \\ -13b & -3b^2 & -22b & 4b^2 \end{bmatrix};$$

$$[k_{B5}^{ij}]_{pq} = \frac{2 D_{xy} I_5}{15 b} \begin{bmatrix} 36 & 3b & -36 & 3b \\ 3b & 4b^2 & -3b & -b^2 \\ -36 & -3b & 36 & -3b \\ 3b & -b^2 & -3b & 4b^2 \end{bmatrix};$$

$$[k_B^{ij}]_{pq} = [k_{B1}^{ij}]_{pq} + [k_{B2}^{ij}]_{pq} + [k_{B3}^{ij}]_{pq} + [k_{B4}^{ij}]_{pq} + [k_{B5}^{ij}]_{pq}. \quad (2.21)$$

As introduced before, the integrals I_1, I_2, I_3, I_4 and I_5 are analytically solved for each boundary condition in the APPENDIX A, given by Li and Schafer [20].

For the stability problem, it is necessary to formulate the geometric matrix due to the initial stress. The finite strip element is a LO2 flat shell, subjected to initial stresses that vary linearly, as shown in Figure 2.6-c. However, the distribution of the edge stress along the longitudinal axis is constant. Thus, the potential energy due to the in-plane forces is given by:

$$V = \frac{1}{2} \iiint_V \{ \sigma_1 - (\sigma_1 - \sigma_2) \bar{x} \} \left\{ \left(\frac{\partial u}{\partial y} \right)^2 + \left(\frac{\partial v}{\partial y} \right)^2 + \left(\frac{\partial w}{\partial y} \right)^2 \right\} dV. \quad (2.22)$$

Considering a uniform thickness of the strip, the edge stresses can turn into edge tractions, $T_1 = \sigma_1 t$ and $T_2 = \sigma_2 t$. Then, setting the appropriate limits of integration and computing the quadratic derivative terms into a matrix form, the Eq. (2.22) can be written as

$$V = \frac{1}{2} \int_0^t \int_0^a \int_0^b \left\{ \frac{T_1}{t} - \left(\frac{T_1}{t} - \frac{T_2}{t} \right) \bar{x} \right\} \left\{ \left[\frac{\partial u}{\partial y} \quad \frac{\partial v}{\partial y} \quad \frac{\partial w}{\partial y} \right] \left[\frac{\partial u}{\partial y} \quad \frac{\partial v}{\partial y} \quad \frac{\partial w}{\partial y} \right]^T \right\} dx dy dz. \quad (2.23)$$

Note that the vectors with the derivatives in Eq. (2.23) represent rates of change of the displacement field with respect to the y direction. These vectors can be written in accordance with the nodal displacements, as already shown in Eq. (2.18) and Eq. (2.14). Thus, in matrix form we have

$$\begin{pmatrix} \frac{\partial u}{\partial y} \\ \frac{\partial v}{\partial y} \\ \frac{\partial w}{\partial y} \end{pmatrix} = [G]\{d\} = \sum_{p=1}^m [G]_p \{d\}_p = \sum_{p=1}^m \begin{bmatrix} [G_{uv}]_p & [0] \\ [0] & [G_w]_p \end{bmatrix} \begin{pmatrix} u_1 \\ v_1 \\ u_2 \\ v_2 \\ w_1 \\ \theta_1 \\ w_2 \\ \theta_2 \end{pmatrix}_p \quad (2.24)$$

where $[G]$ is the matrix with the partial derivatives of the shape functions and $\{d\}$ the nodal displacement.

Introducing Eq. (2.24) into Eq. (2.23), and organizing the terms, the potential energy due to the in-plane forces can be deducted to a compact form, as shown in Eq. (2.27).

$$V = \frac{1}{2} \int_0^a \int_0^b \{T_1 - (T_1 - T_2)\bar{x}\} \{d\}^T [G]^T [G] \{d\} dx dy \quad (2.25)$$

$$= \frac{1}{2} \int_0^a \int_0^b \{T_1 - (T_1 - T_2)\bar{x}\} \sum_{p=1}^m \sum_{q=1}^n \{d\}_p^T [G]_p^T [G]_q \{d\}_q dx dy$$

$$= \frac{1}{2} \sum_{p=1}^m \sum_{q=1}^n \{d\}_p^T \left(\int_0^a \int_0^b \{T_1 - (T_1 - T_2)\bar{x}\} [G]_p^T [G]_q dx dy \right) \{d\}_q \quad (2.26)$$

$$= \frac{1}{2} \sum_{p=1}^m \sum_{q=1}^m \{d\}_p^T [kg]_{pq} \{d\}_q. \quad (2.27)$$

The geometric matrix can also be obtained with the minimization of the total potential energy due to the initial stress. But it is already obvious to notice the geometric matrix, $[kg]_{pq}$, inside the total potential energy, Eq. (2.26). The general expression for the geometric stiffness matrix or the initial stress matrix is written in Eq. (2.28).

$$[kg] = \sum_{k=1}^s \sum_{p=1}^m \sum_{q=1}^m \int_0^a \int_0^b \{T_1^i - (T_1^i - T_2^j)\bar{x}\} [G^i]_p^T [G^j]_q dx dy. \quad (2.28)$$

Similar to the stiffness matrix, the initial stress matrix will be divided into membrane and bending cases. Solving the Eq. (2.28) for the membrane case, which considers the matrix $[G_{uv}]$ with the partial derivatives of the shape functions for the plane

stress ($\{\partial u/\partial y \quad \partial v/\partial y\}^T$), leads to the geometric stiffness matrix for the membrane shown in Eq. (2.29).

$$[kg_{M1}^{ij}]_{pq} = \frac{T_1 b}{12} \begin{bmatrix} 3I_5 & 0 & I_5 & 0 \\ 0 & \frac{3I_4}{\lambda_p \lambda_q} & 0 & \frac{I_4}{\lambda_p \lambda_q} \\ I_5 & 0 & I_5 & 0 \\ 0 & \frac{I_4}{\lambda_p \lambda_q} & 0 & \frac{I_4}{\lambda_p \lambda_q} \end{bmatrix}$$

$$[kg_{M2}^{ij}]_{pq} = \frac{T_2 b}{12} \begin{bmatrix} I_5 & 0 & I_5 & 0 \\ 0 & \frac{I_4}{\lambda_p \lambda_q} & 0 & \frac{I_4}{\lambda_p \lambda_q} \\ I_5 & 0 & 3I_5 & 0 \\ 0 & \frac{I_4}{\lambda_p \lambda_q} & 0 & \frac{3I_4}{\lambda_p \lambda_q} \end{bmatrix}$$

$$[kg_M^{ij}]_{pq} = [kg_{M1}^{ij}]_{pq} + [kg_{M2}^{ij}]_{pq}. \quad (2.29)$$

The integrals I_4 and I_5 are analytically solved for each boundary condition in the Appendix A, given by Li and Schafer [20].

Likewise, solving the Eq. (2.28) for the bending case, which considers the matrix $[G_w]$ with the partial derivatives of the shape functions for the bending and twisting ($\{\partial w/\partial y\}$), leads to geometric stiffness matrix for the bending, shown in Eq. (2.30).

$$[kg_{B1}^{ij}]_{pq} = \frac{T_1 b I_5}{840} \begin{bmatrix} 240 & 30b & 54 & -14b \\ 30b & 5b^2 & 12b & -3b^2 \\ 54 & 12b & 72 & -14b \\ -14b & -3b^2 & -14b & 3b^2 \end{bmatrix}$$

$$[kg_{B2}^{ij}]_{pq} = \frac{T_2 b I_5}{840} \begin{bmatrix} 72 & 14b & 54 & -12b \\ 14b & 3b^2 & 14b & -3b^2 \\ 54 & 14b & 240 & -30b \\ -12b & -3b^2 & -30b & 5b^2 \end{bmatrix}$$

$$[kg_B^{ij}]_{pq} = [kg_{B1}^{ij}]_{pq} + [kg_{B2}^{ij}]_{pq}. \quad (2.30)$$

The integral I_5 is analytically solved for each boundary condition in the Appendix A, given by Li and Schafer [20].

So far, the stiffness and geometric matrices were deduced for local coordinates and only for the p^{th} term of the series. Since a generic structure will be composed of a finite number of strips, it is justified to adopt a common axis for the complete structure. This common space is called here the global coordinate system. Figure 2.8 shows the local (x, y , and z) and global coordinate system (\mathbf{X} , \mathbf{Y} and \mathbf{Z}). Note that the y and \mathbf{Y} axis are common to each other, in which the main space transformation here is the rotation of the y axis, and of course, the coordinates translation for each strip.

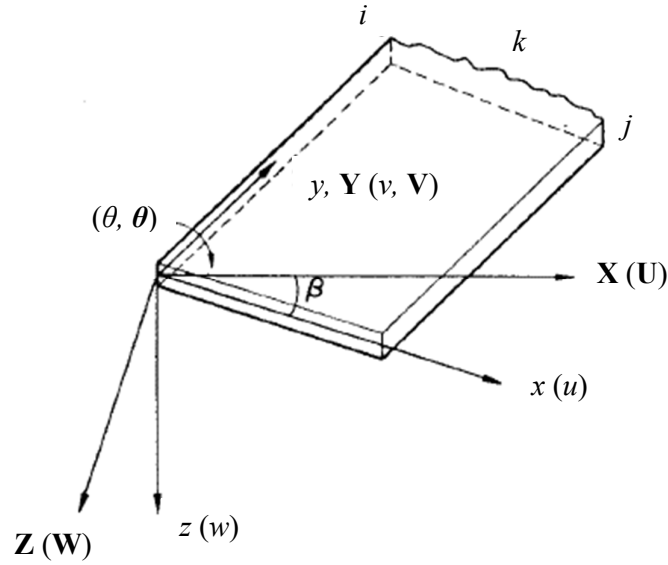


Figure 2.8. Local and Global coordinate system on a rectangular strip. [11].

Before defining the space transformation matrix, the local matrices for each strip need to be defined. In Eq. (2.31) the stiffness and geometric matrix are shown for each strip and for the p^{th} half-wave term of the series. Note that for the assumed flat shell strip (LO2), there is no interaction between the bending and the membrane. Due to that, the elastic stiffness matrix - $[k^{ij}]_{pq}$ - and the geometric matrix - $[kg^{ij}]_{pq}$ - are obtained by assembling the membrane and bending matrices through a simple combination, as described in Eq. (2.31).

$$[k^{ij}]_{pq} = \begin{bmatrix} [k_M^{ij}]_{pq} & [0]_{4 \times 4} \\ [0]_{4 \times 4} & [k_B^{ij}]_{pq} \end{bmatrix}_{8 \times 8} \quad [kg^{ij}]_{pq} = \begin{bmatrix} [kg_M^{ij}]_{pq} & [0]_{4 \times 4} \\ [0]_{4 \times 4} & [kg_B^{ij}]_{pq} \end{bmatrix}_{8 \times 8} \quad (2.31)$$

where $[0]_{4 \times 4}$ is the null matrix, $[k_M^{ij}]_{pq}$ is the elastic stiffness matrix for the membrane case defined in Eq. (2.17), $[k_B^{ij}]_{pq}$ is the elastic stiffness matrix for the bending case defined in Eq. (2.21), $[kg_M^{ij}]_{pq}$ is the geometric matrix for the membrane case defined in Eq. (2.29), $[kg_B^{ij}]_{pq}$ is the geometric matrix for the bending case defined in Eq. (2.30).

Thus, the global matrices are obtained by assembling all the half-wave terms in each corresponding degree of freedom. For the assembling, it is necessary to transform the local coordinate into global coordinates. The displacements are also subjected to this space transformation, as can be observed in Eq. (2.32) for the displacement field transformation and in Eq. (2.33) for the nodal displacement transformation.

$$\begin{Bmatrix} u \\ v \\ w \end{Bmatrix} = \sum_{p=1}^m [R]_{3 \times 3} \begin{Bmatrix} u' \\ v' \\ w' \end{Bmatrix}_p. \quad (2.32)$$

$$\begin{Bmatrix} u_1 \\ v_1 \\ u_2 \\ v_2 \\ w_1 \\ \theta_1 \\ w_2 \\ \theta_2 \end{Bmatrix} = \sum_{p=1}^m [R]_{8 \times 8} \begin{Bmatrix} u'_1 \\ v'_1 \\ u'_2 \\ v'_2 \\ w'_1 \\ \theta'_1 \\ w'_2 \\ \theta'_2 \end{Bmatrix}_p. \quad (2.33)$$

Note that the space transformation from local to global is performed by multiplying the local displacements by a rotation matrix. This matrix can be an 8 by 8 ($[R]_{8 \times 8}$) or 3 by 3 ($[R]_{3 \times 3}$) size, depending on the displacement addressed. These matrices are shown respectively in Eq. (2.34) and Eq. (2.35).

$$[R]_{8 \times 8} = \begin{bmatrix} \cos \beta & 0 & 0 & 0 & -\sin \beta & 0 & 0 & 0 \\ 0 & 1 & 0 & 0 & 0 & 0 & 0 & 0 \\ 0 & 0 & \cos \beta & 0 & 0 & 0 & -\sin \beta & 0 \\ 0 & 0 & 0 & 1 & 0 & 0 & 0 & 0 \\ \sin \beta & 0 & 0 & 0 & \cos \beta & 0 & 0 & 0 \\ 0 & 0 & 0 & 0 & 0 & 1 & 0 & 0 \\ 0 & 0 & \sin \beta & 0 & 0 & 0 & \cos \beta & 0 \\ 0 & 0 & 0 & 0 & 0 & 0 & 0 & 1 \end{bmatrix}. \quad (2.34)$$

$$[R]_{3 \times 3} = \begin{bmatrix} \cos \beta & 0 & -\sin \beta \\ 0 & 1 & 0 \\ \sin \beta & 0 & \cos \beta \end{bmatrix}. \quad (2.35)$$

With the rotation matrix defined, the space transformation and the assembling of the global stiffness and geometric matrices are established in Eq. (2.36) and Eq. (2.37), respectively.

$$[K] = \sum_{k=1}^s \sum_{p=1}^m \sum_{q=1}^m [R]_{8 \times 8} [k^{ij}]_{pq} [R]_{8 \times 8}^T. \quad (2.36)$$

$$[KG] = \sum_{k=1}^s \sum_{p=1}^m \sum_{q=1}^m [R]_{8 \times 8} [kg^{ij}]_{pq} [R]_{8 \times 8}^T. \quad (2.37)$$

It can be observed that the space transformation is performed on the local matrices (Eq. (2.31)), for each term of half-wave and for each strip. Then, the matrices are added in each corresponding degree of freedom in order to form the global matrices.

After the assembling and space transformation, the general stability solution is obtained by solving the classic generalized eigenvalue problem described in the Eq. (2.38).

$$([K] - [\Lambda][KG])[\Phi] = [0] \quad \text{or} \quad [K][\Phi] = [\Lambda][KG][\Phi] \quad (2.38)$$

where $[K]$ is the assembled global elastic stiffness matrix (Eq. (2.36)), $[KG]$ is the assembled global geometric stiffness matrix (Eq. (2.37)), $[\Lambda]$ is the eigenvalue matrix and $[\Phi]$ is the eigenvector matrix. In other words, the matrix $[\Lambda]$ corresponds to a diagonal matrix with the critical stress and $[\Phi]$ refers to a matrix with buckling modes, where each column of the matrix represents one mode, and the first column correspond to the critical buckling mode.

There are some methods to solve the generalized eigenvalue problem described in Eq. (2.38), *e.g.* QZ algorithm; the Cholesky factorization; the implicitly restarted Arnoldi method; Krylov-Schur algorithm. The main references for these methods, that are already formed as a MATLAB [23] built-in function, can be found in Smith *et al.* [24], Garbow *et al.* [25], Moler and Stewart [26], Stewart [27] and Lehoucq *et al.* [28].

To sum up, the finite strip method gives a solution of the critical load and its associated buckling mode. However, this formulation is performed for only a defined longitudinal length L of the structural member. For the case of the buckling analysis of

cold-formed steel sections, it is necessary to perform a multiple and repetitive analysis for a set of lengths. Thereby, with the results of this type of analysis it is possible to determine the number of the local buckling mode half-waves in any possible critical length, associated with its critical load and buckling mode. The same condition is applied when investigating the distortional buckling and its multiple buckling longitudinal half-waves. This analysis brings about a curve, critical load *vs.* length, called signature curve of the cross-section, which presents the solution for local, distortional and global buckling.

Note that adopting a FEM analysis to perform this signature curve will demand a much higher computational effort, due to its large number of degrees of freedom. Therefore, the finite strip method is useful, when analyzing a set of structural member lengths.

The signature curve of a thin-walled member is of utmost importance because it provides three general critical loads associated with local, distortional and global buckling. These critical loads can be determined by an implementation of the buckling modal decomposition or by a user observation of the buckling modes results. In order to understand these critical buckling modes, it is important to define what is a local, distortional and global critical buckling mode. Alongside these critical loads, the strength of the structural element can be determined, through a simple method called the Design Strength Method, which will be described in detail later.

2.3 Critical Buckling Modes

The critical buckling modes are given by solving the classic generalized eigenvalue problem, described in Eq. (2.38), which is symbolized by matrix $[\Phi]$. For each member length, the finite strip method gives the buckling modes of several superior modes, each one corresponding to a superior critical load. Depending on the length and geometry of the structural member, the critical buckling mode shows a different modal shape. Figure 2.9 illustrates the computed results from FStr program, of the modal shapes of a lipped channel cold-formed steel column (LC 100x70x15x2.70 mm) at different lengths in order to show each critical buckling mode.

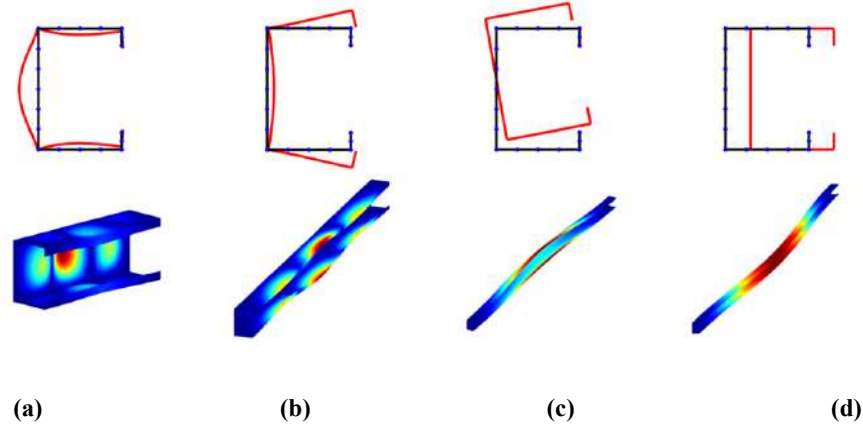


Figure 2.9. Cold-formed steel lipped-channel 100x70x15x2.70 mm fixed-fixed end condition experiencing (a) local $L=252\text{mm}$, (b) distortional $L=1379\text{mm}$, (c) flexural-torsional $L=2557\text{mm}$ and (d) flexural buckling $L=14521\text{mm}$.

Generally, the modal shapes of thin-walled members can be classified by three generic groups: local, distortional and global. According to Schafer and Ádány [29], the widely adopted definition of these three modes are:

- (i) Local mode (L): defined as plate deformation, without interfering in the translation of adjacent points for other plate elements in the member cross-section (Figure 2.9-a).
- (i) Distortional mode (D): characterize for the translation of some points in the intersection of plates elements in the cross-section, mainly noticed as a distortion of the cross-section (Figure 2.9-b).
- (ii) Global mode (G): described as a full translation of the cross-section, preserving un-deformed cross-section (Figure 2.9-c and Figure 2.9-d).

Besides this general definition of these three general critical buckling modes, there are other characterizations of the modal shapes that are related to the wavelength of the buckling mode or related to the membrane versus flexural plate deformations. However, these definitions are not always accurate enough to define the critical buckling modes. In some cases, where the thin-walled structural member are formed by several folded plates and intermediate stiffeners, the general classification for the modal shapes can become quite inaccurate and complex, as is discussed by Schafer and Ádány [29].

Resulting from that complexity on determining the modal shape, it is appropriate to classify the buckling mode as a participation of each classic pure buckling mode. The studies made by Ádány and Schafer [30], [31] & [32] present a complete approach on how to identify and classifying the modal participation on a critical buckling analysis

using the finite strip method. Later, Li [22], Li and Schafer [20], [33] & [34] stated the same approach on modal participation, but for general boundary conditions. The principle to classify the modes are based on the generalized beam theory (GBT) criteria, which takes critical mechanical assumptions. Table 2.2 shows the three criteria for classify the buckling modes, according to Schafer and Ádány [29].

Table 2.2. Critical buckling mode classification (G: Global, D: Distortional, L: Local, ST/O: Other)

Mechanical criteria	<i>G</i>	<i>D</i>	<i>L</i>	<i>ST/O</i>
$\gamma_{xy} = 0$, $\varepsilon_x = 0$, v is linear (Vlasov's hypothesis)	Yes	Yes	Yes	No
$\varepsilon_y \neq 0$ (longitudinal warping)	Yes	Yes	No	—
$\kappa_x = 0$ (undistorted section)	Yes	No	—	—

- (i) The first criterion, takes into account the membrane deformations, which includes shear strains equal to zero, membrane transverse strain also equal to zero and linear longitudinal displacements, in the cross-section plane. Essentially, this first criterion is based on the Vlasov's assumptions [35].
- (ii) The second criterion is related to the longitudinal warping. It states that the longitudinal strains and displacements are non-zero along the member length.
- (iii) The third criterion corresponds to the transverse flexure. This criterion assumption consists of flexure in the transverse direction, retaining the cross-section undistorted.

The buckling modes can be defined using the assumptions defined in Table 2.2. The modes are generally classified as Global (G), Distortional (D), Local (L) and Other (O).

- (i) Global: modes which satisfy all the three assumptions;
- (ii) Distortional: deformation patterns which include Vlasov's hypothesis (first criterion) and longitudinal warping (second criterion); however, the undistorted section (third criterion) is not included, which means that transverse flexure occurs.
- (iii) Local: modes which have a shape configuration that only follow the Vlasov's hypothesis (first criterion), but do not include the second

criterion, which means that longitudinal warping occurs, while the transverse flexure is irrelevant for this case.

- (iv) Other: this mode occurs by Vlasov's hypothesis, which means that it is not qualify for the first criterion, and the second and third criterion are irrelevant. This deformation pattern classification does not exist in the GBT criteria; however, must stand in FSM and FEM, because of the incorporation of the membrane degrees of freedom. In another words, this mode is classified as the Other mode that is not global, distortional or local.

The modal participation formulation for the finite strip method is implemented in the well-known computer program Constrained and Unconstrained Finite Strip Method (CUFSM), by Schafer *et al.* [36], [37], [38] & [39]. Through this program it is possible to determine the (percentage) participation of each general buckling mode. Figure 2.10 shows all the possible deformation patterns for a lipped channel thin-walled member, using the CUFSM software with a total of 40 degrees of freedom.

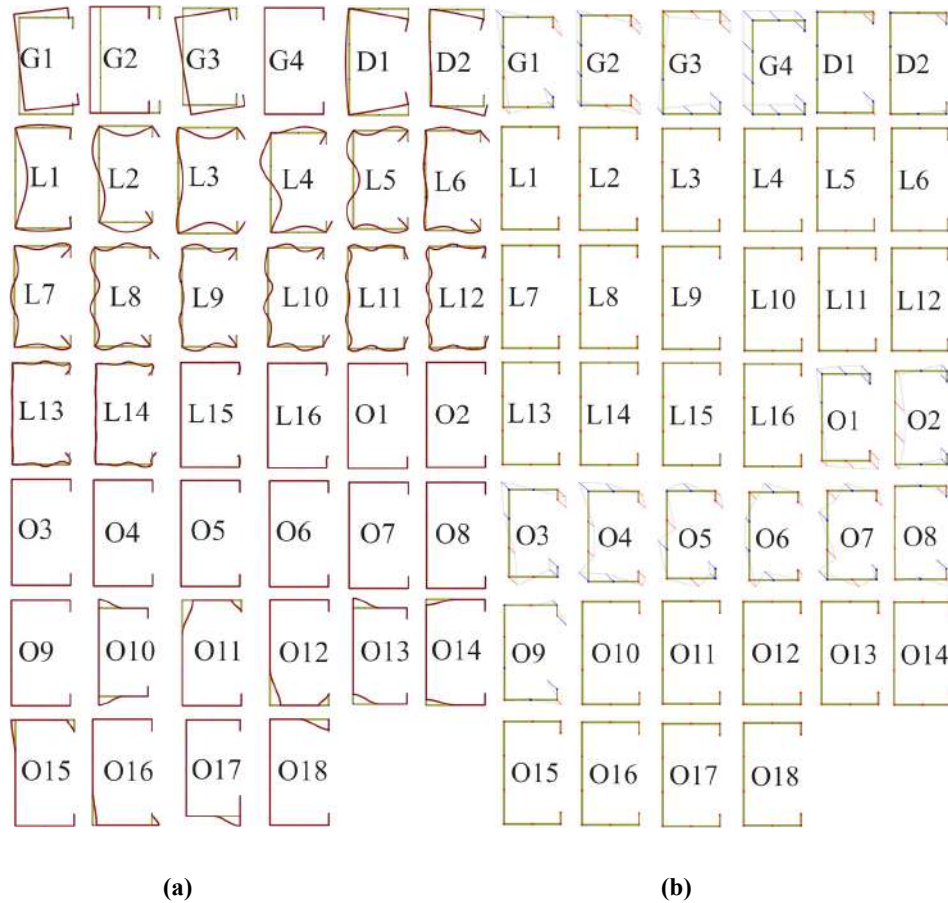


Figure 2.10. Pure deformation patterns for a lipped channel thin-walled member under axial compression, (a) in plane and (b) out of plane (G: Global, D: Distortional, L: Local, O: Other).

2.4 Computer Program Applications and Methods for the Buckling Analysis

So far, the finite strip method is well consolidated in well-known computer programs. The two most famous computer programs that performs a finite strip method are: the Constrained and Unconstrained Finite Strip Method (CUFSM), by Schafer *et al.* [36], [37], [38] & [39], and the THIN-WALL by Hancock *et al.* [40] & [41].

The CUFSM [39] program is a finite strip elastic buckling analysis application, which performs analyses for thin-walled sections. CUFSM is an open free source program created by professor Ben Schafer's thin-walled structures research group at Johns Hopkins University (Baltimore, MD, United States of America) and it was developed in the MATLAB [33] platform. The semi-analytical finite strip method has been updated by the Schafer's research group in the last decade. Ádány [42] implemented the constrained finite strip method (cFSM), providing the modal decomposition and modal identification to a conventional finite strip solution. Li [22] has contributed to the constrained finite strip method with a more general boundary condition, which could extend the cFSM for any boundary condition. The newer version of the computer program is the CUFSM 5.01 [39] and it includes: signature curve analysis; general end boundary conditions; generalized loading; built-in cross-sections; constrained finite strip solutions for modal decomposition and identification; plastic section analysis; section property analysis; analyses to approximate members with holes; interaction with the bar finite element software MASTAN (by McGuire, Gallagher, and Ziemian [43]).

The THIN-WALL is a Semi-Analytical Finite Strip Method (SAFSM), which has been recently updated to the THIN-WALL 2 by Nguyen, Hancock and Pham [41]. The new updated version was developed at The University of Sydney (Sydney, NSW, Australia), with the help of a graphical user interface from MATLAB [23] and Visual Studio C++ computational engines. Originally, the THIN-WALL 2 has two different versions of the SAFSM buckling analysis: *bfinst7.cpp* and *bfinst10.cpp*. The first version (*bfinst7.cpp*), described by Hancock and Pham [44], considers uniform loading that adopts complex mathematical functions with no end-conditions constraints and also includes shear modes and signature curve associated with shear, bending and compression. The second version (*bfinst10.cpp*), described by Hancock and Pham [45], includes localized loading, assuming simply supported end conditions and arbitrary loading. For more information, in Hancock and Pham [46] it is described the theory of

the displacement functions used in the buckling analyses for the THIN-WALL 2 computer program.

Besides the finite strip computer programs, there are other methods for performing the elastic buckling analysis. The Generalized-Beam-Theory (GBT) is a well consolidated method, originally proposed by Schardt [47], and in the last decade has been updated by many authors (*e.g.* Silvestre [48], Bebiano [49], Camotim *et al.* [50] & [51]). In addition, the GBT formulation has been advanced to conduct first-order (*e.g.* Gonçalves and Camotim [52] and Gonçalves *et al.* [53]), buckling (*e.g.* Camotim *et al.* [54] & [55], Basaglia and Camotim [56], Natário *et al.* [57] and Gonçalves and Camotim [58]), vibration (*e.g.* Camotim *et al.* [59] and Bebiano *et al.* [60]), dynamic (Bebiano *et al.* [61]) and post-buckling (Silvestre and Camotim [62] and Basaglia *et al.* [63] & [64]) analysis involving prismatic elements, trusses and frames. The best known computer program that uses this method is the GBTul 2.0, from the Generalized Beam Theory Research Group at Lisboa, Instituto Superior Técnico (IST), University of Lisboa, Portugal, by Bebiano, Camotim and Gonçalves [65]. This software was first created by Bebiano, Silvestre and Camotim [66] & [67] as GBTul 1.0 β , and it has been updated by the IST research group, headed by professor Dinar Camotim. The software performs elastic buckling and vibration analysis with an intuitive graphical user interface. The computer application gives the deformation field of a structural member based on a combination of cross-section deformations. The program makes possible that the user takes into account (*i*) isotropic or orthotropic materials, (*ii*) different support conditions, (*iii*) combination of arbitrary axial force, bending moment and bimoment diagrams.

On a final note, the finite element method offers more robust approaches for performing the elastic buckling analysis. According to the FEM software ANSYS theory reference [68], the Block Lanczos and Subspace Iteration are the eigensolver methods for elastic buckling. The Block Lanczos solver performs the classic Lanczos algorithm that can be found in detail in Rajakumar and Rogers [69] and the block shifted Lanczos algorithm, described in Grimes *et al.* [70]. According to the ANSYS theory reference release 5.6 [71], the Subspace Iteration method is explained by Bathe [72], and some improvements in the method is found in Wilson and Itoh [73]. Since the FEM requires a massive computational effort, compared to continuum discretization alternative methods, this method is not commonly adopted for performing a buckling analysis of thin-walled member for a set of lengths. However, when performing a non-linear analysis (*e.g.* arc-length method, described in Riks [74] & [75] and Wempner [76]), in order to detect the

strength of a structural element, it is convenient to impose geometric initial imperfection of the structure from a previous elastic buckling analysis in FEM.

2.5 Coupled Instability Phenomena

In the literature so far, the coupled instability phenomena can be found as compound buckling, simultaneous buckling, interaction buckling and many other denominations. Historically, Koiter [77] and Budiansky [78], were the first two researchers that included the couple instability phenomena.

The nature of the phenomena is complex and hard to predict. Due to that, many authors try to classify the buckling interaction in various ways. In Gioncu [79] is shown an overall of the couple instability state-of-art from over 230 papers until 1994. Gioncu [79] explains concepts and classifications for the nature of the coupled phenomenon.

According to Batista [1], the coupled phenomena lead to an erosion of the limit load, in other words means loss of the ultimate strength. As stated in Gioncu [79] this erosion can be classified into two major groups: primary erosion and secondary erosion. The primary erosion is induced by the extensional deformations, elastic supports and plastic deformations, while the secondary erosion is caused by the coupled instabilities. Figure 2.11 illustrates an example of the two types of erosions, for a case with a stiffened cylindrical shell.

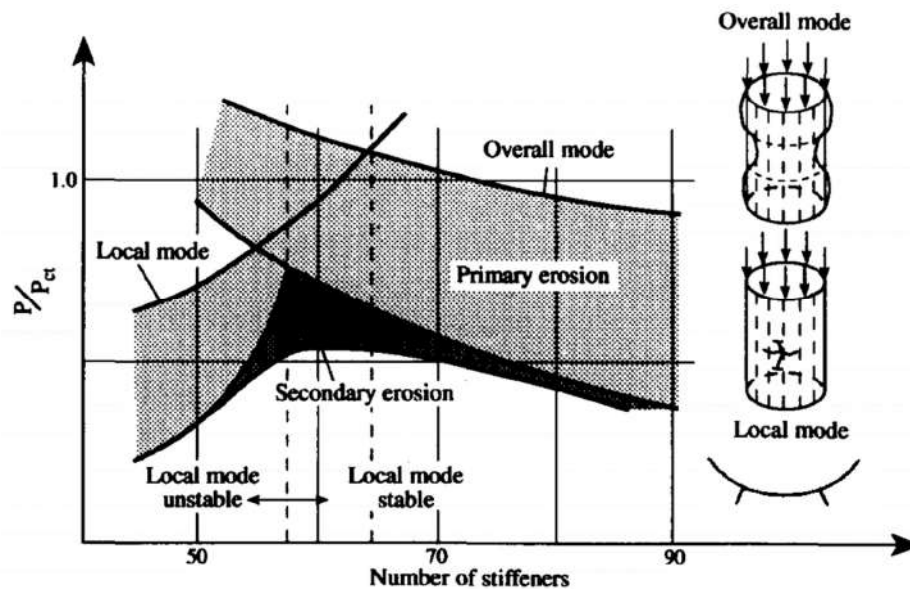


Figure 2.11. Types of erosion for stiffened cylindrical shell under compression. [79].

The graph in the Figure 2.11 shows how the number of stiffeners in the cylindrical shell affects the P/P_{cr} ratio. According to Gioncu [79], the erosion due to the coupling phenomenon is hard to predict, but it must happen in the presence of imperfections, otherwise, the second erosion would not exist, in other words the cut of the cusp formed by the local and global (overall) buckling modes would not take place.

According to Gioncu [80], the buckling interaction can be classified into two very different types: naturally coupled (Figure 2.12-a) and coupling due to design (Figure 2.12-b).

- (i) Naturally coupled instability: formed by coupling individual modes that cannot be separated by any artificial method (*e.g.* longitudinal compressed rectangular plate with four simply supported edges);
- (ii) Coupled instability by design: influenced by the geometry of the structure, which force two or more buckling modes close or even coincidental (*e.g.* combination of flexural and torsional modes in a lipped channel open cross-section under compression).

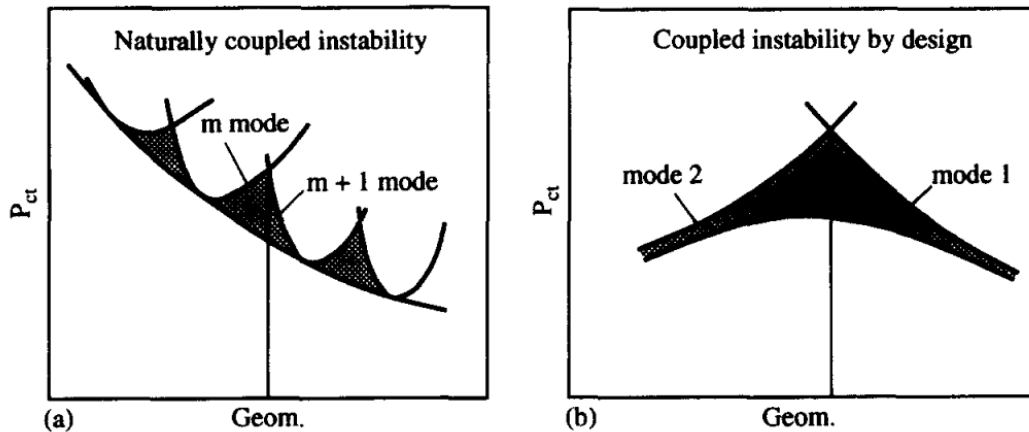


Figure 2.12. Buckling interaction classification from Gioncu [80], (a) naturally coupled and (b) coupling due to design. [79].

Another classification of coupled instabilities reported by Gioncu [79] is related to the coupling linearity.

- (i) Linear coupling: when two modes are coupled, independently of the presence of imperfections (*e.g.* interaction of flexural and torsional modes of mono symmetrical cross-sections);
- (ii) Nonlinear coupling: it only exists in the presence of imperfections, otherwise, for ideal structures, this coupling does not occur (*e.g.*

interaction between flexural and torsional-flexural modes for a mono symmetrical cross-sections).

In addition, Gioncu [81] has suggested another classification for the erosion based on its size: weak, moderate, strong and very strong interaction.

- (i) Weak: erosion under 10% (*e.g.* flexural and flexural-torsional buckling interaction in monosymmetrical columns);
- (ii) Moderate: erosion over 10% and under 30% (*e.g.* overall and local buckling interaction in trusses systems);
- (iii) Strong: erosion over 30% and under 50% (*e.g.* local-global buckling interaction in thin walled columns and beams);
- (iv) Very strong: erosion over 50% (*e.g.* general and local buckling interaction in reticulated shells).

The erosion size classification is important in order to assume design procedures. For example, the cases of weak buckling interaction can be ignored, assuming that the safety coefficients would cover the phenomena of losing strength capacity. On the other hand, for moderate interaction, methods must be used to consider the phenomena, which could be a simple one. On occasions of strong and very strong couple instabilities, special methods are used and must be improved, Gioncu [79].

More specifically, for the case of thin-walled members, the couple instability is a phenomenon which should have special attention. Cold-formed steel members are sensitive to the buckling interaction, due to its very slender geometry with most of cases composed of open cross-sections. For this type of structural element, the coupling due to design classification (Gioncu [80]) takes an important role in the investigation of the strength capacity. As reported in the section 2.3 (Critical Buckling Modes), this structural option has general modes classified as local (L), distortional (D) and global (G). These general buckling modes can interact resulting in a coupled instability by design, influenced by the geometry of the structure. This type of coupled instability is composed of at least two buckling modes and can be identified as L-D, L-G, D-G and L-D-G.

2.5.1 Distortional-Global Interaction concepts

The basic concept of distortional-global (D-G) interaction can be shown in the results of the buckling analysis, performed with the computational program FStr, included in Figure 2.13. Basically, when the critical load resulting from the distortional buckling

is in a domain relatively close to the global buckling, it is highly possible to experience the D-G interaction, which is in the neighborhood of the length $L=1850$ mm, for example. For the signature curve below (Figure 2.13), the method is the finite strip method and the geometry is a lipped channel section LC 100x70x15x2.70 mm, under axial compressive load, with fixed-fixed end condition and for a set of 200 lengths, spaced equally in logarithm scale.

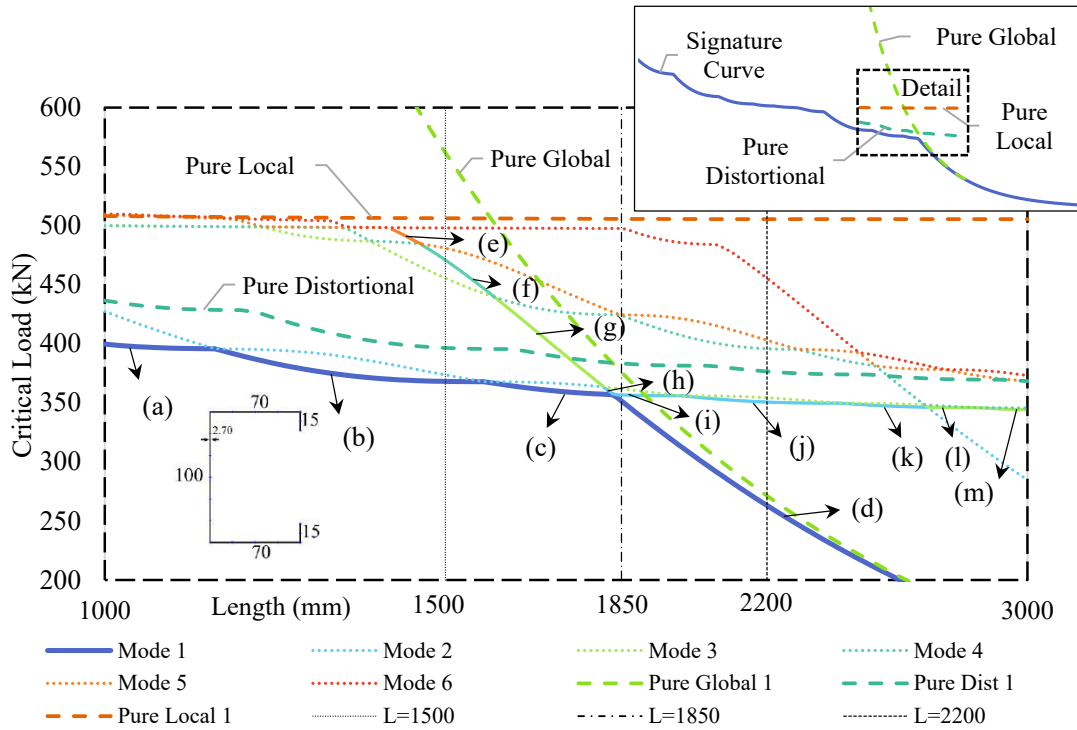


Figure 2.13. Critical load versus length - signature curve, superior modes and pure modes (LC100x70x15x2.70 mm).

- (a) Signature Curve: first mode, distortional buckling with 2 half-waves;
- (b) Signature Curve: first mode, distortional buckling with 3 half-waves;
- (c) Signature Curve: first mode, distortional buckling with 4 half-waves;
- (d) Signature Curve: first mode, flexural-torsional buckling with 1 half-wave;
- (e) Fifth Superior Mode: flexural-torsional buckling with 1 half-wave;
- (f) Fourth Superior Mode: flexural-torsional buckling with 1 half-wave;
- (g) Third Superior Mode: flexural-torsional buckling with 1 half-wave;
- (h) Second Superior Mode: flexural-torsional buckling with 1 half-wave;
- (i) Second Superior Mode: distortional buckling with 4 half-waves;
- (j) Second Superior Mode: distortional buckling with 5 half-waves;
- (k) Second Superior Mode: distortional buckling with 6 half-waves;

- (l) Third Superior Mode: distortional buckling with 6 half-waves;
- (m) Third Superior Mode: distortional buckling with 7 half-waves.

The Figure 2.13 illustrates in detail the superior modes from an elastic buckling analysis, in the length range of 1000 to 3000 mm, with pure local, distortional and global modes. The curves from (a)-(d) correspond to the signature curve, representing the first mode with 10 half-waves terms employed on the finite strip method formulation.

It should be noted that there is a pattern of superior modes continuing the global and distortional modes, (e)-(h) for flexural-torsional mode in distortional length and (i)-(m) for distortional mode in global length. Also, comparing this pattern with pure modes, it is possible to notice an erosion, called primary erosion as classified by Gioncu [79]. It is noticed that the secondary erosion is hard to predict with the elastic buckling analysis, which makes it harder to investigate the D-G interaction behavior.

The distortional-global (D-G) interaction can be classified into its type and nature. As reported by Martins *et al.* [82], the type of distortional-global interaction can change depending on the form of the global buckling mode: (i) distortional/major-axis flexural-torsional (D-FT) and (ii) distortional/minor-axis flexural (D-F). However, for lipped channel columns, the D-FT interaction is more common to occur, while the D-F interaction happens more often on zed-sections columns. In addition, related to the nature of the critical buckling load, Martins *et al.* [82] states another classification. This categorization is based on the ratio between the critical loads from global and distortional modes, $R_{GD} = P_{crG}/P_{crD}$, and it is useful for performing a parametric and behavior study. The categories are classified as:

- (i) *True D-G interaction* (TI): When the distortional and global critical buckling are close, this scenario may always happen for $0.90 < R_{GD} < 1.10$. According to Martins *et al.* [82], this state can behave differently in three different groups, depending on the critical slenderness: (i.1) abruptly collapse for stocky columns, $\lambda_{cr} \leq 1.0$; (i.2) collapse after starting of yielding for slender columns, $1.0 < \lambda_{cr} < 2.0$; (i.3) elastic-plastic strength reserve before collapse for very slender columns, $\lambda_{cr} \geq 2.0$ (this group has shown local deformations, experiencing L-D-G interaction on lipped channel columns). This case can be illustrated by Figure 2.13, when the length is between 1750 mm and 1900mm.

- (ii) *Secondary-distortional bifurcation D-G interaction (SDI)*: Occurs for yield strength sufficiently high, in order to enable the interaction to develop. This situation is more common in the range $R_{GD} \leq 0.90$ and can be exemplified by Figure 2.13, when the length is more than 1900 mm.
- (iii) *Secondary-global bifurcation D-G interaction (SGI)*: Also occurs for yield stress sufficiently high, to enable the interaction to arise, nonetheless this one is more likely to develop, due to its high post-critical strength reserve caused by the distortional buckling. This is more common in the range $R_{GD} \geq 1.10$. This group can be also exemplified by Figure 2.13, when the length is lower than 1750 mm, but not less than 1500 mm, in which the global buckling mode starts to become hard to reach and the local buckling mode is approachable. In this case, there is possible L-D-G interaction or just L-D.

2.6 Analytical Elastic Buckling Analysis

An analytical elastic buckling analysis is the most consolidated approach in the standards, because of its easiness of performing an elastic buckling analysis directly. However, the analytical procedure is fairly specific in some cases, depending on the boundary condition, the geometry of the cross-section and the type of buckling.

In this section, an analytical formulation is presented for local, distortional and global elastic critical buckling of CFS thin-walled members under axial compression. The boundary conditions are simply supported at the end sections. Also, only one half-wave term is considered, which means, the first buckling mode, associated with the shorter column solution. As reported by Timoshenko and Gere [83], the first mode is already sufficient to determine the elastic critical stress for simply supported columns.

2.6.1 Local Buckling

The origin of the analytical expression is given by Bryan [84], which published the first solution providing the critical buckling stress of thin simply-supported rectangular plates under axial compression on two opposite edges. An approximated semi-analytical expression for the local critical stress is given in the Brazilian standard ABNT NBR 14762:2010 [5], proposed by Batista [85]. Descriptively, the critical stress

is given in the Eq. (2.39), in function of the local buckling coefficient for a full section under uniform compression, expressed by Eq. (2.40)⁴. In addition, the formulation is given by a lipped channel section with outside-to-outside measurement, described in Figure 2.14-a.

$$\sigma_{crl} = k_l \frac{\pi^2 E}{12(1-\nu^2)} \left(\frac{t}{b_w} \right)^2 \quad (2.39)$$

$$k_l = 6.8 - 5.8 \left(\frac{b_f}{b_w} \right) + 9.2 \left(\frac{b_f}{b_w} \right)^2 - 6.0 \left(\frac{b_f}{b_w} \right)^3. \quad (2.40)$$

The critical local load can then be determined as $P_{crl} = A \sigma_{crl}$, where A is the area of the full cross-section.

2.6.2 Distortional Buckling

The analytical distortional buckling approach is not provided, specifically, by the ABNT NBR 14762:2010 [5], due to its complexity formulations given in the literature so far. The Australian/New Zealand code AS/NZS 4600 [6] provides an analytical distortional buckling formulation as an option, however, it is still quite complex to manipulate, as well as this procedure proved to be inaccurate for certain CFS sections' geometry. Also, the North-American standard AISI S100-16 [7] presents an analytical elastic distortional buckling expression.

In the following, an expression for the distortional buckling is shown given by Cardoso *et al.* [86]. The procedure is derived from an energy-based approach leading to a relatively simple and reliable closed-form equation for lipped channels subject to uniform compression. The expression displayed here is associated with the second model from Cardoso *et al.* [86] - with flexible flanges - which gives the best approximated results, compared to GBTul 2.0 (Bebiano, Camotim and Gonçalves [65]).

The formulation is presented below, and it is derived from a simply support boundary condition with half of a lipped channel cross-section and only one half-wave term. Also, the geometric parameters are all based on the center line of the cross-section, illustrated in Figure 2.14-b. The critical distortional buckling expression is given by Eq. (2.52).

⁴ Geometry limited to $0.1 \leq (b_f/b_w) \leq 1.0$ and $0.1 \leq (b_s/b_w) \leq 0.3$.

- (i) Area of half-section on center line dimensions;

$$A_{hs} = (\bar{b}_w + 2\bar{b}_f + 2\bar{b}_s) \frac{t}{2}. \quad (2.41)$$

- (ii) Plate stiffness;

$$D = \frac{Et^3}{12(1 - \nu^2)}. \quad (2.42)$$

- (iii) Distance between the web-flange junction and the center of rotation;

$$\Delta Y_s = \frac{\bar{b}_s^2}{2\bar{b}_s + \bar{b}_f}. \quad (2.43)$$

- (iv) Correlation coefficient between overall lipped flange and web rotation;

$$\kappa_1 = \frac{1}{1 + (2\bar{b}_f/3\bar{b}_w)}. \quad (2.44)$$

- (v) Correlation coefficient between overall lipped flange and stiffener rotation;

$$\kappa_2 = \kappa_1 \left(\frac{\bar{b}_f}{\bar{b}_w} + 1 \right). \quad (2.45)$$

- (vi) Correlation parameter corresponding to the cross-section “translation” per unit of flange-stiffener rotation needed to balance moments produced by the warping stress distribution;

$$\beta = \frac{\bar{b}_f \bar{b}_s^2 (2\bar{b}_f + 2\bar{b}_s + \bar{b}_w)}{(\bar{b}_f^2 + 4\bar{b}_f \bar{b}_s + 2\bar{b}_f \bar{b}_w + 6\bar{b}_s \bar{b}_w) (2\bar{b}_s + \bar{b}_f)}. \quad (2.46)$$

(vii) Moment of inertia of half-section about minor axis;

$$I_z = \frac{\bar{b}_f^2 t}{6} \left(\frac{\bar{b}_f^2 + 4\bar{b}_f \bar{b}_s + 2\bar{b}_f \bar{b}_w + 6\bar{b}_s \bar{b}_w}{2\bar{b}_s + 2\bar{b}_f + \bar{b}_w} \right). \quad (2.47)$$

(viii) Stiffened-flange warping constant with respect to the rotation center;

$$I_w = \frac{\bar{b}_f^2 \bar{b}_s^3 t}{3} \left(\frac{\bar{b}_f + \bar{b}_s}{\bar{b}_f + 2\bar{b}_s} \right)^2. \quad (2.48)$$

(ix) Cross-section geometric parameter;

$$I_{zw} = -\frac{1}{6} \left(\frac{\bar{b}_f^3 \bar{b}_s^2 t}{\bar{b}_f + 2\bar{b}_s} \right). \quad (2.49)$$

(x) Lip constant of torsion;

$$J_s = \frac{t^3}{3} \bar{b}_s. \quad (2.50)$$

(xi) Apparent polar moment of inertia with respect to web-flange junction point;

$$I_0^* = t \left[\frac{\bar{b}_w^2 \kappa_1}{60} (\bar{b}_w \kappa_1 + 10\Delta Y_s + 10\beta) + \bar{b}_s^2 \kappa_2 (\Delta Y_s + \beta) + \frac{\bar{b}_s^3 \kappa_2^2}{3} + \bar{b}_f^2 \bar{b}_s \right. \\ \left. + \frac{\bar{b}_w^3 \kappa_1^2}{210\bar{b}_w^2} (22\bar{b}_f^2 + 77\bar{b}_f \bar{b}_w + 70\bar{b}_w^2) \right]. \quad (2.51)$$

(xii) Elastic distortional buckling critical stress.

$$\sigma_{crd,2} = \frac{\left(\begin{array}{l} \frac{\bar{b}_w D \kappa_1^2}{60} \left[\pi^2 \left(\frac{\bar{b}_w}{L} \right)^2 + 20 + \left(\frac{120}{\pi^2} \right) \left(\frac{L}{\bar{b}_w} \right)^2 \right] \\ + \left(\beta^2 \frac{\pi^2 E I_z}{L^2} + 2\beta \frac{\pi^2 E I_{zw}}{L^2} + \frac{\pi^2 E I_w}{L^2} + \kappa_2^2 G J_s \right) \\ + \frac{\bar{b}_f D \kappa_1^2}{210} \left\{ \begin{array}{l} \left[22\pi^2 \left(\frac{\bar{b}_f}{\bar{b}_w} \right)^2 + 77\pi^2 \left(\frac{\bar{b}_f}{\bar{b}_w} \right) + 70\pi^2 \right] \left(\frac{\bar{b}_f}{L} \right)^2 \\ + (224 - 280\nu) \left(\frac{\bar{b}_f}{\bar{b}_w} \right)^2 + (560 - 700\nu) \left(\frac{\bar{b}_f}{\bar{b}_w} \right) \\ + 420(1 - \nu) + \frac{280}{\pi^2} \left(\frac{L}{\bar{b}_w} \right)^2 \end{array} \right\} \end{array} \right)}{I_0^* + A_{hs}(\Delta Y_s + \beta)^2} \quad (2.52)$$

The critical distortional load can then be determined as $P_{crD} = A \sigma_{crd,2}$, where A is the area of the full cross-section.

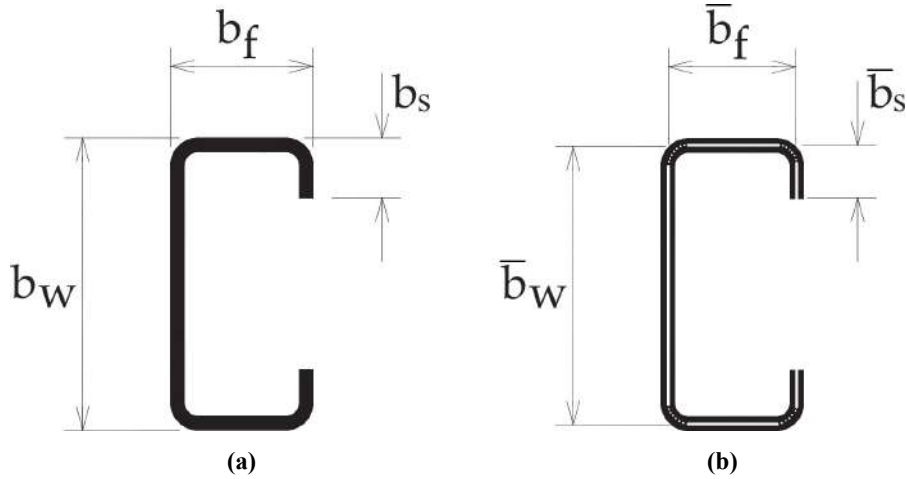


Figure 2.14. Dimensions of a lipped channel cross-section, (a) out-to-out measurement and (b) centerline measurement.

2.6.3 Global Buckling

The origin of the analytical expression is given by Euler⁵ [87]. Euler's analytical expression became so popular that the critical load has been also called Euler load. In the book of Timoshenko and Gere [83], the Euler critical load is deducted from the differential equation of the column. So far, the analytical expression for the global critical load is given in the Brazilian standard ABNT NBR 14762:2010 [5], and many other codes

⁵Appendix "De curvis elasticis" of the book "Methodus inveniendi líneas curvas maximi minimive proprietate gaudentes", Lausanne and Geneva, 1744.

(e.g. Australian/New Zealand code AS/NZS 4600 [6] and North-American standard AISI S100-16 [7]).

The critical Euler stress (σ_e) of a bar is given as the smaller root for the cubic function in Eq. (2.56). In order to detect the critical stress, it is necessary to compute the elastic flexural buckling stress on the major axis x-x (Eq. (2.53)) and minor axis y-y (Eq. (2.54)) and the elastic torsional buckling stress on the longitudinal axis z-z (Eq. (2.55)).

$$\sigma_{ex} = \frac{\pi^2 E}{(k_x L_x / r_x)^2} \quad (2.53)$$

$$\sigma_{ey} = \frac{\pi^2 E}{(k_y L_y / r_y)^2} \quad (2.54)$$

$$\sigma_{ez} = \frac{1}{A r_0^2} \left[\frac{\pi^2 E C_w}{(k_z L_z)^2} + GJ \right] \quad (2.55)$$

$$(\sigma_e - \sigma_{ex})(\sigma_e - \sigma_{ey})(\sigma_e - \sigma_{ez}) - \sigma_e^2(\sigma_e - \sigma_{ey})\frac{x_0^2}{r_0^2} - \sigma_e^2(\sigma_e - \sigma_{ex})\frac{y_0^2}{r_0^2} = 0 \quad (2.56)$$

The critical global load can then be determined as $P_{crG} = A \sigma_{e1}$, where A is the area of the full cross-section, and σ_{e1} is the least positive real root of the cubic equation Eq. (2.56).

The expression in Eq. (2.56) is valid for any cross-section and end boundary condition. For the simply supported and free warping end boundary condition, the buckling coefficients, k_x , k_y and k_z are equal to 1.0.

2.7 Design Procedures for Cold-Formed Steel Columns

In general, the design procedures for CFS columns are based on a previously elastic buckling analysis, in order to determine the critical buckling load, which is a crucial parameter to estimate the strength capacity of the CFS columns.

The effective width method (EWM), effective section method (ESM) and direct strength method (DSM) are the most known design procedures and they are briefly discussed in this section, in order to point and highlight the differences and advantages.

2.7.1 Effective Width Method (EWM)

This is the most traditional method for determining the strength of CFS members. This method is employed in most standards, *e.g.* ABNT NBR 14762:2010 [5], AISI S100-16 [7], AS/NZS 4600 [6], with a semi-empirical calibrated formulation, which takes into account the plate buckling in long slender steel members ($L \gg b$), with length L and maximum width of the walls of the cross-section b , under axial uniform compression with simply supported end conditions. Unfortunately, this method does not consider the distortional buckling phenomenon.

The origin of the method is attributed to Kàrmàn *et al.* [88], which is based on the critical plate buckling stress (Bryan [84]), given by Eq. (2.39), however, changing b_w to b (width of the plate) and k_ρ to k (buckling coefficient for the plate). At first, the EWM was assumed for isolated rectangular plates, and further adapted for folded steel members. Basically, the method consists of splitting a cross-section into isolated plates, and determine the effective section area – or width – for each one of these isolated elements. Finally, the strength of the entire folded steel member is computed as the summation of each isolated plate contribution, as long as all the isolated elements are simultaneously under the yield stress. The boundary condition and the loading case can be considered by virtue of a plate buckling coefficient k (replacing k_ρ to k in Eq. (2.39)). Commonly this coefficient (k) is 4.0 for the case of four sides simply supported, and 0.43 for a situation of three sides simply supported and one longitudinal side free.

Sequentially, the ultimate compressive load is obtained by summing all the effective widths (b_{eff}) of each plate of the cross-section, times the thickness of the section, times the yield stress and dividing by the partial resistance factor.

The effective width equation expressed in Eq. (2.57) was originally proposed by Winter [89] and calibrated from lab tests. This equation was verified by many authors, showing its compatibility with the experiments. The main advantage of the method is its application as a rule of thumb for thin-walled elements, which can be applied not only to cold-formed elements, but also stiffened plated panels (commonly used in naval structures and steel bridges). However, the EWM is composed of equations with approximated coefficients, due to the calibration from lab tests, resulting in a method based on semi-empirical fundamentals.

$$b_{eff} = \left[1 - 0.22 \left(\frac{\sigma_{crl}}{f_y} \right)^{0.5} \right] b \left(\frac{\sigma_{crl}}{f_y} \right)^{0.5} \leq b. \quad (2.57)$$

2.7.2 Effective Section Method (ESM)

This method is an improvement of the original Effective Area Method (EAM), which was established for the design of cold-formed structures in line with the local buckling. The ESM presents the same approach as the EAM, but with calibrated formulation for column and beam resistance. The method originally proposed by Batista [85] is now used in the Brazilian code for the design of CFS members, ABNT NBR 14762:2010 [5]. Also, this method does not consider the distortional buckling phenomenon.

In order to define the strength of the cold-formed member, the method approach is analogous with the direct strength method⁶. It is important to highlight that the strength of thin-walled columns rely on the steel yielding stress and the three most relevant buckling modes: local, distortional and global. However, the ESM aims only at the local and global buckling modes, and also its coupled phenomena include the interaction of local-global buckling modes.

The steps for determining the thin-walled columns strength can be divided into three steps: (i) computing the member global buckling coefficient, expressed by χ in the Eq. (2.58); (ii) afterwards, when the local buckling effect is reached along with the global buckling interaction, expressed in Eq. (2.59) and (iii) lastly when the design value of the column compressive strength is obtained by Eq. (2.60). The global buckling contribution is obtained with appropriate buckling curves and the strength including the local buckling effect is taken by a Winter-type equation [90], with calibrated coefficients.

$$\chi = \begin{cases} (0.658\lambda_c^2), & \lambda_c \leq 1.5 \\ \frac{0.877}{\lambda_c^2}, & \lambda_c > 1.5 \end{cases} \quad \lambda_c = \sqrt{\frac{Af_y}{N_e}} \quad (2.58)$$

⁶ This method is well described in the next subsection.

$$A_{eff} = \begin{cases} A, & \lambda_p \leq 0.776 \\ A \left(1 - \frac{0.15}{\lambda_p}\right) \frac{1}{\lambda_p^{0.8}}, & \lambda_p > 0.776 \end{cases} \quad \lambda_p = \sqrt{\frac{\chi A f_y}{N_t}} \quad (2.59)$$

$$N_{cRd} = \chi A_{eff} f_y / \gamma \quad (2.60)$$

where A is the gross section area of the thin-walled member; f_y is steel yielding stress; N_e is the global buckling axial compressive load given originally by the smallest root of Eq. (2.56), times the gross section area; λ_c is the column slenderness factor; N_ℓ is the local buckling axial compressive load given by Eq. (2.39) times the gross section area; λ_p is the plate slenderness factor; γ is the partial resistance factor.

According to Batista [85] the Effective Section Method is an easy-to-apply method of design and it has a great advantage when compared with the traditional width method, due to its simplicity, comprehensibility and accuracy.

2.7.3 Direct Strength Method and Additional Procedures (DSM)

The direct strength method (DSM) was first proposed by Schafer and Peköz [91], based on an idea from Hancock *et al.* [92]. The method has a simple application for civil engineers' design of thin-walled structural elements, based on the limit states associated with local, distortional, global and the local-global interactive modes. The DSM is based on the Winter-type equation [90] & [89] for the local and distortional curves, and the "classical" design curve for the global mode, taken from specifications of hot-rolled steel structures (*e.g.* ABNT NBR 8800:2008 [93] and ANSI/AISC 360-16 [94]).

In this sub-section the DSM is described for columns under axial compression, and also additional procedures following the DSM. One advantage of the DSM procedure is the capacity to express straightforward interactive equations, as shown by Schafer [95]. In the past few years, additional equations have been proposed considering interactive modes and also recalibration of the Winter-type equation [90] coefficients.

(i) Global Buckling (DSM)

The nominal axial strength for the global buckling is obtained as described in the DSM. The Eq. (2.61) expresses the nominal strength due to global buckling.

$$P_{nG} = \begin{cases} P_y 0.658\lambda_G^2, & \lambda_G \leq 1.5 \\ P_y \frac{0.877}{\lambda_G^2}, & \lambda_G > 1.5 \end{cases} \quad \lambda_G = \sqrt{\frac{P_y}{P_{crG}}} \quad (2.61)$$

where P_y is the squash load, defined as the gross section area times the steel yielding stress; λ_G is the global slenderness; P_{crG} is the elastic critical global buckling load.

It can be noted that the approach is the same as used in the Effective Section Method, Eq. (2.58), however, in the DSM the idea is to determine the strength of the member due to only the global buckling contribution.

(ii) *Local Buckling (DSM)*

The nominal axial strength for the local buckling is obtained as described in the DSM (without the local-global interaction). The Eq. (2.62) expresses the nominal strength due to local buckling.

$$P_{nL} = \begin{cases} P_y, & \lambda_L \leq 0.776 \\ \frac{P_y}{\lambda_L^{0.8}} \left(1 - \frac{0.15}{\lambda_L^{0.8}} \right), & \lambda_L > 0.776 \end{cases} \quad \lambda_L = \sqrt{\frac{P_y}{P_{crL}}} \quad (2.62)$$

where P_y is the squash load, defined as the gross section area times the steel yielding stress; λ_L is the local slenderness; P_{crL} is the elastic critical local buckling load.

As well, the approach is similar to the one shown in the Effective Section Method, Eq. (2.59), however, in the DSM the idea is to determine the strength of the member due to only the local buckling contribution.

(iii) *Distortional Buckling (DSM)*

The nominal axial strength for the distortional buckling is obtained as described in the DSM. The Eq. (2.63) expresses the nominal strength due to distortional buckling.

$$P_{nD} = \begin{cases} P_y, & \lambda_D \leq 0.561 \\ \frac{P_y}{\lambda_D^{1.2}} \left(1 - \frac{0.25}{\lambda_D^{1.2}} \right), & \lambda_D > 0.561 \end{cases} \quad \lambda_D = \sqrt{\frac{P_y}{P_{crD}}} \quad (2.63)$$

where P_y is the squash load, defined as the gross section area times the steel yielding stress; λ_D is the distortional slenderness; P_{crD} is the elastic critical distortional buckling load.

(iv) *Local-Global Interaction Procedure (DSM)*

The nominal axial strength for the local-global (L-G) interactive buckling is obtained as described in the DSM. The Eq. (2.64) expresses the nominal strength due to local-global buckling interaction.

$$P_{nLG} = \begin{cases} P_{nG}, & \lambda_{LG} \leq 0.776 \\ \frac{P_{nG}}{\lambda_{LG}^{0.8}} \left(1 - \frac{0.15}{\lambda_{LG}^{0.8}} \right), & \lambda_{LG} > 0.776 \end{cases} \quad \lambda_{LG} = \sqrt{\frac{P_{nG}}{P_{crL}}} \quad (2.64)$$

where P_{nG} is the nominal axial strength for the global buckling, expressed in Eq. (2.61); λ_{LG} is the local slenderness based on the global strength; P_{crL} is the elastic critical local buckling load.

Note that the local-global interaction approach consists of replacing the squash load P_y from Eq. (2.62) by the nominal strength for the global buckling, expressed in Eq. (2.61). This proposal was first suggested by Schafer [95].

(v) *Local-Distortional Interaction Procedure (Additional Procedure)*

The nominal axial strength for the local-distortional (L-D) interactive buckling has not been included in the standards. However, in the past decade many authors have been developing expressions that consider the local-distortional coupled phenomenon, *e.g.* Schafer [95], Silvestre *et al.* [96], Dinis and Camotim [97], Martins *et al.* [98], Matsubara [99], Matsubara, Batista and Salles [100], Matsubara and Batista [101] and Batista *et al.* [102].

The Eq. (2.65) is an approach based on the Winter-type equation [90], which was proposed initially by Matsubara [99] and Matsubara, Batista and Salles [100]. Later, in Matsubara and Batista [101] and Batista *et al.* [102], the polynomials for determining the coefficients \mathbf{A} and \mathbf{B} , on Eq. (2.66) and Eq. (2.67), respectively, were revised and the degree of the polynomials were reduced.

$$P_{nLD} = \frac{P_y}{\lambda_{maxLD}^B} \left(1 - \frac{A}{\lambda_{maxLD}^B} \right), \quad \lambda_{maxLD} = \max(\lambda_L; \lambda_D) \quad (2.65)$$

$$A = \begin{cases} 0.15, & R_{\lambda DL} < 0.80 \\ 0.40 R_{\lambda DL} - 0.17, & 0.80 \leq R_{\lambda DL} \leq 1.05 \\ 0.25, & R_{\lambda DL} > 1.05 \end{cases} \quad (2.66)$$

$$B = \begin{cases} 0.80, & R_{\lambda DL} < 0.45 \\ -2.26 R_{\lambda DL}^2 + 4.06 R_{\lambda DL} - 0.57, & 0.45 \leq R_{\lambda DL} \leq 1.05 \\ 1.20, & R_{\lambda DL} > 1.05 \end{cases} \quad (2.67)$$

$$R_{\lambda DL} = \frac{\lambda_D}{\lambda_L} = \frac{\sqrt{\frac{P_y}{P_{crD}}}}{\sqrt{\frac{P_y}{P_{crL}}}} = \sqrt{\frac{P_{crL}}{P_{crD}}} \quad (2.68)$$

where P_y is the squash load, defined as the gross section area times the steel yielding stress; λ_{maxLD} is the maximum slenderness, between the distortional (λ_D) and the local (λ_L) slenderness; $R_{\lambda DL}$ is the ratio between the distortional slenderness and local slenderness; P_{crD} is the elastic critical distortional buckling load; P_{crL} is the elastic critical local buckling load.

The proposed local-distortional interactive buckling equation is easy to apply and has a greater accuracy, compared to the other proposed procedures (*e.g.* Silvestre *et al.* [96], Dinis and Camotim [97] and Martins *et al.* [98]).

(vi) *Distortional-Global Interaction Procedure (Additional Procedure)*

The nominal axial strength for the distortional-global (D-G) interactive buckling has not been included yet in the standards. In the past few years, authors have been studying the distortional-global coupled phenomenon behavior, in Dinis and Camotim [103] and Martins *et al.* [104]. However, there is still a lack of studies of this phenomenon, mainly lacking laboratory experiments. Nevertheless, Schafer [95] proposed an approach to the DSM that consider the distortional-global interaction, shown in Eq. (2.69). In addition, the recent study carried out by Martins *et al.* [82], uses the procedure proposed by Schafer [95] with a parametric study, with results showing that the procedure is quite conservative, comparing with the global equation approach. Martins *et al.* [82] also

studied an additional approach that includes the distortional-global interaction shown in Eq. (2.70).

Basically, the approach in Eq. (2.69) involves in replacing the squash load P_y from the distortional buckling equation (Eq. (2.63)) by the nominal strength for global buckling P_{nG} (Eq. (2.61)). Likewise, in Eq. (2.70), the approach consists of replacing the squash load P_y from the global buckling equation (Eq. (2.61)) by the nominal strength for the distortional buckling P_{nD} (Eq. (2.63)).

$$P_{nDG} = \begin{cases} P_{nG}, & \lambda_{DG} \leq 0.561 \\ \frac{P_{nG}}{\lambda_{DG}^{1.2}} \left(1 - \frac{0.25}{\lambda_{DG}^{1.2}} \right), & \lambda_{DG} > 0.561 \end{cases} \quad \lambda_{DG} = \sqrt{\frac{P_{nG}}{P_{crD}}} \quad (2.69)$$

$$P_{nGD} = \begin{cases} P_{nD} 0.658 \lambda_{GD}^2, & \lambda_{GD} \leq 1.5 \\ P_{nD} \frac{0.877}{\lambda_{GD}^2}, & \lambda_{GD} > 1.5 \end{cases} \quad \lambda_{GD} = \sqrt{\frac{P_{nD}}{P_{crG}}} \quad (2.70)$$

where λ_{DG} is the distortional slenderness based on the global strength; P_{crD} is the elastic critical distortional buckling load; λ_{GD} is the global slenderness based on the distortional strength; P_{crG} is the elastic critical global buckling load.

(vii) *Local-Distortional-Global Interaction Procedure (Additional Procedure)*

Likewise the local-distortional and distortional-global interaction procedures, the local-distortional-global (L-D-G) interaction approach has not been well established. However, several authors have been working on the local-distortional-global coupled phenomenon, *e.g.* Dinis *et al.* [105], Santos [106], Santos *et al.* [107], Santos *et al.* [108], Cava *et al.* [109], Young *et al.* [110], Dinis *et al.* [111] and Matsubara and Batista [112].

One of the most recent studies, carried out by Matsubara and Batista [112], has reached a general expression that consider the local-distortional-global coupled phenomenon. The Eq. (2.71) shows the procedure, which is analogous to the local-distortional interactive buckling procedure, but using the same idea as proposed by Schafer [95]. The idea consists of replacing the squash load P_y in the local-distortional interaction expression, Eq. (2.65), by the nominal strength for global buckling P_{nG} , as in the distortional-global interactive buckling equation.

$$P_{nLDG} = \frac{P_{nG}}{\lambda_{LDG} \mathbf{B}} \left(1 - \frac{\mathbf{A}}{\lambda_{LDG} \mathbf{B}} \right), \quad \lambda_{LDG} = \sqrt{\frac{P_{nG}}{\min(P_{crL}; P_{crD})}} \quad (2.71)$$

where λ_{LDG} is the maximum slenderness, based on the minimum L or D critical load and the column strength related to the global buckling P_{nG} ; \mathbf{A} and \mathbf{B} are the Winter's-type equation [90] coefficients, from Eq. (2.66) and Eq. (2.67) respectively; P_{crD} is the elastic critical distortional buckling load; P_{crL} is the elastic critical local buckling load.

2.8 State-of-the-art

So far, the standards for CFS sections do not consider all the possible buckling interaction. The Brazilian (ABNT NBR 14762:2010 [5]), North-American (AISI S100-16 [7]), and Australian/New Zealand (AS/NZS 4600 [6]) codes only consider the Local-Global buckling interaction.

The L-G interaction is already in the standards for hot-rolled and CFS members in the effective section method by Batista [85], as well as in the direct strength method (DSM) by Schafer [113] & [114]. Initially, the first proposal for the DSM was published by Schafer and Peköz [91], based on the original idea of Hancock *et al.* [92]. Up to now, it is the most frequently adopted method for designing CFS structures.

Studies have been undertaken in the last few decades on CFS members under the couple instability phenomena. Schafer [95] proposed a buckling interaction design procedure for L-G, D-G and L-D, using the DSM. The approach is quite straightforward and is based on the idea of replacing the squash load P_y of one mode, with the other mode that is interacting. The author states that with this procedure it is not necessary to consider the formulations for the modes separately, if they have been already considered in the coupled buckling expression. Also, according to Schafer [95], the DSM is a practicable and general approach to predict the strength of the modes separately and their interaction with the global buckling mode.

In addition, the local-distortional (L-D) interaction has been becoming increasingly popular in the past 20 years. Different studies on the post-buckling and strength on this coupled phenomenon were performed by Yang and Hancock [115], Dinis *et al.* [116], Camotim *et al.* [117], Kwon *et al.* [118], Silvestre *et al.* [96], Martins *et al.* [119] and Matsubara *et al.* [100]. Some of these researchers, *e.g.* Yang and Hancock [115], Camotim *et al.* [117], Silvestre *et al.* [96], Matsubara [99], Matsubara *et al.* [100],

Matsubara and Batista [101] and Batista *et al.* [102], publish DSM reviews and predictions considering the L-D interaction.

Furthermore, the L-D-G interaction is the coupled phenomenon that has stimulated the interests of many authors, in numerical and experimental studies. Some of the recent studies on this subject can be found in Dinis *et al.* [105], Santos [106], Santos *et al.* [107], Santos *et al.* [108], Cava *et al.* [109], Young *et al.* [110], Dinis *et al.* [111] and Matsubara and Batista [112].

In the past few years, studies were carried out in relation to the D-G interaction. Schafer [95] explains how the dimension of the lip of a lipped channel section could expose the D-G interaction. The author states that for members with a small b_s , the D-G coupled phenomenon is conceivable, because the deformations and the wavelength of the distortional buckling mode is close to the local mode, with a known possible global interaction in pin-ended columns. On the other hand, for large b_s dimensions, or cross-sections with intermediate stiffeners or even other modification that could make the wavelength of the distortional mode to be significantly longer than the local mode, a D-G interaction may be less likely.

Yang and Hancock [115] performed compression tests with fixed end of high strength steel lipped channel columns with intermediate stiffeners in the web and the flange, with L-D interaction. Their study results in the equation of the D-G interaction, as proposed by Schafer [95] before.

Yap and Hancock [120] also performed compression tests on high-strength CFS columns. The sections were web-stiffened channel and the tests were performed with the intention of mode interaction. The authors also state design procedures for the coupled phenomenon, like distortional buckling interacting with overall buckling, as proposed by Schafer [95].

Nonetheless, the North-American standard, AISI S100-16 [7], and the Australian/New Zealand standard, AS/NZS 4600 [6], follows the effective width method, which carry the D-G interaction, according to Dinis and Camotim [103], based on laboratory experiments, conducted by Desmond *et al.* [121]. However, the studies proposed by Desmond *et al.* do not present an explicit approach for the mechanics of the modal interaction, as it is shown in Dinis and Camotim [103]. Therefore, it is expected that the considerations included in the North-American and Australian/New Zealand standards are conservative.

One of the first studies on the D-G interaction behavior was carried out by Dinis and Camotim [122] & [103]. These researchers performed a post-buckling and strength analysis of CFS lipped channels due to compressive loads under D-G coupled phenomenon. Dinis and Camotim [122] & [103] concluded that in the critical buckling length for D-G interaction, prevails the *distortional-flexural-torsional* mode, as an asymmetrical modal form of the distortional mode. This study contradicts the general concept of exclusively global buckling in that specifically critical buckling length. Also, the authors corroborate that the asymmetrical modal form (*distortional-flexural-torsional*) reduces the post-critic strength, due to the instable post-buckling behavior. In addition, they noticed that the equilibrium path is very sensible to initial geometric imperfections. Practically, the columns with pure global initial imperfection have a lower ultimate load than the columns with pure distortional imperfection.

Recent studies with experimental tests for D-G interaction in lipped channel columns is presented by Rossi *et al.* [123] and Anbarasu and Murugapandian [124]. In Rossi *et al.* [123], the authors performed experiments on 48 full-scale stainless steel lipped channel section columns, experiencing distortional, flexural-torsional and combined *distortional-flexural-torsional* buckling mode. Moreover, Anbarasu and Murugapandian [124] carried out an experimental study on CFS web stiffened lipped channel columns undergoing distortional–global interaction.

There are recent studies about the D-G interaction that were performed on beams in pure bending. Niu *et al.* [125] & [126] developed an experimental and numerical investigation of stainless steel lipped channels beams in two parts. Another study on beams was accomplished by Martins *et al.* [127] & [128], using the generalized beam theory (GBT) as an analysis method. The study was also divided in two parts: Mechanics and Elastic Behavior [127]; Strength, Relevance and DSM Design [128]. Martins *et al.* [129] carried out the same study, but with zed-sections beams, published in a single version.

The most recent studies on CFS lipped channel columns under D-G coupled phenomenon are mainly focused on the mechanics of the D-G interaction and design procedures. However, Anbarasu [130] performed experimental tests and numeric finite element method, in order to provide a parametric study and design recommendations for the D-G interaction behavior.

Martins *et al.* [131] & [82] provided a numerical study on CFS lipped channel columns, with fixed-fixed end conditions under D-G interaction, which presents design

procedures for the direct strength method. The most interesting conclusions was that the pure global imperfections on the columns with D-G interaction, gives a lower strength capacity with significant post-critical strengths. Also, the authors concluded that the DSM global strength curve is capable to predict the three types of D-G interaction (true interaction, secondary-distortional bifurcation and secondary-global bifurcation). The authors state that this accurate prediction was due to the DSM global design strength curve safety margin. However, the cited strength curve underestimates the ultimate load for the columns under global modes (flexural-torsional), mostly in high slenderness factors ($\lambda_G > 2.0$).

3 FStr - Computer Application Program

The finite strip method is implemented in MATLAB platform, MathWorks [23]. Entitled FStr Computer Application Program, the program performs an elastic buckling analysis of thin-walled structures. A graphical user interface (GUI) of the program is designed in order to make the program a useful and easy tool to perform the buckling analysis. This section presents the FStr Computer Application Program and its validation.

3.1 Program Description

FStr Computer Application Program is a software developed on the basis of the Finite Strip Method formulation, as described on item 2.2 (The Finite Strip Method), which is based on the book written by Cheung [11] and other sources: Cheung [17], Cheung [18], Bradford and Azhari [19], Li and Shafer [20], Schafer [21] and Li [22]. The FStr is implemented in MATLAB platform (MathWorks [23]) and is inspired in the CUFSM 5 [39] and GBTul 2.0 [65] graphical user interface. The program logotype is illustrated in Figure 3.1 (the graphical user interface application itself is not an open source software, however, it is free to use).

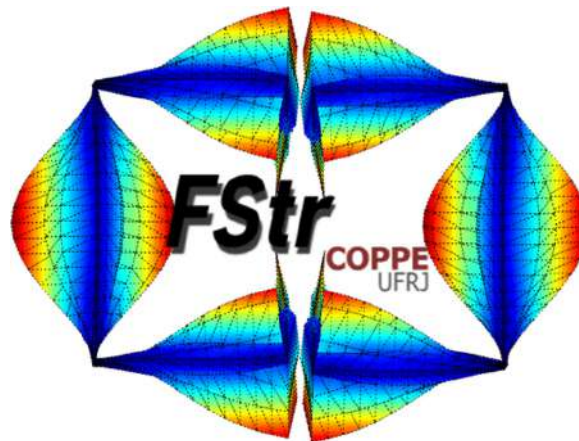


Figure 3.1 FStr Computer Application Program logotype.
<https://github.com/joaoadelazzari/FStr>
<https://www.mathworks.com/matlabcentral/fileexchange/74306>

The code structure can be separated in four groups: (i) data input; (ii) data preprocessing; (iii) finite strip analysis; (iv) data output. In Figure 3.2 is displayed the code structure and its groups. Firstly, in the data input group, the initial parameters are set up, e.g. cross-section coordinates and thickness, orthotropic material properties, boundary conditions and lengths of the structural member and the number of half-waves terms. Secondly, in the data preprocessing category, is just performed an arrangement of the initial parameters, in order to perform the finite strip analysis. At this point, the analysis is performed in three main loops: (iii.a) half-wave loop, (iii.b) strip loop and (iii.c) length loop. For each half-wave number is assembled the local elastic stiffness and geometric matrices, Eq. (2.31). These matrices are organized in the global matrices, for each strip. In the end of all strips and all half-wave terms loop, there are two global matrices, expressed in Eq. (2.36) and Eq. (2.37), for the elastic stiffness and geometric matrix, respectively. Finally, the data output are the results from the generalized eigenvalue problem, from Eq. (2.38), in other words, the signature curve and the critical modal shapes.

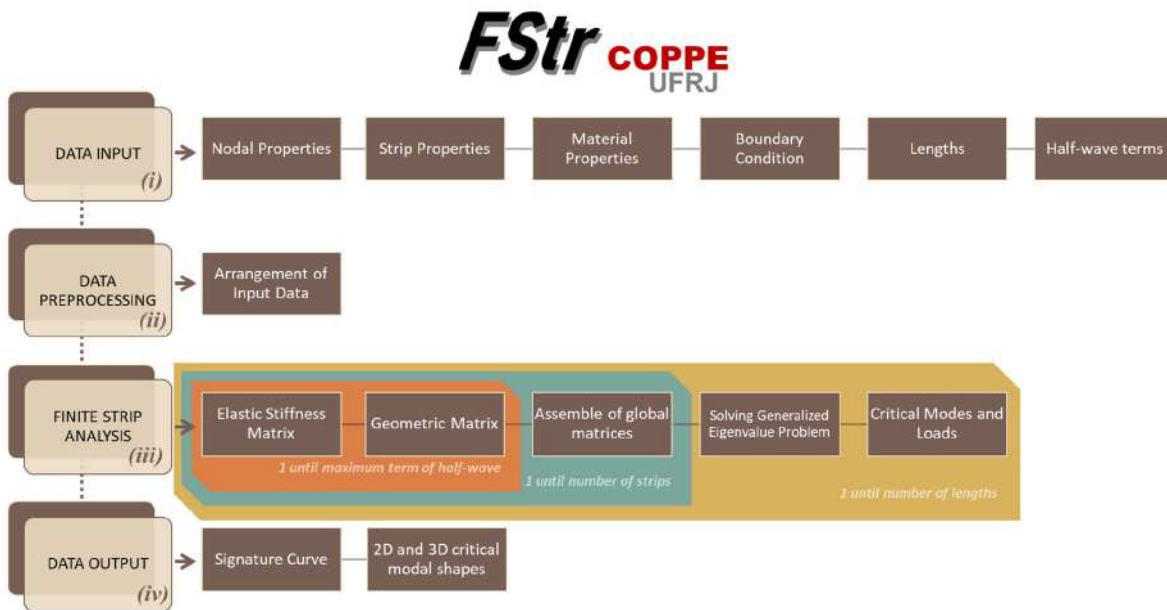


Figure 3.2. FStr Computer Application Program code structure.

The Graphical User Interface (GUI) is implemented in the MATLAB App Designer [23]. The App Designer from MATLAB is a powerful tool to create professional apps without having to be a professional software developer. This tool is a complete environment with built-in functions, visual components, object-oriented code, code

analyzer for identifying errors and many others gadgets. The purpose of the GUI is to make it easier to the user to set up the data input and to analyze the data output.

Figure 3.3 shows the FStr GUI with the data input and output panel. Comparing to the code structure in Figure 3.2, the data input is marked from (1-8), the data preprocessing and the finite strip analysis are marked as (9) and the data output are indicated from (10-16).

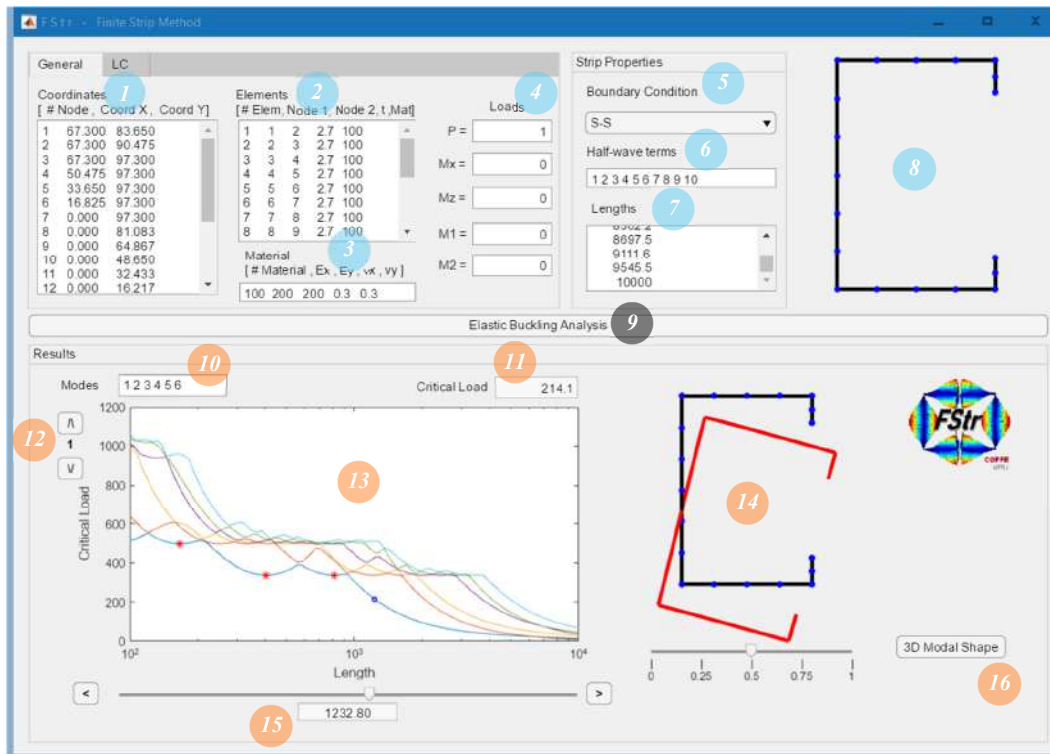


Figure 3.3. FStr Graphical User Interface index description.

- 1 Coordinates Panel
[Node Number; Coordinate in x direction; Coordinate in y direction];
- 2 Elements Panel
[Element Number; First Node; Second Node; Thickness; Material Name]
- 3 Orthotropic Material Panel
[Material Name; Elastic Modulus for x direction; Elastic Modulus for y direction; Poisson's ratio for x direction; Poisson's ratio for y direction]
- 4 Loading
[P: Compression]

[Mx: Moment about geometric x axis]
[My: Moment about geometric y axis]
[M1: Moment about major principal axis]
[M2: Moment about minor principal axis]

- 5 Boundary Condition
(S-S, C-C, C-S, C-G, C-F, see Table 2.1)
- 6 Half-wave terms for trigonometric series
[1 2 3 4 ... m] { $m \in \mathbf{N}$ }
- 7 Longitudinal length of structural element
(e.g. `logspace(1,4,200)`, `(10:100:10000)`)
- 8 Dynamic 2D thin-walled cross-section geometry
- 9 Elastic Buckling Analysis Button
- 10 Number of superior modes displayed
[1 2 3 ... n] { $n \in \mathbf{N} \mid n \leq 20$ }
- 11 Critical Load or Critical Stress or Critical Moment
- 12 Selection of Superior Modes
- 13 Signature Curve and Superior Modes (Critical Load *versus* Longitudinal Length)
- 14 Dynamic 2D Modal Shape, for each Longitudinal Length and Transversal Position
Ratio ($\bar{y} = y/a$)
- 15 Selection of Longitudinal Length
- 16 3D Modal Shape for the selected Longitudinal Length (Figure 3.4)

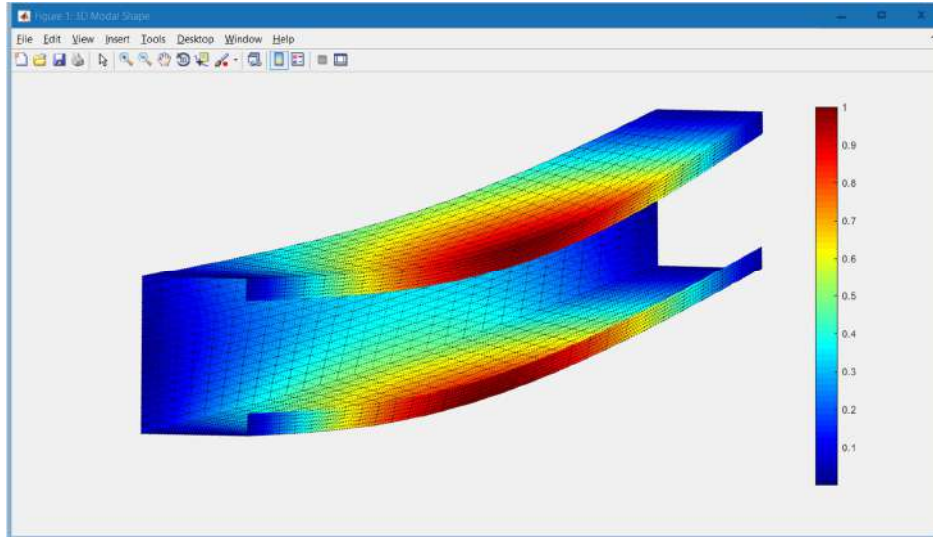


Figure 3.4. FStr 3D modal shape with vector sum normalized displacement colormap visualization.

The program itself has an easy interface and it is faster in some cases, compared to the CUFSM and GBTul. The FStr program performance depends mostly of the number of strips and terms of half-waves, the fewer of these parameters, faster is the analysis.

There are some important tips for the users: (i) firstly, it is recommended that the user adopt millimeters for length unit and kilonewton for force unit in axial compression, e.g. the elastic modulus with 200 kN/mm^2 (steel elastic modulus $\approx 200 \text{ GPa}$); (ii) secondly, the software data input corresponds to the CUFSM data input, this means that the coordinates, elements and material “data box”, can be copied from the CUFSM and paste into the FStr; (iii) every space corresponds to a new column and every enter key hit is a new row in the data input, in order to set up the coordinates, elements, material, half-wave terms and lengths; (iv) the length’s “data box” understand MATLAB functions⁷, this means that instead of typing all the lengths, the user can type e.g. *logspace*(1,4,200), 10:100:10000 or *linspace*(10,10000,200).

The FStr is a free computer application program, and it is an elastic buckling analysis alternative for research activities and engineering design of steel thin-walled structures. The program can be accessed in the GitHub website <https://github.com/joaoadelazzari/FStr> or in the file exchange from MathWorks website <https://www.mathworks.com/matlabcentral/fileexchange/74306>.

⁷ For MATLAB Documentation Help, access [mathworks.com/help](https://www.mathworks.com/help)

3.2 Elastic Buckling Analysis Validation

In order to show the accuracy, performance and parallelism of the FStr Computer Application Program, in this section some structural models are analyzed and compared to other elastic buckling analysis results. The purpose is to validate the FStr solution, with Constrained and Unconstrained Finite Strip Method (CUFSM) and Generalized Beam Theory (GBT) in most cases, for parallelism intention, and also to the classic FEM, from ANSYS [68], and analytical procedures, for comparing performance and accuracy.

The validation is performed for a total of 9 different models. First, 5 models of flat rectangular plates under compression are analyzed, with 5 different boundary condition⁸ on the extremities and free in the longitudinal edges. Secondly, 5 more flat rectangular plates under compression are analyzed, but with longitudinal clamped edges. Thirdly, a more complex model is analyzed of a lipped channel column, one with simply-simply end condition and other with clamped-clamped end condition. Lastly, a stiffened lipped channel and a zed section beam are analyzed, under uniform unrestricted bending and simply-simply end condition.

The material employed to validate all the models are uniformized as a CFS, with elastic modulus of 200 *GPa*, Poisson's ratio of 0.3 and transversal modulus of 76.92 *GPa*.

3.2.1 End Boundary Condition Validation

Firstly, the models for this validation are flat rectangular plates with free longitudinal edges, and different end boundary condition. The FStr Computer Application program is validated comparing its results with the GBTul 2.0 [65], CUFSM 5 [39] and analytical formulation for global buckling (Eq. (2.56)). The analysis consists of a set of 100 lengths (L) from 100 to 1000, in logarithmic scale. The geometry of the plate is illustrated in Figure 3.5, with $b = 100 \text{ mm}$ and $t = 5 \text{ mm}$.

Even though in all methods are defined the same geometry and end conditions, there are some parameters that are exclusively for each method. For the GBT the model has 2 natural nodes and 3 internal nodes in the cross-section. Additionally, the analysis is performed with all conventional modes and a numerical solution with 10 beam finite

⁸ S-S, C-C, C-S, C-G and C-F, see Table 2.1.

elements. Moreover, for the FStr and CUFSM programs, the geometry has 5 nodal lines (4 strips) in the cross-section and considering a total of 10 terms of half-waves. Lastly, for the analytical solution, it is managed the Eq. (2.56), with different buckling coefficients, depending on the boundary condition: (i) Simply-Simply, k_x , k_y and k_z equal to 1.0; (ii) Clamped-Clamped, k_x , k_y and k_z equal to 0.5; (iii) Clamped -Simply, k_x and k_y equal to 0.7 and k_z equal to 1.0; (iv) Clamped -Free, k_x and k_y equal to 2.0 and k_z equal to 1.0; (v) Clamped -Guided, k_x , k_y and k_z equal to 1.0.

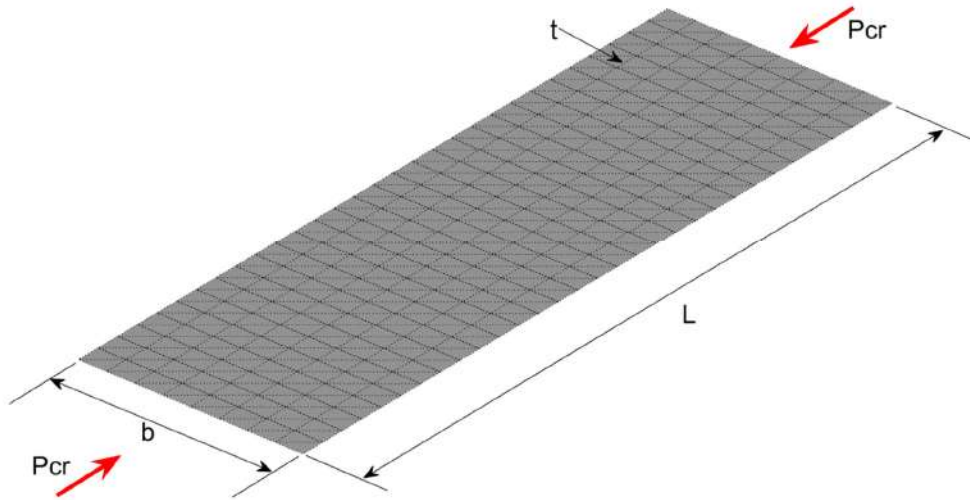


Figure 3.5. Geometry of flat rectangular plate with free longitudinal edges.

The graph critical load *versus* length is shown in Figure 3.6, Figure 3.7, Figure 3.8, Figure 3.9 and Figure 3.10, for the S-S, C-C, C-S, C-F and C-G end boundary condition, respectively. The graphs show the critical load in the left axis, and the relative difference between the FStr with each method in the right axis. Furthermore, the first three critical buckling modes for $L = 298mm$ are illustrated in Figure 3.11, Figure 3.12, Figure 3.13, Figure 3.14 and Figure 3.15 for the S-S, C-C, C-S, C-F and C-G end boundary condition, respectively.

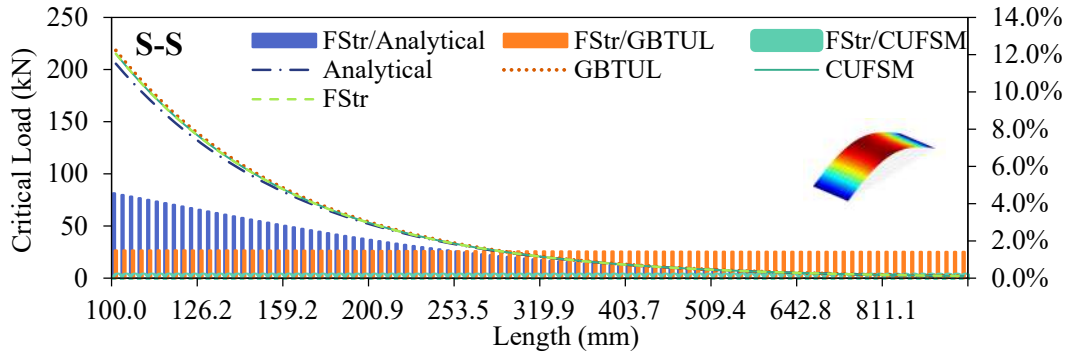


Figure 3.6. [S-S] Rectangular plate critical load validation with GBTul, CUFSM and Global Buckling Analytical formulation.

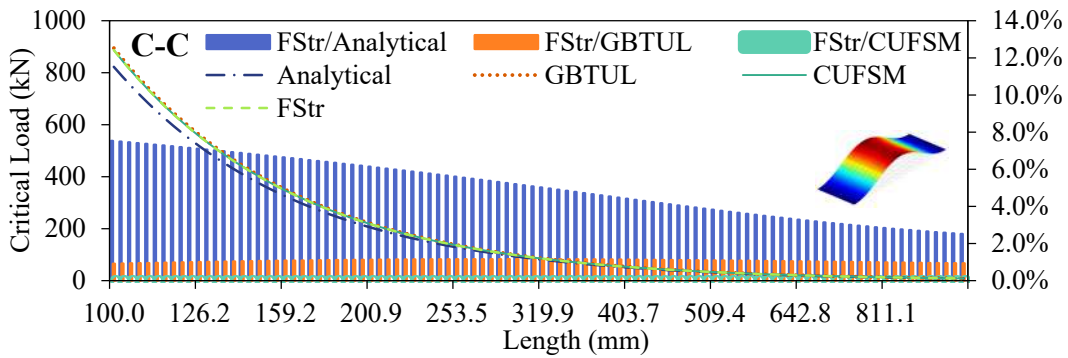


Figure 3.7. [C-C] Rectangular plate critical load validation with GBTul, CUFSM and Global Buckling Analytical formulation.

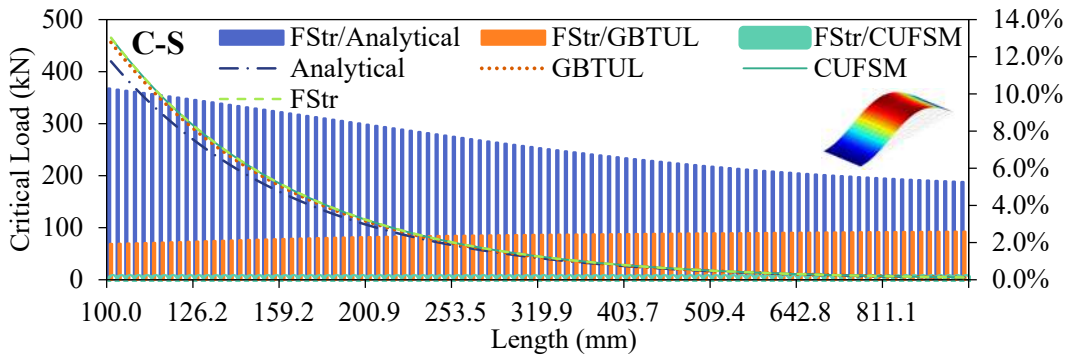


Figure 3.8. [C-G] Rectangular plate critical load validation with GBTul, CUFSM and Global Buckling Analytical formulation.

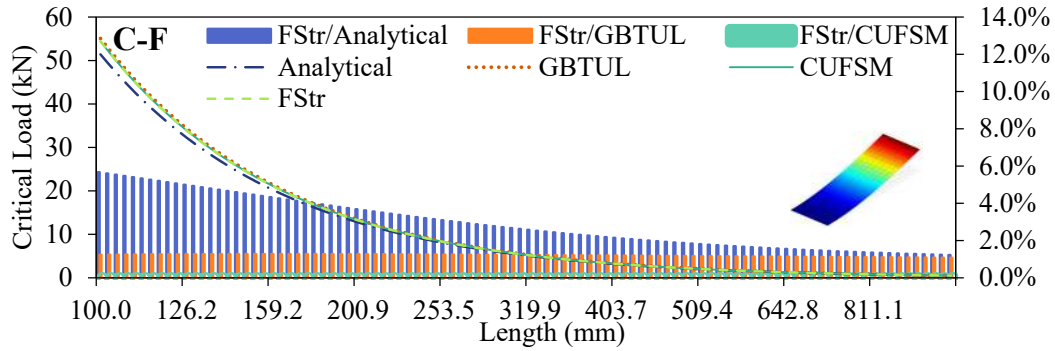


Figure 3.9. [C-F] Rectangular plate critical load validation with GBTul, CUFSM and Global Buckling Analytical formulation.

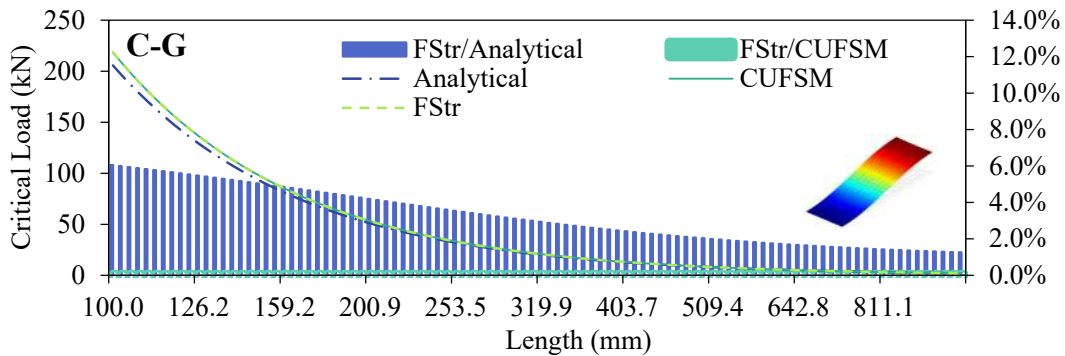


Figure 3.10. [C-G] Rectangular plate critical load validation with CUFSM and Global Buckling Analytical formulation.

Note that in all cases, the relative difference between the FStr and the CUFSM is nearly to zero, with the maximum difference of 0.00016%. This shows that the FStr and CUFSM are in accordance with the FSM formulation applied in both programs. On the other hand, comparing to the GBT method and the analytical formulation, the relative differences are slightly higher. Comparing FStr to GBTul, the maximum relative difference is 2.58% for the C-S end boundary condition. For the others end conditions, the maximum relative difference is around 1.5%. Comparing the FStr to the global buckling analytical formulation, the relative difference is fairly higher. For shorter lengths, the global buckling formulation has shown the highest relative difference, while for long lengths, the global buckling equation tends to FStr solution. Also, note that the relative difference from the analytical solution is decreasing almost proportionally to the increasing of length, differently from the GBT method, where the relative difference remains almost constant.

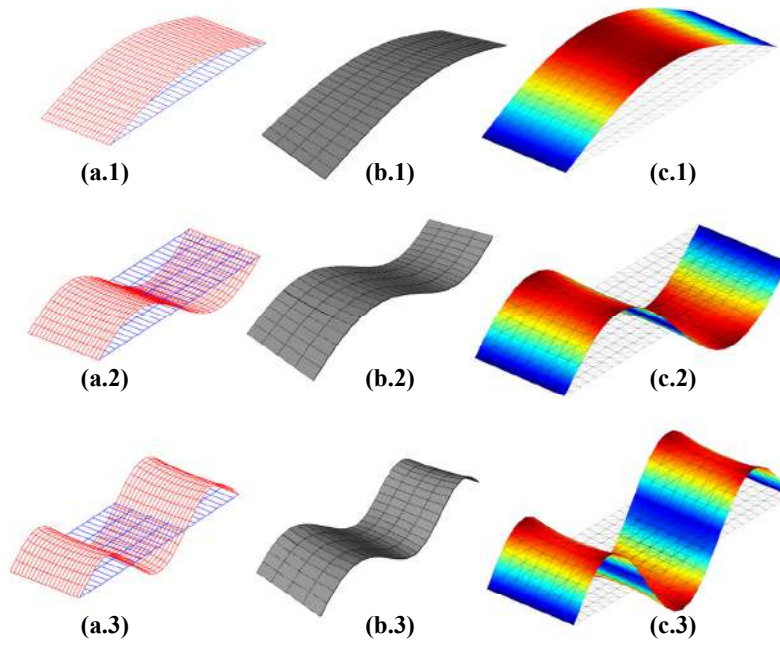


Figure 3.11. Tridimensional buckling modes for S-S end condition at $L=298$ mm: (a) CUFSM, (a.1) 1st mode, (a.2) 2nd mode, (a.3) 3rd mode; (b) GBTul, (b.1) 1st mode, (b.2) 2nd mode, (b.3) 3rd mode; (c) FStr, (c.1) 1st mode, (c.2) 2nd mode, (c.3) 3rd mode.

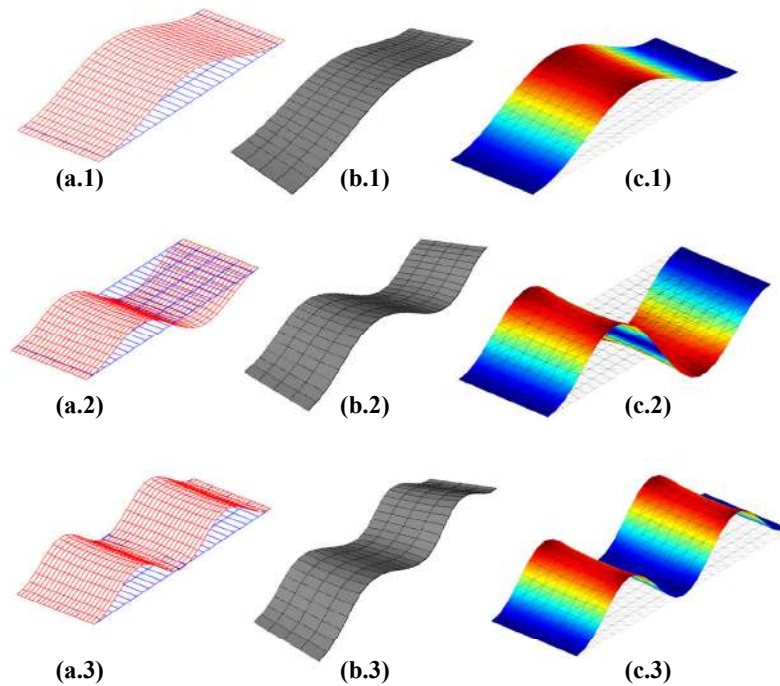


Figure 3.12. Tridimensional buckling modes for C-C end condition at $L=298$ mm: (a) CUFSM, (a.1) 1st mode, (a.2) 2nd mode, (a.3) 3rd mode; (b) GBTul, (b.1) 1st mode, (b.2) 2nd mode, (b.3) 3rd mode; (c) FStr, (c.1) 1st mode, (c.2) 2nd mode, (c.3) 3rd mode.

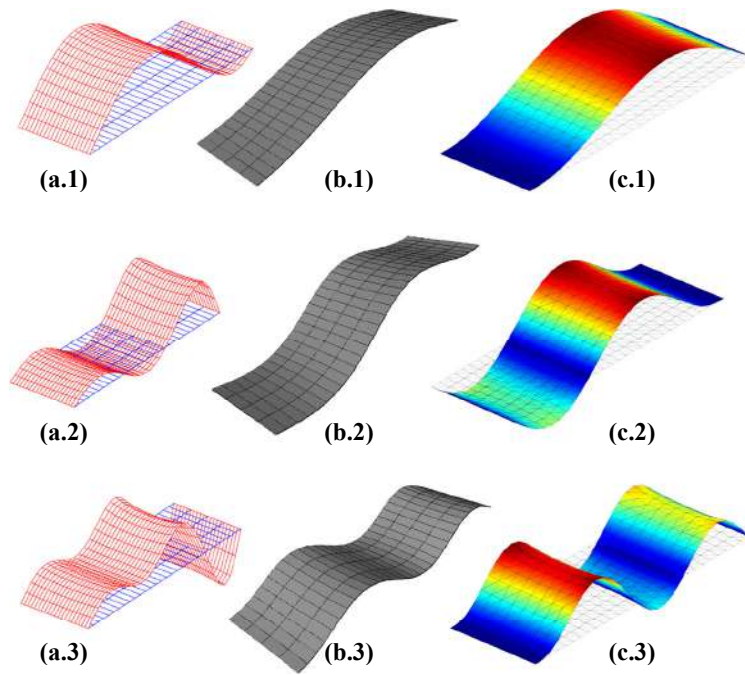


Figure 3.13. Tridimensional buckling modes for C-S end condition at $L=298$ mm: (a) CUFSM, (a.1) 1st mode, (a.2) 2nd mode, (a.3) 3rd mode; (b) GBTul, (b.1) 1st mode, (b.2) 2nd mode, (b.3) 3rd mode; (c) FStr, (c.1) 1st mode, (c.2) 2nd mode, (c.3) 3rd mode.

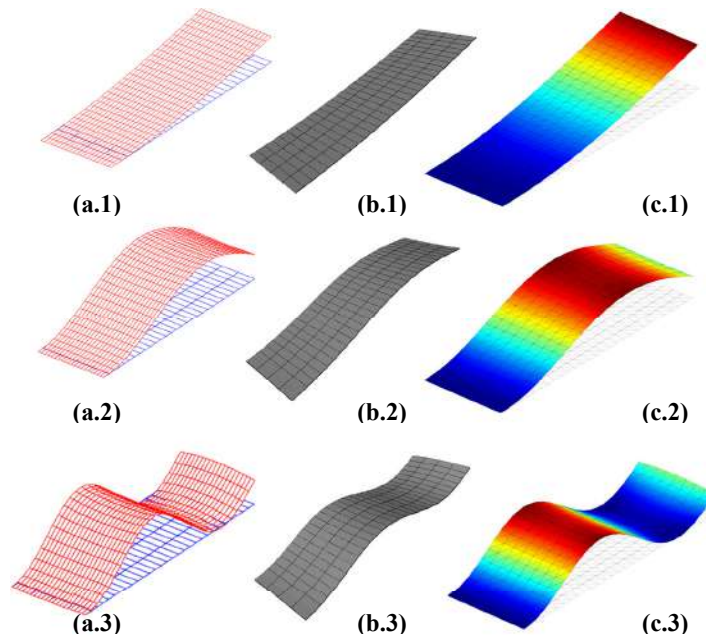


Figure 3.14. Tridimensional buckling modes for C-F end condition at $L=298$ mm: (a) CUFSM, (a.1) 1st mode, (a.2) 2nd mode, (a.3) 3rd mode; (b) GBTul, (b.1) 1st mode, (b.2) 2nd mode, (b.3) 3rd mode; (c) FStr, (c.1) 1st mode, (c.2) 2nd mode, (c.3) 3rd mode.

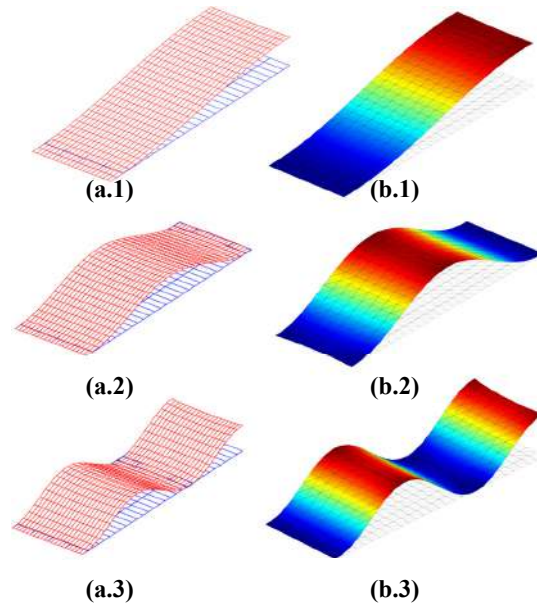


Figure 3.15. Tridimensional buckling modes for C-G end condition at $L=298$ mm: (a) CUFSM, (a.1) 1st mode, (a.2) 2nd mode, (a.3) 3rd mode; (b) FStr, (b.1) 1st mode, (b.2) 2nd mode, (b.3) 3rd mode.

It can be observed that all the modal shapes are shown as expected by each method. However, it is important to point some interesting observations. First, the 3D generation of the CUFSM takes a while to show the modal shape and the GBTul 3D mode generation sometimes crashes, resulting in unexpected closing of the program, while the FStr 3D generation is quite faster with a light performance. Secondly, comparing the modal shapes from the C-S end boundary condition, note that the CUFSM program shown a not equivalent shape. The expected form for the first mode was supposed to have rotation equal to zero in one extremity and different to zero in the other extremity, with only one half-wave length. However, the CUFSM does not appear to present a correspondent modal shape, which the GBTul and FStr seems to perform a correct buckling mode. Since all the equations for performing the elastic buckling analysis are in accordance with the FStr program, it is believed that the mistake should be in the interpolation of the modes, in order to print the modal shape in the screen. Lastly, note that for the C-G boundary condition, there is no buckling mode for the GBTul program, due to the lack of this boundary condition in the program.

In order to compare each boundary condition, Figure 3.16 shows the critical load *versus* the length of the plates with different boundary conditions.

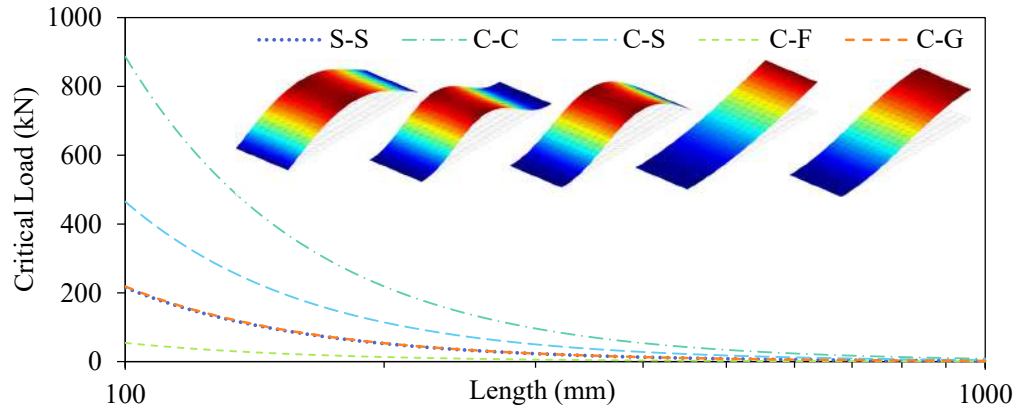


Figure 3.16. Critical Buckling Load comparison between plates with different end boundary condition (FStr Computer Application Program).

It should be noted that as more degrees of freedom are restricted, *e.g.* C-C, higher is the critical load. Alternatively, for plates with less restricted degrees of freedom, *e.g.* C-F, lower is the critical load, as it was expected. The same conclusions can be found in Bradford and Azhari [19].

3.2.2 Local Buckling Validation

In this section, the FStr Computer Application Program is validated with flat rectangular plates with clamped longitudinal edges, and different end boundary condition. The results are compared with CUFSM 5 [39] and findings from Li and Schafer [20]. The analysis also consists on a set of 100 lengths (L) from 100 to 1000, in logarithmic scale, with a total of 10 terms of half-waves, for both FStr and CUFSM programs. The geometry of the plate is illustrated in Figure 3.17, with $b = 100 \text{ mm}$ and $t = 5 \text{ mm}$, and the longitudinal boundary condition is modeled with an addition of a thicker plate ($40t$), in order to stiff the longitudinal edges, and simulate a clamped condition.

With respect to Figure 3.17, the geometry of the plate has a total width of two times the nominal width, half for each edge side. For this additional plate parts, the thickness are forty times the nominal thickness. This alternative model has the purpose of reproduce a plate with width of b and thickness of t , but with clamped longitudinal edges. Since the FStr does not restrict the degrees of freedom yet (this approach must be improved in future works), the model in Figure 3.17 is adopted for the FStr Computer Application Program. To the point that in the CUFSM the longitudinal edges are restricted for the twist, x , y and z direction.

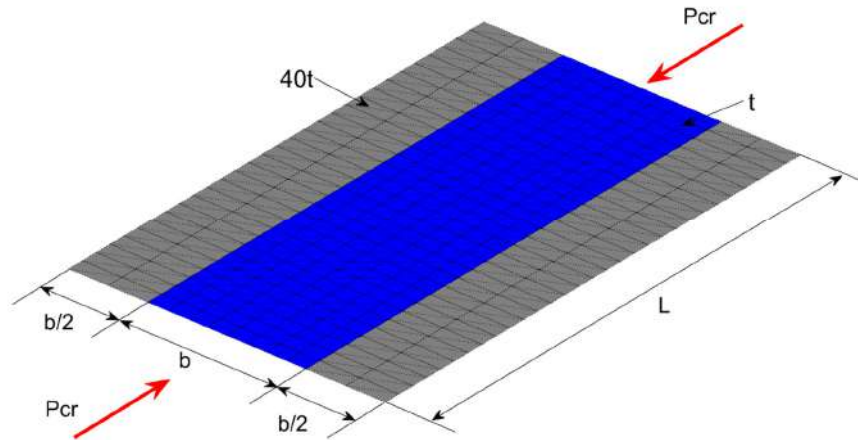


Figure 3.17. Geometry of flat rectangular plate with “clamped” longitudinal edges (c-c).

Since the plate are restricted in all edges, the local buckling is more likely to develop. Due to that, the equation that governs the phenomenon is expressed in Eq. (2.39). Through this equation, it can be seen that only the k_ρ parameter is variable, depending on the plate’s length, since all the others parameters are constants. According to Li and Schafer [20], for plates with all four edges clamped, the buckling coefficient from the local buckling equation, tends to 6.97. With this conclusion, the plate model from FStr is validated, comparing the variation of the buckling coefficient along the ratio between the plate’s length and its width, with the solution provided by CUFSM and Li and Schafer [20], illustrated in Figure 3.18.

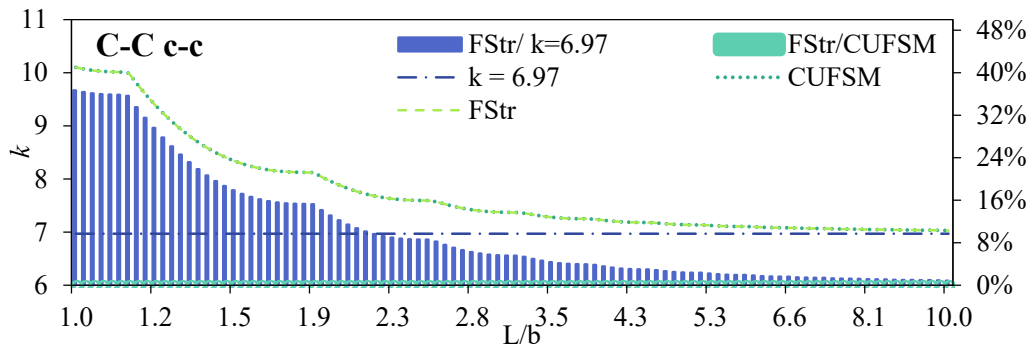


Figure 3.18. Buckling Coefficient versus the ratio between length and width for the C-C c-c plate, comparing FStr and CUFSM.

One important observation about the graph in Figure 3.18 is the trend of the buckling coefficient to 6.97 for longer plates. For ratios L/b higher than 8, the relative

difference among FSM and the buckling coefficient tendency are minimal. Also, note that the relative difference between the FStr and CUFSM is also almost null.

In order to compare the buckling modes, Figure 3.19 shows the modal shapes for the first mode in four different lengths from CUFSM and FStr. Notice that the buckling modes from FStr has wider strips next to the edge to restrict the longitudinal edges, which is part of the model. But this difference in the model, did not interfere in the modal shapes.

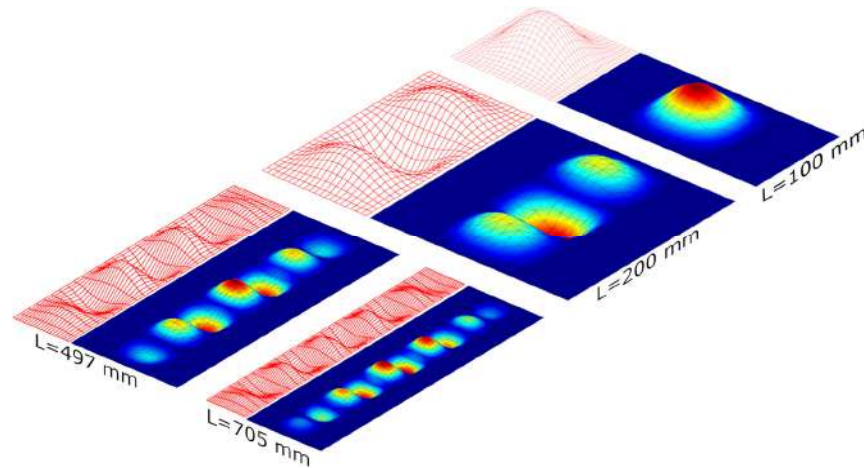


Figure 3.19. 3D buckling modes comparison between CUFSM and FStr for the C-C c-c plate, at L=100 mm, L=200 mm, L=497 mm and L=705 mm.

Additionally, for the same plate model, an analysis varying the end boundary condition, but maintaining edge longitudinal boundary condition as clamped, is also performed. Figure 3.20 shows the variation of the buckling coefficient along the ratio between the plate's length and its width, for five different end boundary condition.

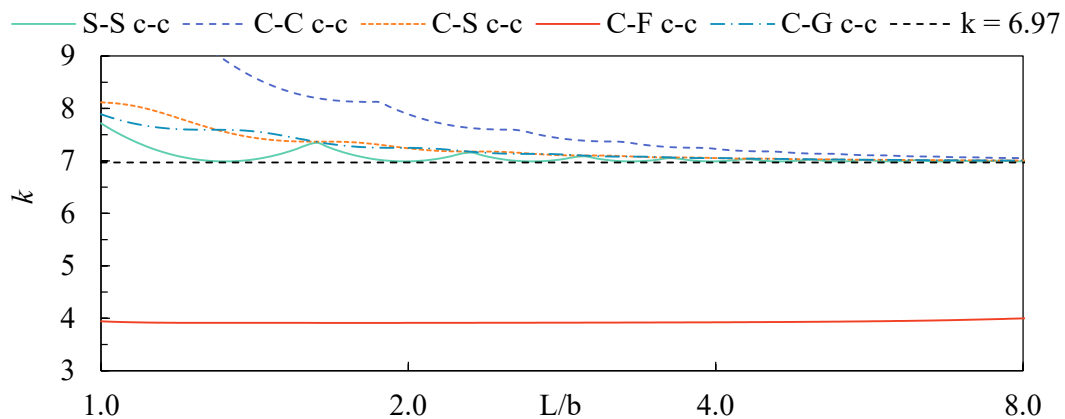


Figure 3.20. Buckling Coefficient versus the ratio between length and width for S-S, C-C, C-S, C-F and C-G end boundary condition, and c-c longitudinal edges boundary condition.

Li and Schafer [20] shown that for clamped-clamped longitudinal edges boundary condition, k tends to 6.97 for S-S, C-C, C-S and C-G end boundary condition, and 3.9 for C-F end boundary condition, as has been found by the program FStr, illustrated in Figure 3.20. In Figure 3.21 is displayed the top view of the buckling modes at $L/b = 3.12$ or length of 312 mm. Notice the variation of the number of the half-waves and its distribution along the plate's length.

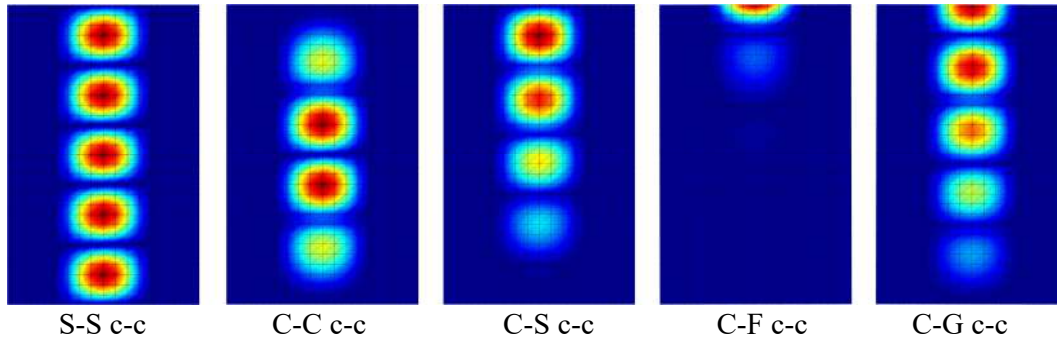


Figure 3.21. Top view of plates from FStr under local buckling for the c-c longitudinal edge boundary condition, at $L/b=3.12$ or $L=312$ mm, for different end boundary condition.

3.2.3 Analytical Validation

The main goal for this validation is to compare a lipped channel section signature curve, with analytical procedures in the literature. For this model, only the simply supported end boundary condition, with all the longitudinal edges free, and only one term of half-wave is analyzed. The geometry of the cross-section illustrated in Figure 2.14-a has $b_w = 100$ mm, $b_f = 70$ mm, $b_s = 15$ mm and $t = 2.70$ mm.

The critical buckling load from FStr is compared to: (i) local buckling equation, Eq. (2.39), retrieved from ABNT NBR 14762:2010 [5]; (ii) distortional buckling equation, Eq. (2.52), from Cardoso *et al.* [86]; (iii) global buckling equation, Eq. (2.56), found in Timoshenko and Gere [83] and mostly into the codes, *e.g.* ABNT NBR 14762:2010 [5], AS/NZS 4600 [6] and AISI S100-16 [7]. Also, results from CUFSM and GBTul are compared to the analytical procedures and FStr.

Figure 3.22 presents the signature curve from FStr, CUFSM and GBTul programs, in addition to the analytical equations for local, distortional and global buckling. Moreover, Figure 3.23 shows the critical buckling modes for (i) local, (ii) distortional (iii) flexural-torsional and (iv) flexural, from the FStr Computer Application Program.

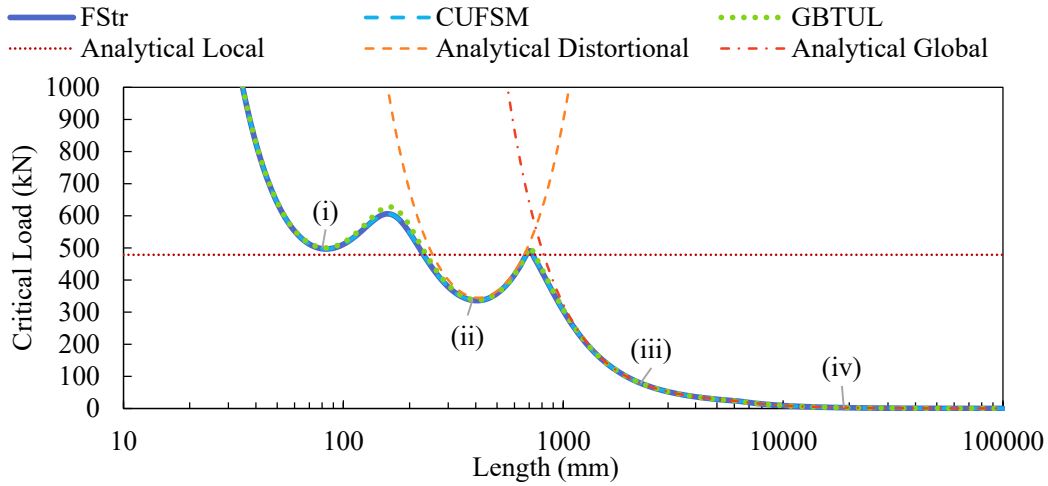


Figure 3.22. Signature Curve comparison between FStr, CUFSM, GBTul and analytical procedures of LC 100x70x15x2.70 with S-S end boundary condition with one term of half-wave.

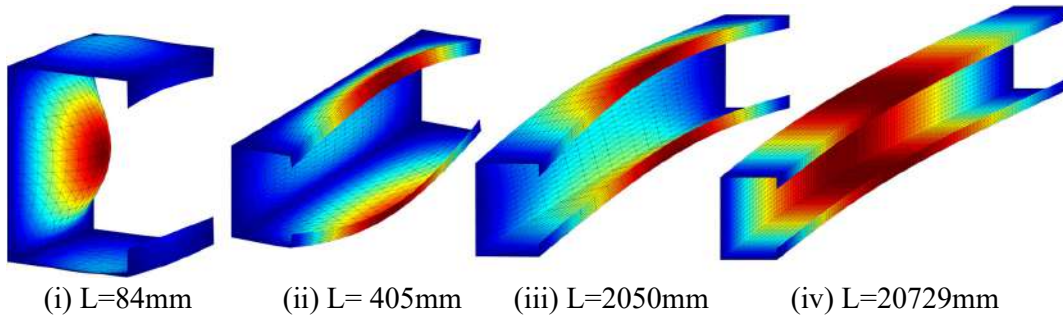


Figure 3.23. Critical Buckling modes from FStr, for a Lipped Channel section with one half-wave term.

Notice that the FStr program obtained practically the same signature curve as the CUFSM. The GBTul program also provided a solution close to the finite strip method. Further, the analytical procedures offered a great precision for the critical loads at critical lengths. As can be shown in Table 3.1, the critical buckling ratios between the FStr with analytical procedures at critical lengths for local and distortional length has demonstrated that the matrix formulation from FStr is following the analytical formulations. With a relative difference of 3.8% for local buckling (NBR 14762 [5]) and 2.5% for distortional buckling (Cardoso *et al.* [86]), the FStr accuracy against analytical formulation is validated.

Table 3.1. Critical Buckling comparison at critical lengths.

Critical Length [mm]	Mode	FStr/CUFSM	FStr/GBTul	FStr/Analytical
(i) 84	Local	1.000	0.993	1.038 (NBR 14762 [5])
(ii) 405	Distortional	1.000	0.995	0.975 (Cardoso <i>et al.</i> [86])

3.2.4 Finite Element Method Validation

In this section, the FStr Computer Application program is validated comparing its results with the Finite Element Method (FEM), Generalized Beam Theory (GBT) and Constrained and Unconstrained Finite Strip Method (CUFSM).

For this validation, an elastic buckling analysis for a range of 200 lengths of lipped channel columns is performed. Also, for all the methods studied, it is treated a column under uniform axial compression, with fixed-fixed end condition. The geometry of the cross-section is illustrated in Figure 3.24. Additionally, the buckling analysis of the lipped channel cross-section studied in this section, is the same as shown in Figure 2.13, and their buckling modes are illustrated in Figure 2.9.

The FEM is employed with assistance of the ANSYS Mechanical APDL [68]. The main mode extraction method to be applied for the buckling analysis is the subspace iteration⁹, which is suitable to detect the modes for large models. Additional finite element model specifications about the column discretization, type of element, boundary conditions, etc. is well detailed in the subsection 4.1 (Model description).

The other method appropriated for comparison, the GBT, is performed with GBTul 2.0 [65] computer application. For this method, all the conventional modes, numerical solution with 20 beam finite elements and clamped-clamped end condition are considered.

Lastly, the CUFSM 5 [39] is a method based on the FSM, which is also the same method as applied for the developed computer application program, FStr. For this method, the same initial parameters as applied in the FStr program, are employed: 10 half-wave terms, clamped-clamped end condition and 18 strips.

⁹ This method is explained in the book from Bathe [72], and additional improvements is found in Wilson and Itoh [73].

The graph of critical load *versus* column's length is illustrated in the Figure 3.24 in accordance with the relative difference between the FStr Computer Application Program with other numerical solutions.

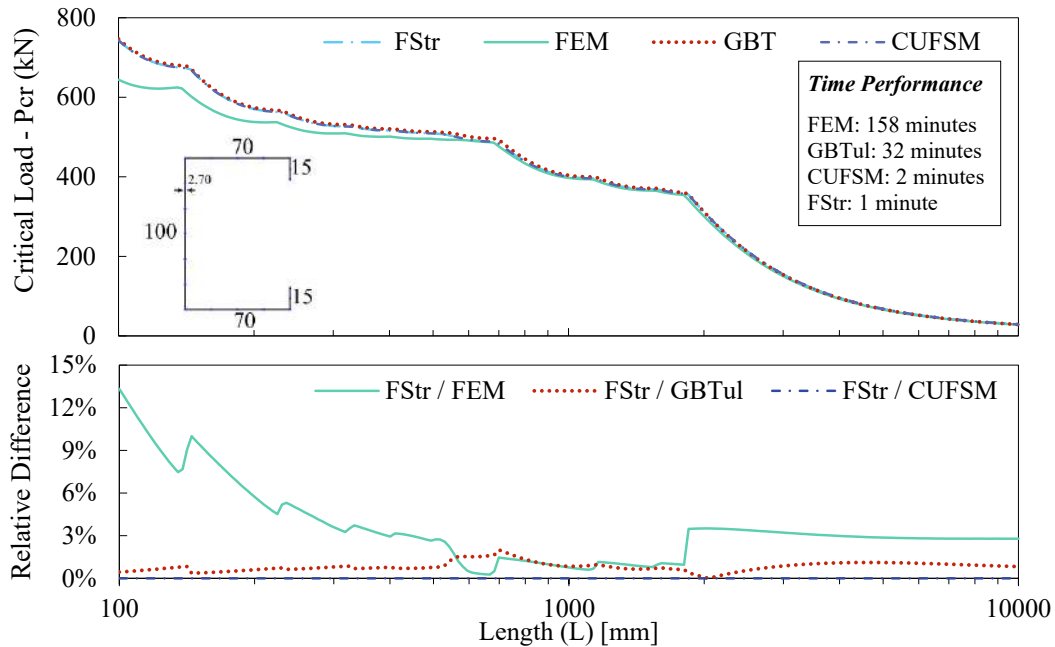


Figure 3.24. Signature Curve and Relative Difference comparing FEM, GBTul and CUFSM with the FStr computer application program.

First, comparing the two graphs in the Figure 3.24, it can be seen that the CUFSM and the FStr provides the same results, with a maximum difference of 0.000056%, which is probably a difference occasioned by an inevitable numerical precision. Also, the FStr reached close to the GBT method, with a maximum relative difference of 2.0%. However, comparing the FStr with the FEM, the maximum relative difference is 13.3%, which can be seen clearly in the signature curve. On the other hand, this maximum difference occurs in short column's length, which is irrelevant for the purposes of structural members design. As shown in Figure 2.13, the D-G modal interaction is stronger near to the length 1850 mm. For a certain length range near to $L=1850\text{mm}$, the maximum relative difference is around 3.51%, which is an acceptable relative difference between the FEM and FSM.

With respect to the modal shape, Figure 3.25 shows the FEM vs FSM comparison of the buckling mode shape for the column's length of 1722 mm and 2222 mm. Note that the FStr provides the same buckling mode with same maximum amplitude, as it is given by the FEM.

Further, the time of performance of each method is shown in Figure 3.24. Note that the FStr is the faster method (for this particular model), with a great precision, compared to the other methods. Additionally, observe that the CUFSM is quite faster as the FStr. Even though both programs employ the same matrix method, the FStr eigenvalue problem solver is faster, and the code structure is optimized with the purpose of avoid repeated loops. Moreover, the GBT method has shown a quite slow method. The most probable reason for this slowness is because the model has a clamped-clamped end boundary condition, which imposes the GBTul program performs a numerical interactive analysis, which takes a huge computational effort. With respect to the FEM, its clearly the slowest method, as expected, caused by its higher number of degrees of freedom.

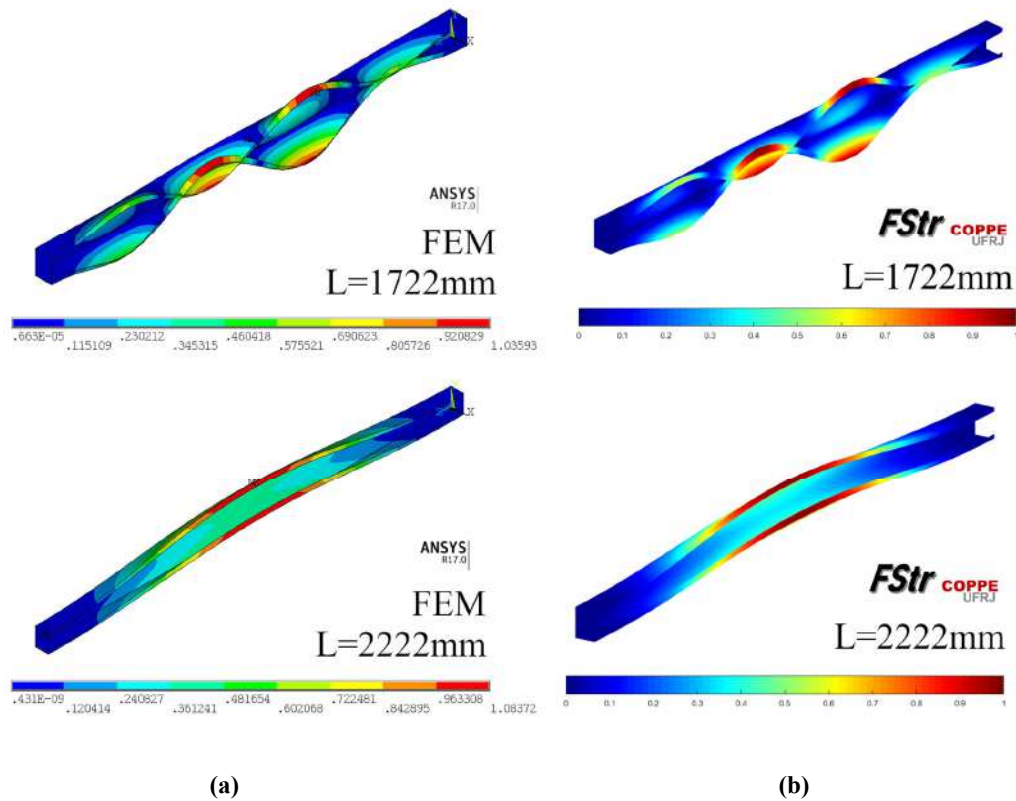


Figure 3.25. Tridimensional modal shapes comparison between (a) FEM and (b) FStr at distortional and global lengths.

Accordingly, the FStr computer program application, is a powerful tool for an elastic buckling analysis, that can be applied, for example, for optimization problems or large number of buckling analysis.

3.2.5 Unrestricted Bending Validation

The last validation is the buckling analysis of beams under unrestricted pure bending, where there is not axial, shear or torsional forces. For this validation case, it is performed only simply supported end boundary condition, with all the longitudinal edges free, and ten terms of half-waves. The results from FStr are again compared to the CUFSM and GBTul programs.

In order to validate the uniform bending, it is applied two different geometries, a lipped channel section with web stiffener (Figure 3.26-a) and an asymmetric zed section (Figure 3.29-a). For both models the moment is applied at the geometric central x-x axis, however, for the zed section, the principal 1-1 axis is rotated by 19.34 degrees clockwise, while for the lipped channel section with web stiffener, the central x-x axis coincides with the principal 1-1 axis. Another important condition is that the pure bending is unrestricted, this means that the neutral line is not parallel to the flanges. Additionally, the geometric sections are consisted of rounded corners, with a more realistic form and analysis.

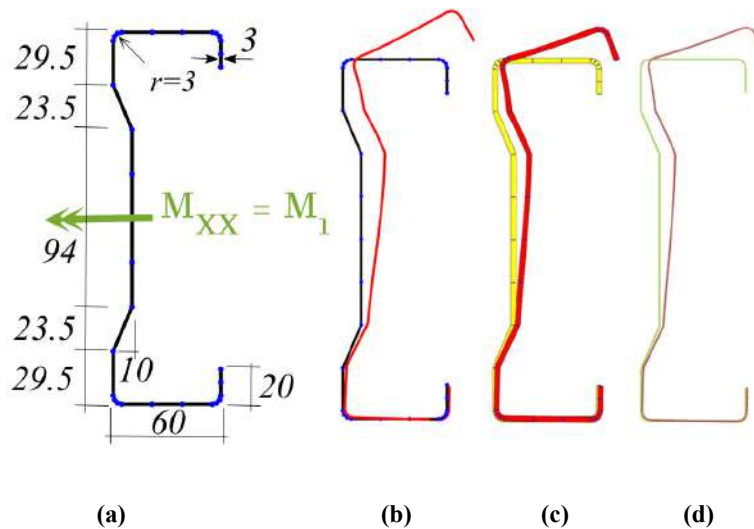


Figure 3.26. Lipped Channel section with web stiffener, (a) cross-section geometry, (b) FStr, (c) CUFSM and (d) GBTul 2D buckling mode at $L=849$ mm and $\bar{y}=0.3L$.

First, for the lipped channel section with web stiffener model (Figure 3.26-a), the signature curve is displayed in Figure 3.27. As can clearly be seen, the relative difference between the FStr and GBTul hits to a maximum of 13%. The same maximum difference is also noted compared the CUFSM with the GBTul, since the maximum relative difference between CUFSM and FStr is 0.007%.

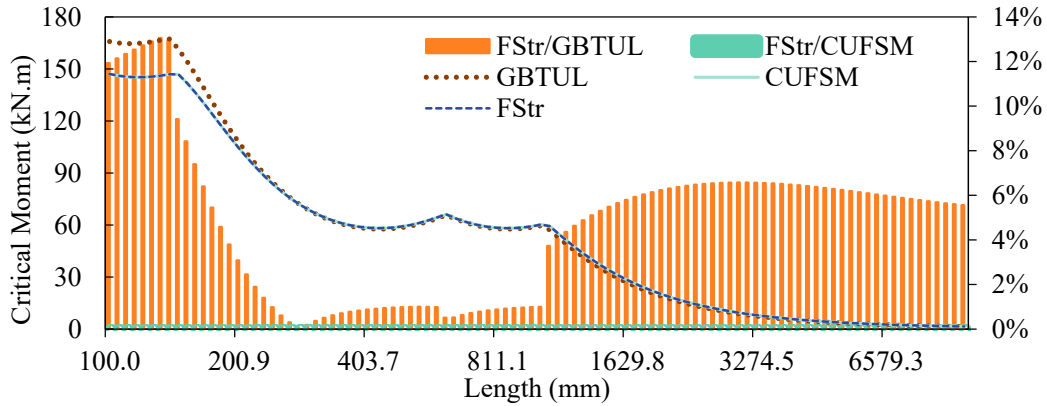


Figure 3.27. Lipped channel section with web stiffener critical bending validation with GBTul and CUFMSM.

However, as shown in Figure 3.27, the maximum relative difference between FStr and GBTul occurs at short lengths with local buckling mode. For distortional modes, this difference approaches to a maximum of 1%, while for global buckling mode has a maximum of 6.5%. In order to compare the modal shapes, Figure 3.26 shows the 2D buckling modes at $L = 849$ mm, for FStr, CUFMSM and GBTul programs, and Figure 3.28 shows the 3D modal shape for the FStr Computer Application Program.

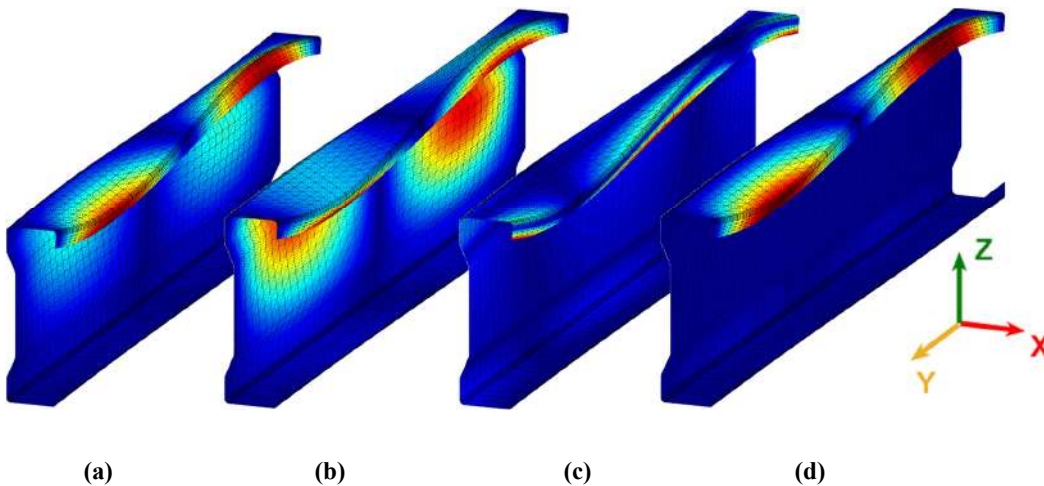


Figure 3.28. 3D modal shapes for a beam with lipped channel and web stiffener section from FStr at $L=849$ mm, showing contour plot for (a) resultant, (b) x-direction, (c) y-direction and (d) z-direction displacements.

In order to illustrate the modal shape displacement in the geometric orthogonal directions, Figure 3.28 shows the FStr buckling mode at $L=849$ mm, in four different contour plots. The plot shows that the resultant contour plot not always shows the apparent modal shape contour plot. As can be noticed, the contour plot for the y-direction,

Figure 3.28-c, shows displacements in the transversal section plane, that is not trivial to observe in the resultant contour plot.

Secondly, discussing about the asymmetric zed section beam, details about its asymmetry (geometry illustrated in Figure 3.29-a) are important to point out. Since this model has its principal axis rotated - 19.34 degrees clockwise - the moment applied in the x-x axis can be decomposed into the 1-1 and 2-2 principal axis. Attributable to this fact, the model in CUFSM and FStr has the option to add the moment in the x-x axis. However, in GBTul, the only possible option is to apply the moment in the principal axis. As a result of this, the moment of 1 kN.m applied at x-x axis, is analogous as two orthogonal moments of 0.944 kN.m at 1-1 principal axis and 0.331 at 2-2 principal axis. The signature curve for the asymmetric zed beam is displayed in Figure 3.30.

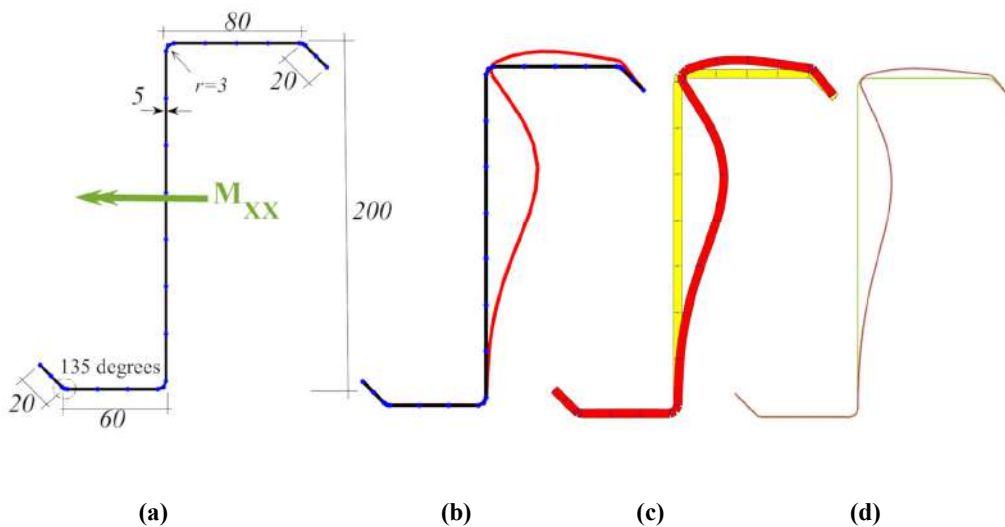


Figure 3.29. Asymmetric zed beam section, (a) cross-section geometry, (b) FStr, (c) CUFSM and (d) GBTul 2D buckling mode at $L=351$ mm and $\bar{y}=0.5L$.

Notice that the relative difference between the FStr and GBTul have a smaller deviation, with a maximum relative difference of 2.8%. Also, this relative difference approaches to almost zero when the length is increased in the global buckling mode. The CUFSM again showed a minimal relative difference compared to FStr, with a maximum of 0.005%.

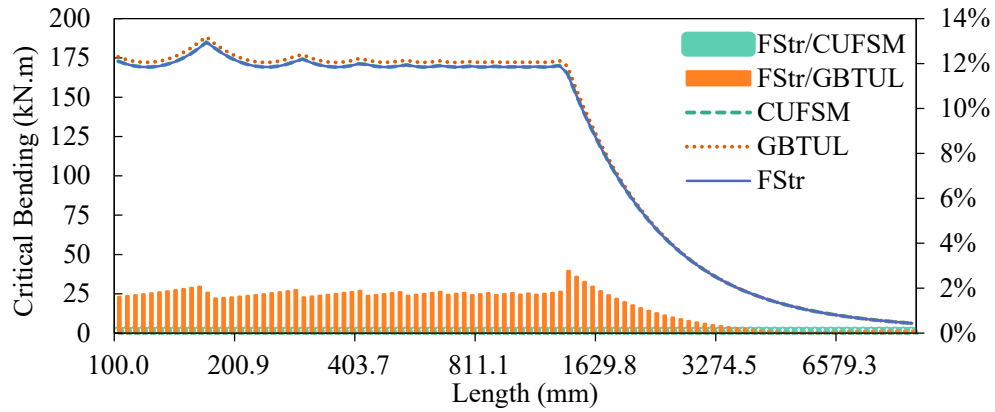


Figure 3.30. Asymmetric zed section critical bending validation with GBTul and CUFSM.

In order to compare the modal shapes, Figure 3.29 shows the buckling modes at $L = 351$ mm, for FStr, CUFSM and GBTul programs. The buckling modes in 2D form illustrates the conformity of the developed program, FStr, with the usual programs, CUFSM and GBTul.

4 Numerical Modeling

For a numerical investigation of D-G buckling interaction, a Finite Element Analysis (FEM) is performed in order to understand the structural behavior. Also, the FEM is employed with assistance of ANSYS Mechanical APDL [68]. The analysis using the FEM is addressed to capture and observe the nonlinear equilibrium path and detect the strength of the structural element. In this section, the finite element model is described and validated with compression tests provided from laboratory experiments.

4.1 Model description

The FEM numerical model performs an important task to the parametric study of CFS columns under D-G buckling interaction. Through a calibrated finite element model, based on experimental tests, the model can reproduce real experiments numerically. This approach save time in order to perform a parametric study, and also leads it to a more practical structural investigation that is almost impossible to test in real physical conditions. Consequently, it is fundamental that the numerical model is well calibrated to behaves as expected, avoiding untrustworthy results, that could compromise the parametric study and influencing the conclusions of the study. Due to that, the description of the numerical modeling needs to be precise and detailed, reporting every type of consideration in the FEM implementation.

The adopted model is described in five different groups: *(i)* discretization, *(ii)* end boundary condition, *(iii)* loading, *(iv)* material model and *(v)* initial geometric imperfections. For each group, the model is explained in detail, according to the ANSYS Mechanical APDL reference [68] and considerations retrieved from the literature.

Figure 4.1 shows an illustration of a CFS column with a lipped channel section and both ends fixed. This figure illustrates some of the main components of the numerical model, as discretization, end boundary condition and loading. In Figure 4.1-a is illustrated the meshes, as well as the real thickness of the end plate and the structural CFS element. Figure 4.1-b and Figure 4.1-e displays both end boundary condition with the loading and

restrictions. Figure 4.1-c also exhibits the mesh, but in the structural element. Finally, Figure 4.1-d shows the restriction on longitudinal direction.

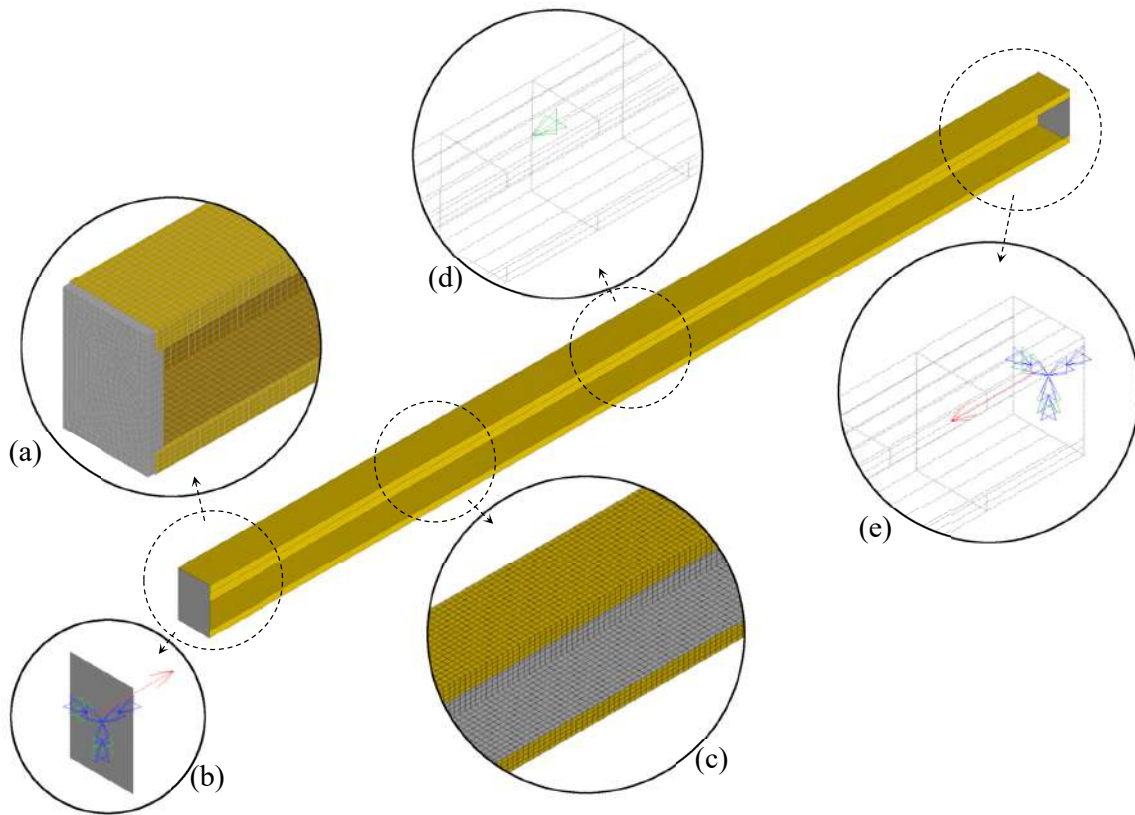


Figure 4.1. Finite Element Model description: (a) Shell element mesh and thickness on fixed-ended end; (b) boundary condition and loading on extremity; (c) mesh of structural element along the length; (d) restriction to longitudinal direction movement at mid span; (e) boundary condition and loading on the other extremity.

4.1.1 Discretization

This section describes the type of element and mesh properties. First, the type of element is restricted to a shell type. This type of element is adequate for analyzing thin to moderately-thick shell based structures. Secondly, the mesh properties include a mixed mesh with quadrilateral and triangular shell element with a fixed element size. Illustrations of shell element and mesh configuration is shown in Figure 4.1-a and Figure 4.1-c.

The adopted finite element type is the SHELL281, Figure 4.2-b. According to the ANSYS Theory Reference [68], the SHELL281 has 8 nodes, with 6 degrees of freedom¹⁰ per node, and is appropriate for linear, large rotation and large strain nonlinear situations. In addition, the SHELL281 formulation is placed on logarithmic strain and true stress measures. For this research, the finite element option contemplates the shell structural stiffness with bending and membrane considerations.

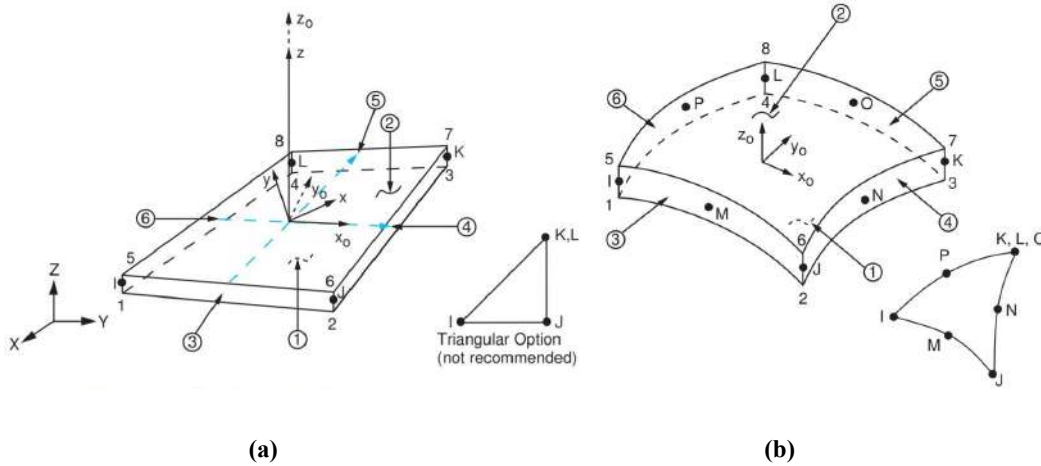


Figure 4.2. Degrees of freedom of (a) SHELL181 and (b) SHELL281, retrieved from ANSYS Mechanical APDL reference [68].

The mesh generation has a particularity, it generates quadrilateral and triangle-shaped elements with an element size of 5 mm. This mixed mesh occurs resulting from the predefined imperfections from the FStr Computer Application Program and also due to the automatic mesh generation in the plates at the ends of the column. Even though the element shape chosen for the whole column is quadrilateral-shaped, triangle-shaped elements may be emerged, when the mesh is generated. This happens because the areas generation for the mesh are formed by non-planar surfaces. This is the reason why in this research the SHELL218 is employed instead of SHELL181 (Figure 4.2-a), which has less nodes and degrees of freedom. According to ANSYS Theory Reference [68], SHELL281 provides more reliable results for triangular elements, while SHELL181 is not recommend for triangular-shaped elements. Figure 4.3 shows the mesh at the end plate of the column, detailing both types of possible meshes occurrences, quadrilateral and triangular shell element.

¹⁰ Translations in the x, y, and z axes, and rotations about the x, y, and z-axes.

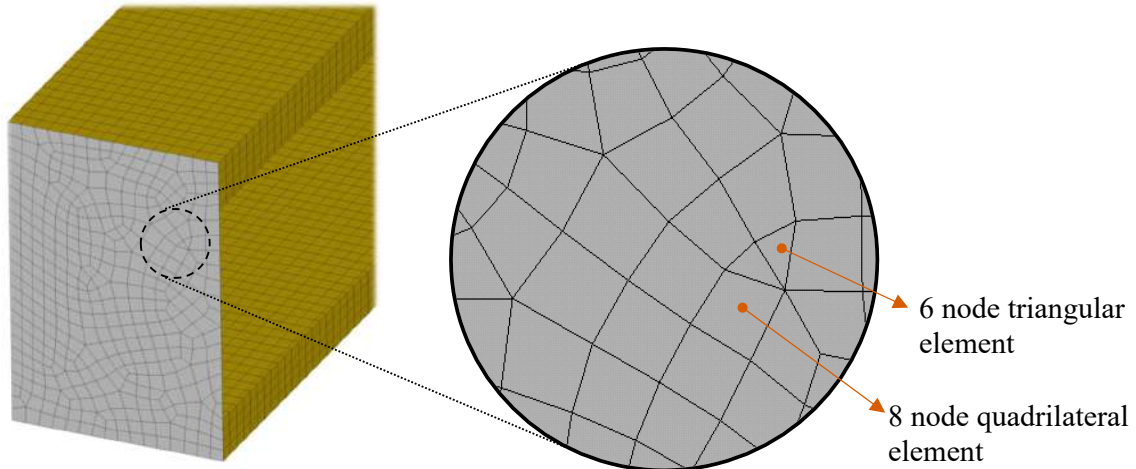


Figure 4.3. Detail of the end plate, showing the type of possible meshes occurrences, quadrilateral and triangular shell element.

More details and specifications about the formulation of SHELL281 element can be found in Ahmad *et al.* [132], Dvorkin [133], Dvorkin and Bathe [134], Allman [135], Bathe and Dvorkin [136], Cook [137], MacNeal and Harder [138] and Cook *et al.* [139].

4.1.2 End boundary conditions

With respect to the boundary conditions, the column has fixed-fixed end condition. The constraints in the extremities of the column are designed to be a stiff plate rigidly fixed to the end of the column, illustrated in Figure 4.1-a and Figure 4.4.

For this type of model, both extremities of the column have constraints on displacements in x and y direction, and constraints on rotation in x , y and z direction (see Figure 4.1-b, Figure 4.1-e and Figure 4.4-c). Another constraint is necessary in the middle of the column, in a node in the middle of web, which prevent displacement in z direction (Figure 4.1-d). This additional constraint in the middle of the columns is needed to avoid free body translation, taking into account that symmetric behavior develops in the longitudinal direction of the column, imposed by the symmetric end boundary condition.

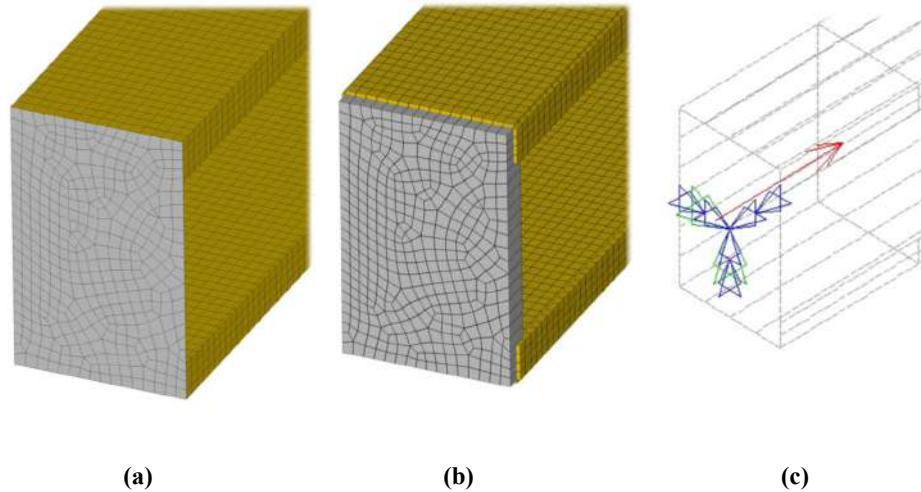


Figure 4.4. Plate rigidly fixed to the end of the column, representing a fixed-ended end support conditions, (a) without shell thickness, (b) with illustration of shell thickness and (c) representation of restricted degrees of freedom.

The stiff plate is generated covering all the points in the extremity section. In this condition, a unique surface is formed and the boundary conditions restrictions are applied, as shown in Figure 4.4-c. Sequentially, the end plate mesh is shaped automatically by ANSYS. Even so, the plate rigidly fixed is considered with a fixed thickness of 12 mm, and the section thickness can vary (*e.g.* for a parametric study). The value of the plate thickness is based on laboratory experiments performed by Salles [140] and Santos [106]. The thickness difference from the plate and the cross-section can be observed in Figure 4.4-c.

4.1.3 Loading

Since the numerical model is a column, the only type of load is an axial compressive force. Equal compressive loads are applied to the ends of the column (see Figure 4.1-b, Figure 4.1-e and Figure 4.4-c). The external load is applied as a punctual concentrated load in the centroid of the section, at both ends, generated automatically by ANSYS as a HARDPOINT, where the compressive load can be easily applied. For the buckling analysis, the force magnitude is equal to the squash load $P_y = A \cdot f_y$. The non-linear analysis, up to the column strength capacity, increases the load based on load steps.

The maximum load is set up to be 1 N/N , and the load steps are 0.05 N/N for the arc-length method¹¹.

4.1.4 *Material Model*

A structure composed of an elastic material behaves linearly and constantly for any kind of external load applied to the structure. However, a real structure never behaves always linear and elastic. In this case, a ductile material with nonlinear characteristics should be considered. In order to perform a nonlinear material analysis, the elastic-plastic assumptions of cold-formed steel must be introduced.

The material model here is defined as a balance of simplicity and accordance with reality for perform an acceptable parametric study. In this case, a material with bilinear isotropic hardening (elastic-perfect plastic model) is considered, which applies the von Mises yield criteria with an isotropic work hardening presumption. This hardening assumption consider an initial slope of the strain-stress curve with an elastic modulus in the elastic strain region and a tangent slope modulus (E_t) with small magnitude, compared to the elastic modulus, in the plastic strain region. The yield strength of the material varies, depending on the study, however, it is defined for all cases an elastic modulus of 200 GPa (200 kN/mm²) and the major Poisson's ratio equal 0.3. Also, the material for the plate rigidly fixed to the end of the column have the same properties and characteristics as the structural element. In Figure 4.5 is shown an example of a strain-stress curve given by a tensile test and the material model adopted here. For the cases where the material has a high strength yield stress, it is adopted $\sigma_0 = f_y$ and $E_t = 0$.

With respect to the residual stresses and corner effects by the CFS material, the major part of investigations neglected these effects. In Dinis and Camotim [97] has been shown an insignificant impact in the ultimate column load. Also, according to Ellobody and Young [141], the small membrane residual stresses has been demonstrated an irrelevant effect on the ultimate load, stiffness of the column, load-shortening behavior and in the failure mode. In Matsubara *et al.* [100], a recent finite element modeling of local-distortional coupled phenomena in lipped channel CFS columns, the residual stresses and rounded corners effects are also neglected.

¹¹ Described in subsection 4.1.6 (Analysis Methods)

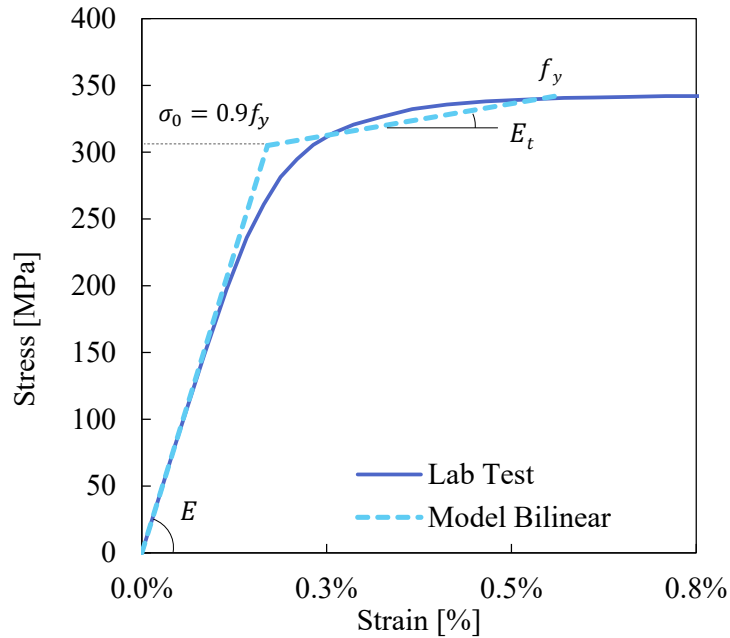


Figure 4.5. Strain-Stress curve of a Bilinear Model comparing with tensile test performed by Salles [140].

4.1.5 Initial geometric imperfections

All the structural members include geometric imperfections, originating on their fabrication, transportation, precision on measurement tools and many others. CFS members are never completely flat or perfectly straight. In this case, definition of the geometric imperfections performs an important task in the nonlinear analysis, in order to represent a structural model as close as possible of the reality.

For the present work the original perfect geometry and imperfections of the column are created with the help of the previous FSM analysis. The FStr program (described in chapter 3) performs the elastic buckling analysis and, with the corresponded modal critical shape, generates points that are inserted into an APDL routine code as KEYPOINTS. The modal critical shape is inserted as an initial imperfection, with a maximum amplitude depending on the mode. In this case, the initial imperfect geometry of the column is composed of non-planar surfaces, connecting 4 nearby KEYPOINTS. Figure 4.6 shows the structural geometry generation with predefined imperfections given by KEYPOINTS, from FStr Computer Application Program.

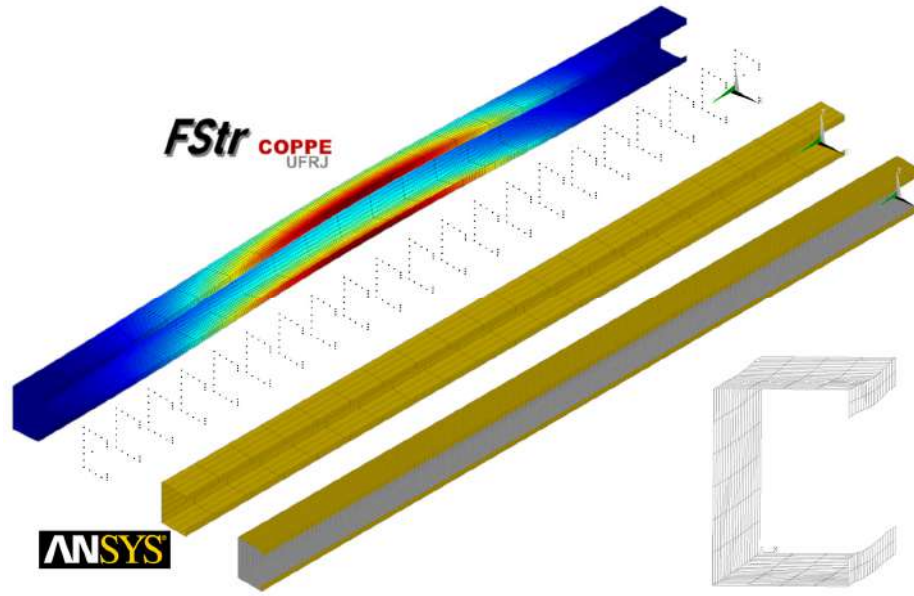


Figure 4.6. Geometry and initial geometric imperfections generation from FStr Computer Application Program into the ANSYS Mechanical APDL.

The maximum amplitudes parameters for global and distortional buckling are different. As proposed by Martins *et al.* [82], the present research adopts $L/1000$ for global imperfection and $0.94t$ for distortional imperfection. The reason for the distortional imperfection as $0.94t$ is presented by Schafer and Pekoz [142], as corresponding to 50% probability that a random imperfection amplitude is below or above this value. However, in the study of Santos [143], with end-bolted CFS columns under distortional critical length, it has been shown that the ultimate load has not changed excessively with the variation of the maximum amplitude from $0.1t$ up to $1.0t$ (failure load variation below 5%). Anyway, $0.94t$ is adopted and applied to the distortional buckling initial geometric imperfection amplitude.

4.1.6 Analysis Methods

The main goal in using a finite element method, is its flexibility to perform complex analysis, involving nonlinearities. For the present case a material and geometry nonlinearities are considered in a post-buckling behavior. The ANSYS built-in method using to execute this type of analysis is based on the arc-length method, known as “*The modified Riks method*” (introduced by Riks [74], [75] and Wempner [76] with modifications being carried out later by many authors, *e.g.* Crisfield [144] & [145]). The

method has a displacement control, during the loading, in order to find the fundamental paths before and after the bifurcation point. This method is convenient for solutions of unstable problems that has a nonlinear static equilibrium.

4.2 Numerical model validation

Since there is an absence of laboratory testing experiencing the D-G interaction, the finite element model is validated for columns that demonstrated only global buckling mode and distortional buckling mode, before collapsing. For the validation, the experimental results from Heva [146], Gunalan *et al.* [147], Kankanamge and Mahendran [148], Salles [140] and Matsubara, Batista and Salles [100] are taken.

4.2.1 Global Buckling Mode Validation

The global (flexural-torsional) buckling validation is performed using three columns tested by Heva [146], described in Table 4.1. This author has performed laboratory tests of multiple columns under different temperatures developing the flexural-torsional buckling. Updated information about the experiments can be found in Gunalan *et al.* [147]. For the present research, only the results for the specimen with room temperature (20°C) are considered. Table 4.1 shows all the parameters and Table 4.2 the results of the numerical and laboratory tests performed by Heva [146] and also the results obtained in the present research. Also, Table 4.1 includes all the measured geometries of the specimen, the material properties given by standard tensile tests and the measured specimen imperfections.

Table 4.1. Measured geometry and material properties of specimens from Heva [146].

Column	Measured Geometry					f_y	E	Imperf.
	t	b_w	b_f	b_s	L			
[#]	[mm]	[mm]	[mm]	[mm]	[mm]	[MPa]	[N/mm ²]	[]
G250-1.95-1800	1.95	74.82	50.06	14.87	1740	271	188000	L/2558
G450-1.90-1800	1.88	74.67	49.94	14.51	1740	515	206000	L/2949
G550-0.95-1800	0.95	54.94	34.88	8.00	1740	615	205000	L/2485

Detailed information about the stress-strain curves and mechanical properties of CFS described in Table 4.1, can be found in Kankanamge and Mahendran [148], for 250 and 450 steel grades, and in Ranawaka and Mahendran [149], for 550 steel grade.

The actual stress-strain curves are obtained with a strain gauge at ambient temperature, and they are illustrated in Figure 4.7, Figure 4.8 and Figure 4.9. Based on the stress-strain tests, the material models adopted here are bilinear and multilinear isotropic hardening, also graphically illustrated in Figure 4.7, Figure 4.8 and Figure 4.9. The bilinear model is adopted with $\sigma_0 = f_y$ and $E_t = 0$ (see Figure 4.5). According to ANSYS APDL Theory Reference [68] the multilinear model is described by pieces of stress-strain curve, starting at the origin and defined by sets of positive stress and strain values with always positive slopes of the stress-strain curve.

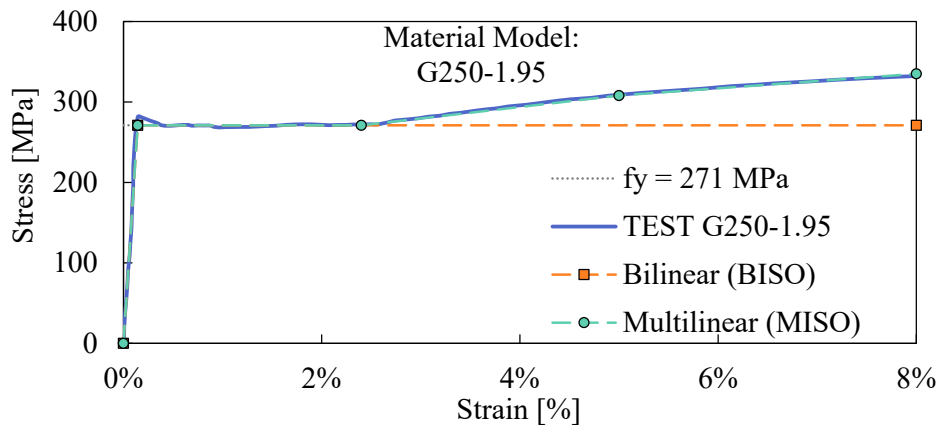


Figure 4.7. Stress-Strain models for 1.95mm and 250 MPa cold-formed steel.

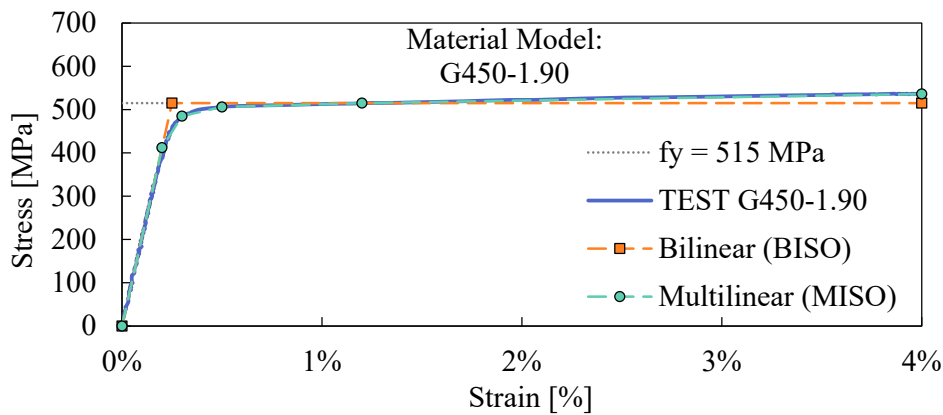


Figure 4.8. Stress-Strain models for 1.90mm and 450 MPa cold-formed steel.

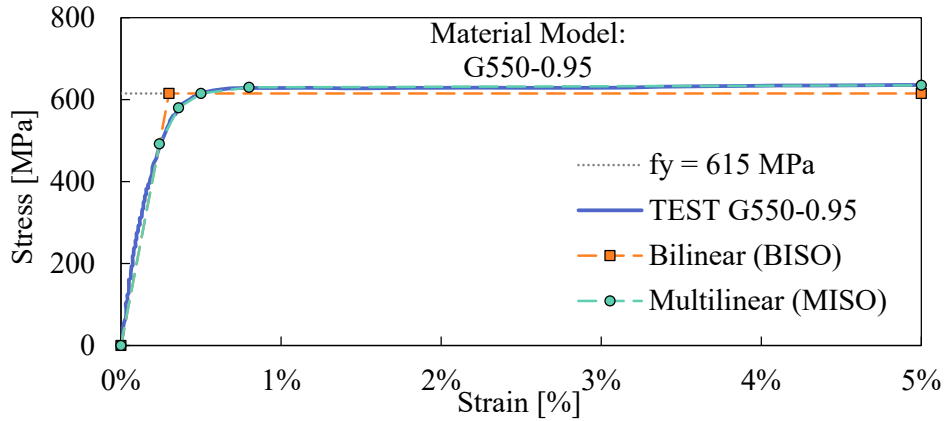


Figure 4.9. Stress-Strain models for 0.95mm and 550 MPa cold-formed steel.

Table 4.2 provides the column strength for 4 cases: (i) the column strength $P_{U.FEM}$ from FEM analysis by Heva [146], (ii) from the experimental tests $P_{U.TEST}$ performed by Heva [146], (iii) the column strength $P_{U.B.FEM}$ with the bilinear material FEM model given by the present investigation and (iv) with the multilinear material model FEM $P_{U.M.FEM}$ also given by the present work.

Table 4.2. Ultimate load results for room temperature (20°C) of specimens from Heva [146], both numerical and lab tests, and the numerical results obtained in the present research.

Column [#]	Ultimate Load			
	Heva [146]		Author's Bilinear	Author's Multilinear
	$P_{U.TEST}$	$P_{U.FEM}$	$P_{U.B.FEM}$	$P_{U.M.FEM}$
	[kN]	[kN]	[kN]	[kN]
G250-1.95-1800	87.94	90.7	93.59	93.81
G450-1.90-1800	120.42	129	127.60	121.77
G550-0.95-1800	24.72	25.4	25.71	24.72

Notice that the author's present work numerical ultimate load is similar to the numerical model and laboratory tests given by Heva [146]. The proposed numerical bilinear model has a relative difference of 6.4%, 6.0% and 4.0% regarding with tests of Heva [146] and 3.2%, -1.1% and 1.2% differences regarding with the numerical solution of Heva [146], respectively for the models G250-1.95-1800, G450-1.90-1800 and G550-0.95-1800. Relatively to the multilinear model, the relative difference is 6.7%, 1.1% and

0.0% regarding with tests of Heva [146] and 3.4%, -5.6% and -2.7% differences regarding with the numerical solution of Heva [146], respectively for the models G250-1.95-1800, G450-1.90-1800 and G550-0.95-1800. The results from Table 4.2 are graphically displayed in Figure 4.10.

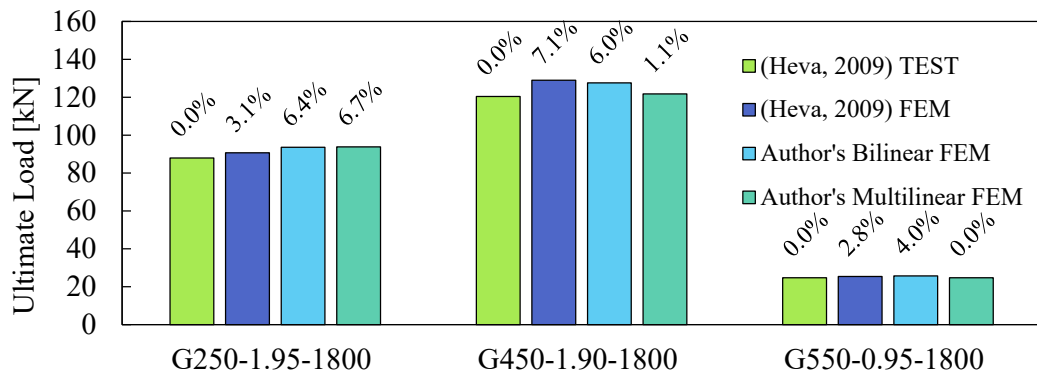


Figure 4.10. Graphical results of ultimate load for room temperature (20°C) of specimens from Heva [146], both numerical and lab tests, and the numerical results obtained in the present research (relative difference with respect to the tests from Heva [146]).

For more convincing results, the graphs load *versus* displacement out of plane in the middle top flange at mid span (displacement position exemplified in Figure 4.11-b) for the 3 column specimens in Table 4.1 are shown in Figure 4.11 and Figure 4.12. These graphs show the displacement behavior of a specific point during the loading procedure.

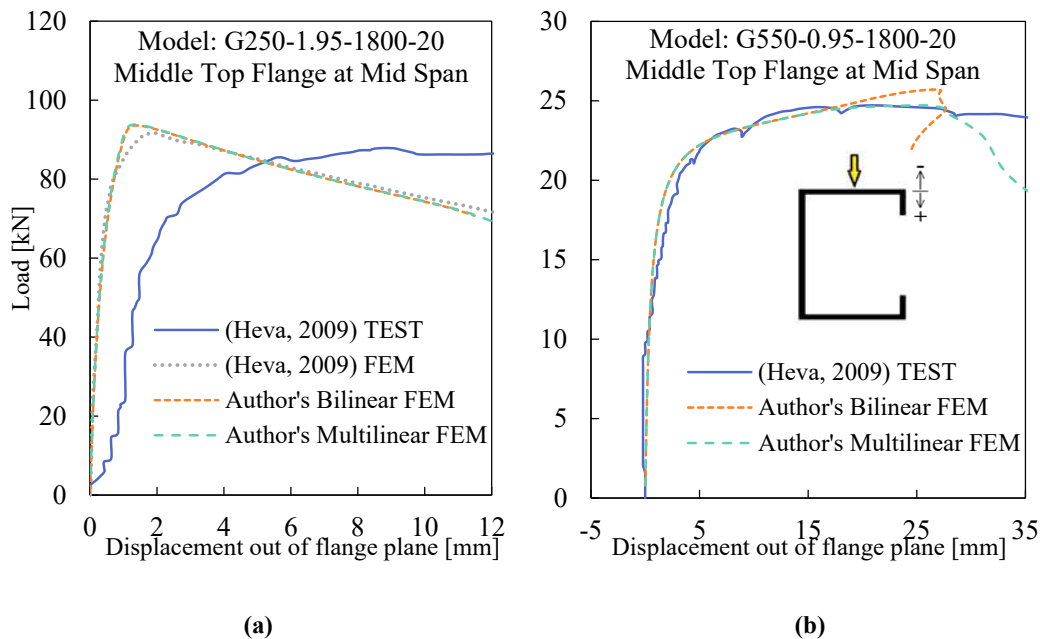


Figure 4.11. Load versus displacement out of plane in the middle top flange at mid span of models (a) G250-1.95-1800 and (b) G550-0.95-1800 (both for room temperature 20°C).

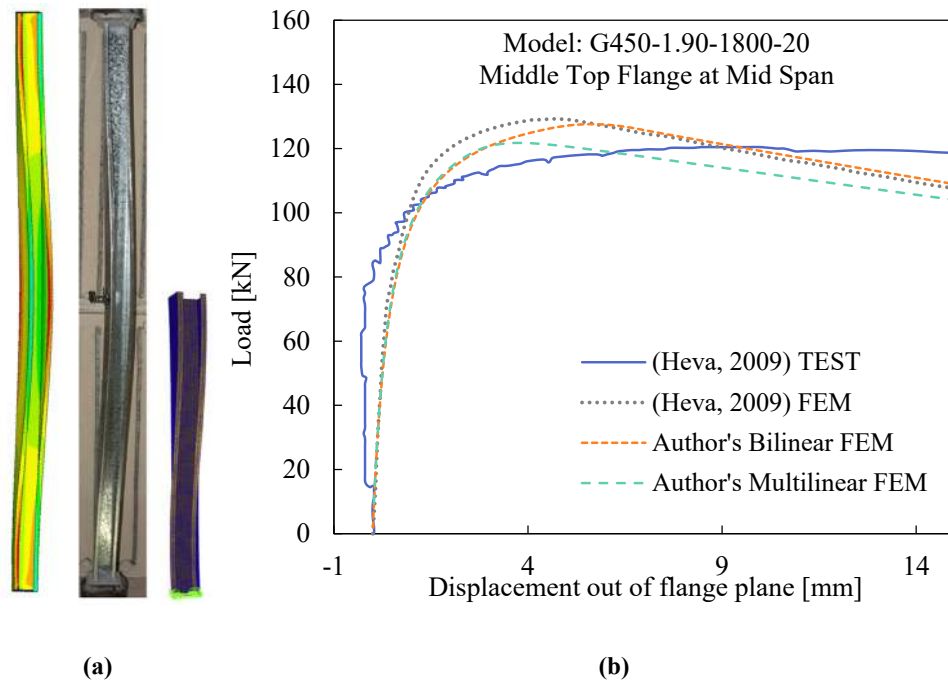


Figure 4.12. Results from model G450-1.90-1800: (a) comparison of flexural-torsional failure mode for the present numerical model, the laboratory test from Heva [146] and numerical model from Heva [146]; (b) load versus displacement out of plane in the middle top flange at mid span.

It can be noted in Figure 4.11-b that the author's FEM have a similar equilibrium path as Heva's [146] test, with a better fit with the multilinear model. On the other hand, in Figure 4.12-b, the laboratory tests are kindly translated on the displacement direction. However, the bilinear numerical model performed in this research has a very close behavior to the numerical model performed by Heva [146]. Another important observation, is about the model G250-1.95-1800. Note that comparing to the experiment, the present numerical model does not fit well with the experimental records. However, comparing the author's present work, both bilinear and multilinear, with the numerical model from Heva [146], it is noticed an almost exact fit of the equilibrium paths.

Even though, the multilinear material model has indicated better results for the column strength, it is more convenient to adopt the bilinear isotropic hardening model for the parametric study. Moreover, adopting the bilinear model, makes the finite element analysis simpler, with satisfactory results. To sum up, the obtained results allow concluding that the developed finite element model is validated for flexural-torsional buckling analysis.

4.2.2 Distortional Buckling Mode Validation

The distortional buckling validation is performed using a single column tested by Salles [140]. The testing was performed at the COPPE Laboratory of Structures and Materials Professor Lobo Carneiro (LabEST). Updated information about the tested column is in Matsubara, Batista and Salles [100].

The column cross-section geometry is shown in Figure 4.13. The lipped channel CFS column specimen was 2529 millimeters long, with material properties of 342 MPa of yield strength, 179.468 GPa of elastic modulus (quite low average Young modulus extracted from a set of standard tensile tests) and 9.845 GPa of tangent slope modulus (E_t). As a result, the specimen reached its experimental column strength of 33.4 kN, while the finite element model in this research, leads to an ultimate load of 35.3 kN. A maximum amplitude of $0.1t$ for the distortional buckling mode as initial geometric imperfection and a bilinear model for the strain-stress curve, as shown in Figure 4.5, is considered. Figure 4.13 shows a comparison of the equilibrium path of the web extremities at mid span, for the experimental test and the FEM solution.

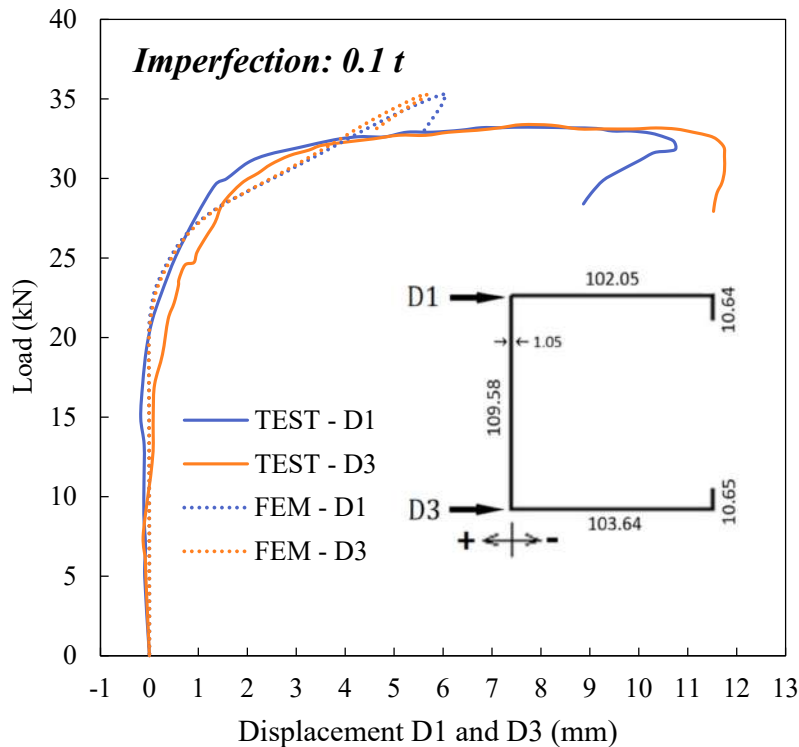


Figure 4.13. Load versus displacement of the web extremities at mid span of LC specimen by Salles [140] and numerical FEM results for the present work.

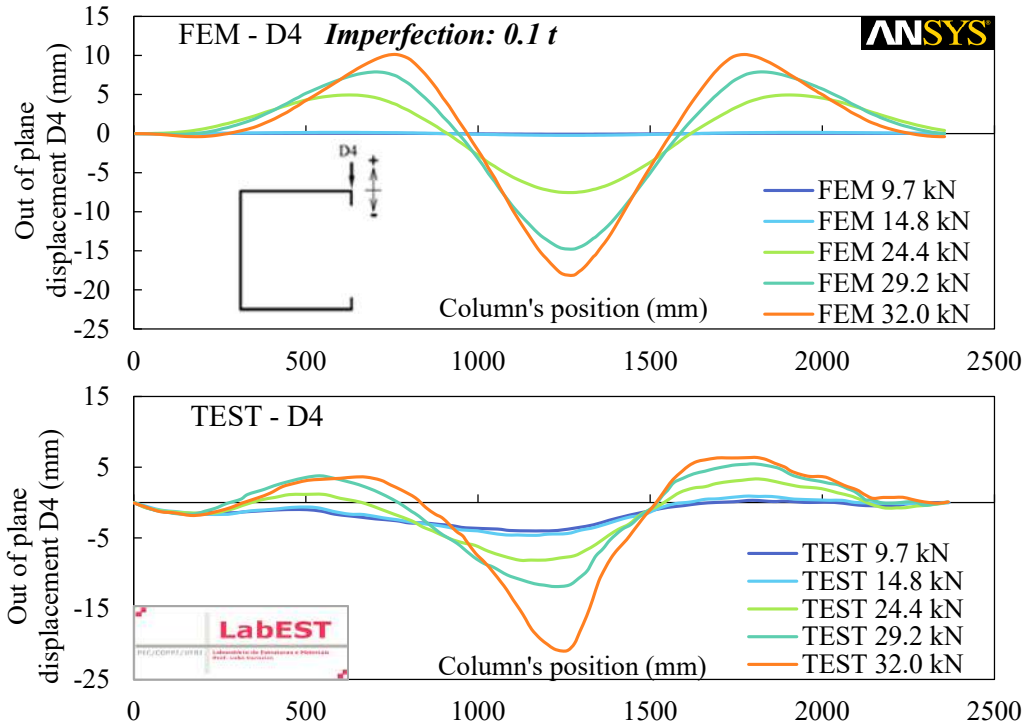


Figure 4.14. Displacement D4 along the column's position, with 5 load increments of numerical FEM results for the present work and specimen tested by Salles [140].

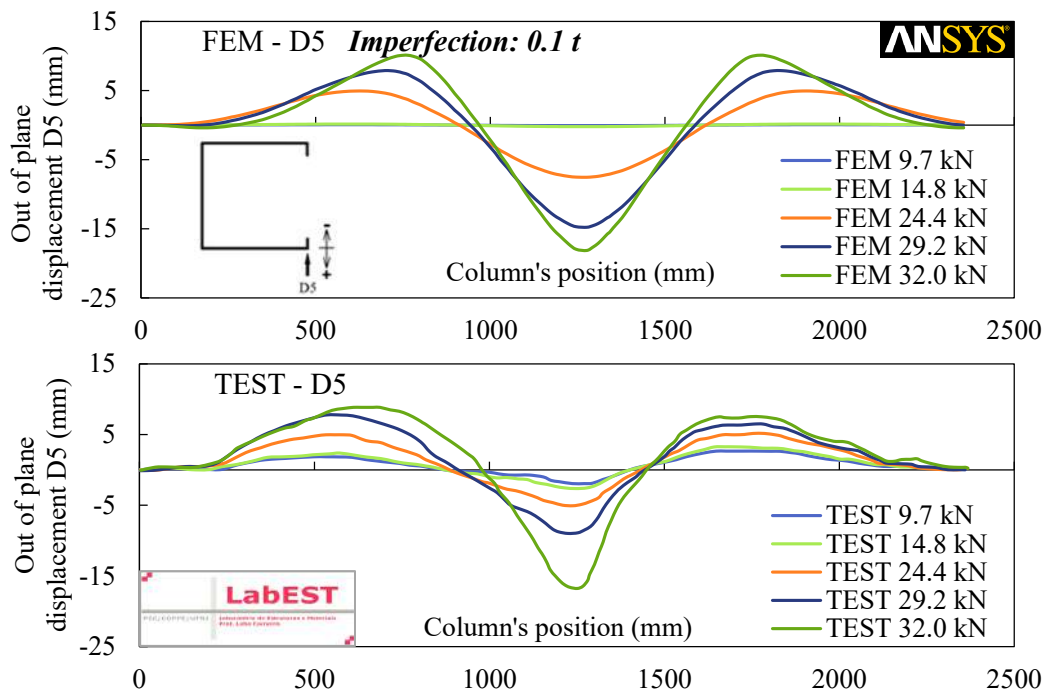


Figure 4.15. Displacement D5 along the column's position, with 5 load increments of numerical FEM results for the present work and specimen tested by Salles [140].

Note that in Figure 4.13 that the equilibrium path of the FEM is pretty close to the experimental results for small displacements. For larger displacements, the FEM model tends to behave into a stiffer linear path until it collapses, while the laboratory test shows a long plateau before collapse. Figure 4.14 shows the shape of the flange displacement out of plane D4 along the column length, and Figure 4.15 for the shape displacement out of plane D5 along the column's position, both for 5 loading steps. It can be observed that the same behavior of distortional buckling is clearly shown in the FEM and in the experimental test, with 3 half-waves of distortional modal shape. In addition, the buckling behavior is increased with the load increment, until the column collapse.

5 Parametric Analysis on Distortional-Global Buckling Interaction

In this chapter, the results of a parametric study are presented in order to understand the D-G coupled phenomenon. Following the previously explained methodology, the combination of the FStr Computer Application Program for the elastic buckling analysis and the nonlinear FEM model allowed obtaining the set of column strengths and equilibrium paths. The numerical study is addressed to a set of lipped channel cold-formed steel columns under true D-G interaction, with different combinations of initial geometric imperfections. Additionally, the study included variation of the yield stress and longitudinal length takes place in order to understand the column strength and behavior of D-G interaction in a large range of slenderness.

5.1 Study of Initial Geometric Imperfection Combination

This study consists in analyzing the structural behavior of a cold-formed lipped channel section LC 100x70x15x2.70 mm (out-to-out dimensions) with $L=1850$ mm (Table 5.1) with different initial geometric imperfections and yield strength. The goal of this study is to identify the column's strength and behavior sensibility to initial geometrical imperfections using "impure" modal combination. The geometry is determined for a column experiencing strong D-G interaction, for a length L characterizing True D-G interaction¹² (TI).

The main reason of combining the buckling modes as initial geometric imperfection, emerged due to its difficulty in finding the D-G buckling interaction in a simple elastic buckling analysis.

¹² This categorization is based on the ratio between the critical loads from global and distortional modes, proposed by Martins *et al.* [82], which True D-G interaction is characterized by similar values of distortional and global critical loads. The definition is well commented in subsection 2.5.1 (Distortional-Global Interaction concepts).

The combination of elastic buckling modes, as an alternative to include the distortional and global buckling modes as initial geometric imperfection in the nonlinear analysis, arose as a result of the difficulty in obtaining a true distortional-global buckling shape through an elastic buckling analysis. Thereby, combining the global and distortional shapes as initial geometric imperfection, enables the possibility of occur the D-G coupled phenomenon. Figure 2.13 shows the signature curve for the proposed geometry and, as can be observed, the derivative of the signature curve before $L=1850$ mm and after this length, changes drastically, as well as the modal shape. In this case, it is hard to get a shape that presents a clear D-G interaction. Because of this obstacle of getting a D-G interaction shape mode, the first (Figure 5.1-a) and second mode (Figure 5.1-b) are combined.

Table 5.1. Column LC 100x70x15x2.70 geometry, out-to-out dimensions.

Column Name	b_w	b_f	b_s	t	Area	Length	Imperfections	
							First Mode	Second Mode
							(Global)	(Distortional)
LC100x70x15x2.70	100	70	15	2.70	699.84	1850	L/1000	0.94 t

The modal combination is performed using the first and the second mode shape, for a length of 1850mm. The buckling modes and the modal participation of the first and second modes are illustrated in Figure 5.1, and details about mode composition and critical loads are exposed in Table 5.2. The critical load and the modal shapes are given by the FStr Computer Application Program. The modal participation percentages are given by the CUFISM computer program, confirming, in addition, the same critical loads and modes for FStr and CUFISM results (see subsection 3.2 Elastic Buckling Analysis Validation).

Table 5.2. Critical load and modal buckling participation for first and second mode of LC 100x70x15x2.70.

Mode		Critical Load	Half-wave	Modal Participation (CUFISM Vector Norm)				
Type	Shape			Mode #	Global	Distortional	Local	Other
		[#]	[kN]	[#]	[%]	[%]	[%]	[%]
First Mode	Global	1°	354.5	1	88.6%	11.0%	0.3%	0.1%
Second Mode	Distortional	2°	356.2	4	1.6%	95.8%	2.4%	0.1%

It can be noted that the first mode (Figure 5.1-a) is clearly a “global”, which is more precisely defined as a flexural-torsional mode. In this case, the D-G buckling interaction is mainly focused in the distortional-flexural-torsional (D-FT) interaction of lipped channel cross sections. In order to study additional D-G buckling interaction, such as flexural-distortional and torsional-distortional coupled phenomena, it is required another geometric cross section that exhibit the flexural or torsional buckling mode, in transition with the distortional mode. Also, the first and second buckling modes (Figure 5.1) are not pure modes, since they are obtained with the signature curve.

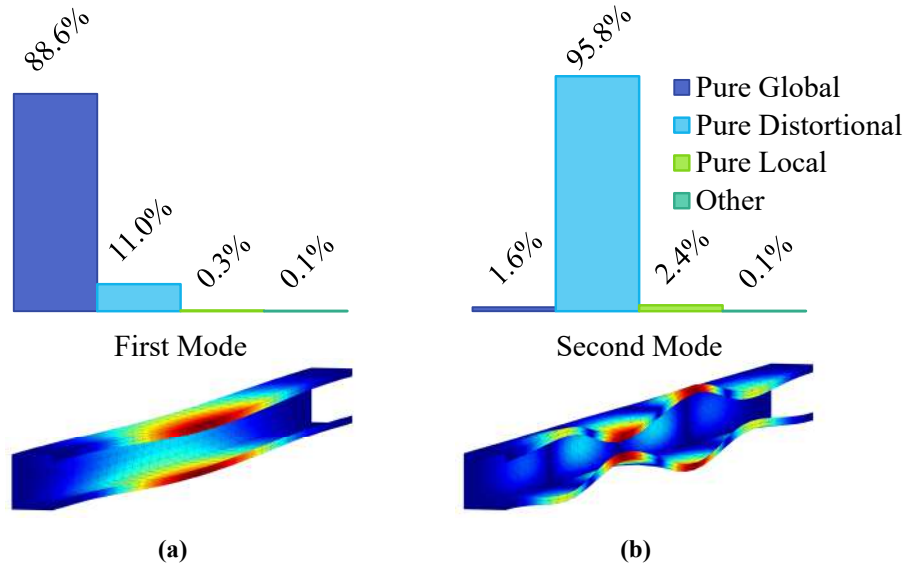


Figure 5.1. Modal buckling participation of (a) first (flexural-torsional) and (b) second mode (distortional) given by CUFSM Vector Norm.

Table 5.3 shows the slenderness factors, the ratios between slenderness factors and the column strength computed with the direct strength method for both distortional and global buckling, for each value of the yield stress and geometry described in Table 5.1.

Table 5.3. Slenderness, ratios and DSM strength of LC 100x70x15x2.70 at different yield stress.

f_y [MPa]	λ_L	λ_D	λ_G	$R_{\lambda GD}$	$R_{\lambda DL}$	P_y/P_{cr}	P_{nD} [kN]	P_{nG} [kN]
345	0.69	0.82	0.83	1.00	1.20	0.7	208.6	181.6
508	0.83	1.00	1.00	1.00	1.20	1.0	266.8	233.6
1016	1.18	1.41	1.42	1.00	1.20	2.0	392.1	307.1
1523	1.44	1.73	1.73	1.00	1.20	3.0	480.6	310.9
Inf.	Inf.	Inf.	Inf.	1.00	1.20	Elastic	-	-

In Table 6.3: λ_L , λ_D and λ_G are the local, distortional and global slenderness factor given in Eq. (2.62), Eq. (2.63) and Eq. (2.61), respectively; $R_{\lambda_{GD}} = \lambda_G/\lambda_D$ is the ratio between λ_G and λ_D ; $R_{\lambda_{DL}} = \lambda_D/\lambda_L$ is the ratio between λ_D and λ_L , given by Eq. (2.68); P_y/P_{cr} is the ratio between the squash load over the minimum critical load (in this case of True D-G buckling interaction, $P_{crD} \approx P_{crG}$); P_{nD} and P_{nG} are the nominal axial strength given by DSM for distortional and global buckling, given by Eq. (2.63) and Eq. (2.61), respectively.

According to Matsubara, Batista and Salles [100], for values of $R_{\lambda_{DL}}$ higher than 1.20, the L-D buckling interaction will not develop. Also, notice that the proposed L-D interaction equation Eq. (2.65), and its coefficients expressed in Eq. (2.66) and Eq. (2.67), converts to the pure distortional Winter-type equation when $R_{\lambda_{DL}} \geq 1.05$. Based on the ratio values in Table 5.3, $R_{\lambda_{DL}} = 1.2$ and $R_{\lambda_{GD}} = 1.0$, probably True D-G buckling interaction will occur.

Now, related to the modal combination, it is carried out using the displacement field ($\{u \ v \ w\}^T$) obtained in the finite strip method, Eq. (2.1), and combining linearly the first and second mode displacements. Equation (6.1) shows the linear combination of the displacements. These displacements are obtained from the eigenvectors $[\Phi]$, given by the eigenvalue equation, Eq. (2.38). The matrix of the critical modal shapes $[\Phi]$ represents the nodal line displacements for the degrees of freedom shown in Figure 2.6-b for each mode. This means that each column of the matrix $[\Phi]$ represents the critical modal shape for one mode. In order to obtain the displacement field on any point inside each strip, Eq. (2.1) performs the linear transformation from the nodal line solution to the displacement field, with assistance of the shape function matrix $[N]$, Eq. (2.2).

$$\begin{Bmatrix} u \\ v \\ w \end{Bmatrix} = \beta_1 \begin{Bmatrix} u \\ v \\ w \end{Bmatrix}_{Mode\ 1} + \beta_2 \begin{Bmatrix} u \\ v \\ w \end{Bmatrix}_{Mode\ 2} . \quad (6.1)$$

Since the displacement field is normalized, with maximum displacement of 1.0, the coefficients β_1 and β_2 are the parameters of amplification of these shapes. These parameters are defined in Eq. (6.2), where: $C1 = \cos(\theta)$; $C2 = \sin(\theta)$; θ is an angle for changing the modal combination; A_1 and A_2 are the maximum amplitude for initial geometric imperfection, for the first and second mode respectively.

$$\beta_1 = \frac{C_1}{|C_1| + |C_2|} A_1, \quad \beta_2 = \frac{C_2}{|C_1| + |C_2|} A_2. \quad (6.2)$$

It should be noted that Eq. (6.2) shows a combination of the maximum amplitude for the initial imperfection. When $\theta = 0^\circ$, then, $\beta_1 = A_1$ and $\beta_2 = 0$, on the other hand, when $\theta = 90^\circ$, then, $\beta_1 = 0$ and $\beta_2 = A_2$. Basically, the parameter θ is a single parameter that allows changing the initial geometric imperfections and consequently the modal combination shape. In order to illustrate the modes combination, Figure 5.2 shows the product C_1A_1 and C_2A_2 varying in a “trigonometric ellipse”. This idea of combining the buckling modes in a “trigonometric ellipse” is inspired in a similar procedure proposed by Martins *et al.* [82].

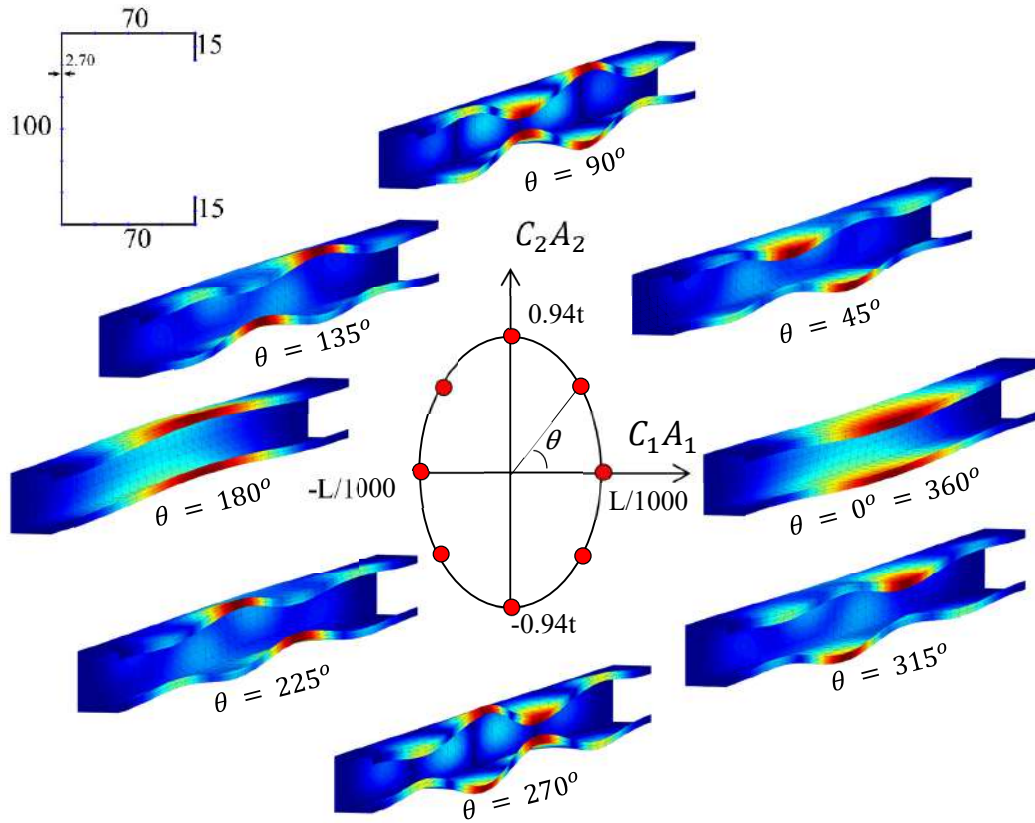


Figure 5.2. Analogy of modal shape initial imperfection combination in function of θ initial imperfection parameter (modal shapes amplified 10 times).

The maximum amplitude for the initial geometric imperfection, which is $A_1 = L / 1000$ and $A_2 = 0.94 t$, are chosen based on studies from Martins *et al.* [82] and Schafer and Peköz [142]. Regard to these amplitudes, Table 5.4 provides the percentage

of each initial imperfection, in function of the θ initial imperfection parameter. This table shows the mode contribution changing from 100% to -100% for each mode, but with a total modulus summation of 100%. Basically, the negative percentage of the mode represents a modal combination in opposite modal shape. Thereby, all the possible cases are combined.

Notice in Table 5.4 that there is a type of symmetry on combining the imperfections. Basically, the columns with initial geometric imperfection combination from $\theta = 0^\circ$ until $\theta = 180^\circ$ (first and second quadrant) are the same columns with $\theta = 180^\circ$ until $\theta = 360^\circ$ (third and fourth quadrant). This symmetry behavior can be easily seen through a graph of ultimate load versus the θ parameter. For this case only, the 24 columns with initial imperfections of Table 5.4 are modeled with yield stress of 345 MPa. The graph displaying the ultimate load variation is shown in Figure 5.3.

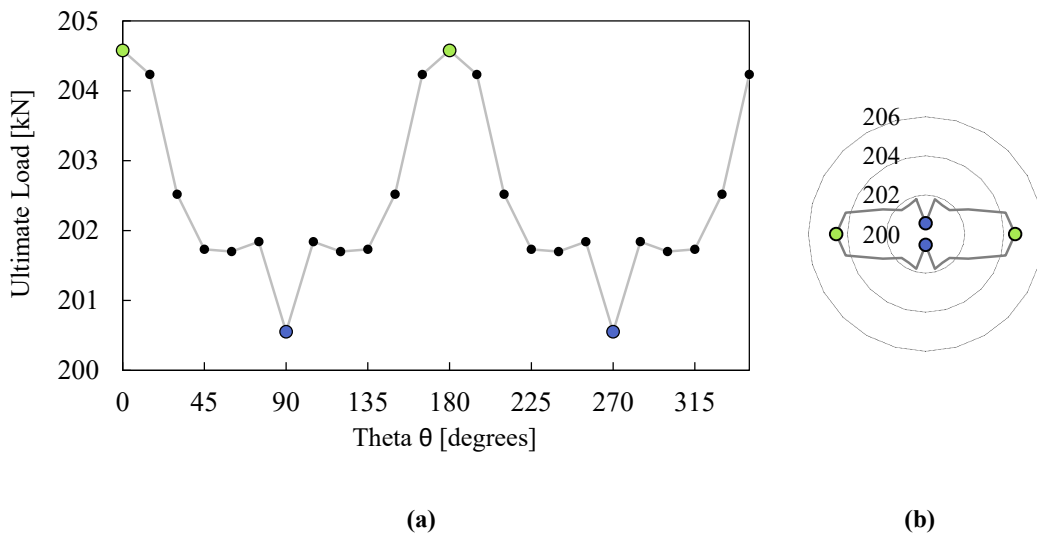


Figure 5.3. Ultimate load versus θ parameter for 345 MPa: (a) cartesian system; (b) polar system.

Figure 5.3-a shows clearly a cyclic behavior of the ultimate load. Also, in Figure 5.3-b it can be seen the symmetry of the behavior in the first quadrant. Basically, the behavior from the first and second quadrant are the same as the third and fourth. Another way to see this cyclic behavior can be done with the deformed columns at the ultimate load step displayed in Figure 5.4.

Table 5.4. Absolute value of initial geometric imperfection amplification parameters and their correspondent percentage.

Theta	MODE*	β_1	β_2	% Mode 1	% Mode 2	Name
<i>[Degrees]</i>		<i>[mm]</i>	<i>[mm]</i>	<i>[%]</i>	<i>[%]</i>	
0	G (+)	1.85	0.00	100%	0%	1G+0D
15	DG (+)	1.46	0.54	79%	21%	0.8G+0.2D
30	DG (+)	1.17	0.93	63%	37%	0.6G+0.4D
45	DG (+)	0.93	1.27	50%	50%	0.5G+0.5D
60	DG (+)	0.68	1.61	37%	63%	0.4G+0.6D
75	DG (+)	0.39	2.00	21%	79%	0.2G+0.8D
90	D (+)	0.00	2.54	0%	100%	0G+1D
105	DG (-)	-0.39	2.00	-21%	79%	-0.2G+0.8D
120	DG (-)	-0.68	1.61	-37%	63%	-0.4G+0.6D
135	DG (-)	-0.93	1.27	-50%	50%	-0.5G+0.5D
150	DG (-)	-1.17	0.93	-63%	37%	-0.6G+0.4D
165	DG (-)	-1.46	0.54	-79%	21%	-0.8G+0.2D
180	G (-)	-1.85	0.00	-100%	0%	-1G+0D
195	DG (+)	-1.46	-0.54	-79%	-21%	-0.8G-0.2D
210	DG (+)	-1.17	-0.93	-63%	-37%	-0.6G-0.4D
225	DG (+)	-0.93	-1.27	-50%	-50%	-0.5G-0.5D
240	DG (+)	-0.68	-1.61	-37%	-63%	-0.4G-0.6D
255	DG (+)	-0.39	-2.00	-21%	-79%	-0.2G-0.8D
270	D (-)	0.00	-2.54	0%	-100%	0G-1D
285	DG (-)	0.39	-2.00	21%	-79%	0.2G-0.8D
300	DG (-)	0.68	-1.61	37%	-63%	0.4G-0.6D
315	DG (-)	0.93	-1.27	50%	-50%	0.5G-0.5D
330	DG (-)	1.17	-0.93	63%	-37%	0.6G-0.4D
345	DG (-)	1.46	-0.54	79%	-21%	0.8G-0.2D

* Modal shape of the initial geometric imperfection, where (+) is the modal shape in original form and (-) is the modal shape multiplied by -1.

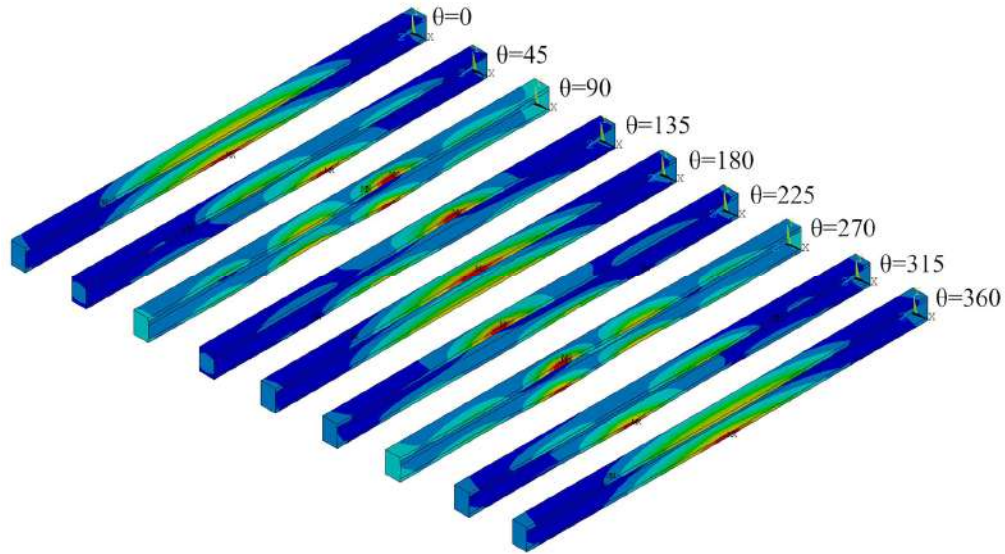
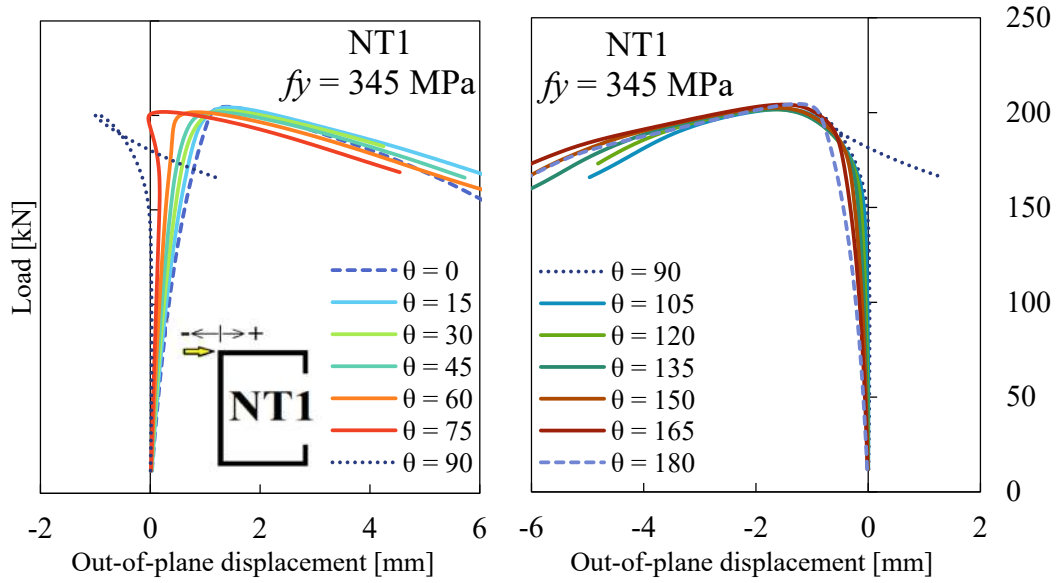


Figure 5.4. Maximum vector displacement at the limit load (or column strength) step for $\theta = 0^\circ$ to 360° , incremented by 45° .

Note that in Figure 5.4 that the maximum displacement at ultimate load step changes based on the initial geometric imperfection shape. This shows the sensitivity of the column structural behavior depending on the initial geometric imperfection shape. Also, the cyclic behavior of the maximum displacement, from a global failure to a distortional one, is even clearer to notice. The maximum displacement cycle starts at mid span at the top flange and moves to the nearest distortional maximum half-wave deformation (around 40% of the maximum length). From that, the maximum displacement “jumps” to the bottom flange, with a distortional shape collapse. From that point, the maximum displacement moves to the mid span again, but at the bottom flange and, after that, the cycle repeats. Those modal shapes on the column strength step shows that an analysis from $\theta = 0^\circ$ until $\theta = 180^\circ$ is already enough to perform a D-G interaction investigation.

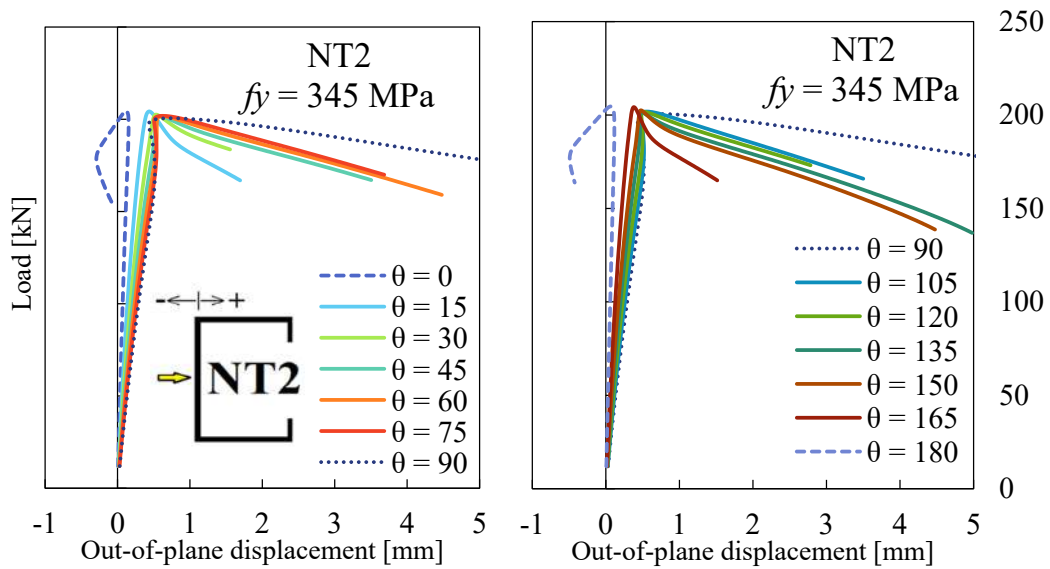
However, it is noticed another cyclic and symmetric behavior for θ in first and second quadrant. To conclude complete description of the relation between buckling modes combination (definition of the initial geometric imperfection) and the collapse mechanism, deeper analysis based on accurate observation of the equilibrium paths of the columns is required to avoid mistaken conclusions. In this case, the post-buckling equilibrium paths for $\theta = [0^\circ, 180^\circ]$, spaced with an increment of 15° , are illustrated below in Figure 5.5, Figure 5.6, Figure 5.7, Figure 5.8 and Figure 5.9. Each figure reveals the FEM results of the post-buckling paths for a different point in the cross-section.



(a)

(b)

Figure 5.5. Post-buckling equilibrium paths, load steps vs. out-of-plane displacement NT1, with $f_y = 345 \text{ MPa}$ and $P_{cr} = 354.5 \text{ kN}$ ($P_y/P_{cr} = 0.7$) at $0.4L$, from (a) $\theta = [0^\circ, 90^\circ]$ and (b) $\theta = [90^\circ, 180^\circ]$.



(a)

(b)

Figure 5.6. Post-buckling equilibrium paths, load steps vs. out-of-plane displacement NT2, with $f_y = 345 \text{ MPa}$ and $P_{cr} = 354.5 \text{ kN}$ ($P_y/P_{cr} = 0.7$) at $0.4L$, from (a) $\theta = [0^\circ, 90^\circ]$ and (b) $\theta = [90^\circ, 180^\circ]$.

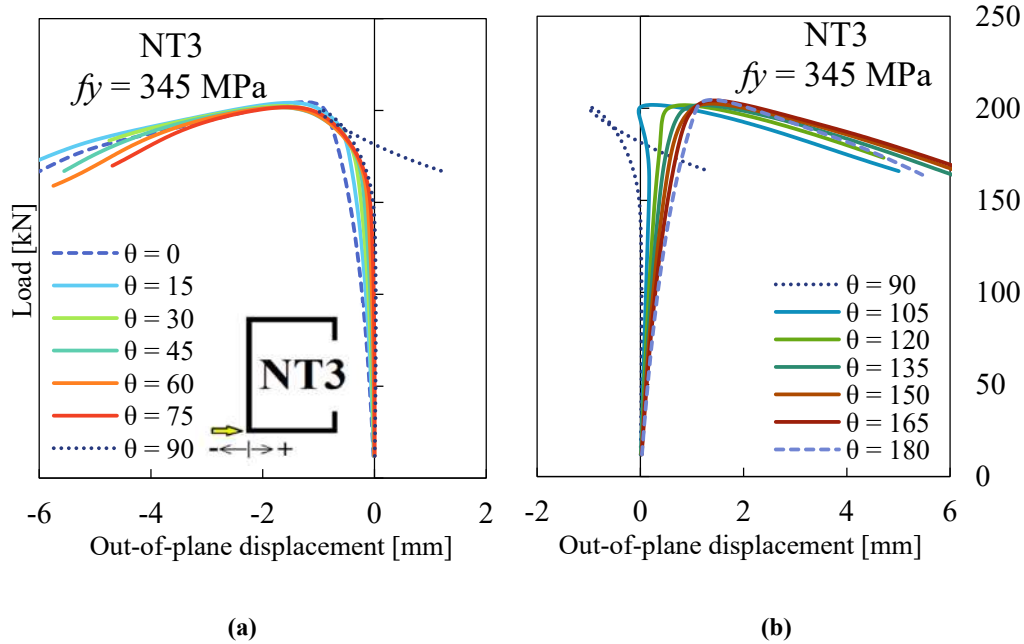


Figure 5.7. Post-buckling equilibrium paths, load steps vs. out-of-plane displacement NT3, with $f_y = 345 \text{ MPa}$ and $P_{cr} = 354.5 \text{ kN}$ ($P_y/P_{cr} = 0.7$) at $0.4L$, from (a) $\theta = [0^\circ, 90^\circ]$ and (b) $\theta = [90^\circ, 180^\circ]$.

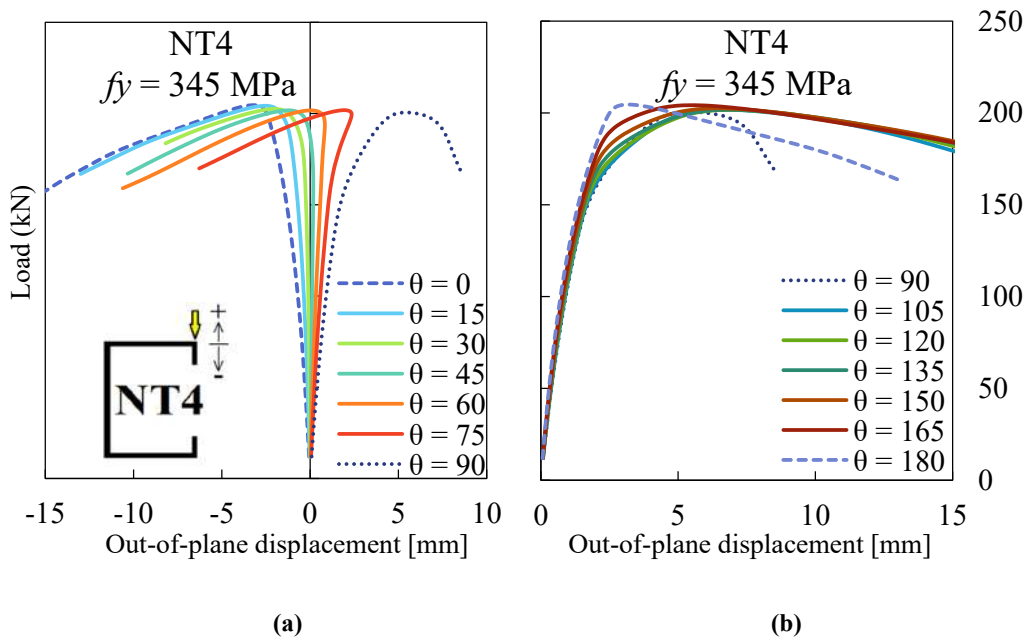


Figure 5.8. Post-buckling equilibrium paths, load steps vs. out-of-plane displacement NT4, with $f_y = 345 \text{ MPa}$ and $P_{cr} = 354.5 \text{ kN}$ ($P_y/P_{cr} = 0.7$) at $0.4L$, from (a) $\theta = [0^\circ, 90^\circ]$ and (b) $\theta = [90^\circ, 180^\circ]$.

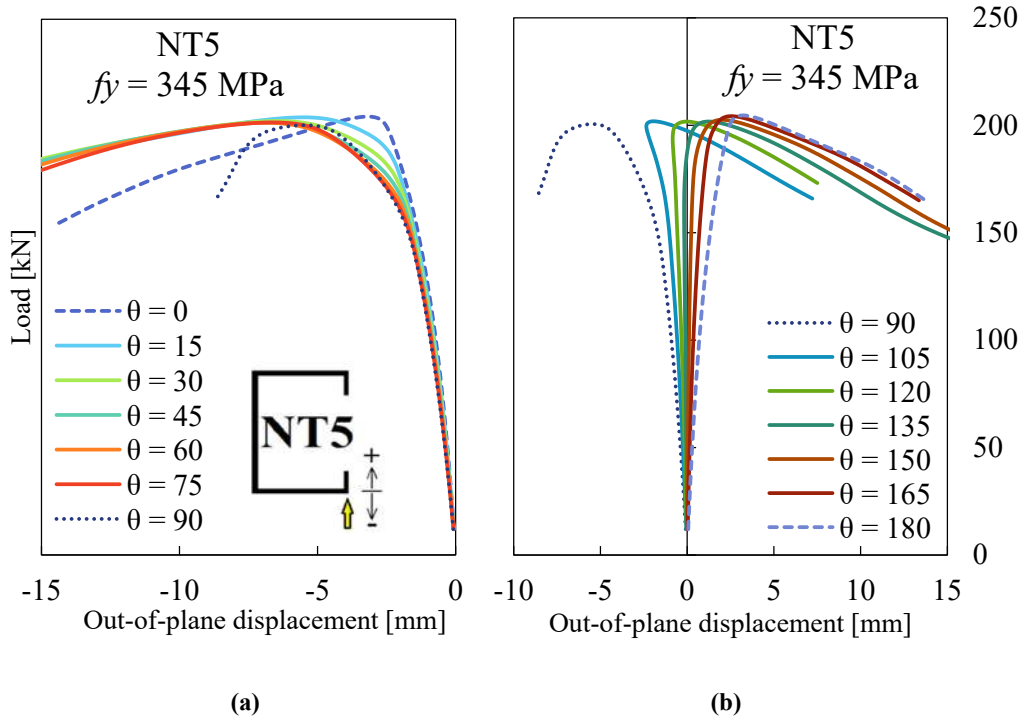


Figure 5.9. Post-buckling equilibrium paths, load steps vs. out-of-plane displacement NT5, with $f_y = 345 \text{ MPa}$ and $P_{cr} = 354.5 \text{ kN}$ ($P_y/P_{cr} = 0.7$) at $0.4L$, from (a) $\theta = [0^\circ, 90^\circ]$ and (b) $\theta = [90^\circ, 180^\circ]$.

Comparing the post-buckling paths, a symmetric behavior between the initial imperfections with $\theta = [0^\circ, 90^\circ]$ and $\theta = [90^\circ, 180^\circ]$, is detected. Analyzing the NT1 and NT3 displacements, Figure 5.5 and Figure 5.7 respectively, it is found that the initial imperfections with $\theta = [0^\circ, 90^\circ]$ for the NT1 displacement, has the same behavior as the initial imperfection with $\theta = [90^\circ, 180^\circ]$ for the NT3 displacement, as well as vice-versa. The same behavior happens comparing the displacement NT4 and NT5. While for the NT2 displacement, it has a symmetric behavior between its initial imperfection with $\theta = [0^\circ, 90^\circ]$ and $\theta = [90^\circ, 180^\circ]$. Basically, this symmetric behavior evidences a “mirroring” behavior of the initial imperfection with θ from the first and second quadrant. This conclusion supports the parametric analysis of a large set of columns, to be conducted only with the initial imperfection for $\theta = [0^\circ, 90^\circ]$.

5.1.1 Imperfection Combination with different yield stress

The next step is to investigate columns with higher yield strength. The same analysis conducted for columns with 345 MPa ($P_y/P_{cr} = 0.7$) yield stress, are performed

for columns with 508 MPa ($P_y/P_{cr} = 1.0$), 1016 MPa ($P_y/P_{cr} = 2.0$), 1523 MPa ($P_y/P_{cr} = 3.0$) and an elastic behavior analysis ($P_y/P_{cr} \rightarrow \infty$), taking $\theta = [0^\circ, 90^\circ]$. The results for these analysis are shown in APPENDIX B, and the table with slenderness, ratios and DSM strength, is shown in Table 5.3.

In order to visualize and compare the influence of each yield strength in the column structural behavior, the post-buckling equilibrium paths are presented, for only one type of initial imperfection combination. These results are shown in Figure 5.10, Figure 5.11, Figure 5.12 and Figure 5.13, for $\theta = 0^\circ, 45^\circ, 75^\circ$ and 90° , respectively, related to NT5 displacement. Results with $\theta = 15^\circ, 30^\circ$ and 60° are in APPENDIX B. Those figures also show the deformed column at the ultimate load with equivalent stress contour plots, related to the von Mises yield criterion (the red areas represent the material reached to yielding condition). The color scale is proportional to the yield stress of each column.

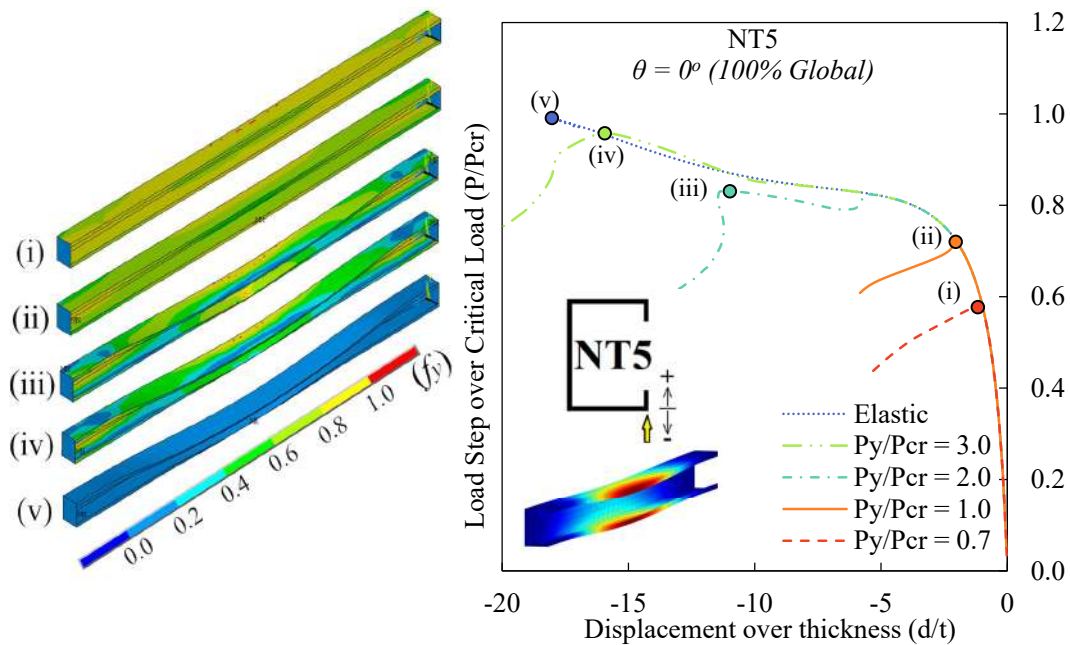


Figure 5.10. Post-buckling equilibrium paths, P/P_{cr} vs. d/t of displacement NT5 at $0.4L$, with $\theta = 0^\circ$ (100% Global mode), for different ratios of P_y/P_{cr} , where $P_{cr} = 354.5 \text{ kN}$ and $t = 2.70 \text{ mm}$.

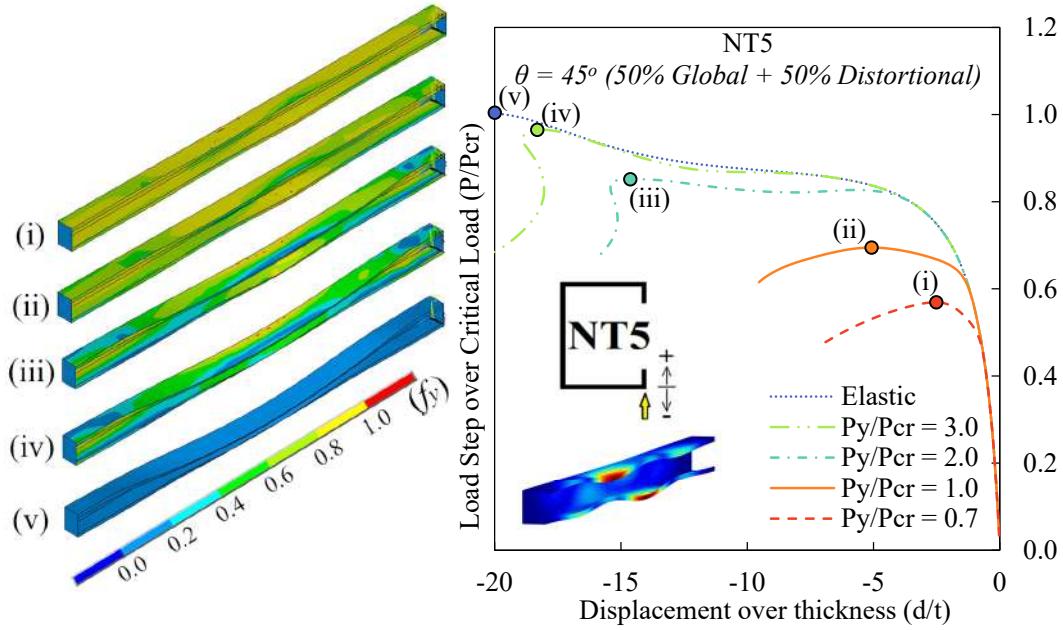


Figure 5.11. Post-buckling equilibrium paths, P/P_{cr} vs. d/t of displacement NT5 at $0.4L$, with $\theta = 45^\circ$ (50% Global and 50% Distortional mode), for different ratios of P_y/P_{cr} , where $P_{cr} = 354.5 \text{ kN}$ and $t = 2.70 \text{ mm}$.

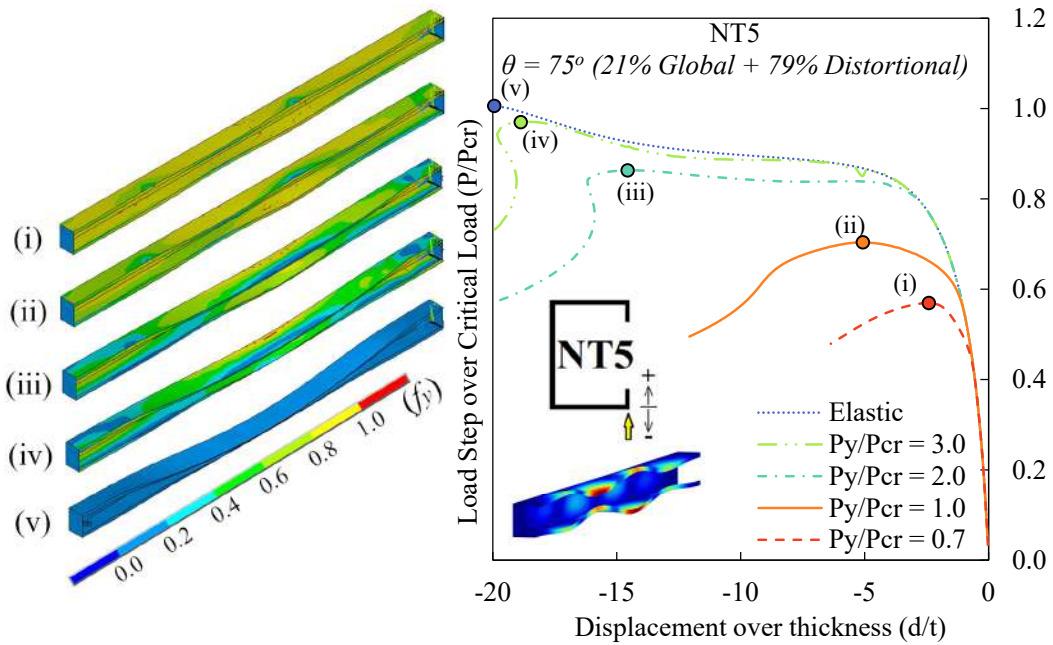


Figure 5.12. Post-buckling equilibrium paths, P/P_{cr} vs. d/t of displacement NT5 at $0.4L$, with $\theta = 0^\circ$ (21% Global and 79% Distortional mode), for different ratios of P_y/P_{cr} , where $P_{cr} = 354.5 \text{ kN}$ and $t = 2.70 \text{ mm}$.

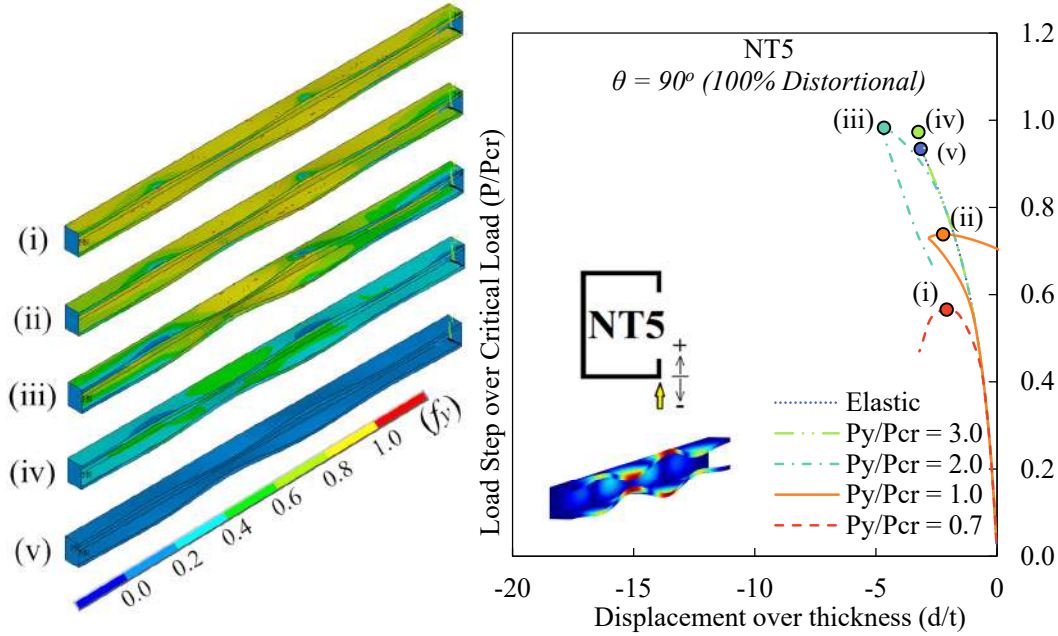


Figure 5.13. Post-buckling equilibrium paths, P/P_{cr} vs. d/t of displacement NT5 at $0.4L$, with $\theta = 90^\circ$ (100% Distortional mode), for different ratios of P_y/P_{cr} , where $P_{cr} = 354.5 \text{ kN}$ and $t = 2.70 \text{ mm}$.

Firstly, note that all equilibrium paths follow the elastic behavior until a bifurcation point. Specifically, for $\theta = 0^\circ$ (100% global initial geometric imperfection, Figure 5.10) the bifurcation point is located on the elastic path for $P_y/P_{cr} \leq 1.0$. Clearly, the stability behavior for $\theta = [0^\circ, 75^\circ]$ (see Figure 5.10, Figure 5.11 and Figure 5.12) - which means only global and mixed global + distortional initial geometric imperfection - shows a transition behavior, while, surprisingly, for only distortional initial imperfection ($\theta = 90^\circ$, Figure 5.13), the behavior is quite unique, with a smaller maximum displacement. This singular behavior is probably affected by an absence of the global mode, and also because the position of $0.4L$ does not coincide to the cross section with maximum displacement of the distortional modal shape. Furthermore, for θ initial imperfection combination parameter near to 90° , the ultimate load happens on higher displacements, but for $\theta = 90^\circ$ (distortional only initial geometric imperfection), the ultimate load happens in small displacements. Unfortunately, the finite element model with initial imperfection of $\theta = 90^\circ$ did not converge for higher squash load.

Evidently, all the elastic columns behave in global mode for higher displacements (except for columns with only distortional initial geometric imperfection, Figure 5.13). While for columns with lower yield strength, the distortional mode has a chance to behave

in the beginning of the loading process, when the distortional initial imperfection has a significant influence (see Figure 5.12).

The yielding is more common on columns with lower yielding stress over critical stress ratios, which was already expected. Moreover, it is noticed that for columns with more global initial geometric imperfection, the yield of the material is symmetric and more concentrated at mid span. Whereas for columns with more distortional initial imperfection, the yielding process is more distributed.

Now, comparing the strength of these columns with different initial geometric imperfection combination and different yield strength, it is possible to notice which initial imperfection has more influence in the column's load capacity. Figure 5.14 shows the column strength vs. squash load, normalized with critical load in both axes.

As it was expected, in Figure 5.14, for more elastic columns, the ultimate load increases. For $P_y/P_{cr} = 0.7$, the lower ultimate load occurs with only distortional initial imperfection ($\theta = 90^\circ$). However, for $P_y/P_{cr} = 1.0$, the most detrimental load takes place with 50% of global and 50% of distortional mode contribution ($\theta = 45^\circ$ or 0.5G+0.5D) of initial imperfection. Moreover, for high yield stress, the lower ultimate load is affected with only by global initial imperfection ($\theta = 0^\circ$).

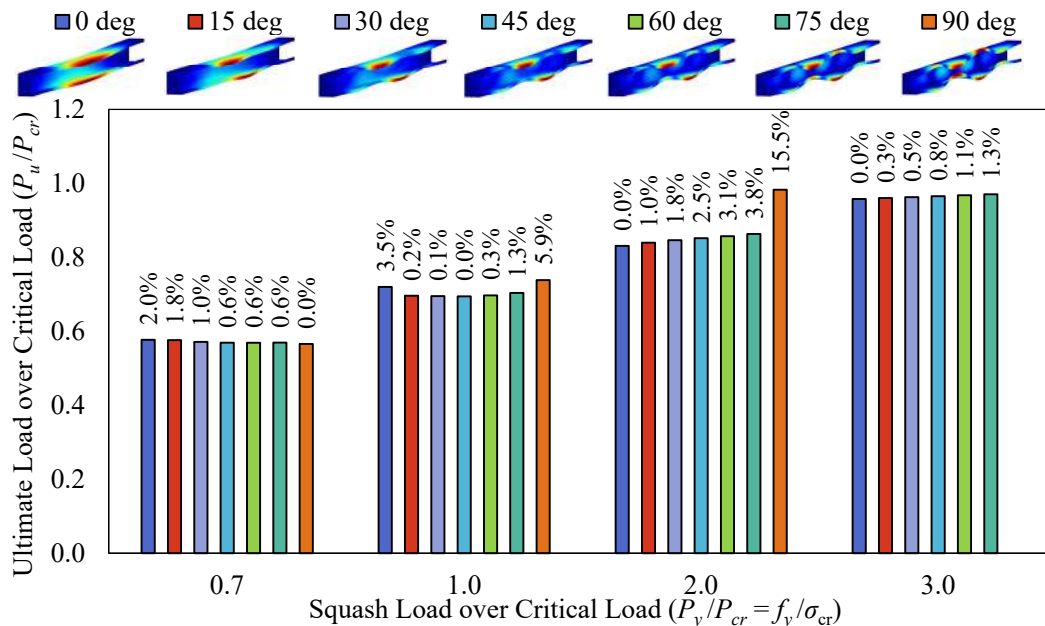


Figure 5.14. P_u/P_{cr} vs. P_y/P_{cr} of columns under different initial geometric imperfection combination, $\theta = [0^\circ, 90^\circ]$ and with yield strength of 345 MPa, 508 MPa, 1016 MPa and 1523 MPa.

Basically, the proposed study of initial geometric imperfection combination allowed a deep understanding of the complex behavior of the True D-G buckling interaction (TI). It has shown that the different initial imperfection combination affects the ultimate load and structural behavior for a column under the TI D-G buckling interaction nature. Now, it is important to study the behavior of the D-G buckling interaction behaves with different type of their nature¹³. The following study consists of evaluating the performance of the load capacity of columns in Secondary-distortional bifurcation D-G interaction (SDI) and Secondary-global bifurcation D-G interaction (SGI) regions.

5.2 Study of D-G buckling interaction nature

This study consists in investigating columns with different slenderness factors, in order to understand the influence of the interaction nature in the column strength. For this study the section LC 100x70x15x2.70 mm is considered, the same geometry employed in the initial geometric imperfection combination analysis. However, the length of the column is diversified, from 1500 to 2200 mm, with an increment step of 50 mm. This changing of column's length permits a modification of the global and distortional slenderness ratios and its contribution on the column behavior.

Basically, the investigation is performed for columns with the three different natures: secondary-global bifurcation D-G interaction (SGI), true D-G interaction (TI) and secondary-distortional bifurcation D-G interaction (SDI). In the sense of illustrating graphically the D-G interaction nature investigation, Figure 5.15 shows the signature curve in contrast with the pure local, distortional and global buckling mode curves. Figure 5.15 displays the same analysis illustrated in Figure 2.13, however, Figure 5.15 shows the signature curve in function of the D-G slenderness ratio, $R_{\lambda GD} = \lambda_G / \lambda_D = \sqrt{P_{crD} / P_{crG}}$. This ratio measures how far the critical loads of global and distortional modes are from each other. According to Martins *et al.* [82], when $0.95 < R_{\lambda GD} < 1.05$ there is TI, $R_{\lambda GD} \geq 1.05$ there is SDI and $R_{\lambda GD} \leq 0.95$ there is SGI (where $R_{\lambda GD} = \sqrt{1/R_{GD}}$, since

¹³ The types of D-G coupled phenomenon natures studied at this research is well commented in subsection 2.5.1 (Distortional-Global Interaction concepts).

this author employs $R_{GD} = P_{crG} / P_{crD}$ as the main factor for the evaluation of D-G buckling interaction).

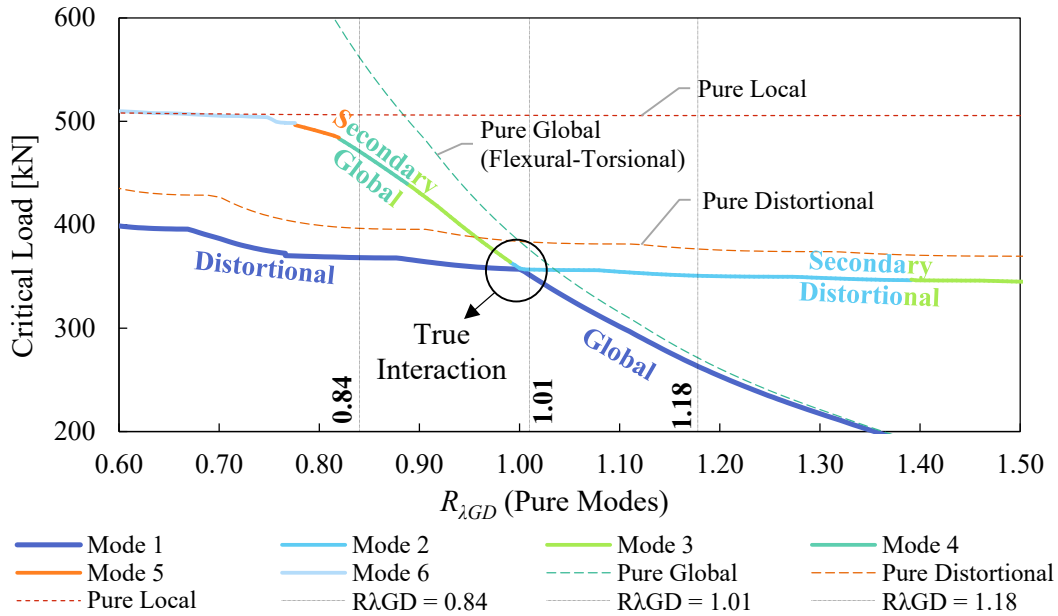


Figure 5.15. Critical load vs. $R_{\lambda_{GD}}$ for LC 100x70x15x2.70 mm, illustrating SGI, TI and SDI regions in all mode analysis (signature curve) and pure mode analysis.

Notice in Figure 5.15 that $R_{\lambda_{GD}} = 0.84$ represents the length of 1500 mm, $R_{\lambda_{GD}} = 1.10$ is correlated with length of 1850 mm and $R_{\lambda_{GD}} = 1.18$ is associated with length of 2200 mm. As can be observed, the range of SGI and SDI is not that extensive, because the analysis is limited to only one cross-section geometry. For a deeper understanding of the D-G buckling interaction nature, it would be necessary a wider variety of cross-section geometries (larger $R_{\lambda_{GD}}$ range). The analysis performed in this research is focused on the TI nature, with fewer columns in the SGI and SDI regions.

Before starting the parametric analysis, it is important to define the initial geometric imperfection. In this investigation, two different types of initial geometric imperfection are concerned: 100% Global (1G+0D) buckling mode initial imperfection and 50% Distortional + 50% Global buckling mode initial imperfection (0.5G+0.5D). The reason of adopting these two initial imperfections is based on the results from the last study in the subsection 5.1 (Study of Initial Geometric Imperfection Combination). Founded on that study, it is concluded that for columns with higher yield strength, 1G+0D mode presents the lower ultimate column capacity. However, for columns with lower yield strength, the 0.5G+0.5D mode combination can give the lower column strength.

These results revealed that a parametric study taking both initial imperfections could indicate a difference in the column's strength, and consequently, some unconformity with the Direct Strength Method (DSM).

As a result of the initial geometric imperfection combination analysis, the following parametric study consists of using two different initial geometric imperfection (1G+0D and 0.5G+0.5D) for three different yielding stress, 345 MPa, 508 MPa and 1016 MPa, *i.e.* applying 1G+0D with the three yield stress, and 0.5G+0.5D with also the three yield stress. For each of these yield stresses, the column strength capacity is reached, for 15 lengths (from 1500 mm to 2200 mm with increment step of 50 mm), and compared with the actual distortional (Eq. (2.63)) and global direct strength method (Eq. (2.61)). In addition, the strength is also compared to the proposed D-G buckling interaction equations, proposed by Schafer [95] (Eq. (2.69)) and by Martins *et al.* [82] (Eq. (2.70)).

To sum up, 15 columns with different lengths, 3 types of yield stress and 2 different initial geometric imperfection, totalizing 90 columns, are analyzed. The critical loads, slenderness factors, ultimate loads and nominal axial strength for the 90 columns are reported in APPENDIX C. With the purpose of a clear data visualization, Figure 5.16, Figure 5.17 and Figure 5.18 illustrates graphically all the columns strength compared with normative equations, divided into its yielding and initial geometric imperfection. Each graph shows a comparison with the distortional (Eq. (2.63)), global (Eq. (2.61)), distortional-global (Eq. (2.69)) and global-distortional (Eq. (2.70)) equations. More specifically, Figure 5.16 shows the results for 345 MPa, Figure 5.17 displays the results for 508 MPa and Figure 5.18 reveal the results for 1016 MPa.

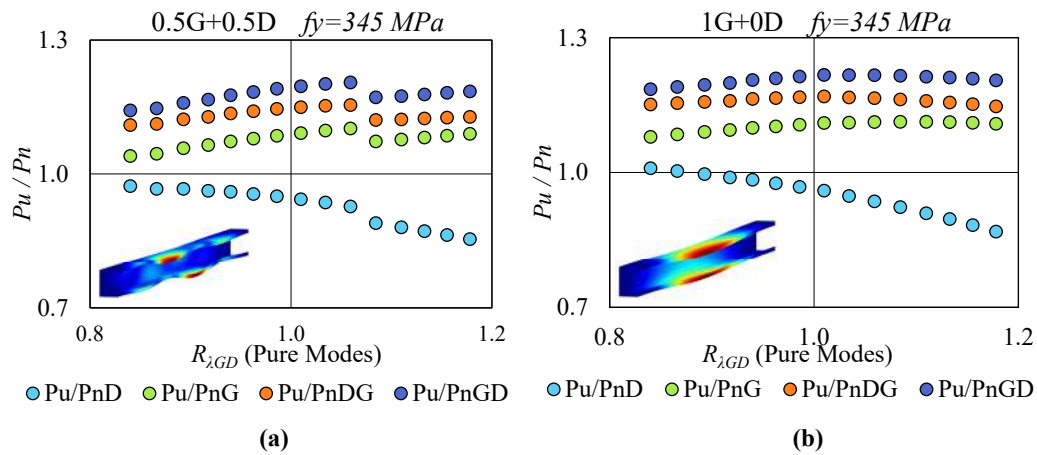


Figure 5.16. Ultimate Load over Nominal Axial Strength vs D-G slenderness ratio, for distortional (Eq. 2.63), global (Eq. 2.61), distortional-global (Eq. 2.69) and global-distortional (Eq. 2.70) DSM equations, with yielding of 345 MPa and (a) 0.5G+0.5D and (b) 1G+0D initial imperfection.

Several observations can be drawn from Figure 5.16. First of all, the strength equation global-distortional, P_{nGD} , (Eq. (2.70)) provides the most conservative approach, compared to the distortional-global (Eq. (2.69)) and global (Eq. (2.61)) equations, respectively P_{nDG} and P_{nG} . Secondly, the nominal axial strength for global buckling (Eq. (2.61)), gives explicit the lowest nominal strength, when compared to the nominal strength for distortional buckling, P_{nD} , (Eq. (2.63)), because all the P_u/P_{nD} data is below the P_u/P_{nG} data, and since the P_u value is constant for both cases, it means that P_{nD} is higher than P_{nG} . Thirdly, in Figure 5.16-a it is noticed a small discontinuous gap for all the P_u/P_n ratios ($R_{\lambda GD} \approx 1.07$). The reason for this gap refers to the half-wave switch from 4 to 5 waves, in the distortional buckling mode as initial geometric imperfection. Realize that this half-wave change interfered in the ultimate load, resulting in a slight reduction of the column strength. With respect to the type of initial imperfection, notice that the 1G+0D initial imperfection has showed a smoother changing of the ultimate load, without discontinuous gaps. Finally, another interesting observation is the variation of the ratio P_u/P_{nD} , which displays continuous decreasing related to the ratio $R_{\lambda GD}$. This illustrates the fact that the column is approaching a global critical buckling region, since it is “leaving” the distortional critical buckling region.

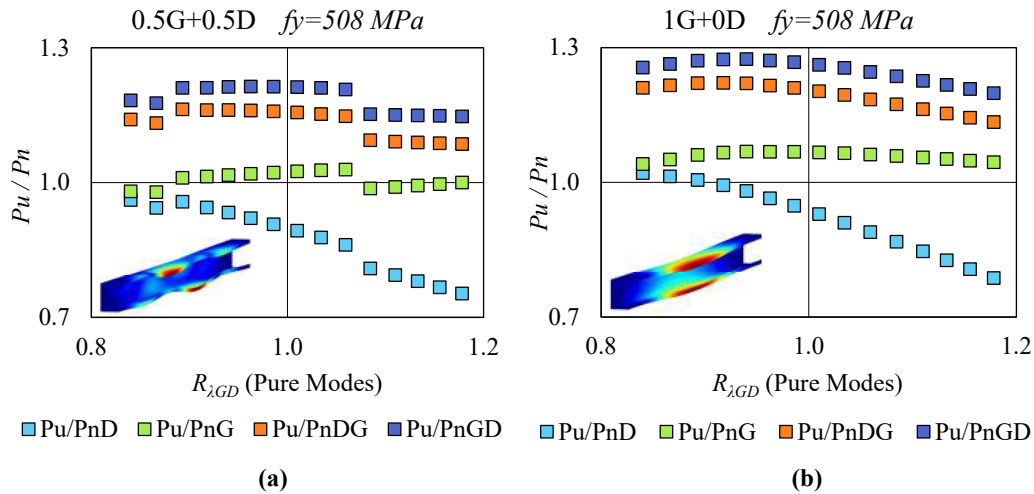


Figure 5.17. Ultimate Load over Nominal Axial Strength vs D-G slenderness ratio, for distortional (Eq. 2.63), global (Eq. 2.61), distortional-global (Eq. 2.69) and global-distortional (Eq. 2.70) DSM equations, with yielding of 345 MPa and (a) 0.5G+0.5D and (b) 1G+0D initial imperfection.

There are a few remarks concerning to the results for yield stress of 508 MPa, displayed in Figure 5.17, that analogous of those for yielding stress of 345 MPa in Figure 5.16. As reported by yielding of 345 MPa, the strength equation global-distortional P_{nGD} (Eq. (2.70)) provides the most conservative approach. Moreover, the nominal axial

strength for global buckling, P_{nG} , is lower than the P_{nD} equation, which according to the DSM, the global buckling mode is the one which governs the instability limit state of the structural element in all $R_{\lambda GD}$ range. Related to the initial geometric imperfection, the 1G+0D combination also has shown a softer changing of the ultimate load, without discontinuous gaps. As a final remark, the ratio P_u/P_{nD} has also demonstrated a similar behavior, as well as for yielding of 345 MPa. This undoubtedly emphasizes the assumption of the columns reaching to a global critical buckling region.

One important observation in Figure 5.17-a is the presence of two discontinuous gaps ($R_{\lambda DG} \approx 0.87$ and $R_{\lambda DG} \approx 1.07$). These gaps are related to the change of the half-wave number of the initial geometric imperfection for the distortional buckling mode. Notice that the first gap corresponds to the half-wave switch from 3 to 4 waves, and the second gap from 4 to 5 half-waves. It might be advisable to perceive that with even numbers of half-waves, there is a slight increase in the ultimate load. The possible reason for this strength rise is due to the initial imperfection maximum displacement. When the half-wave number is odd, the maximum displacement from global and distortional modes coincides in the same cross-section, which is at mid span. Consequently, the maximum initial imperfection amplitude from each mode amplifies the maximum total displacement in the column, which end up resulting in a lower column strength capacity.

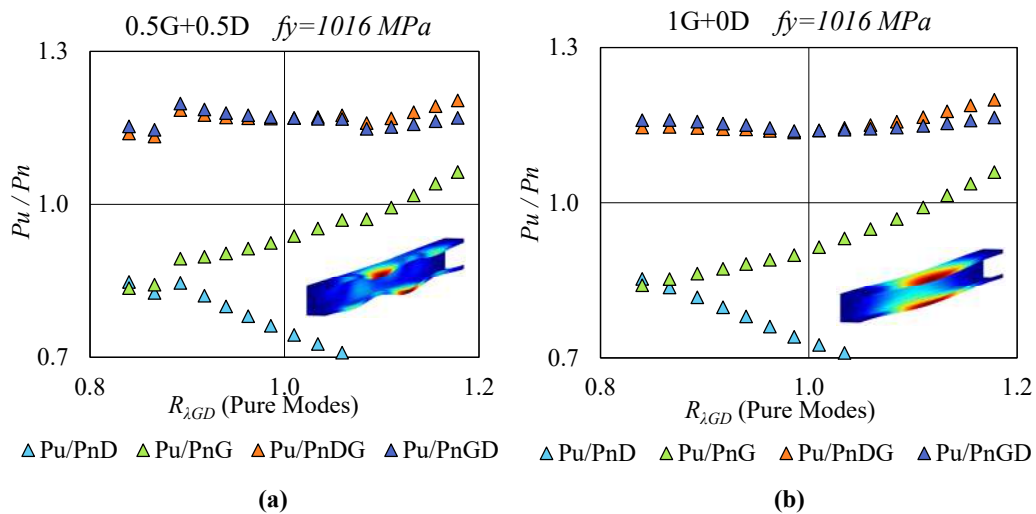


Figure 5.18. Ultimate Load over Nominal Axial Strength vs D-G slenderness ratio, for distortional (Eq. 2.63), global (Eq. 2.61), distortional-global (Eq. 2.69) and global-distortional (Eq. 2.70) DSM equations, with yielding of 345 MPa and (a) 0.5G+0.5D and (b) 1G+0D initial imperfection.

Even though the data results for yielding of 345 and 508 MPa are similar in some aspects, the results for yield stress of 1016 MPa, included in Figure 5.18, has shown a particular response. Since the columns with yield strength of 1016 MPa became further

elastic, the behavior of the ultimate load has changed. It is noticed that the ratio P_u/P_{nD} decreases faster when $R_{\lambda GD}$ is increased. Furthermore, the P_u/P_{nG} begins with 0.84 and speedily rise to 1.06 in both cases of initial geometric imperfection, showing that the ultimate load from the FEM approaches to the DSM global equation quickly. On the other hand, the distortional-global P_{nDG} (Eq. (2.69)) and global-distortional P_{nGD} (Eq. (2.70)) interaction equations seems to stabilize on a plateau, with no harsh changes.

So far, the FEM results data is analyzed with the four possible equations separately. In order to compare the ultimate load with the available standard DSM approach, Figure 5.19 provides a graphical illustration, where $P_{nDSM} = \min(P_{nLG}, P_{nD}, P_{nG})$, and P_{nLG} is given by Eq. (2.64), P_{nD} by Eq. (2.63) and P_{nG} by Eq. (2.61). Figure 5.19-a shows the results for 50% distortional + 50% global initial imperfection combination, and Figure 5.19-b exhibit the results for 100% global initial imperfection combination.

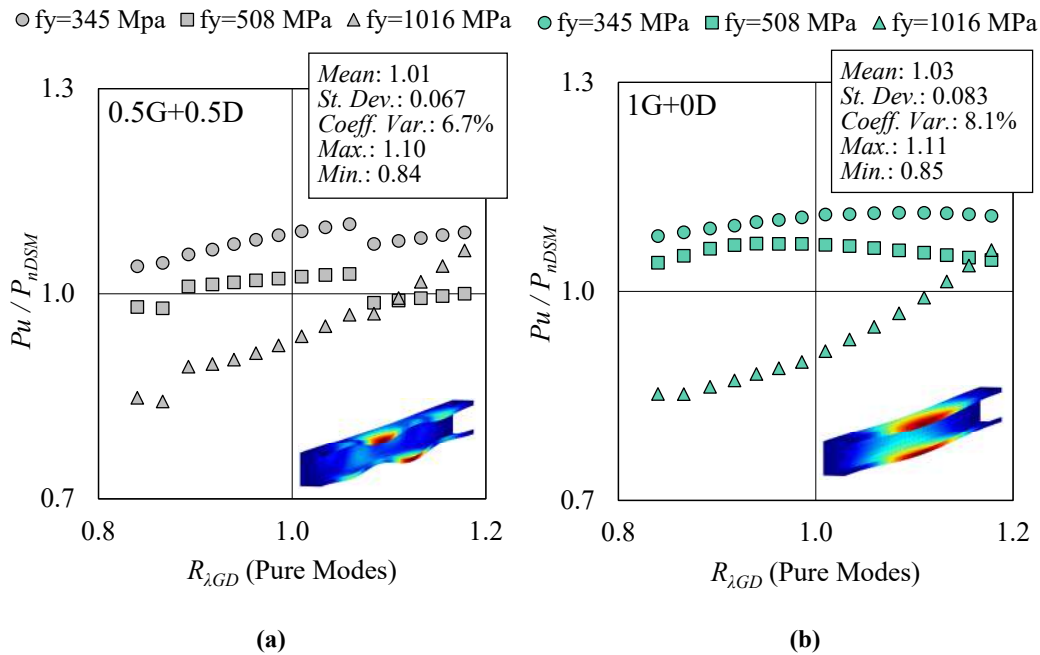


Figure 5.19. Ultimate Load over DSM Nominal Axial Strength versus D-G slenderness ratio, considering (a) 50% global + 50% distortional initial imperfection and (b) 100% global initial imperfection.

It is noticeable that as the larger is the elastic behavior range, corresponding to higher yielding stress, the lower is the P_u/P_{nDSM} ratio, for $R_{\lambda GD} < 1.08$ with 0.5G+0.5D initial geometric imperfection combination, and for $R_{\lambda GD} < 1.15$ with 1G+0D initial geometric imperfection combination. Additionally, these columns with lower values of

$R_{\lambda_{GD}}$ and higher yielding, seem to diverge from the original DSM equation, due to a possible high evidence of D-G buckling interaction in a secondary-global bifurcation D-G interaction (SGI) region. Lastly, comparing the two cases of initial imperfection combination, it is noticed that the mean, maximum and minimum value of P_u/P_{nDSM} ratio, are similar to each type of imperfection, while the 0.5G+0.5D initial imperfection combination presents the lower standard deviation and coefficient of variation.

Another approach to visualize the FEM results P_u in Figure 5.19, is to display the corresponding data into the traditional column strength design curve (P_u/P_y) versus global slenderness factor (λ_G), taking the nominal column strength equation (Eq. (2.61)), restricted to the global buckling mode. This graphical data illustration is exposed in Figure 5.20. This figure basically shows all the 90 columns strength over squash load ratio versus the global buckling slenderness factor, in addition with the global DSM equation and the Euler column curve for reference $1/\lambda_G^2$.

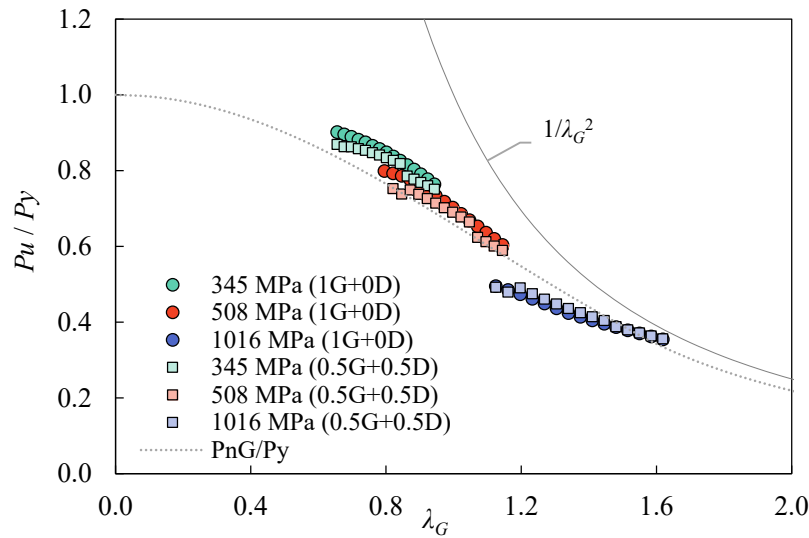


Figure 5.20. Column strength over Squash Load versus global slenderness factor for all the 90 FEM results for columns, with different yield stress and initial geometric imperfection, compared with the global DSM equation (Eq. (2.61)) and Euler $1/\lambda_G^2$ curve.

Notice in Figure 5.20, that the difference of the 0.5G+0.5D and 1G+0D initial geometric imperfection in the global DSM equation is negligible. One important observation is the influence of the yielding stress. For yielding of 345 and 508 MPa, the P_u/P_y ratios are above the P_{nG} equation, while for yielding of 1016 MPa, the P_u/P_y ratios are mostly below the P_{nG} equation. These results indicate that the global DSM equation

handle well the columns under different D-G types of buckling interaction nature (*i.e.* TI, SDI and SGI).

One important observation can be retrieved from Figure 5.20, related to the data from 1016 MPa. The data with P_u/P_y in the range of $R_{\lambda_{GD}} < 0.87$ (*i.e.* $\lambda_G \approx 1.20$) seems to be far from the nominal axial strength for global buckling. However, these values of nominal strength, are close to the distortional equation. Because of this, these columns are probably in a region of distortional or D-G coupled phenomenon failure.

Finally, the FEM results are compared with the proposed distortional-global equation (Eq. (2.69)) and global-distortional equation (Eq. (2.70)). Figure 5.21 and Figure 5.22 display the finite element column strength over nominal axial strength (P_u/P_n) versus D-G slenderness ratio ($R_{\lambda_{GD}}$). The graphs illustrate the effectivity of the formulations considering the D-G buckling interaction studied in this work, where Figure 5.21 and Figure 5.22 are addressed to 0.5G+0.5D and 1G+0D initial imperfection combination, respectively.

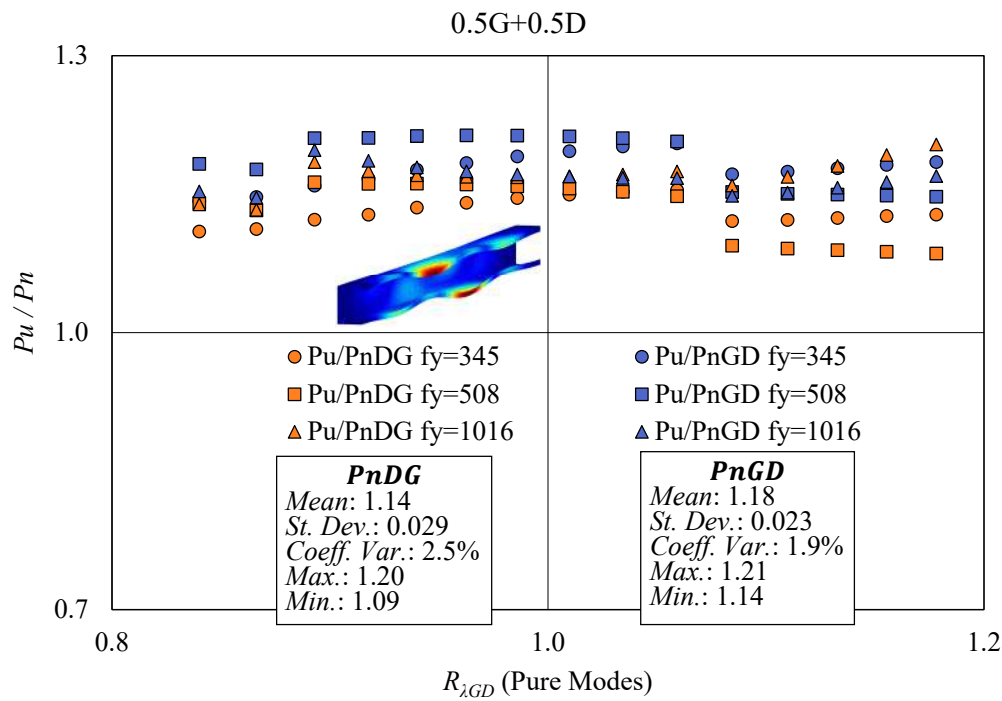


Figure 5.21. Ultimate Load over Nominal Axial Strength versus D-G slenderness ratio for distortional-global (Eq. 2.69) and global-distortional (Eq. 2.70) equations taking 50% global + 50% distortional initial imperfection.

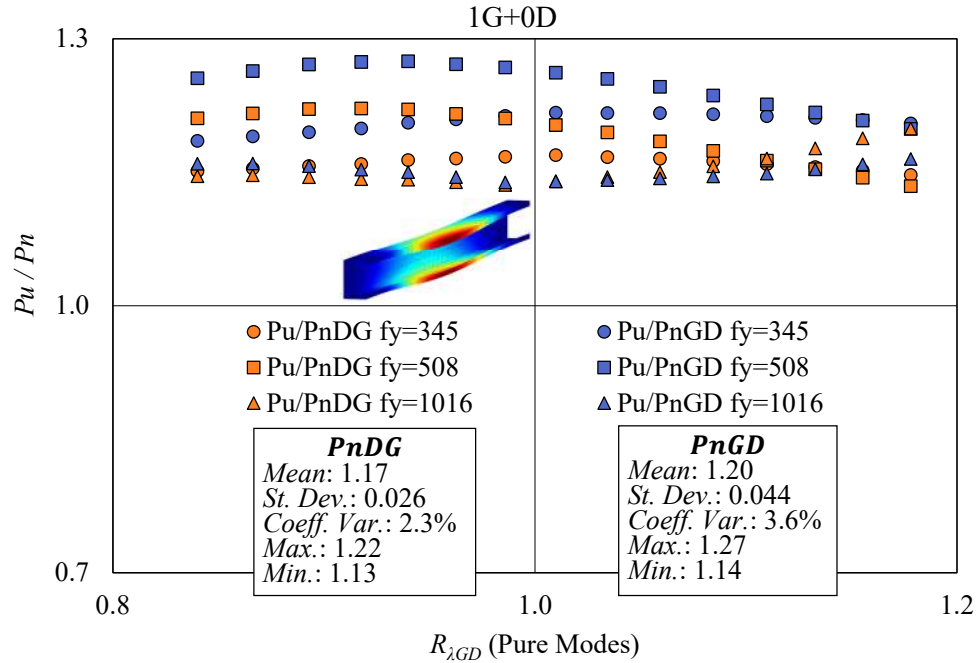


Figure 5.22. Ultimate Load over Nominal Axial Strength versus D-G slenderness ratio for distortional-global (Eq. 2.69) and global-distortional (Eq. 2.70) equations taking 100% global initial imperfection.

Overall, Figure 5.21 and Figure 5.22 has shown that the proposed equations by Schafer [95] (Eq. (2.69)) and by Martins *et al.* [82] (Eq. (2.70)) show good agreement. Even though the standard deviation and coefficient of variation for both equations and both initial geometric imperfection combinations are relatively low, the mean, maximum, and minimum values have demonstrated that the proposed formulations are conservative. This means that the nominal axial strength for the global buckling presented in the codes (Eq. (2.61)) is accurate enough for D-G buckling interaction. These results are obviously limited by set of the available column results. Meanwhile, the proposed D-G buckling interaction equations handle quite conservative the nominal strength comparing to the ultimate load from the FEM. More specifically, note that the P_{nDG} equation is less conservative than the P_{nGD} , which can be justified by comparing the mean, standard deviation, coefficient of variation, minimum and maximum values. Note that P_{nDG} provides a lower mean, minimum and maximum value. In the meantime, the P_{nDG} and P_{nGD} equations give values of standard deviation and coefficient of variation relatively low (less than 0.044 and 3.6%, respectively).

In addition, it is noticed that the influence of the initial geometric imperfection type is not a relevant factor for the FEM performance of the columns. Even though the

1G+0D initial imperfection combination (Figure 5.22) has shown a sparser data for the P_{nGD} equation, compared to the results from the P_{nGD} equation with the 0.5G+0.5D initial imperfection (Figure 5.21), the influence in the ultimate load is minimal. On the other hand, the P_{nDG} equation revealed to have a minor impact in the data dispersion, comparing both initial imperfections standard deviation and coefficient of variation.

Comparing the P_{nDG} , P_{nGD} and P_{nG} approaches, it is drawn the conclusion that the P_{nG} procedure, already presented in the codes, handle the D-G coupled phenomenon properly, for lipped channel columns. The nominal axial strength equation for global buckling from the DSM, was calibrated with many experiments of columns under global buckling. The coefficients calibrated for this equation, was revised for many authors, and it is a quite consolidated formulation. It is plausible that some of these experiments has considered columns with D-G buckling interaction failure. However, this is only a hypothesis, that should be investigated.

6 Concluding Remarks

The present research mainly provided (i) an FSM-based elastic buckling computational analysis tool and (ii) the improvement of the comprehension of the distortional-global interaction buckling phenomenon, including both (ii-a) its post-buckling behavior and (ii-b) the column ultimate load and strength. The investigation was addressed to CFS lipped channel columns, since these are CFS widely applied in steel construction and are prone to develop D-G of buckling interaction. The final conclusions are separated into three parts: (i) FStr Computer Application Program, (ii) Finite Element nonlinear Analysis and (iii) Distortional-Global Buckling Interaction.

6.1 Finite strip method computational tool

The FSM computer application program FStr was developed, in order to assist the elastic buckling analysis. The program implemented in MATLAB, has an accessible and easy graphical user interface, and was conceived to attend research activities as well as engineering design of steel thin-walled structures. The FStr was validated with the help of several models in different types of validation:

- (i) For the end boundary condition validation, 5 models of flat rectangular plates with free longitudinal edges and different end boundary condition, under compression, were analyzed;
- (ii) For local buckling validation, five more models were analyzed, but with all longitudinal edges clamped and different end boundary conditions, in order to force the flat plate to develop the local buckling;
- (iii) An analytical validation was performed, comparing the results from the FStr program with analytical procedures for local, distortional and global elastic buckling, for a single lipped-channel section model and simply-simply end boundary condition, under uniform compression;
- (iv) A validation with the finite element method was also performed, in order to support a strong proof of analysis authentication, which was carried out

with a lipped-channel column under axial compression and clamped-clamped end boundary condition;

- (v) For an unrestricted bending validation, two different beams were analyzed, a lipped channel section with web stiffener and an unsymmetrical zed section, in order to approve the uniform bending load condition and the accuracy of unsymmetrical sections.

In summary, with all these validations the FStr Computer Application Program is certified as a reliable source for an elastic buckling analysis.

6.2 Finite element method nonlinear analysis

The non-linear analysis of a large set of lipped channel columns displaying D-G buckling interaction was performed, based on a developed finite element method model. The finite element model was described in detail and validated with experimental test results from the literature. The available experimental results allowed calibration of the FEM model, which proved to be accurate to accomplish the equilibrium path of the columns under D-G interaction. The FEM model includes the ductile material (steel) and initial geometric imperfections, the former described from tensile standard tests and the later obtained with the help of the FStr computational tool, including appropriate buckling modes combinations (G and D in the present study). To sum up, the finite element model has shown good agreement with global and distortional post-buckling analysis.

6.3 The Global-Distortional buckling mode of CFS lipped channel columns

Based on the previous results and the numerical/computational support, the parametric study on distortional-global buckling interaction was carried out. The parametric analysis involved the FStr program for the definition of the initial geometric imperfections to be considered by the FEM non-linear analysis. Basically, only one cross-section of a lipped-channel was considered, with many combinations of the yield stress f_y and the column length L . The study was separated into two different investigations: (i) initial geometric imperfection combination and (ii) distortional-global buckling interaction nature, namely Secondary Distortional, Secondary Global and True Interaction, respectively SDI, SGI and TI.

With respect to the initial geometric imperfection combination, the following remarks must be pointed out:

- (i) Combining the initial geometric imperfection as first and second mode (which were classified as global and distortional mode), was an approach to include the distortional-global coupled phenomenon behavior into the post-buckling analysis, which was not clearly predictable by the elastic buckling analysis;
- (ii) Using an initial imperfection combination parameter θ , the initial geometric imperfection was modified, combining the global (flexural-torsional) with the distortional mode in different participation levels. Through this combination, the column strength analysis was performed and it was concluded that when θ belongs to the first and second quadrant, it was noticeable a symmetric behavior with the third and fourth quadrant. Indeed, the columns with initial imperfection combination with $0^\circ < \theta < 180^\circ$ show the same results of the columns with $180^\circ < \theta < 360^\circ$, because in theory, the initial geometric imperfections were basically rotated, *i.e.* the modes were multiplied by minus one.
- (iii) In addition to the initial imperfection combination parameter θ , it was noticed an additional cyclic behavior. The post-buckling equilibrium path results, with $0^\circ \leq \theta \leq 180^\circ$, show “mirroring” behavior in the ranges $0^\circ < \theta < 90^\circ$ and $90^\circ < \theta < 180^\circ$. This conclusion indicate next FEM analyses will be satisfactorily completed by simply varying θ from 0° to 90° ;
- (iv) Surprisingly, the columns with only distortional initial geometric imperfection ($\theta = 90^\circ$) has shown a post-buckling behavior completely different from columns $0^\circ \leq \theta < 90^\circ$. This curious behavior was probably triggered by the missing of the global buckling mode. On the other hand, the columns at the range $0^\circ \leq \theta < 90^\circ$ has shown a predictable transitional behavior in the stability path.
- (v) For the columns with higher yield stress (developing larger elastic equilibrium path) and the geometric imperfections in the range $0^\circ \leq \theta < 90^\circ$, it was evident the predominance of the global mode with larger displacements. On the other hand, columns with lower yield strength (less

slender columns) developed pronounced distortional buckling mode in the very beginning of the loading process, showing the distortional initial imperfection has a significant influence at the early steps of the loading;

- (vi) It has been shown that columns with lower yield strength, the distortional initial geometric imperfection (0G+1D) provides the lower ultimate load. For columns with intermediate slenderness, controlled in the present study by the variation of the yield stress, the combined initial geometric imperfection with 50% of global and 50% of distortional mode (0.5G+0.5D) gives the lower ultimate load. While for columns with very high yielding, the most detrimental ultimate load takes place with only global initial geometric imperfection (1G+0D). In conclusion, this analysis has shown that the initial geometric imperfection may affect the ultimate load and the column strength in different manners, according to the nature of D-G buckling interaction.

6.4 The role of the nature of the D-G buckling interaction in the behavior of the columns

Regarding the investigation of the distortional-global buckling interaction nature, the following observations were reported:

- (i) It has been noticed that for high yield strength columns in secondary-global bifurcation D-G interaction region (which means lower values of $R_{\lambda GD}$) appears to diverge from the original direct strength method, which indicates a strong evidence of D-G buckling interaction;
- (ii) Comparing the results with the two types of initial geometric imperfection considered (0.5G+0.5D and 1G+0D), it was concluded that the influence of the initial imperfection form was negligible in the ultimate load. Thereby, using an initial geometric imperfection with only global (flexural-torsional) mode shape is sufficient to perform a parametric study on distortional-flexural-torsional coupled phenomenon;
- (iii) Generally speaking, the direct strength method equation addressed to global buckling is able to handle quite well the columns under the different D-G nature (of the buckling interaction). However, the limits of the present investigation must be pointed, addressed only to lipped channel columns.

Additional results of columns with different cross-section shapes are needed to strengthen this assumption as a general rule;

- (iv) The proposed equations by Schafer [95] (Eq. (2.69)) and Martins *et al.* [82] (Eq. (2.70)) addressed somewhat conservative results for the strength of the lipped channel columns described in the present research. More specifically, between the two approaches investigated here, the P_{nGD} equation (Eq. (2.70)) has demonstrated more conservative than the P_{nDG} (Eq. (2.69)) approach.

The conclusions obtained from the D-G buckling interaction behavior are basically aligned with the ones found in and Martins *et al.* [82], Dinis and Camotim [103] and Martins *et al.* [104]. However, more investigations on this topic, is still needed, in order to better understands the phenomenon, since there is a lack of experimental tests of columns experiencing the distortional-global buckling interaction, in different types of nature.

To sum up, this work was mainly responsible for a deeper understanding of cold-formed lipped-channel columns under D-G buckling interaction, with assistance of an elastic buckling analysis by the finite strip method, complimented by nonlinear FEM analysis. As initially proposed, the goal of this study has been achieved, with possible open topics that may be investigate in future research activities.

6.5 Suggestions for future works

The results and conclusions given by this research has shown some gaps, that may be filled in future works. Therefore, the present author suggests the following topics to be carried out:

- (i) Perform a mesh convergence study of the finite element model using the element SHEL281, with the purpose of rise the element size, and consequently, decrease the total number of elements, which results in a faster non-linear analysis;
- (ii) Conduct an initial geometric imperfection sensitivity study, in order to see the influence of the maximum global and distortional amplitude;
- (iii) Add several updates in the next FStr Computer Application Program version: save results option; easy geometry generation; geometric properties of cross-section; Portuguese/English swap language; modal

participation calculation; direct strength method automatic calculation; finite element model generator for a finite element analysis;

- (iv) Perform a more robust parametric study on secondary-distortional and secondary-global bifurcation D-G interaction natures;
- (v) Varying cross-section parameters, such as b_f/b_w , b_s/b_f and b_s/t for investigating the influence of the geometry in the D-G buckling interaction;
- (vi) Verify the columns studied in this work with the new global and distortional calibrated equations proposed in the literature by many authors (*e.g.* Dinis *et al.* [150] & [151] and Landesmann and Camotim [152]);
- (vii) Expand the analysis with experimental tests, in order to confirm the finite element model and the D-G buckling interaction behavior;
- (viii) Include new types of cross-sections geometries (*e.g.* rack, zeta and lipped-channel with intermediate stiffeners), in the behavior and strength analysis in order to determine a general equation, that might include not only the D-G interaction, but a L-D-G buckling interaction.

In the future, it is expected that the contribution of this research becomes useful for the development of general solution taking into account all the possible buckling modes interaction. In this case, the design approach should be efficient with respect to take into account all the possible failure events.

7 Bibliography

- [1] E. de M. Batista, “Modelling Buckling Interaction,” in *Phenomenological and Mathematical Modelling of Structural Instabilities*, vol. 470, M. Pignataro and V. Gioncu, Eds. Vienna: Springer Vienna, 2005, pp. 135–194.
- [2] CBCA, “CONSTRUÇÃO EM AÇO | Vantagens,” *Centro Brasileiro da Construção em Aço*, 2020. [Online]. Available: <https://www.cbca-acobrasil.org.br/site/construcao-em-aco-vantagens.php>.
- [3] G. . Hancock, “Cold-formed steel structures,” *J. Constr. Steel Res.*, vol. 59, no. 4, pp. 473–487, Apr. 2003, doi: 10.1016/S0143-974X(02)00103-7.
- [4] MARKO, “ROLL-ON NO POUPAKI ATACADISTA GUARULHOS,” 2019. [Online]. Available: <http://www.marko.com.br/roll-on-no-poupaki-atacadista-guarulhos/>.
- [5] ABNT - ASSOCIAÇÃO BRASILEIRA DE NORMAS TÉCNICAS and ABNT, *NBR 14762 - Dimensionamento de estruturas de aço constituídas por perfis formados a frio*, Segunda. Rio de Janeiro, RJ, Brazil, Brasil: ABNT, 2010.
- [6] AS/NZS 4600, *Cold-formed steel structures, Standards Australia & Standard New Zealand*. Australian/New Zealand Standard™, 2018.
- [7] AISI S100-16, *North American Specification for the Design of Cold-Formed Steel Structural Members*. American Iron and Steel Institute, 2016.
- [8] T. V. Galambos and A. E. Surovek, *Structural Stability of Steel: Concepts and Applications for Structural Engineers*. Hoboken, New Jersey: John Wiley & Sons, INC., 2008.
- [9] A. Chajes, *Principles of structural stability theory*. New Jersey, 1974.
- [10] M. A. Crisfield, *Non-linear Finite Element Analysis of Solid and Structures*, VOLUME 1: London, UK, 1991.
- [11] Y. K. Cheung, *Finite Strip Method in Structural Analysis*, vol. 3, no. 2. Adelaide: Pergamon Press, 1976.
- [12] G. J. Hancock, “Local, Distortional, and Lateral Buckling of I-Beams,” *J. Struct.*

- Div.*, vol. 104, no. 11, pp. 1787–1798, 1978.
- [13] G. J. Hancock, N. S. Trahair, and M. A. Bradford, “Web Distortion and Flexural-Torsional Buckling,” *J. Struct. Div.*, vol. 106, no. 7, pp. 1557–1571, 1980.
- [14] G. J. Hancock, “Interaction Buckling in I-Section Columns,” *J. Struct. Div.*, vol. 107, no. 1, pp. 165–179, 1981.
- [15] G. Hancock, T. Murray, and D. Ellifritt, *Cold-Formed Steel Structures to the AISI Specification*. 2001.
- [16] S. P. Timoshenko and S. Woinowsky-Krieger, *Theory of Plates and Shells*, no. 2. McGraw-Hill Book Company, Inc, 1959.
- [17] Y. K. Cheung, “The Finite Strip Method in the Analysis of Elastic Plates with two opposite Simply Supported Ends,” *Proc. Inst. Civ. Eng.*, vol. 40, no. 1, pp. 1–7, 1969, doi: 10.1680/iicep.1969.7550.
- [18] Y. K. Cheung, “Finite Strip Method Analysis of Elastic Slabs,” *J. Eng. Mech. Div.*, vol. 94, no. 6, pp. 1365–1378, 1968.
- [19] M. A. Bradford and M. Azhari, “Buckling of plates with different end conditions using the finite strip method,” *Comput. Struct.*, vol. 56, no. 1, pp. 75–83, 1995, doi: 10.1016/0045-7949(94)00528-B.
- [20] Z. Li and B. W. Schafer, “Finite Strip Stability Solutions for General Boundary Conditions and the Extension of the Constrained Finite Strip Method,” in *Computational Science, Engineering & Technology Series*, no. August 2016, B. H. V. Topping, L. F. Costa Neves, and R. C. Barros, Eds. Madeira, Portugal, 2009, pp. 103–130.
- [21] B. W. Schafer, “Chapter 2: Elastic Buckling Solution Methods for Cold-formed Steel Elements and Members,” Ph.D. Thesis, Cornell University, 1998.
- [22] Z. Li, “Buckling Analysis of the Finite Strip Method and Theoretical Extension of the Constrained Finite Strip Method for General Boundary Conditions.,” Research Report, Baltimore, MD, 2009.
- [23] MathWorks, “MATLAB Using MATLAB Graphics,” *Matlab*, 2000.
- [24] B. T. Smith *et al.*, *Matrix Eigensystem Routines - EISPACK Guide*, Second edi. Springer-Verlag, 1976.
- [25] B. S. Garbow, J. M. Boyle, J. J. Dongarra, and C. B. Moler, *Matrix Eigensystem Routines - EISPACK Guide Extension*. Springer-Verlag, 1977.
- [26] C. B. Moler and G. W. Stewart, “An Algorithm for Generalized Matrix Eigenvalue Problems,” *SIAM J. Numer. Anal.*, vol. 10, no. 2, pp. 241–256, 1973, doi:

10.1137/0710024.

- [27] G. W. Stewart, “A Krylov-Schur algorithm for large eigenproblems,” *SIAM J. Matrix Anal. Appl.*, vol. 23, no. 3, pp. 601–614, 2001, doi: 10.1137/S0895479800371529.
- [28] R. B. Lehoucq, D. C. Sorensen, and C. Yang, *ARPACK Users’ Guide: Solution of Large-Scale Eigenvalue Problems with Implicitly Restarted Arnoldi Methods*. Philadelphia, PA: SIAM, 1998.
- [29] B. W. Schafer and S. Ádány, “Understanding and classifying local, distortional and global buckling in open thin-walled members,” in *Structural Stability Research Council - Proceedings 2005 Annual Stability Conference*, 2005.
- [30] S. Ádány and B. W. Schafer, “Buckling mode decomposition of single-branched open cross-section members via finite strip method: Application and examples,” *Thin-Walled Struct.*, vol. 44, no. 5, pp. 585–600, May 2006, doi: 10.1016/j.tws.2006.03.014.
- [31] S. Ádány and B. W. Schafer, “Buckling mode decomposition of single-branched open cross-section members via finite strip method: Derivation,” *Thin-Walled Struct.*, vol. 44, no. 5, pp. 563–584, May 2006, doi: 10.1016/j.tws.2006.03.013.
- [32] S. Ádány and B. W. Schafer, “A full modal decomposition of thin-walled, single-branched open cross-section members via the constrained finite strip method,” *J. Constr. Steel Res.*, vol. 64, no. 1, pp. 12–29, Jan. 2008, doi: 10.1016/j.jcsr.2007.04.004.
- [33] Z. Li and B. W. Schafer, “Buckling analysis of cold-formed steel members with general boundary conditions using CUFSM: Conventional and constrained finite strip methods,” in *20th International Specialty Conference on Cold-Formed Steel Structures - Recent Research and Developments in Cold-Formed Steel Design and Construction*, 2010.
- [34] Z. Li and B. W. Schafer, “Constrained Finite Strip Method for Thin-Walled Members with General End Boundary Conditions,” *J. Eng. Mech.*, vol. 139, no. 11, pp. 1566–1576, Nov. 2013, doi: 10.1061/(ASCE)EM.1943-7889.0000591.
- [35] V. Vlasov, “Thin-walled elastic beams,” *2nd ed. Jerusalem, Isr. Isr. Progr. Sci. Transl.*, 1961, doi: 10.1007/s13398-014-0173-7.2.
- [36] S. Ádány and B. W. Schafer, “Buckling analysis of cold-formed steel members using CUFSM: Conventional and constrained finite strip methods,” in *18th International Specialty Conference on Cold-Formed Steel Structures*, 2006, doi:

10.1016/j.tws.2006.03.013.

- [37] B. W. Schafer, “Cold-formed steel behavior and design: analytical and numerical modeling of elements and members with longitudinal stiffeners,” PhD dissertation, Cornell University, Ithaca, NY, 1997.
- [38] S. Ádány and B. W. Schafer, “Buckling mode decomposition of single-branched open cross-section members via finite strip method: Derivation,” *Thin-Walled Struct.*, vol. 44, no. 5, pp. 563–584, May 2006, doi: 10.1016/j.tws.2006.03.013.
- [39] B. W. Schafer, “CUFSM 5 - Finite Strip Elastic Buckling Analysis Application.” Baltimore, MD, 2018.
- [40] J. P. Papangelis and G. J. Hancock, “Computer analysis of thin-walled structural members,” *Comput. Struct.*, 1995, doi: 10.1016/0045-7949(94)00545-E.
- [41] V. V. Nguyen, G. J. Hancock, and C. H. Pham, “Development of the Thin-Wall-2 Program for Buckling Analysis of Thin-Walled Sections Under Generalised Loading,” in *Eighth International Conference on ADVANCES IN STEEL STRUCTURES*, 2015.
- [42] S. Ádány, “Buckling mode classification of members with open thin-walled cross-sections by using the finite strip method,” Baltimore, MD, USA, 2004.
- [43] W. McGuire, R. H. Gallagher, and R. D. Ziemian, *Matrix Structural Analysis*, Second Edi. 2014.
- [44] G. J. Hancock and C. H. Pham, “Direct strength method of design for shear of cold-formed channels based on a shear signature curve,” in *21st International Specialty Conference on Cold-Formed Steel Structures - Recent Research and Developments in Cold-Formed Steel Design and Construction*, 2012.
- [45] G. J. Hancock and C. H. Pham, “Buckling analysis of thin-walled sections under localised loading using the semi-analytical finite strip method,” *Thin-Walled Struct.*, vol. 86, pp. 35–46, Jan. 2015, doi: 10.1016/J.TWS.2014.09.017.
- [46] G. J. Hancock and C. H. Pham, “Relationship between the Semi-Analytical Finite Strip Method for Buckling of Thin-Walled Sections under uniform and localised loading,” in *Eighth International Conference on ADVANCES IN STEEL STRUCTURES 2015*, 2015.
- [47] R. Schardt, *Verallgemeinerte Technische Biegetheorie*. Berlin, Heidelberg: Springer Berlin Heidelberg, 1989.
- [48] N. Silvestre, “Generalised Beam Theory: New Formulations, Numerical Implementation and Applications,” PhD Theses, Civil Engineering, IST, Technical

University of Lisbon, 2005.

- [49] R. Bebiano, “Stability and dynamics of thin-walled members: Application of generalised beam theory,” IST - Technical University of Lisbon, 2010.
- [50] D. Camotim, C. Basaglia, R. Bebiano, R. Gonçalves, and N. Silvestre, “Latest developments in the GBT analysis of thin-walled steel structures,” in *STABILITY AND DUCTILITY OF STEEL STRUCTURES*, 2010, pp. 33–58.
- [51] D. Camotim, C. Basaglia, N. M. . Silva, and N. Silvestre, “Numerical Analysis of Thin-Walled Structures using Generalised Beam Theory: Recent and Future Developments,” *Comput. Technol. Rev.*, vol. 1, pp. 315–354, Sep. 2010, doi: 10.4203/ctr.1.11.
- [52] R. Goncalves and D. Camotim, “Steel-concrete composite bridge analysis using generalised beam theory,” *Steel Compos. Struct.*, vol. 10, no. 3, pp. 223–243, May 2010, doi: 10.12989/scs.2010.10.3.223.
- [53] R. Gonçalves, M. Ritto-Corrêa, and D. Camotim, “A new approach to the calculation of cross-section deformation modes in the framework of generalized beam theory,” *Comput. Mech.*, vol. 46, no. 5, pp. 759–781, Oct. 2010, doi: 10.1007/s00466-010-0512-2.
- [54] D. Camotim, N. Silvestre, C. Basaglia, and R. Bebiano, “GBT-based buckling analysis of thin-walled members with non-standard support conditions,” *Thin-Walled Struct.*, vol. 46, no. 7–9, pp. 800–815, Jul. 2008, doi: 10.1016/j.tws.2008.01.019.
- [55] D. Camotim, C. Basaglia, and N. Silvestre, “GBT buckling analysis of thin-walled steel frames: A state-of-the-art report,” *Thin-Walled Struct.*, vol. 48, no. 10–11, pp. 726–743, Oct. 2010, doi: 10.1016/j.tws.2009.12.003.
- [56] C. Basaglia and D. Camotim, “Enhanced generalised beam theory buckling formulation to handle transverse load application effects,” *Int. J. Solids Struct.*, vol. 50, no. 3–4, pp. 531–547, Feb. 2013, doi: 10.1016/j.ijsolstr.2012.10.010.
- [57] P. Natário, N. Silvestre, and D. Camotim, “Localized web buckling analysis of beams subjected to concentrated loads using GBT,” *Thin-Walled Struct.*, vol. 61, pp. 27–41, Dec. 2012, doi: 10.1016/j.tws.2012.05.014.
- [58] R. Gonçalves and D. Camotim, “Elastic buckling of uniformly compressed thin-walled regular polygonal tubes,” *Thin-Walled Struct.*, vol. 71, pp. 35–45, Oct. 2013, doi: 10.1016/j.tws.2013.04.016.
- [59] D. Camotim, N. Silvestre, and R. Bebiano, “GBT-based local and global vibration

- analysis of thin-walled members,” in *Analysis and Design of Plated Structures*, Woodhead P., N. E. Shanmugam and C. M. Wang, Eds. Cambridge: Elsevier, 2007, pp. 36–76.
- [60] R. Bebiano, N. Silvestre, and D. Camotim, “Local and global vibration of thin-walled members subjected to compression and non-uniform bending,” *J. Sound Vib.*, vol. 315, no. 3, pp. 509–535, 2008, doi: 10.1016/j.jsv.2008.02.036.
- [61] R. Bebiano, D. Camotim, and N. Silvestre, “Dynamic analysis of thin-walled members using Generalised Beam Theory (GBT),” *Thin-Walled Struct.*, vol. 72, pp. 188–205, Nov. 2013, doi: 10.1016/j.tws.2013.07.004.
- [62] N. Silvestre and D. Camotim, “Nonlinear Generalised Beam Theory for cold-formed steel members,” *Int. J. Struct. Stab. Dyn.*, vol. 3, no. 4, pp. 461–490, 2003, doi: 10.1142/s0219455403001002.
- [63] C. Basaglia, D. Camotim, and N. Silvestre, “Non-linear GBT formulation for open-section thin-walled members with arbitrary support conditions,” *Comput. Struct.*, vol. 89, no. 21–22, pp. 1906–1919, 2011, doi: 10.1016/j.compstruc.2011.07.001.
- [64] C. Basaglia, D. Camotim, and N. Silvestre, “Post-buckling analysis of thin-walled steel frames using generalised beam theory (GBT),” *Thin-Walled Struct.*, vol. 62, pp. 229–242, 2013, doi: 10.1016/j.tws.2012.07.003.
- [65] R. Bebiano, D. Camotim, and R. Gonçalves, “GBTul 2.0 – A second-generation code for the GBT-based buckling and vibration analysis of thin-walled members,” *Thin-Walled Struct.*, vol. 124, pp. 235–257, Mar. 2018, doi: 10.1016/j.tws.2017.12.002.
- [66] R. Bebiano, N. Silvestre, and D. Camotim, “GBTul 1.0 - Buckling and Vibration Analysis of Thin-Walled Members: USER MANUAL,” Department of Civil Engineering and Architecture, DECivil/IST, Lisbon, Portugal, 2010.
- [67] R. Bebiano, N. Silvestre, and D. Camotim, “GBTul 1.0 - Buckling and Vibration Analysis of Thin-Walled Members: GBT THEORETICAL BACKGROUND,” Department of Civil Engineering and Architecture, DECivil/IST, Lisbon, Portugal, 2010.
- [68] ANSYS Inc., *ANSYS Mechanical APDL Theory Reference - Release 15.0*. Canonsburg, PA, 2013.
- [69] C. Rajakumar and C. R. Rogers, “The Lanczos algorithm applied to unsymmetric generalized eigenvalue problem,” *Int. J. Numer. Methods Eng.*, vol. 32, no. 5, pp. 1009–1026, Oct. 1991, doi: 10.1002/nme.1620320506.

- [70] R. G. Grimes, J. G. Lewis, and H. D. Simon, “A Shifted Block Lanczos Algorithm for Solving Sparse Symmetric Generalized Eigenproblems,” *SIAM J. Matrix Anal. Appl.*, vol. 15, no. 1, pp. 228–272, Jan. 1994, doi: 10.1137/S0895479888151111.
- [71] ANSYS Inc., *ANSYS Theory Reference - Release 5.6*. Canonsburg, PA, 1999.
- [72] K. J. Bathe, *Finite Element Procedures*. 1996.
- [73] E. L. Wilson and T. Itoh, “An eigensolution strategy for large systems,” *Comput. Struct.*, vol. 16, no. 1–4, pp. 259–265, Jan. 1983, doi: 10.1016/0045-7949(83)90166-9.
- [74] E. Riks, “An incremental approach to the solution of snapping and buckling problems,” *Int. J. Solids Struct.*, 1979, doi: 10.1016/0020-7683(79)90081-7.
- [75] E. Riks, “The application of newton’s method to the problem of elastic stability,” *J. Appl. Mech. Trans. ASME*, 1972, doi: 10.1115/1.3422829.
- [76] G. A. Wempner, “Discrete approximations related to nonlinear theories of solids,” *Int. J. Solids Struct.*, 1971, doi: 10.1016/0020-7683(71)90038-2.
- [77] W. T. Koiter, “Over de stabiliteit van her elastisch evenwicht,” PhD Thesis, H.J. Paris, Amsterdam, The Netherlands, 1945.
- [78] B. Budiansky, “Theory of Buckling and Post-Buckling Behavior of Elastic Structures,” in *Advances in Applied Mechanics*, Chia-Shum Yih, Ed. Academic Press, New York, USA, 1974, pp. 1–65.
- [79] V. Gioncu, “General theory of coupled instabilities,” *Thin-Walled Struct.*, vol. 19, no. 2–4, pp. 81–127, Jan. 1994, doi: 10.1016/0263-8231(94)90024-8.
- [80] V. Gioncu, “New conceptions, trends and perspectives in the theory of postcritical behaviour of structures,” in *The 3rd Int. Coll. “Stability,”* 1982, pp. 2–17.
- [81] V. Gioncu, “Coupled instabilities in bar structures: Phenomenon, theory, practice,” in *Structural Stability Research Council: International Colloquium on Stability of Metal Structures 4th. Proceedings*, 1989, p. 357.
- [82] A. D. Martins, D. Camotim, and P. B. Dinis, “On the distortional-global interaction in cold-formed steel columns: Relevance, post-buckling behaviour, strength and DSM design,” *J. Constr. Steel Res.*, vol. 145, pp. 449–470, Jun. 2018, doi: 10.1016/j.jcsr.2018.02.031.
- [83] S. P. Timoshenko and J. M. Gere, “Theory of Elastic Stability,” in *McGraw-Hill Book Company Inc*, McGraw-Hill International Book Company, 1961, p. 535.
- [84] G. H. Bryan, “On the Stability of a Plane Plate under Thrusts in its own Plane, with Applications to the ‘Buckling’ of the Sides of a Ship,” *Proc. London Math. Soc.*,

- vol. s1-22, no. 1, pp. 54–67, Nov. 1890, doi: 10.1112/plms/s1-22.1.54.
- [85] E. de M. Batista, “Effective section method: A general direct method for the design of steel cold-formed members under local-global buckling interaction,” *Thin-Walled Struct.*, vol. 48, no. 4–5, pp. 345–356, 2010, doi: 10.1016/j.tws.2009.11.003.
- [86] D. C. T. Cardoso, G. C. De Salles, E. de M. Batista, and P. B. Gonçalves, “Thin-Walled Structures Explicit equations for distortional buckling of cold-formed steel lipped channel columns,” *Thin Walled Struct.*, vol. 119, no. April, pp. 925–933, 2017, doi: 10.1016/j.tws.2017.08.014.
- [87] L. Euler, “De curvis elasticis,” in *Methodus inveniendi lineas curvas maximi minimive proprietate gaudentes*, Lausanne and Geneva, 1744.
- [88] T. Von Kármán, E. . Sechler, and L. . Donnel, “The strength of thin plates in compression,” *Trans. ASME*, vol. 54, p. APM 54-5, 1932.
- [89] G. Winter, “Strength of thin-walled compression flanges,” *Trans. ASME*, vol. 112, 1947.
- [90] G. Winter, “Thin-Walled Structures-Theoretical Solutions and Test Results,” 1968, pp. 101–112.
- [91] B. W. Schafer and T. Peköz, “Direct Strength Prediction of Cold-Formed Steel Members Using Numerical Elastic Buckling Solutions,” in *14th International Specialty Conference on Cold-Formed Steel Structures*, 1998, pp. 69–76.
- [92] G. J. Hancock, Y. B. Kwon, and E. S. Bernard, “Strength design curves for thin-walled sections undergoing distortional buckling,” *J. Constr. Steel Res.*, vol. 31, no. 2–3, pp. 169–186, Jan. 1994, doi: 10.1016/0143-974X(94)90009-4.
- [93] ABNT, *Associação Brasileira De Normas Técnicas, NBR 8800:2008 - Projeto de estruturas de aço e de estruturas mistas de aço e concreto de edifícios*. Rio de Janeiro, RJ, Brazil, 2008.
- [94] ANSI/AISC 360-16, *American National Standards Institute and American Institute of Steel Construction: Specification for Structural Steel Buildings*. Chicago, Illinois, 2016.
- [95] B. W. Schafer, “Local, Distortional, and Euler Buckling of Thin-Walled Columns,” *Journal of Structural Engineering*, vol. 128, pp. 289–299, 2002.
- [96] N. Silvestre, D. Camotim, and P. B. Dinis, “Post-buckling behaviour and direct strength design of lipped channel columns experiencing local/distortional interaction,” *J. Constr. Steel Res.*, vol. 73, no. 6, pp. 12–30, Jun. 2012, doi:

- 10.1016/j.jcsr.2012.01.005.
- [97] P. B. Dinis and D. Camotim, “Cold-formed steel columns undergoing local-distortional coupling: Behaviour and direct strength prediction against interactive failure,” *Comput. Struct.*, 2015, doi: 10.1016/j.compstruc.2014.09.012.
- [98] A. D. Martins, D. Camotim, and P. Borges Dinis, “On the direct strength design of cold-formed steel columns failing in local-distortional interactive modes,” *Thin-Walled Struct.*, vol. 120, no. March, pp. 432–445, Nov. 2017, doi: 10.1016/j.tws.2017.06.027.
- [99] G. Y. Matsubara, “Análise da interação entre modos de flambagem local e distorcional em perfis de aço formados a frio com seção U enrijecido sob compressão axial,” Master’s Dissertation, Programa de Pós-graduação em Engenharia Civil, COPPE, Universidade Federal do Rio de Janeiro, 2018.
- [100] G. Y. Matsubara, E. de M. Batista, and G. C. Salles, “Lipped channel cold-formed steel columns under local-distortional buckling mode interaction,” *Thin-Walled Struct.*, vol. 137, pp. 251–270, Apr. 2019, doi: 10.1016/j.tws.2018.12.041.
- [101] G. Y. Matsubara and E. de M. Batista, “Perfis de Aço Formados a Frio sob Compressão Axial Sujeitos a Interação LD entre os modos de Flambagem Local e Distorcional,” in *CONSTRUMETAL - 8º Congresso Latino-americano da Construção Metálica, São Paulo, SP, Brazil*, 2019.
- [102] E. de M. Batista, G. Y. Matsubara, and J. M. S. Franco, “Local-distortional buckling interaction of cold-formed steel columns design approach,” in *SDSS 2019 - International Colloquium on Stability and Ductility of Steel Structures*, 2019.
- [103] P. B. Dinis and D. Camotim, “Post-buckling behaviour and strength of cold-formed steel lipped channel columns experiencing distortional/global interaction,” *Comput. Struct.*, vol. 89, no. 3–4, pp. 422–434, 2011, doi: 10.1016/j.compstruc.2010.11.015.
- [104] A. D. Martins, D. Camotim, R. Gonçalves, and P. B. Dinis, “On the mechanics of distortional-global interaction in fixed-ended columns,” *Thin-Walled Struct.*, vol. 123, pp. 162–184, Feb. 2018, doi: 10.1016/j.tws.2017.11.001.
- [105] P. B. Dinis, D. Camotim, E. de M. Batista, and E. S. dos Santos, “LOCAL / DISTORTIONAL / GLOBAL MODE COUPLING IN FIXED LIPPED CHANNEL COLUMNS ;,” *Adv. Steel Constr.*, vol. 7, no. 1, pp. 113–130, 2011.
- [106] E. S. dos Santos, “Interação entre os modos de flambagem local-distorcional-global em perfis de aço formados a frio com seção U enrijecido na compressão

- axial,” Tese de Doutorado, COPPE/ Universidade Federal do Rio de Janeiro, 2014.
- [107] E. S. dos Santos, Pedro Borges Dinis, Eduardo M. Batista, and Dinar Camotim, “Cold-Formed Steel Lipped Channel Columns Undergoing Local-Distortional-Global Interaction : Experimental and Numerical Investigation,” in *Twenty-Second International Specialty Conference on Cold-Formed Steel Structures St. Louis, Missouri*, 2014.
- [108] E. S. dos Santos, E. de Miranda Batista, and D. Camotim, “Cold-formed steel columns under L-D-G interaction,” *Steel Constr.*, vol. 7, no. 3, pp. 193–198, Sep. 2014, doi: 10.1002/stco.201410034.
- [109] D. Cava, D. Camotim, P. B. Dinis, and A. Madeo, “Numerical investigation and direct strength design of cold-formed steel lipped channel columns experiencing local–distortional–global interaction,” *Thin-Walled Struct.*, vol. 105, pp. 231–247, Aug. 2016, doi: 10.1016/j.tws.2016.03.025.
- [110] B. Young, P. B. Dinis, and D. Camotim, “CFS lipped channel columns affected by L-D-G interaction. Part I: Experimental investigation,” *Comput. Struct.*, vol. 207, pp. 219–232, Sep. 2018, doi: 10.1016/j.compstruc.2017.03.016.
- [111] P. B. Dinis, D. Camotim, B. Young, and E. de M. Batista, “CFS lipped channel columns affected by L-D-G interaction. Part II: Numerical simulations and design considerations,” *Comput. Struct.*, vol. 207, pp. 200–218, Sep. 2018, doi: 10.1016/j.compstruc.2017.03.017.
- [112] G. Y. Matsubara and E. de M. Batista, “Cold-Formed Steel Columns Under Local-Distortional-Global Buckling Mode Interaction,” in *Proceedings of the XL Ibero-Latin-American Congress on Computational Methods in Engineering, ABMEC, Natal, RN, Brazil*, 2019.
- [113] B. W. Schafer, “Direct Strength Method (DSM) Design Guide,” in *Design Guide CFXX-X, American Iron and Steel Institute*, Committee on Specifications for the Design of Cold-Formed Steel Structural Members, Ed. American Iron and Steel Institute, 2006.
- [114] B. W. Schafer, “Review: The Direct Strength Method of cold-formed steel member design,” *J. Constr. Steel Res.*, vol. 64, no. 7–8, pp. 766–778, Jul. 2008, doi: 10.1016/j.jcsr.2008.01.022.
- [115] D. Yang and G. J. Hancock, “Compression Tests of High Strength Steel Channel Columns with Interaction between Local and Distortional Buckling,” *J. Struct. Eng.*, vol. 130, no. 12, pp. 1954–1963, Dec. 2004, doi: 10.1061/(ASCE)0733-

9445(2004)130:12(1954).

- [116] D. Camotim, P. Borges Dinis, and N. Silvestre, “FEM-based analysis of the local-plate/distortional mode interaction in cold-formed steel lipped channel columns,” *Comput. Struct.*, vol. 85, pp. 1461–1474, 2007, doi: 10.1016/j.compstruc.2007.02.013.
- [117] D. Camotim, N. Silvestre, and P. B. Dinis, “Direct strength prediction of lipped channel columns experiencing local-plate/distortional interaction,” *Adv. Steel Constr.*, vol. 5, no. 1, pp. 49–71, 2009.
- [118] Y. B. Kwon, B. S. Kim, and G. J. Hancock, “Compression tests of high strength cold-formed steel channels with buckling interaction,” *J. Constr. Steel Res.*, 2009, doi: 10.1016/j.jcsr.2008.07.005.
- [119] A. D. Martins, P. B. Dinis, D. Camotim, and P. Providencia, “Interacção local-distorcional em colunas de aço enformadas a frio com secção em C reforçada na alma,” in *Congresso de Métodos Numéricos em Engenharia*, 2015, p. 20.
- [120] D. C. Y. Yap and G. J. Hancock, “Experimental study of high-strength cold-formed stiffened-web C-sections in compression,” *J. Struct. Eng.*, vol. 137, no. 2, pp. 162–172, 2011, doi: 10.1061/(ASCE)ST.1943-541X.0000271.
- [121] T. P. Desmond, T. Peköz, and G. Winter, “Edge Stiffeners for Cold-formed Steel Members,” *Int. Spec. Conf. Cold-Formed Steel Struct.*, p. 38, 1978.
- [122] P. B. Dinis and Camotim D., “Post-buckling behavior and strength of cold-formed steel lipped channel columns affected by distortional/global mode interaction,” in *Structural Stability Research Council, Annual Stability Conference*, 2008, pp. 405–431.
- [123] B. Rossi, J.-P. Jaspart, and K. J. R. Rasmussen, “Combined Distortional and Overall Flexural-Torsional Buckling of Cold-Formed Stainless Steel Sections: Experimental Investigations,” *J. Struct. Eng.*, vol. 136, no. 4, pp. 354–360, 2010, doi: 10.1061/(asce)st.1943-541x.0000147.
- [124] M. Anbarasu and G. Murugapandian, “Experimental study on cold-formed steel web stiffened lipped channel columns undergoing distortional–global interaction,” *Mater. Struct. Constr.*, vol. 49, no. 4, pp. 1433–1442, 2016, doi: 10.1617/s11527-015-0586-6.
- [125] S. Niu, K. J. R. Rasmussen, and F. Fan, “Distortional–global interaction buckling of stainless steel C-beams: Part I — Experimental investigation,” *J. Constr. Steel Res.*, vol. 96, pp. 127–139, 2014, doi: 10.1061/(asce)st.1943-541x.0001137.

- [126] S. Niu, K. J. R. Rasmussen, and F. Fan, “Distortional–global interaction buckling of stainless steel C-beams: Part II — Numerical study and design,” *J. Constr. Steel Res. Distortional–global*, vol. 96, pp. 40–53, 2014, doi: 10.1061/(asce)st.1943-541x.0001131.
- [127] A. D. Martins, D. Camotim, R. Gonçalves, and P. B. Dinis, “Distortional-global interaction in lipped channel beams: Part I: Mechanics and elastic behaviour,” *ce/papers*, vol. 1, no. 2–3, pp. 1493–1502, Sep. 2017, doi: 10.1002/cepa.192.
- [128] A. D. Martins, D. Camotim, and P. B. Dinis, “Distortional-global interaction in lipped channel beams: Part II: Strength, relevance and DSM design,” *ce/papers*, vol. 1, no. 2–3, pp. 1503–1512, Sep. 2017, doi: 10.1002/cepa.193.
- [129] A. D. Martins, D. Camotim, and P. B. Dinis, “Distortional-global interaction in lipped channel and zed-section beams: Strength, relevance and DSM design,” *Thin-Walled Struct.*, vol. 129, pp. 289–308, Aug. 2018, doi: 10.1016/j.tws.2018.02.015.
- [130] M. Anbarasu, “Influence on ultimate strength of Cold- Formed Steel Lipped Channel Columns subjected to Interaction on Distortional- Global Buckling,” *Adv. Nat. Appl. Sci.*, vol. 8, no. July, pp. 192–201, 2017.
- [131] A. D. Martins, D. Camotim, R. Goncalves, and P. B. Dinis, “Mechanics of the local-distortional interaction in fixed-ended lipped channel columns,” in *Proceedings of the International Colloquium on Stability and Ductility of Steel Structures, SDSS 2016*, 2016, pp. 1–22.
- [132] S. Ahmad, B. M. Irons, and O. C. Zienkiewicz, “Analysis of thick and thin shell structures by curved finite elements,” *Int. J. Numer. Methods Eng.*, 1970, doi: 10.1002/nme.1620020310.
- [133] E. N. Dvorkin, “On Nonlinear Finite Element Analysis of Shell Structures,” Ph.D Thesis. Massachusetts Institute of Technology, 1984.
- [134] E. N. Dvorkin and K. Bathe, “A continuum mechanics based four-node shell element for general non-linear analysis,” *Eng. Comput.*, vol. 1, no. 1, pp. 77–88, Jan. 1984, doi: 10.1108/eb023562.
- [135] D. J. Allman, “A compatible triangular element including vertex rotations for plane elasticity analysis,” *Comput. Struct.*, vol. 19, no. 1–2, pp. 1–8, Jan. 1984, doi: 10.1016/0045-7949(84)90197-4.
- [136] K.-J. Bathe and E. N. Dvorkin, “A formulation of general shell elements—the use of mixed interpolation of tensorial components,” *Int. J. Numer. Methods Eng.*, vol.

- 22, no. 3, pp. 697–722, Mar. 1986, doi: 10.1002/nme.1620220312.
- [137] R. D. Cook, “On the allman triangle and a related quadrilateral element,” *Comput. Struct.*, vol. 22, no. 6, pp. 1065–1067, Jan. 1986, doi: 10.1016/0045-7949(86)90167-7.
- [138] R. H. Macneal and R. L. Harder, “A refined four-noded membrane element with rotational degrees of freedom,” *Comput. Struct.*, 1988, doi: 10.1016/0045-7949(88)90094-6.
- [139] R. D. Cook, D. S. Malkus, M. E. Plesha, and R. J. Witt, *Concepts and Applications of Finite Element Analysis*, 4th Editio. University of Wisconsin - Madison: John Wiley & Sons, Inc., 2001.
- [140] G. C. de Salles, “Investigação Analítica, Numérica e Experimental do Modo de Flambagem Distorcional em Perfis Formados a Frio,” Dissertação de Mestrado, Universidade Federal do Rio de Janeiro, COPPE, 2017.
- [141] E. Ellobody and B. Young, “Behavior of Cold-Formed Steel Plain Angle Columns,” *J. Struct. Eng.*, vol. 131, no. 3, pp. 457–466, Mar. 2005, doi: 10.1061/(ASCE)0733-9445(2005)131:3(457).
- [142] B. W. Schafer and T. Pekoz, “Computational modeling of cold-formed steel : characterizing geometric imperfections and residual stresses,” *J. Constr. Steel Res.* 47, vol. 47, pp. 193–210, 1998, doi: 0143-974X/98/\$19.00.
- [143] W. S. Santos, “On the Strength and DSM Design of End-Bolted Cold-Formed Steel Columns Buckling in Distortional Modes,” Tese de Doutorado, COPPE/ Universidade Federal do Rio de Janeiro, 2017.
- [144] M. A. Crisfield, “A fast incremental/iterative solution procedure that handles ‘snap-through,’” *Comput. Struct.*, vol. 13, no. 1–3, pp. 55–62, Jun. 1981, doi: 10.1016/0045-7949(81)90108-5.
- [145] M. A. Crisfield, “An arc-length method including line searches and accelerations,” *Int. J. Numer. Methods Eng.*, 1983, doi: 10.1002/nme.1620190902.
- [146] Y. B. Heva, “Behaviour and design of cold- formed steel compression members at elevated temperatures,” Thesis, School of Urban Developments Queensland University of Technology, 2009.
- [147] S. Gunalan, Y. B. Heva, and M. Mahendran, “Flexural–torsional buckling behaviour and design of cold-formed steel compression members at elevated temperatures,” *Eng. Struct.*, vol. 79, pp. 149–168, Nov. 2014, doi: 10.1016/j.engstruct.2014.07.036.

- [148] N. D. Kankanamge and M. Mahendran, “Mechanical properties of cold-formed steels at elevated temperatures,” *Thin-Walled Struct.*, vol. 49, no. 1, pp. 26–44, Jan. 2011, doi: 10.1016/j.tws.2010.08.004.
- [149] T. Ranawaka and M. Mahendran, “Experimental study of the mechanical properties of light gauge cold-formed steels at elevated temperatures,” *Fire Saf. J.*, vol. 44, no. 2, pp. 219–229, Feb. 2009, doi: 10.1016/j.firesaf.2008.06.006.
- [150] P. B. Dinis, D. Camotim, A. Landesmann, and A. D. Martins, “On the direct strength method design of columns against global failures,” *Thin-Walled Struct.*, vol. 139, no. October 2018, pp. 242–270, Jun. 2019, doi: 10.1016/j.tws.2019.02.027.
- [151] P. B. Dinis, D. Camotim, A. Landesmann, and A. D. Martins, “Improving the Direct Strength Method prediction of column flexural-torsional failure loads,” *Thin-Walled Struct.*, no. October 2019, 2019, doi: 10.1016/j.tws.2019.106461.
- [152] A. Landesmann and D. Camotim, “On the Direct Strength Method (DSM) design of cold-formed steel columns against distortional failure,” *Thin-Walled Struct.*, vol. 67, pp. 168–187, Jun. 2013, doi: 10.1016/j.tws.2013.01.016.

APPENDIX A

Analytical solution for integrals I_1, I_2, I_3, I_4 and I_5 , for different end boundary condition.

(Source: K. Li [22] and Bradford and Azhari, [19])

$$I_1 = \int_0^a Y_p Y_q dy; I_2 = \int_0^a Y_p' Y_q' dy; I_3 = \int_0^a Y_p Y_q'' dy;$$

$$I_4 = \int_0^a Y_p'' Y_q'' dy; I_5 = \int_0^a Y_p'' Y_q dy$$

- Simply-Simply (S-S)

$$\left. \begin{aligned} I_1 &= \frac{a}{2} \\ I_2 &= -\frac{\pi^2}{2a} p^2 \\ I_3 &= -\frac{\pi^2}{2a} q^2 \\ I_4 &= \frac{\pi^4}{2a^3} p^4 \\ I_5 &= \frac{\pi^2}{2a} p^2 \end{aligned} \right\} \text{for } p = q \quad (\text{A.1})$$

$$\left. \begin{aligned} I_1 &= 0 \\ I_2 &= 0 \\ I_3 &= 0 \\ I_4 &= 0 \\ I_5 &= 0 \end{aligned} \right\} \text{for } p \neq q \quad (\text{A.2})$$

- Clamped-Clamped (C-C)

$$\left. \begin{aligned} I_1 &= \frac{3a}{8} \\ I_2 &= -\frac{\pi^2}{2a} \\ I_3 &= -\frac{\pi^2}{2a} \\ I_4 &= \frac{2\pi^4}{a^3} \\ I_5 &= \frac{\pi^2}{a} \end{aligned} \right\} \text{for } p = q = 1 \quad (\text{A.3})$$

$$\left. \begin{aligned} I_1 &= \frac{a}{4} \\ I_2 &= -\frac{\pi^2}{4a}(p^2 + 1) \\ I_3 &= -\frac{\pi^2}{4a}(q^2 + 1) \\ I_4 &= \frac{\pi^4}{4a^3}[(p^2 + 1)^2 + 4p^2] \\ I_5 &= \frac{\pi^2}{4a}(p + 1)^2 \end{aligned} \right\} \text{for } p = q > 1 \quad (\text{A.4})$$

$$\left. \begin{aligned} I_1 &= -\frac{a}{8} \\ I_2 &= \frac{\pi^2}{4a} \left[\frac{(p^2 + 1)}{2} - p \right] \\ I_3 &= \frac{\pi^2}{4a} \left[\frac{(q^2 + 1)}{2} + q \right] \\ I_4 &= -\frac{\pi^4}{8a^3} (p - 1)^2 (q + 1)^2 \\ I_5 &= -\frac{\pi^2}{8a} (pq + 1) \end{aligned} \right\} \text{for } p - q = 2 \quad (\text{A.5})$$

$$\left. \begin{aligned}
I_1 &= -\frac{a}{8} \\
I_2 &= \frac{\pi^2}{4a} \left[\frac{(p^2 + 1)}{2} + p \right] \\
I_3 &= \frac{\pi^2}{4a} \left[\frac{(q^2 + 1)}{2} - q \right] \\
I_4 &= -\frac{\pi^4}{8a^3} (q - 1)^2 (p + 1)^2 \\
I_5 &= -\frac{\pi^2}{8a} (qp + 1)
\end{aligned} \right\} \text{for } p - q = -2 \quad (\text{A.6})$$

$$\left. \begin{aligned}
I_1 &= 0 \\
I_2 &= 0 \\
I_3 &= 0 \\
I_4 &= 0 \\
I_5 &= 0
\end{aligned} \right\} \text{for all other cases} \quad (\text{A.7})$$

- Simply-Clamped (S-C)

$$\left. \begin{aligned}
I_1 &= \frac{a}{2} \left[\frac{(p + 1)^2}{p^2} + 1 \right] \\
I_2 &= -\frac{\pi^2}{a} (p + 1)^2 \\
I_3 &= -\frac{\pi^2}{a} (q + 1)^2 \\
I_4 &= \frac{\pi^4}{2a^3} (p + 1)^2 [(p + 1)^2 + p^2] \\
I_5 &= \frac{\pi^2}{a} (p + 1)^2
\end{aligned} \right\} \text{for } p = q \quad (\text{A.8})$$

$$\left. \begin{aligned}
I_1 &= \frac{a(p + 1)}{2p} \\
I_2 &= -\frac{\pi^2}{2a} (p + 1)p \\
I_3 &= -\frac{\pi^2 p^2 (p + 1)}{2a p} \\
I_4 &= \frac{\pi^4}{2a^3} (p + 1)p^3 \\
I_5 &= \frac{\pi^2}{2a} (p + 1)p
\end{aligned} \right\} \text{for } p - q = 1 \quad (\text{A.9})$$

$$\left. \begin{aligned}
I_1 &= \frac{a(q+1)}{2q} \\
I_2 &= -\frac{\pi^2 q^2 (q+1)}{2a q} \\
I_3 &= -\frac{\pi^2}{2a} (q+1)q \\
I_4 &= \frac{\pi^4}{2a^3} (q+1)q^3 \\
I_5 &= \frac{\pi^2}{2a} (q+1)q
\end{aligned} \right\} \text{for } p - q = -1 \quad (\text{A.10})$$

$$\left. \begin{aligned}
I_1 &= 0 \\
I_2 &= 0 \\
I_3 &= 0 \\
I_4 &= 0 \\
I_5 &= 0
\end{aligned} \right\} \text{for all other cases} \quad (\text{A.11})$$

- Free-Clamped (F-C)

$$\left. \begin{aligned}
I_1 &= \frac{a}{2} \left[3 - \frac{4(-1)^{p-1}}{\pi \left(p - \frac{1}{2} \right)} \right] \\
I_2 &= -\frac{\pi^2}{a} \left(p - \frac{1}{2} \right)^2 \left[\frac{(-1)^{p-1}}{\pi \left(p - \frac{1}{2} \right)} - \frac{1}{2} \right] \\
I_3 &= -\frac{\pi^2}{a} \left(q - \frac{1}{2} \right)^2 \left[\frac{(-1)^{q-1}}{\pi \left(q - \frac{1}{2} \right)} - \frac{1}{2} \right] \\
I_4 &= \frac{\pi^4}{2a^3} \left(p - \frac{1}{2} \right)^4 \\
I_5 &= \frac{\pi^2}{2a} \left(p - \frac{1}{2} \right)^2
\end{aligned} \right\} \text{for } p = q \quad (\text{A.12})$$

$$\left. \begin{aligned}
I_1 &= \frac{a}{\pi} \left[\pi - \frac{(-1)^{p-1}}{\left(p - \frac{1}{2}\right)} - \frac{(-1)^{q-1}}{\left(q - \frac{1}{2}\right)} \right] \\
I_2 &= -\frac{\pi}{a} \left(p - \frac{1}{2}\right) (-1)^{p-1} \\
I_3 &= -\frac{\pi}{a} \left(q - \frac{1}{2}\right) (-1)^{q-1} \\
I_4 &= 0 \\
I_5 &= 0
\end{aligned} \right\} \text{for } p \neq q \quad (\text{A.13})$$

- Guided-Clamped (G-C)

$$\left. \begin{aligned}
I_1 &= \frac{3a}{8} \\
I_2 &= -\frac{\pi^2}{8a} \\
I_3 &= -\frac{\pi^2}{8a} \\
I_4 &= \frac{\pi^4}{8a^3} \\
I_5 &= \frac{\pi^2}{8a}
\end{aligned} \right\} \text{for } p = q = 1 \quad (\text{A.14})$$

$$\left. \begin{aligned}
I_1 &= \frac{a}{4} \\
I_2 &= -\frac{\pi^2}{8a} [(p-1)^2 + p^2] \\
I_3 &= -\frac{\pi^2}{8a} [(q-1)^2 + q^2] \\
I_4 &= \frac{\pi^4}{8a^3} [(p-1)^4 + p^4] \\
I_5 &= \frac{\pi^2}{8a} [(p-1)^2 + p^2]
\end{aligned} \right\} \text{for } p = q > 1 \quad (\text{A.15})$$

$$\left. \begin{aligned}
 I_1 &= -\frac{a}{8} \\
 I_2 &= \frac{\pi^2}{8a}(p-1)^2 \\
 I_3 &= \frac{\pi^2}{8a}q^2 \\
 I_4 &= -\frac{\pi^4}{8a^3}q^4 \\
 I_5 &= -\frac{\pi^2}{8a}q^2
 \end{aligned} \right\} \text{for } p - q = 1 \quad (\text{A.16})$$

$$\left. \begin{aligned}
 I_1 &= -\frac{a}{8} \\
 I_2 &= \frac{\pi^2}{8a}p^2 \\
 I_3 &= \frac{\pi^2}{8a}(q-1)^2 \\
 I_4 &= -\frac{\pi^4}{8a^3}p^4 \\
 I_5 &= -\frac{\pi^2}{8a}p^2
 \end{aligned} \right\} \text{for } p - q = -1 \quad (\text{A.17})$$

$$\left. \begin{aligned}
 I_1 &= 0 \\
 I_2 &= 0 \\
 I_3 &= 0 \\
 I_4 &= 0 \\
 I_5 &= 0
 \end{aligned} \right\} \text{for all other cases} \quad (\text{A.18})$$

APPENDIX B

Post-buckling equilibrium paths for different type of initial geometric imperfection combination, and different yield stress of LC 100x70x15x2.70 mm, L=1850 mm.

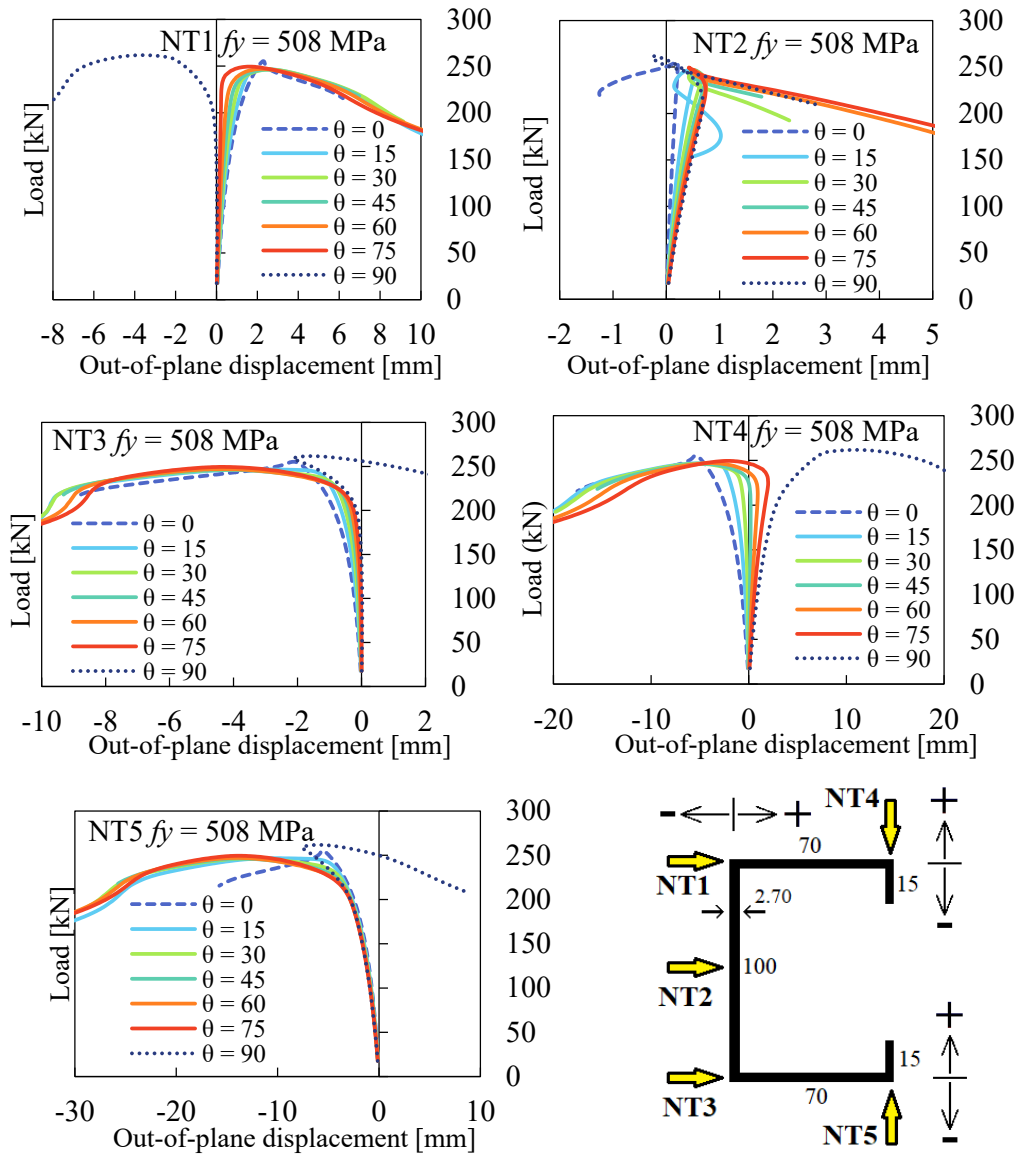


Figure B.1. Post-buckling equilibrium paths, load steps vs. out-of-plane displacements (a) NT1, (b) NT2, (c) NT3, (d) NT4 and (e) NT5, with $f_y = 508 \text{ MPa}$ and $P_{cr} = 354.5 \text{ kN}$ ($P_y/P_{cr} = 1.0$) at $0.4L$, from $\theta = [0^\circ, 90^\circ]$.

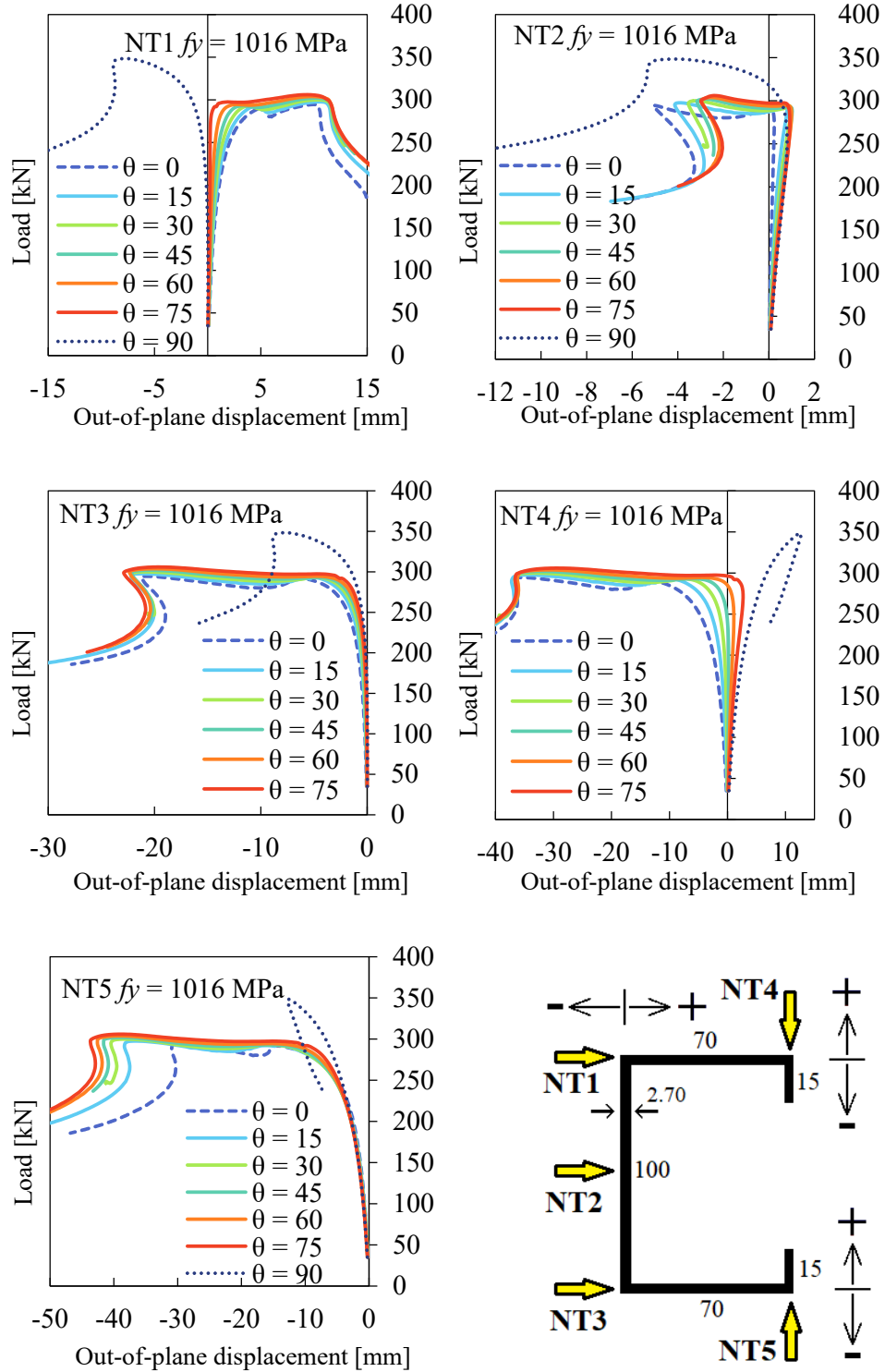


Figure B.2. Post-buckling equilibrium paths, load steps vs. out-of-plane displacements (a) NT1, (b) NT2, (c) NT3, (d) NT4 and (e) NT5, with $f_y = 1016 \text{ MPa}$ and $P_{cr} = 354.5 \text{ kN}$ ($P_y/P_{cr} = 2.0$) at $0.4L$, from $\theta = [0^\circ, 90^\circ]$.

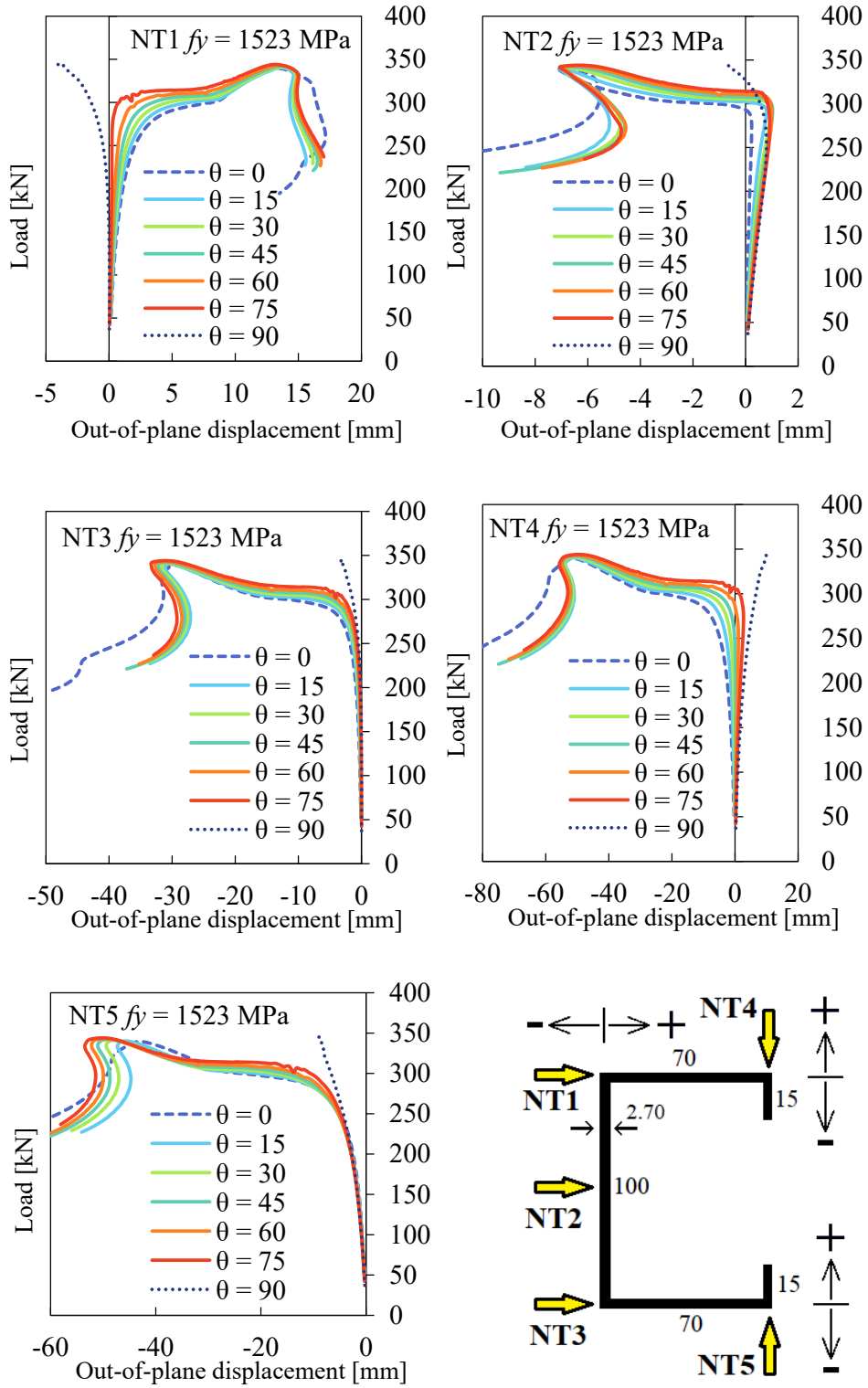


Figure B.3. Post-buckling equilibrium paths, load steps vs. out-of-plane displacements (a) NT1, (b) NT2, (c) NT3, (d) NT4 and (e) NT5, with $f_y = 1532$ MPa and $P_{cr} = 354.5$ kN ($P_y/P_{cr} = 3.0$) at $0.4L$, from $\theta = [0^\circ, 90^\circ]$.

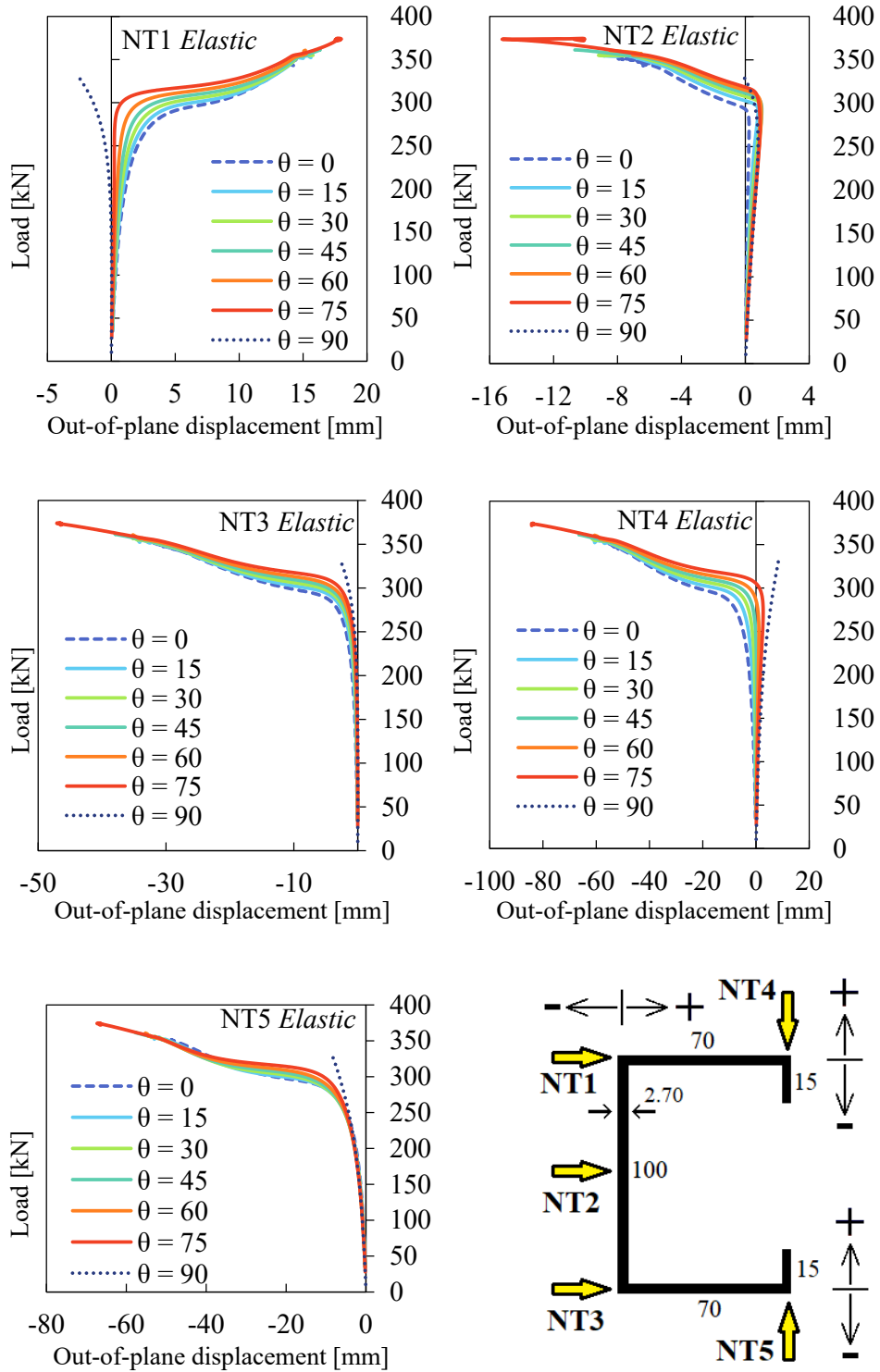


Figure B.4. Post-buckling equilibrium paths, load steps vs. out-of-plane displacements (a) NT1, (b) NT2, (c) NT3, (d) NT4 and (e) NT5, with $f_y = Inf. MPa$ and $P_{cr} = 354.5 kN$ (elastic behavior) at $0.4L$, from $\theta = [0^\circ, 90^\circ]$.

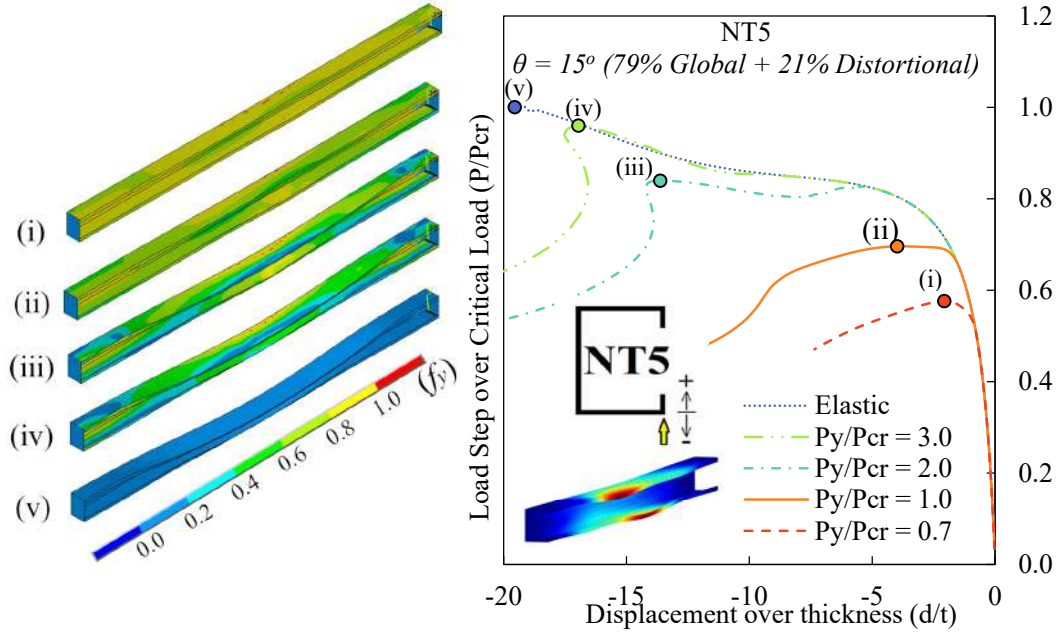


Figure B.5. Post-buckling equilibrium paths, P/P_{cr} vs. d/t of displacement NT5 at $0.4L$, with $\theta = 15^\circ$ (79% Global and 21% Distortional mode), for different ratios of P_y/P_{cr} , where $P_{cr} = 354.5 \text{ kN}$ and $t = 2.70 \text{ mm}$.

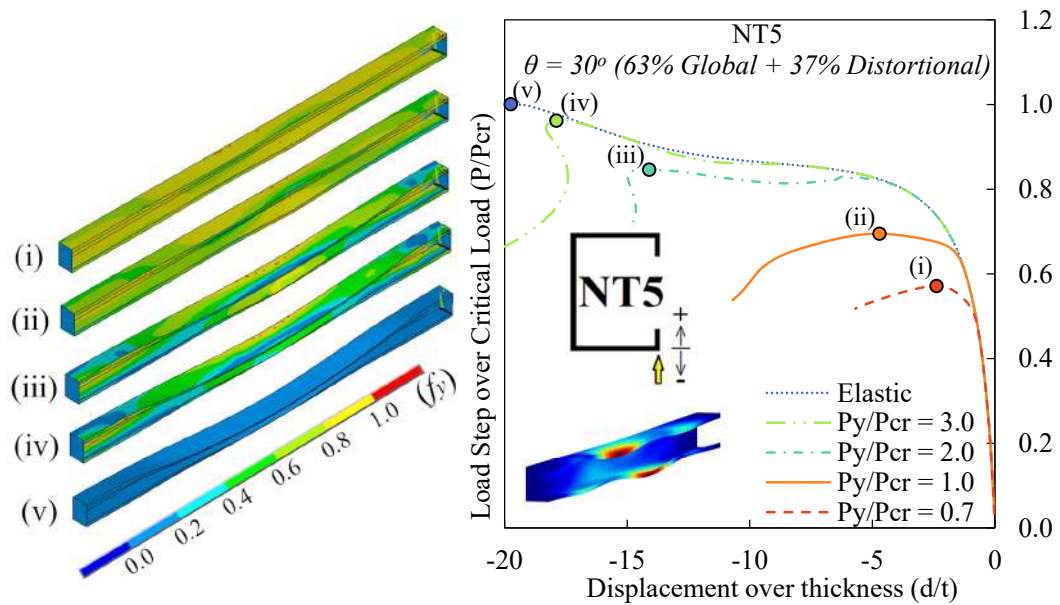


Figure B.6. Post-buckling equilibrium paths, P/P_{cr} vs. d/t of displacement NT5 at $0.4L$, with $\theta = 30^\circ$ (63% Global and 37% Distortional mode), for different ratios of P_y/P_{cr} , where $P_{cr} = 354.5 \text{ kN}$ and $t = 2.70 \text{ mm}$.

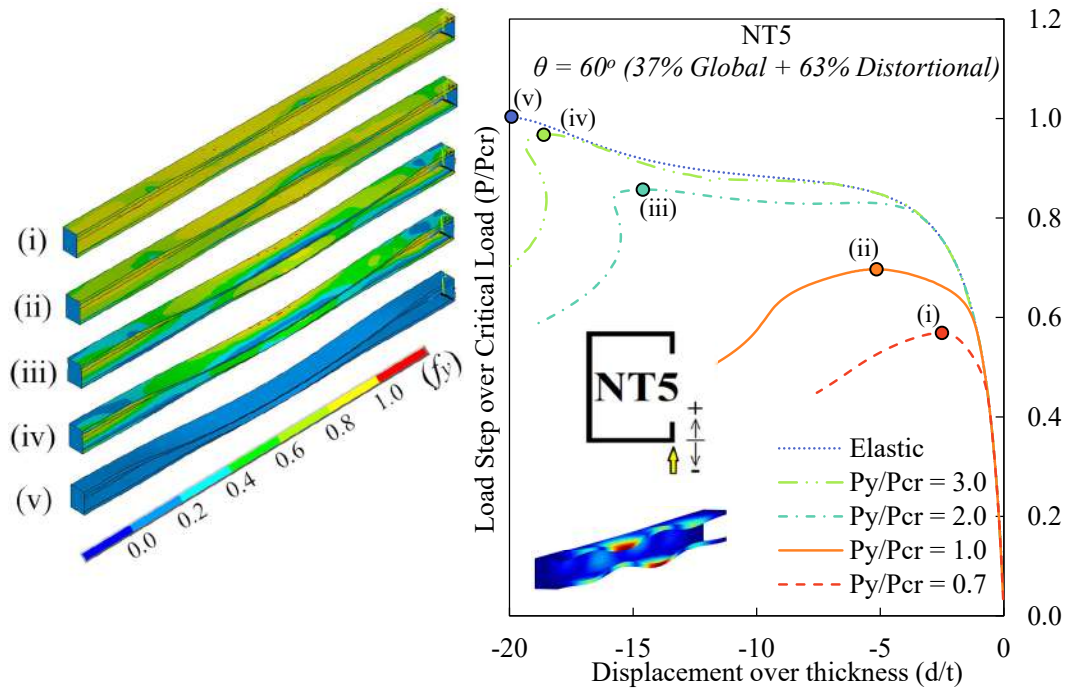


Figure B.7. Post-buckling equilibrium paths, P/P_{cr} vs. d/t of displacement NT5 at $0.4L$, with $\theta = 60^\circ$ (37% Global and 63% Distortional mode), for different ratios of P_y/P_{cr} , where $P_{cr} = 354.5 \text{ kN}$ and $t = 2.70 \text{ mm}$.

APPENDIX C

Table C.1. Complete modal participation of LC 100x70x15x2.70 mm columns with different lengths, for first and second mode.

<i>Initial geometric imperfections Information</i>								
Imp. Mode	<i>L</i> [mm]	Mode Type*	Critical Load [kN]	Half-wave [#]	Modal Participation (CUFSM Vector Norm)			
					Global [%]	Distortional [%]	Local [%]	Other [%]
First Mode (Signature Curve)	1500	D 1	367.6	3	2.8%	94.3%	2.7%	0.1%
	1550	D 1	367.3	3	3.0%	94.2%	2.8%	0.1%
	1600	D 1	365.5	4	1.6%	95.4%	2.9%	0.1%
	1650	D 1	362.5	4	1.6%	95.5%	2.7%	0.1%
	1700	D 1	360.1	4	1.6%	95.7%	2.6%	0.1%
	1750	D 1	358.3	4	1.6%	95.8%	2.5%	0.1%
	1800	D 1	357.0	4	1.6%	95.8%	2.5%	0.1%
	1850	G 1	354.5	1	88.6%	11.0%	0.3%	0.1%
	1900	G 1	339.6	1	89.7%	9.9%	0.3%	0.1%
	1950	G 1	325.4	1	90.7%	9.0%	0.3%	0.1%
	2000	G 1	312.0	1	91.5%	8.2%	0.3%	0.1%
	2050	G 1	299.4	1	92.3%	7.4%	0.2%	0.1%
	2100	G 1	287.4	1	92.9%	6.8%	0.2%	0.1%
	2150	G 1	276.2	1	93.5%	6.2%	0.2%	0.1%
2200	G 1	265.5	1	94.1%	5.7%	0.2%	0.1%	
Superior Mode	1500	G 4	473.1	1	73.1%	26.1%	0.7%	0.1%
	1550	G 4	456.5	1	76.8%	22.5%	0.6%	0.1%
	1600	G 3	438.9	1	79.8%	19.6%	0.6%	0.1%
	1650	G 3	421.1	1	82.2%	17.2%	0.5%	0.1%
	1700	G 3	403.6	1	84.2%	15.3%	0.5%	0.1%
	1750	G 3	386.5	1	85.9%	13.6%	0.4%	0.1%
	1800	G 3	370.1	1	87.3%	12.2%	0.4%	0.1%
	1850	D 2	356.2	4	1.6%	95.8%	2.4%	0.1%
	1900	D 2	355.7	4	1.7%	95.8%	2.5%	0.1%
	1950	D 2	355.5	4	1.7%	95.7%	2.5%	0.1%
	2000	D 2	355.1	5	1.7%	95.5%	2.6%	0.1%
	2050	D 2	353.5	5	2.0%	95.4%	2.5%	0.1%
	2100	D 2	352.1	5	2.3%	95.3%	2.3%	0.1%
	2150	D 2	351.1	5	2.6%	95.0%	2.2%	0.1%
2200	D 2	350.3	5	2.9%	94.8%	2.2%	0.1%	

* Mode abbreviation name and superior buckling order, e.g. D 2: Distortional Second Buckling Mode, G 1: Global (Flexural-Torsional) First Buckling Mode

Table C.2. Modal combination of all modes and pure modes for distortional and global modal shapes, of LC 100x70x15x2.70 mm columns with different lengths.

Analysis Type	L [mm]	Distortional Buckling Mode				Global Buckling Mode			
		Mode* [#]	Half-wave [#]	%Dist.† [%]	P_{crD} [kN]	Mode* [#]	Half-wave [#]	%Global† [%]	P_{crG} [kN]
All Modes (Signature Curve)	1500	1	3	94.3%	367.6	4	1	73.1%	473.1
	1550	1	3	94.2%	367.3	4	1	76.8%	456.5
	1600	1	4	95.4%	365.5	3	1	79.8%	438.9
	1650	1	4	95.5%	362.5	3	1	82.2%	421.1
	1700	1	4	95.7%	360.1	3	1	84.2%	403.6
	1750	1	4	95.8%	358.3	3	1	85.9%	386.5
	1800	1	4	95.8%	357.0	3	1	87.3%	370.1
	1850	2	4	95.8%	356.2	1	1	88.6%	354.5
	1900	2	4	95.8%	355.7	1	1	89.7%	339.6
	1950	2	4	95.7%	355.5	1	1	90.7%	325.4
	2000	2	5	95.5%	355.1	1	1	91.5%	312.0
	2050	2	5	95.4%	353.5	1	1	92.3%	299.4
	2100	2	5	95.3%	352.1	1	1	92.9%	287.4
	2150	2	5	95.0%	351.1	1	1	93.5%	276.2
	2200	2	5	94.8%	350.3	1	1	94.1%	265.5
Pure Modes‡	1500	1	3	100%	396.5	2	1	100%	561.9
	1550	1	3	100%	395.8	2	1	100%	527.4
	1600	1	3	100%	395.6	2	1	100%	496.1
	1650	1	4	100%	393.8	2	1	100%	467.7
	1700	1	4	100%	390.1	2	1	100%	441.7
	1750	1	4	100%	387.2	2	1	100%	417.8
	1800	1	4	100%	384.9	2	1	100%	396.0
	1850	1	4	100%	383.3	2	1	100%	375.9
	1900	1	4	100%	382.3	2	1	100%	357.3
	1950	2	4	100%	381.7	1	1	100%	340.2
	2000	2	4	100%	381.5	1	1	100%	324.3
	2050	2	5	100%	381.4	1	1	100%	309.6
	2100	2	5	100%	379.8	1	1	100%	295.9
	2150	2	5	100%	378.0	1	1	100%	283.2
	2200	2	5	100%	376.6	1	1	100%	271.3

* Buckling mode order number

† Modal Participation from CUFSM in Vector Norm

‡ Pure modes obtained with CUFSM

Table C.3. Ultimate load of LC 100x70x15x2.70 mm columns under different type of initial geometric imperfection combination with L=1850 mm.

<i>fy</i>	Theta	Pu
[MPa]	[Degrees]	[kN]
345	0	204.6
	15	204.2
	30	202.5
	45	201.7
	60	201.7
	75	201.8
	90	200.6
	105	201.8
	120	201.7
	135	201.7
	150	202.5
	165	204.2
	180	204.6
	195	204.2
	210	202.5
	225	201.7
	240	201.7
	255	201.8
	270	200.6
	285	201.8
300	201.7	
315	201.7	
330	202.5	
345	204.2	
508	0	255.2
	15	246.8
	30	246.4
	45	246.2
	60	247.0
	75	249.5
	90	261.7
1016	0	294.5
	15	297.6
	30	300.0
	45	301.9
	60	303.8
	75	306.0
	90	348.4
1523	0	339.4
	15	340.4
	30	341.2
	45	342.1
	60	343.1
	75	344.0
	90	Not Conv.

Table C.4. Slenderness and ratios of LC 100x70x15x2.70 mm column, with different yield stress and length.

f_y	L	Pure Critical Load*		λ_D	λ_G	λ_{max}	$R_{\lambda GD}$	R_{GD}
		P_{crD}	P_{crG}					
		[kN]	[kN]					
345	1500	396.5	561.9	0.78	0.66	0.78	0.84	1.42
	1550	395.8	527.4	0.78	0.68	0.78	0.87	1.33
	1600	395.6	496.1	0.78	0.70	0.78	0.89	1.25
	1650	393.8	467.7	0.78	0.72	0.78	0.92	1.19
	1700	390.1	441.7	0.79	0.74	0.79	0.94	1.13
	1750	387.2	417.8	0.79	0.76	0.79	0.96	1.08
	1800	384.9	396.0	0.79	0.78	0.79	0.99	1.03
	1850	383.3	375.9	0.79	0.80	0.80	1.01	0.98
	1900	382.3	357.3	0.79	0.82	0.82	1.03	0.93
	1950	381.7	340.2	0.80	0.84	0.84	1.06	0.89
	2000	381.5	324.3	0.80	0.86	0.86	1.08	0.85
	2050	381.4	309.6	0.80	0.88	0.88	1.11	0.81
	2100	379.8	295.9	0.80	0.90	0.90	1.13	0.78
	2150	378.0	283.2	0.80	0.92	0.92	1.16	0.75
	2200	376.6	271.3	0.80	0.94	0.94	1.18	0.72
508	1500	396.5	561.9	0.95	0.80	0.95	0.84	1.42
	1550	395.8	527.4	0.95	0.82	0.95	0.87	1.33
	1600	395.6	496.1	0.95	0.85	0.95	0.89	1.25
	1650	393.8	467.7	0.95	0.87	0.95	0.92	1.19
	1700	390.1	441.7	0.95	0.90	0.95	0.94	1.13
	1750	387.2	417.8	0.96	0.92	0.96	0.96	1.08
	1800	384.9	396.0	0.96	0.95	0.96	0.99	1.03
	1850	383.3	375.9	0.96	0.97	0.97	1.01	0.98
	1900	382.3	357.3	0.96	1.00	1.00	1.03	0.93
	1950	381.7	340.2	0.97	1.02	1.02	1.06	0.89
	2000	381.5	324.3	0.97	1.05	1.05	1.08	0.85
	2050	381.4	309.6	0.97	1.07	1.07	1.11	0.81
	2100	379.8	295.9	0.97	1.10	1.10	1.13	0.78
	2150	378.0	283.2	0.97	1.12	1.12	1.16	0.75
	2200	376.6	271.3	0.97	1.14	1.14	1.18	0.72
1016	1500	396.5	561.9	1.34	1.12	1.34	0.84	1.42
	1550	395.8	527.4	1.34	1.16	1.34	0.87	1.33
	1600	395.6	496.1	1.34	1.20	1.34	0.89	1.25
	1650	393.8	467.7	1.34	1.23	1.34	0.92	1.19
	1700	390.1	441.7	1.35	1.27	1.35	0.94	1.13
	1750	387.2	417.8	1.36	1.30	1.36	0.96	1.08
	1800	384.9	396.0	1.36	1.34	1.36	0.99	1.03

1850	383.3	375.9	1.36	1.38	1.38	1.01	0.98
1900	382.3	357.3	1.36	1.41	1.41	1.03	0.93
1950	381.7	340.2	1.36	1.45	1.45	1.06	0.89
2000	381.5	324.3	1.37	1.48	1.48	1.08	0.85
2050	381.4	309.6	1.37	1.52	1.52	1.11	0.81
2100	379.8	295.9	1.37	1.55	1.55	1.13	0.78
2150	378.0	283.2	1.37	1.58	1.58	1.16	0.75
2200	376.6	271.3	1.37	1.62	1.62	1.18	0.72

LC 100x70x15x2.70 mm, with area of the cross-section 699.8 mm²

* Obtained as pure modes from CUFSM

Table C.5. Ultimate load and nominal axial strength of LC 100x70x15x2.70 mm columns for different yield stress and length.

<i>f_y</i>	<i>L</i>	<i>P_u</i>		<i>P_{nD}</i>	<i>P_{nG}</i>	<i>P_{nDG}</i>	<i>P_{nGD}</i>
		<i>0.5G+0.5D</i>	<i>1G+0G</i>				
[MPa]	[mm]	[kN]	[kN]	[kN]	[kN]	[kN]	[kN]
345	1500	209.8	217.70	215.7	201.7	189.1	183.7
	1550	208.3	216.25	215.6	199.3	187.3	181.7
	1600	208.3	214.73	215.5	197.0	185.6	179.7
	1650	207.1	212.89	215.2	194.5	183.6	177.5
	1700	206.0	211.16	214.6	192.1	181.5	175.1
	1750	204.5	209.00	214.2	189.6	179.3	172.8
	1800	203.1	206.93	213.8	187.1	177.2	170.5
	1850	201.4	204.86	213.5	184.5	175.2	168.3
	1900	199.7	202.14	213.3	182.0	173.2	166.2
	1950	197.7	199.53	213.2	179.4	171.2	164.0
	2000	189.7	196.75	213.2	176.8	169.2	161.9
	2050	187.7	193.85	213.2	174.2	167.2	159.8
	2100	185.6	190.83	212.9	171.6	165.1	157.5
	2150	183.5	187.68	212.6	169.0	162.9	155.3
2200	181.3	184.39	212.3	166.4	160.7	153.0	
508	1500	267.5	284.0	278.3	272.8	234.6	226.2
	1550	262.4	281.8	278.1	268.1	231.7	223.0
	1600	266.2	279.5	278.0	263.4	228.9	219.9
	1650	262.2	275.8	277.5	258.6	225.8	216.5
	1700	258.1	271.2	276.5	253.8	222.2	212.8
	1750	253.9	266.0	275.7	249.0	218.8	209.2
	1800	249.6	260.8	275.1	244.2	215.4	205.7
	1850	245.3	255.3	274.7	239.3	212.2	202.3
	1900	240.9	249.7	274.4	234.4	209.0	199.0
	1950	236.2	243.8	274.2	229.6	205.8	195.7
	2000	221.8	237.9	274.1	224.7	202.7	192.5
	2050	217.7	232.1	274.1	219.9	199.5	189.2
2100	213.6	226.2	273.7	215.0	196.1	185.8	

	2150	209.5	220.4	273.2	210.2	192.7	182.4
	2200	205.5	214.7	272.8	205.4	189.2	179.1
1016	1500	349.9	351.9	412.7	418.7	307.2	303.5
	1550	340.7	344.8	412.3	404.4	300.7	297.2
	1600	348.7	336.8	412.2	390.3	294.3	291.1
	1650	337.6	328.2	411.3	376.3	287.4	284.7
	1700	327.5	319.5	409.5	362.4	279.8	277.8
	1750	318.5	310.3	408.0	348.8	272.5	271.1
	1800	310.0	301.4	406.9	335.3	265.3	264.7
	1850	302.1	294.5	406.1	322.1	258.3	258.4
	1900	294.5	287.8	405.6	309.2	251.4	252.2
	1950	287.4	281.4	405.3	296.5	244.6	246.2
	2000	275.8	275.1	405.2	284.1	237.9	240.2
	2050	269.8	269.1	405.1	271.5	230.9	234.3
	2100	264.1	263.2	404.3	259.5	223.7	228.2
	2150	258.5	257.6	403.4	248.4	216.8	222.2
	2200	253.1	252.1	402.7	237.9	210.2	216.4